

ISSN 1913-1844

MODERN APPLIED SCIENCE

**Vol. 3, No. 1
January 2009**



Canadian Center of Science and Education



Contents

Use of Biplane Grids for On-site Studies of Hurricanes <i>S. Firasat Ali</i>	3
The Design of Oil Port Accident Exercise Experiment System Based on Virtual Environment <i>Xin Cao & Shidong Fan</i>	7
Comparative Study on the Antifungal Activity of Some Di- and Tributyltin(IV) Carboxylate Compounds <i>Sutopo Hadi, Mita Rilyanti & Nurhasanah</i>	12
Web Service with Chinese Language in Great Toronto Area <i>Feng Ding & Yanzhang Wang</i>	18
Free Convection over a Vertical Plate in a Micropolar Fluid Subjected to a Step Change in Surface Temperature <i>Azizah Mohd. Rohni, Zurni Omar & Adyda Ibrahim</i>	22
Study on Characteristics of Sound Absorption of Underwater Visco-elastic Coated Compound Structures <i>Zhihong Liu & Meiping Sheng</i>	32
Mapping and Quantification of Land Area and Cover Types with Landsat TM in Carey Island, Selangor, Malaysia <i>Hj. Kamaruzaman, J & Mohd Hasmadi, I</i>	42
Microwave Dielectric Characteristics of Single-walled Carbon Nanotubes <i>Xiaolai Liu, Qinghuai Li & Donglin Zhao</i>	51
Laser Effects on Skin Melanin <i>Khalid M. Omar, Khaled A. Al-Khaza'leh, M.S. Jaafar, Y. JIDIN & N. N. Bidi</i>	57
Damage Analysis of 3D Frame Structure under Impulsive Load <i>Wenzhao Fan, Julin Wang, Liming Gao & Shougao Tang</i>	63
Study on Public Agricultural Insurance in China—Based on Xinjiang Mode <i>Yu Zheng, Juan Zhang & Wangxi Wang</i>	71
Fabrication of LaNiO ₃ Porous Hollow Nanofibers via an Electrospinning Technique <i>Xiangting Dong, Jinxian Wang, Qizheng Cui, Guixia Liu & Wensheng Yu</i>	75
Investigation of Differences of Topographical Map and GIS-derived Spatial Map with Actual Ground Data in Peninsular Malaysia <i>Mohd Hasmadi Ismail & Taylor, J.C.</i>	81
Application of Nano-ZnO on Antistatic Finishing to the Polyester Fabric <i>Fan Zhang & Junling Yang</i>	89
A Proposed Technique for Analyzing Experiments Of Type 2^p3^m <i>Abbas F. M. Alkarkhi & H. C. Low</i>	95
Application Study of Xylo-oligosaccharide in Layer Production <i>Enku Zhou, Xiaoliang Pan & Xiuzhi Tian</i>	103
On the Comparison of Capacitance-Based Tomography Data Normalization Methods for Multilayer Perceptron Recognition of Gas-Oil Flow Patterns <i>Hafizah Talib, Junita Mohamad-Saleh, Khursiah Zainal-Mokhtar & Najwan Osman-Ali</i>	108



Contents

Analysis of Factors to Influence Yarn Dynamical Mechanical Property <i>Qian Wang, Jiankun Wang & Ling Cheng</i>	117
Natural Language Processing for Foreign Languages Learning as Computer-based Learning Tools <i>Ying Zhang & Junyan Liu</i>	125
Treatment and Reuse of Tannery Waste Water by Embedded System <i>S.Krishnamoorthi, Dr.V.Sivakumar, Dr.K.Saravanan & T.V.Sriram Prabhu</i>	129
Study on the Tensile Performance of PTT Fiber <i>Yuanyuan Zheng, Jialu Li & Ruizhou Li</i>	135
Acid Resistance Behavior of Concrete Made Using Untreated and Treated Tannery Effluent <i>K Nirmalkumar & V Sivakumar</i>	139
Study of PVDF Tubular Ultrafiltration Membrane for Separating Oil/water Emulsion and Effect of Cleaning Method on Membrane <i>Huazhang Zhu & Yujie Zhu</i>	144
Strategies for Non-Parametric Smoothing of the Location Model in Mixed-Variable Discriminant Analysis <i>Nor Idayu Mahat, W.J. Krzanowski & A. Hernandez</i>	151
Microstructure and Creep Behaviour of as-cast Ti-48Al-4Cr <i>Esah Hamzah, Maiyeealagan Kanniah & Mohd Harun</i>	164
A Study on the Effects of Higher Order Mode Wave on Mufflers Performance <i>Hongguang Liu, Senlin Lu, Falin Zeng, Zhangping Lu & Jiangkun Zhou</i>	170
Development and Analysis of Taper Tool Path for Micro Turning Operation <i>Azuddin Mamat & Mohd Afif Mohd Rosli</i>	176
The Dynamic Properties of a Perturbation System <i>Lizhen Zhang & Li Jia</i>	187



Use of Biplane Grids for On-site Studies of Hurricanes

S. Firasat Ali

Aerospace Science Engineering Department, Tuskegee University

Tuskegee, AL 36088, USA

Tel: 1-334-727-8853 E-mail: fali@tuskegee.edu

Abstract

For the interactive study of a hurricane after its landfall, a fleet of remotely operated, identical vehicles is proposed to be stationed in its path. Each vehicle would support two biplane grids placed parallel to one another. The positions and orientations of the vehicles would be remotely controlled to steer the frontal area of each grid to be nearly perpendicular to the wind's direction. The paper discusses the expected role of the grids in affecting the mixing of different flow regimes of the hurricane and the decay of its power.

Keywords: Hurricane, Decay, Landfall, Biplane grids, Turbulence, Mixing, Remotely operated vehicles, Interactive study

1. Introduction

Tropical cyclones with different ranges of maximum wind speed have different names. The maximum speed for tropical depressions is 17 m/s or less. For tropical storms, wind speeds range from 18 to 32 m/s. At 33 m/s or more, severe tropical cyclones that are also called hurricanes or typhoons are produced (see Emanuel, 2003). A hurricane, typhoon, or severe tropical cyclone is a magnificent weather phenomenon that will be known primarily for its power of destruction until we develop ways to affect its dynamics and cause decay in its power. As reported by Anthes (1982), attempts to modify a hurricane before its landfall have been made in the past. Our approach is to conduct interactive studies of hurricanes after landfall in an effort to avoid the destruction of dwellings and other property by unusually strong hurricane winds.

In the literature, we find numerous studies of hurricanes at their landfalls. Anthes (1982) has discussed the major physical effects that cause the decay of a hurricane over land. Kaplan and Demaria (1995 and 2001) have developed empirical models for predicting the decay of tropical cyclone winds after landfall. Their 1995 decay model is based on the National Hurricane Center (NHC) wind estimates for storms that made landfall south of 37 degree N latitude in the U.S. from 1967 to 1993. Their 2001 decay model is based on the storms that made landfall north of 37 degree N latitude in the U.S. from 1938 to 1991. Kaplan and DeMaria (2001) have also indicated that their 1995 decay model has been incorporated in the software for emergency management by FEMA (Federal Emergency Management Agency). Demaria et al (2005) have reported that starting from 2000, the effect of storm decay over land has been included in the NHC's Statistical Hurricane Intensity Prediction Scheme (SHIPS). For tropical cyclones that move over narrow landmasses, DeMaria et al (2006) have provided a modified decay model, which reduced the intensity forecast errors by up to 8% relative to the original decay model for several storms from 2001 to 2004. Schneider and Barnes (2005) have reported measurements and analysis for Hurricane Bonnie at its landfall. Bonnie made its landfall at the North Carolina Coastline on August 26, 1998.

Anthes (1982) provides a comprehensive literature-based account of the physics of tropical cyclones and methods of forecasting. Chan (2005) highlights the roles of flow speed, vorticity and latent heat in the tropical cyclone dynamics. He recognizes that with the development of the satellite technology, the predictions of tropical cyclone movement have improved significantly over the past two decades. In making this recognition, Chan has cited Goerss (2000), who notes the use of an ensemble of dynamical models for the predictions. In the official NHC estimates for the Atlantic Basin, the mean hurricane track error for 12 hour prediction was 56 km; since 1990, the 24 – 72 h forecast errors have been reduced by 50% (see Franklin, 2007).

The literature on a hurricane's dynamics after its landfall, including the prediction of its track, provides adequate knowledge for promoting research aimed at interactive in-field studies. For extending this knowledge, it appears worthwhile to explore different methods of physical interaction with hurricanes over land. As a method of physical interaction, this presentation proposes the use of biplane grids placed in the path of a hurricane to affect its dynamics and probably to stimulate its decay process. The following paragraphs present the known factors that affect the decay of a hurricane at its landfall; a conceptual configuration for placing biplane grids in a hurricane's path at its landfall; and the anticipated effect on the decay of hurricane power.

2. Hurricane's decay at its landfall

A relatively detailed account of a hurricane's structure is provided by Holland, Simpson and Simpson (2002) in the McGraw-Hill Encyclopedia of Science and Technology. A hurricane consists of a cloud-free eye encircled by an eye wall of clouds, which is surrounded by spiral bands of rain. Speeds of air flow are different in different regions. Highest speeds occur in the eye wall region. To gauge typical sizes of hurricanes, Emanuel (1991) notes that near the ocean surface the radius of high winds ranges from 10 to 100 km and the height of spiral bands of clouds and precipitation ranges from 3 to 15 km.

Anthes (1982) mentions three major physical effects leading to the decay of a hurricane over land. First is the reduction in evaporation as the storm leaves the ocean, which decreases one source of the hurricane's energy, that coming from the condensation of vapors. A second effect is that the land is cooler than the ocean, and thus the low-level air is cooled. The third effect is the increase in surface roughness which produces a corresponding increase in the drag. The roughness parameter over land is 30 or more times that of the ocean surface. Emphasizing that over land a hurricane has no increase in its power, Hayden (2006) declares that landfall is a death sentence for a hurricane. As an exceptional case study, however, Bosart and Lackman (1995) have identified the post-landfall re-intensification of Hurricane David in 1979. Emanuel (2005), in his discussion on post landfall decay of a hurricane, has included factors that can lead to the occasional rejuvenation.

3. Turbulence and mixing from a biplane grid

A biplane grid consists of a number of solid cylindrical rods placed parallel to each other and equally spaced in a plane (the first plane), with the same number of rods of the same size placed in a second plane that is parallel and close to the first one. Every rod in the second plane is perpendicular to those in the first plane. A nonturbulent flow, when it passes through such a biplane grid, would become turbulent. Pope (2000) has used the name "turbulence generating grid" for "biplane grid," and has provided a sketch that illustrates its mesh size. In routine studies, a grid is placed in a flow with its area being perpendicular to the flow direction; that area may be termed the frontal area. The turbulence research community has essentially used biplane grids in wind tunnels to study the behavior of homogeneous isotropic turbulence (see Comte-Bellot and Corrsin, 1966). Environmental engineers have also used biplane grids to affect mixing in fluids (see Liem and Smith, 1999). For a study of homogeneous turbulence in a wind tunnel, Tucker and Ali (1976) have used a perforated sheet instead of a biplane grid. For this study, however, we propose the use of a biplane grid.

If any fluid flow has turbulent and nonturbulent flow regimes, they are separated by a sharp interface known as the viscous super layer (see Pope, 2002 and Ali and Ibrahim, 1996). In a hurricane, we recognize an eye, an eye wall, and spiral rain bands as distinct flow regimes. Therefore, we expect that a hurricane includes both turbulent and nonturbulent flow regimes separated by viscous super layers. Imagine a system of biplane grids of an effective mesh size smaller than a meter, and a frontal area of a few thousand sq m placed in the path of a hurricane at its landfall. In the flow subjected to passing through the grid system, the viscous super layers would tear apart and different flow regimes would get mixed. The grid-affected flow would become turbulent everywhere. The phenomenon of mixing would cause decay in the hurricane's power. Ordinarily, such mixing is limited to a small height from the ground. The presence of a grid would affect a relatively larger height of the flow. Therefore, we anticipate that by encountering a grid in its path, a hurricane would experience appreciable decay in its power.

4. Conceptual configuration of transportable biplane grids

Researchers of turbulent flows have used biplane grids in wind tunnels (see Pope, 2002). A wind tunnel typically has a confined flow. The fan or blower in a wind tunnel maintains the flow through the grid by overcoming its blocking effect. A grid placed in a hurricane would not have any walls or nozzles around it to capture and confine the flow. It would act as an obstacle for blocking the flow, and a significant fraction of the flow would tend to go around the grid instead of going through it. That might jeopardize the desired effect of the grid on the flow.

The proposed transportable grid configuration would consist of 200 identical but non-joined modules, which would be remotely controlled from a central station. A module would consist of two biplane grids placed parallel to each other on a truck trailer or specially designed vehicle. The length of each grid would be nearly the same as the length of the trailer. The height of the grid would not be restricted by the trailer dimensions. The space between the two parallel grids would be the same as the trailer width. For each grid, the proposed approximate dimensions of the frontal area are 10 m length x 10 m height, and the proposed mesh sizes for the front and rear grids are one meter and 0.75 meter, respectively. The space between the front and rear parallel grids would be 3 m. The proposed two-grid configuration is expected to have a smaller blocking effect than a single grid of the same effective mesh size. At any given location being traversed by a hurricane, the wind directions would vary with time. The orientation of each vehicle would be remotely controlled so that the airflow would remain nearly perpendicular to the frontal areas of the grids despite varying wind directions.

A vehicle, together with its grids, is a transportable module so that two hundred modules placed in a certain order make up the complete grid configuration at a target location calculated to encounter a predicted hurricane at its landfall. A driver moves each vehicle from its parking site to the target site, then the driver leaves and the vehicle's movement and maneuvers are thereafter remotely controlled. Each vehicle is equipped with sensors for prescribed flow parameters, so that the sensor signals serve as inputs for remote control of its orientation and movement. A few of the vehicles also accommodate measuring instruments and a data recording facility for study of the flows upstream and downstream of the grid configuration. Measurements of flow velocity, temperature, pressure, and humidity would be of primary interest.

5. Discussion

The mobile biplane grid formation comprised of 200 identical vehicles as non-joined modules, is proposed for on-site interactive study of hurricanes at their landfalls. The remotely controlled vehicle system would have sufficient maneuverability to allow each vehicle to be placed in the predicted hurricane track. The presence of the grid formation in a hurricane's path after its landfall would affect the flow through an area of 2 000 m width x 10 m height. Within 10 m height from the ground, the grid formation would capture the high-speed flow including certain parts of the hurricane's eye and its eye wall. We expect that mixing of different flow regimes in the grid-affected flow would cause a measurable loss in the hurricane's power. The proposed number of vehicles and grid dimensions are open to critical review and changes. For repeated use to study several hurricane landfalls over a few years, every vehicle would have both permanent structural features and non-permanent biplane grids. The biplane grid's geometry and configuration could be progressively evaluated and improved as needed.

The hurricane features that cause damage to dwellings are strong winds, water surges, thunder, and tornadoes. The use of a grid structure has a limited scope of addressing the strong winds at a hurricane's landfall. For the damage due to strong winds, Emanuel (2003) suggests that the amount of damage increases roughly as the square of the intensity of the storms, as measured by their maximum speed. The drags, which contribute to the hurricane's decay, whether due to ground friction or biplane grids, are also proportional to the square of the velocity of the flow stream. Therefore, the placing of a grid formation in the path of a hurricane at its landfall would cause appreciable decrease in the damaging effect.

The challenging tasks required in the conduct of the proposed field study include: (a) to adopt appropriate standards so that the configured modules or vehicles remain structurally stable in strong winds and their functions are not affected by a water surge; (b) to station the grid formation at such a location where the hurricane's eye wall must pass through it, which is highly challenging because the width of the grid formation is only 2 km, whereas a twelve-hour prediction would have a track error of 65 km; (c) to pre-determine the travel routes for moving the vehicles from their parking areas to the anticipated target sites; (d) to obtain the required permissions in advance from relevant administrative bodies for the movement and stationing of the vehicles to be used for interactive hurricane study; (e) to monitor and control the vehicles so that their respective grid frontal areas remain nearly perpendicular to the rapidly changing flow directions.

In support of his global weather control system, Hoffman (2002) hypothesizes that increased accuracy in prediction of atmospheric phenomena would enhance our ability to effectively control them by small perturbations. If we consider the presence of a grid formation of a few thousand square meter frontal area in the path of a hurricane as a small perturbation, then Hoffman's hypothesis encourages us to suggest that an appreciable decay in hurricane power due to the biplane grid is a realistic expectation. In these contexts, however, we must remain cautious that a perturbation of a complex organized flow field may also lead to instability and havoc. List (2004) says, "Interfering with tornadoes and hurricanes is hazardous, should it work, and is encumbered by possible legal challenges. It should await better scientific understanding." For the proposed grid configuration, we would minimize the risks by addressing the above-listed (a) to (e) challenges and requirements.

For measuring the performance of the grid configuration in aiding a hurricane's decay, the velocity data upstream and downstream of the configuration may be compared with the available decay models; for example, the 1995 and 2001 models by Kaplan and Demaria. Moreover, the measurements of different flow parameters upstream and downstream of the grid configuration will be valuable for learning about turbulence characteristics of the hurricane. Therefore, it appears worthwhile to conduct in-field studies to determine these characteristics and the effects of placing a biplane grid in the path of a hurricane at its landfall.

6. Conclusion

It is well recognized that a hurricane decays after landfall due to decreased evaporation, increased surface roughness, and the cooler surface of the land compared with that of the ocean. This study suggests that as an effective turbulence-generating or mixing device, the use of a biplane grid formation would augment the ground effect in causing the hurricane's decay.

The conceptual configuration of biplane grids, which is offered for conducting interactive on-site studies of hurricanes at their landfalls, has the potential to be considered by teams of researchers for further improvements and development. Besides the possibility of augmenting the decay process of hurricane power at its landfall, the interactive studies would generate valuable data on turbulence characteristics of hurricanes. It is understood that enormous challenges will be faced in performing the proposed experiments.

Acknowledgement

The author gratefully acknowledges the editing consultation by the Reverend Diana Allende of Auburn, Alabama, and the encouragement of research pursuits at Tuskegee University.

References

- Ali, S.F. & Ibrahim, E.A. (1996). Coincidence of Turbulent-Nonturbulent Interface and Hot-Cold Interface in a Plane Turbulent Wake, *Mechanics Research Communications*, 23, 91-102.
- Anthes, R.A. (1982). Tropical Cyclones: Their Evolution, Structure and Effects, Meteorological Monograph No. 41, Boston: American Meteorological Society, (Chapter 2).
- Bosart, L.F., & Lackman, G.M. (1995). Postlandfall Tropical Cyclone Reintensification in a Weakly Baroclinic Environment: A Case Study of Hurricane David (September 1979), *Monthly Weather Review*, 123, 3268 – 3291.
- Chan, J.C.L. (2005). The Physics of Tropical Cyclone Motion, *Annual Rev. Fluid Mechanics*, 37, 99-128.
- Comte Bellot, G., & Corrsin, S. (1966). The Use of a Contraction to Improve the Isotropy of Grid Generated Turbulence, *Journal of Fluid Mechanics*, 25, 657-682.
- DeMaria, M., Knaff, J.A., & Kaplan, J. (2006). On the Decay of Tropical Cyclone Winds Crossing Narrow Landmasses, *Journal of Applied Meteorology and Climatology*, 45, 491 – 499.
- Demaria, M., Mainelli, M., Shay, L.K., Knaff, J.A., & Kaplan, J. (2005). Further Improvements to the Statistical Hurricane Intensity Prediction Scheme (SHIPS), *Weather & Forecasting*, 20, 531-543.
- Emanuel, K.. (2005). *Divine Wind*, New York: Oxford, (Chapter 16).
- Emanuel, K.. (2003). Tropical Cyclones, *Annual Rev. Earth and Planetary Sciences*, 31, 75-104.
- Emanuel, K.. (1991). The Theory of Hurricanes, *Annual Rev. Fluid Mechanics*, 23, 179-196.
- Franklin, J.L. (2007). “2006 National Hurricane Center Forecast Verification Report”, 22 February 2007, http://www.nhc.noaa.gov/verification/pdfs/Verification_2006.pdf, visited on May 21, 2008.
- Goerss, J.S. (2000). Tropical Cyclone Track Forecasts Using an Ensemble of Dynamical Models, *Monthly Weather Review*, 128, 1187-93.
- Hayden, T. (2006). Super Storms, *National Geographic*, v210, n2, p 66 - 77
- Hoffman, R.N. (2002). Controlling the Global Weather, *Bulletin of American Meteorological Society*, 83, 241-248.
- Holland, G., Simpson, J., & Simpson, R. (2002). Hurricane, *McGraw-Hill Encyclopedia of Science and Technology*, 9th ed., 8, 653-658.
- Kaplan, J., & DeMaria M. (2001). On the Decay of Tropical Cyclone Winds after Landfall in the New England Area, *Journal of Applied Meteorology*, 40, 280-287
- Kaplan, J., & DeMaria M. (1995). A Simple Empirical Model for Predicting the Decay of Tropical Cyclone Winds after Landfall, *Journal of Applied Meteorology*, 34, 2499-2512.
- Liem, L.E., & Smith, D.W. (1999). Turbulent Velocity in Flocculation by Means of Grids, *Journal of Environmental Engineering*, 125, 224-233.
- List, R. (2004). Weather Modification – A Scenario for the Future, *Bulletin of American Meteorological Society*, 85, 51-63.
- Pope, S.B. (2000). *Turbulent Flows*, Cambridge: Cambridge University Press, (Chapter 5).
- Schneider, R., & Barnes, G. (2005). Low Level Kinematic, Thermodynamic and Reflectivity Fields Associated with Hurricane Bonnie (1998) at Landfall, *Monthly Weather Review*, 133, 3243-3259.
- Tucker, H.J., & Ali, S.F. (1976). Decay of Anisotropic Turbulence, *AIAA Journal*, 11, 546-548.



The Design of Oil Port Accident Exercise Experiment System Based on Virtual Environment

Xin Cao

School of Energy and Power Engineering

Wuhan University of Technology

Wuhan 430063, China

Nanjing Maritime Safety Administration of the People's Republic of China

Nanjing 210011, China

Tel: 86-25-5187-7538 E-mail: caoxin1981@163.com

Shidong Fan

School of Energy and Power Engineering

Wuhan University of Technology

Wuhan 430063, China

Abstract

Taking large scale equipments of oil storage and transportation port as research objects, in this article, we establish the oil port accident exercise experiment system under the virtual environment, which mainly includes the visual modeling construction of oil port equipment, the virtual equipment accident reasoning system and the reliability evaluation and safety evaluation system of oil equipment, in order to realize the accident reasoning, simulation, demonstration, and danger and reliability evaluation of oil equipments under the virtual environment.

Keywords: Virtual simulation, Accident exercise, Oil port safety evaluation

1. Research background and meanings

With the quick development of Chinese economy and society, oil has been the energy with maximum import demand and quick increase. At present, the oil import of China is mainly from Middle East, Africa and South America, and the transportation is mainly completed by ocean shipping. To fulfill the developmental demand of oil ocean shipping, Chinese oil special dock and oil storage business are developed quickly, and various regions establish special docks for the oil storage and transportation, and form the oil transportation port area with certain scale, which are mainly centralized in the eastern littoral from Bohai Bay to Beibu Gulf.

The shipping of oil has many characters such as large capacity, few middle tache, quick turnover, charge savings of package, barrel, storage, cleanout and disposal, few goods loss and large economic benefit and social benefit. But it has also large hidden dangers, and the security of oil storage and transportation dock comes down to the load and unload of oil ship, the acceptance and dispatch operation of oil goods, the oil storage in the storeroom, the oil pipe and other important danger sources. Because the dock stores large base oil, and oil is a sort of flammable, toxic and harmful chemical material, once accident happens, it will induce not only large fortune loss and personnel casualty, but abominable social influence and serious environmental pollution. Therefore, the safe production of oil storage and transportation dock has important meaning. In the 41st chapter of "Outline of the 11th Five-Years Plan for National Economic and Social Development", China had definitely put forward the requirement to implement supervision and alarming for important danger sources.

In the present stage, Chinese oil port storage and transportation still have many hidden troubles of security, which are mainly represented in that the security management mode of oil dock storage and transportation is not mature, and the timely danger evaluation in the process of oil dock storage and transportation and the application degrees of modern security management based on the computer technology in oil port personnel training, information sharing, production and preparation, accident emergency rescue are low. So, the security production of oil storage and transportation dock must follow the strategy of "Modern Technology to improve Safety", use modern information technology to establish the security supervision and management information system, and enhance the securities of oil load and unload, oil tank,

oil pipe and oil transportation vehicle to enhance the security production management level of enterprise through informationization.

2. Research contents of virtual accident excise system

The study of the oil port accident excise experiment system under the virtual environment takes the large scale equipment of oil storage and transportation dock as research objects, starts from the establishment of 3D entity model, establishes the high visual information carrier based on equipment component, takes equipment status parameters, accident mode and accident class as information source, studies the large equipment accident reasoning technology and simulation (demonstration) technology in the virtual environment, and forms the accident simulation system.

The design and research content of the system mainly include following aspects.

(1) High visual failure modeling technology of oil port equipment component

Adopt OO technology, take status parameters of key equipment component in oil port (including equipment figure structure, physical attribute, functional attribute, mechanical attribute and electric attribute), accident mode and accident class as character attributes, establish the 3D entity model of equipment component, and establish the high visual equipment failure model of oil port equipment components.

(2) Establish the equipment accident reasoning system in the virtual environment

Apply the accident excise technology, establish the representative accident reasoning system of oil port key equipment, and establish the representative accident process demonstration system of oil port key equipments.

(3) Establish the reliability evaluation and safety evaluation system of oil port equipment

Establish the reliability mode and safety model of oil port key equipments, and establish the reliability and security evaluation system of oil port key equipments.

(4) Establish the base of emergency rescue strategy and emergency rescue program

Establish the emergency rescue strategy decision system and emergency rescue program based on oil port storage and transportation, constitute the preventative maintenance strategy, maintenance measure and repair program after accident for oil port equipments.

(5) Research and develop 3D virtual repair system

Develop the 3D virtual repair system based on oil port key equipment for the failure orientation demonstration, accident happening process demonstration, preventative maintenance demonstration, repair process demonstration after accident and accident influence sequent demonstration.

3. Anticipated aims of system research and development

The anticipated total aim of the oil port accident excise system based on virtual environment is to offer the high visual model of oil port equipment system, realize the virtual visual reasoning of accident, offer repair strategy and repair program support for various representative accidents and demonstrate them in the virtual environment.

The anticipated function and aim are seen in Figure 1, and the concrete aims include following aspects.

(1) Establish high visual accident model

As an object, the model should not only express the figure structure of equipment, but include the physical attribute, function attribute, mechanic attribute and electric attribute of equipment, and present the equipment attributes by the obvious and convenient form.

(2) Realize representative accident reason reasoning

Classify the accident, summarize the inducing factor of accident, form the accident expert knowledge base, adopt the outline analysis method, apply the fishbone diagram description to realize the accident orientation reasoning.

(3) Realize the process demonstration of representative accident

Present the accident by the simple forms (diagram, simulation and table) to the decision-maker to realize scientific decisions. The demonstration system could bring forth the process of the equipment from normal working status to the failure status, present the terrain range influenced by the accident, calculate the economic loss and evaluate the influencing degree to the public security.

(4) Design and establish complete emergency rescue program base

(5) Virtual accident simulation

4. System structure and technical method

The system structure and technical method are seen in Figure 2, which include following aspects.

4.1 High virtual failure modeling technology of oil equipment components

Model is a necessary tool in the development process of information system, and modeling is the basic and necessary work to establish the information system. The information system could be regarded as composing by a series of ordered models which usually include function model, information model, data model, control model and decision-making model.

In the development process of this system, we need information system modeling and 3D entity modeling. To establish the failure model of oil port equipment component mainly comes down to the 3D entity modeling technology.

There are many 3D entity modeling tools, and common modeling software include Pro/E, UG, SolidWorks, 3DMax and so on (Ren, 2005), and some of them have simple function and some have complex function, and some modeling methods are based on the character, and some modeling methods are entity geometry modeling. Above modeling tools all can obtain geometric entity, and relative to the requirement of equipment accident excise system, they still lack necessary attribute information, physical character and failure character information. When applying existing entity modeling tools, we should emphasize to study many information problems such as function attribute, mechanic attribute and accident mode attribute based on the geometric model.

However, because the geometric model constructed by common 3D modeling software is usually large, and when making cartoon simulation by directly introducing virtual scene, the existing PC could not acquire smooth cartoon effect. In recent years, VRML technology (Dong, 2002, p.210-214, Feng, 2006, p.387-390, Ren, 2005 & Sang, 2001) has been applied in simulation cartoon better, and it is a good choice to adopt VRML to describe the entity geometric model, attribute information and failure information.

This system will adopt OO information modeling method, apply VRML technology (or Pro-e, 3DMax, UG and SolidWorka) entity modeling tool, establish the equipment model and system model, describe attribute information and failure information aiming at the oil port storage and transportation system and large scale equipment, and modify the equipment model according the historical data of actual operation, and finally obtain the operation rule of equipment at the reaction locale and the coupling relationship among various parameters, and these relationships will be basic proof as the reasoning deduction of accident and form the expert knowledge base.

Another research emphasis of the oil port equipment component failure modeling technology is the complementary information taking the oil port equipment coupling danger as 3D entity model. At present, the security of oil port mainly takes the hidden danger and failure mode of independent equipment part as the research object (Wu, 2005), but the oil port equipments and work flow are the organic integration connecting and coupling each other, so any failure happens to any one point or any problem occurs in any one equipment which will influence and affect the whole system instantly, and if the disposal is not timely and the control measure is not proper, the chain-reaction will always be induced and the accident will be extended. Therefore, we should fully consider the coupling problem of multiple factors and multiple type failures when establishing the oil port equipment failure mode mechanism base.

4.2 Accident reasoning system of oil port equipment

The accident reasoning is the process to deduce the conclusion from existing facts according to certain accident happening rules. At present, usual methods to analyze the accident reasoning include the reasoning method based on signal transformation, the reasoning method based on the expert system, the reasoning method based ANN, and the reasoning method based on integrated intelligent system. Above methods have their own problems more or less, especially when complex failure occurs in the system or the interference happens because of various reasons, information will lose and uncertain factors will increase, so the forward and backward reasoning is more and more favored by people.

In the research domain of safety science, usual methods in accident reasoning mainly include fault tree analysis (FTA) and event tree analysis (ETA). FTA and ETA study accident mode through system safety analysis (SSA), summarize inducing factors of accident, form the accident reasoning demonstration of fishbone diagram by the tree structure analysis method, and realize the accident orientation reasoning. In recent years, with the large-scale tendency and complication of the industrial system, the research of accident deduction technology based on fuzzy reasoning is continually deepening. The fuzzy reasoning is a sort of uncertain reasoning by fuzzy knowledge, and the thing disposed by it is fuzzy, and the concept has not specific extension, and it is hard to definitely denote whether one object accords with the concept, so the fuzzy reasoning is the expression and disposal for the uncertainty (Xiang, 2005).

The oil port equipment accident reasoning system will comprehensively utilize the example reasoning (Wu, 2005), forward and backward reasoning (Nie, 2005) and fuzzy reasoning technology to analyze the parameter association in potential accident according to the early failure alarming information of equipment, and find out the possibility which will induce the accident of equipment, and use the virtual visual method to deduct the happening and development process of accident, and accordingly arrange proper equipment examining and maintenance plan, constitute relative anti-accident measure and program, and finally realize the real-time maintenance for equipments.

4.3 Virtual simulation system

The virtual simulation system is a sort of technology which utilizes the computer software to simulate actual locale and objects to implement scientific experiment, and it is the necessary measure to implement analysis, design, experiment and evaluation for many complex system (engineering or non-engineering). According to the applied object, it could be divided into the model simulation and view simulation.

The research and development hotspots of virtual simulation technology mainly include OO simulation, DIS (distributed interactive simulation), intelligent simulation, visual simulation, multimedia simulation and virtual reality simulation (Zhao, 2007). The virtual visual technology, simulation technology and virtual reality technology are more and more concerned in the domain of equipment safety by people, but present foreign and domestic researches still have not apply the virtual simulation technology combining visual technology, simulation technology and virtual reality technology in accident diagnosis and orientation, accident development process demonstration, accident statues expression and accident damage evaluation for oil port equipments.

The oil port equipment virtual simulation system takes the Windows NT ADAMS (automatic dynamic analysis of mechanical system) 10.0 as the original version, comprehensively utilizes the visual simulation technology, multimedia simulation technology and virtual reality simulation technology to realize the oil equipment and liquid transportation (3D) virtual scene, places different equipments in the virtual scene according to the distribution of oil port establishment (equipments), and establishes living 3D system through particularly describing the attributes of equipments and visual interactive interface. For the software construction, the system is composed by basic simulation demonstration units which have complete network interface and could realize the connection with the main control platform, the association with multiple personnel and the cooperative demonstration.

4.4 Reliability evaluation and safety evaluation system of oil port equipment

The project of oil port safety evaluation relates to many aspects such as the intrinsic harm of goods, the berthing and unberthing work, the loading and unloading work, and the storage work. Oil products generally possess many characters such as flammability, explosion hazard, volatility, static charge accumulation, diffusion and fluidity, heat dilatibility, toxicity, oxidant contact hazard and high acid, so the project of oil storage and transportation dock generally possess many potential dangerous factors such as fire, explosion, poisoning asphyxia, chemical burn, electric harm, mechanical harm, object shocking, high falling, collapse, drowning, ship collision, poison harm and yawp harm. In addition, in the dock work process, many potential dangers such as cable breaking, oil pipe breaking and personnel dropping and being smashed still exist.

At present, the evaluation methods used in oil port storage and transportation dock mainly include advance danger analysis method, safety checking table method, important danger source differentiation method, fault tree analysis method, work condition danger evaluation method, large accident consequence analysis method, liquid leaking model evaluation method and some safety evaluation methods combing quantitative analysis with qualitative analysis. According the time stage of safety evaluation, the evaluations include oil port safety prevaluation, oil port checking and accepting safety evaluation, oil port storage and transportation actuality safety evaluation and oil port special safety evaluation.

The safety evaluation content of the system is mainly to establish the reliability evaluation model and danger evaluation model of oil port key equipments. Combining the Weibull distributed information of oil port equipment life, we utilize Monte Carlo simulation method to simulate the accident happening frequency in certain term, establish the reliability evaluation system of oil port equipment through building the reliability block diagram (RBD) of key equipments. We take many key equipments and work flows such as oil ship loading and unloading work, oil tank accepting and dispatching flow and oil pipe as research objects, take oil port overall arrangement, overall plane collocation, oil dock loading and unloading technology, berthing ability, fire fighting establishment, electric safety, anti-thunder and anti-static, special equipments, oil port loading and unloading machines, dock engineering quality and structure safety, dock affiliated establishment, safety management, labor and sanitation and emergency rescue as main contents of safety evaluation, consider the influencing degree of accident consequence degree (including induced social influence, economic loss and environmental influence) based on the reliability evaluation system, and establish the accident danger evaluation model of oil equipments.

5. Conclusions

To design and study the oil port accident exercise experiment system in virtual environment could realize the accident simulation of oil port equipment. In this article, we take the oil port key equipments (oil tanker, oil storeroom, transportation pipe and so on) as objects, take the representative accident mode of oil equipment as information source, take the high visual equipment model as information carrier, study the oil port equipment accident excise technology in the virtual environment, and realize the virtual support environment and platform of accident analysis and danger evaluation.

References

- Dong, Xinghui & Xu, Xiaohui. (2002). Implementation of Visualization for 3D Collaborative Assembling Based on VRML. *Journal of Engineering Graphics*. No. 23(2). p. 210-214.
- Feng, Guizhen, Chi, Jianbin, Wangchen & Wang, Daming. (2006). Design and Implementation of Visual Interactive Manipulation in Model Builder of VRML. *Journal of System Simulation*. No. 18(2). p. 387-390.
- Nie, Xiaotang, Duan, Qizhi & Peng, Zhiquan. (2005). Study on Fault Diagnosis Method for Transmission Network. *Central China Electric Power*. No. 5.
- Ren, Yilin, Wen, Youxian & Li, Xurong. (2005). Application of 3D Modeling on Engineer Designing. *Journal of Agricultural Mechanization Research*. No. 4.
- Sang, Haiquan, Liuji & Wei, Lijun. (2001). Research of Safety Monitoring System for The Petrochemicals Dock of Haven. *China Science and Technology Information*. No. 22.
- Wu, Lianggang. (2005). *Study on the Fuzzy Expert System Based on Examples*. Master's Thesis of Central South University.
- Xiangyan & Wang, Hongyuan. (2005). Research and Application of Expert System Based on Fuzzy Inference Model. *Computer Engineering*. No. 31(10).
- Zhao, Haihui, Meng, Chuicheng & Shuqi. (2007). The Application of VR Design and Simulation in Oil Machinery Design. *Journal of Engineering Graphics*. No. 4.

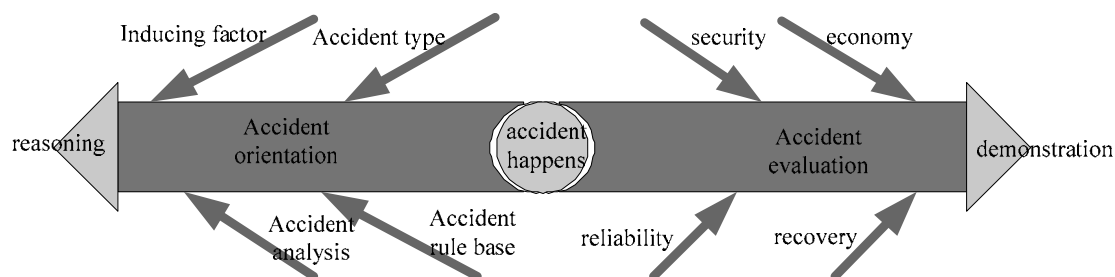


Figure 1. Total Aim of System

Oil Port Accident Exercise Experiment Platform in Virtual Environment

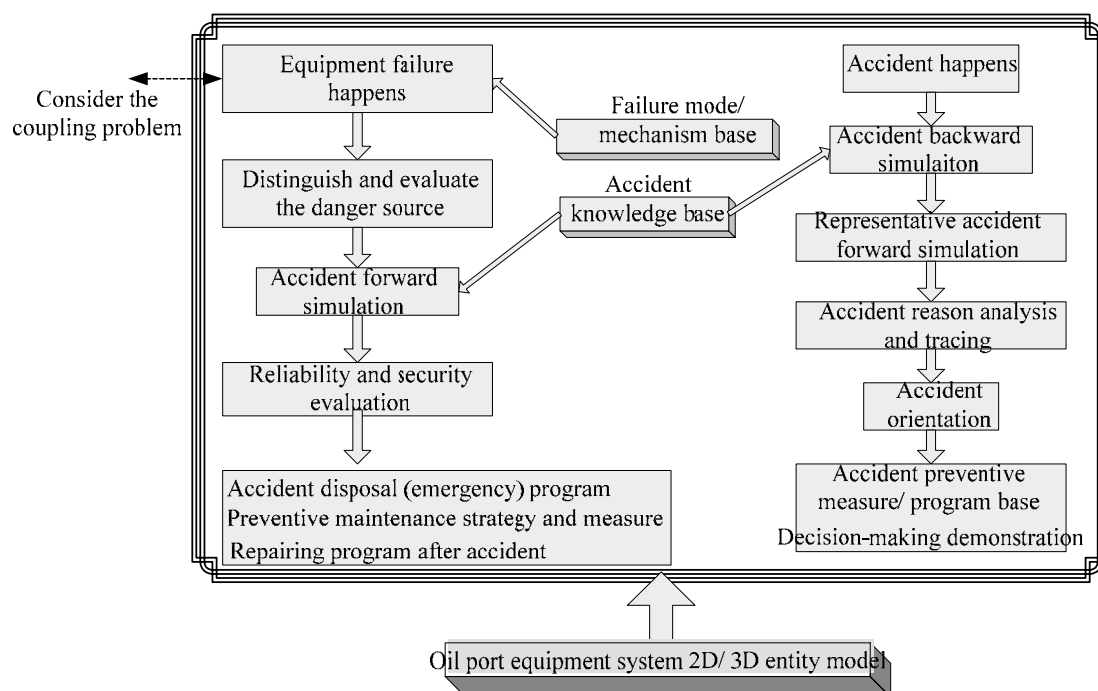


Figure 2. Technical Method



Comparative Study on the Antifungal Activity of Some Di- and Tributyltin(IV) Carboxylate Compounds

Sutopo Hadi (Corresponding author)

Mita Rilyanti

Nurhasanah

Department of Chemistry

University of Lampung

Bandar Lampung 35145 Indonesia

Tel: 62-813-6905-9733 E-mail: sutopohadi@unila.ac.id

Abstract

A series of di- and tributyltin(IV) carboxylate compounds prepared by reacting the dibutyltin(IV) dichloride and tributyltin(IV) chloride respectively *via* the organotin(IV) oxide with the respective carboxylic acids have been tested for antifungal activity against *Fusarium oxysporum* and *Aspergillus niger* in potatoes dextrose agar. The compounds synthesized were mainly characterized with IR and UV-Vis spectroscopies as well as based on the microanalytical data. The results showed that di- and tributyltin(IV) carboxylates prepared in general exhibit greater fungitoxicity than the organotin chlorides, the intermediate products and the free carboxylic acids. The organotin moiety plays an important role in deciding the antifungal activity of an organotin compound indeed true in our respect that the antifungal activity of tributyltin(IV) carboxylates is more active than dibutyltin(IV) carboxylates.

Keywords: Antifungal activity test, Minimum inhibition concentration, Organotin(IV) carboxylates

1. Introduction

The organotin(IV) compounds continue to be of interest on account of their interesting structural features (Tiekink, 1991; Shahid et al., 2003; Bhatti et al., 2005) and also because of their wide applications as catalysts, antifouling agents, agricultural biocides, antitumor agents and other biological activities (Blunden and Hill, 1990; Bonire et al., 1998; Pellerito and Nagy, 2002; Gielen, 2003). The organotin(IV) compounds are characterized by the presence of at least one covalent Sn – C bond. These compounds contain tetravalent Sn centers and can be classified as mono-, di-, tri-, and tetraorganotin(IV), depending on the number of alkyl (R) or aryl (Ar) moieties attached to the tin metal. The counter anion is usually chloride, oxide, fluoride, hydroxide, and thiolate (Pellerito and Nagy, 2002). Carboxylate has also been used successfully as counter anion (Bonire et al., 1998; Pellerito and Nagy, 2002; Szorsick et al., 2002; Gielen, 2003).

The organotin(IV) compounds are known to display strong biological activity. Their compounds are normally exhibit high toxicity, even at very low concentration. Their biological activities are fundamentally determined by the number and nature of organic groups bound to the central Sn atom (Pellerito and Nagy, 2002). The nature of the anionic groups seems only as a secondary factor. The current investigations on the coordinating properties of carboxylates toward organotin compounds have led to the isolation of some new organotin(IV) carboxylates and carboxylate derivatives which have shown some interesting biological activities such as antimicrobial (Bonire et al., 1998; Mahmood et al., 2003), anti-tumor (de Vos et al., 1998), and antifungal activity (Ruzika et al., 2002; Mahmood et al., 2003; Hadi et al., 2007; Hadi et al., 2008). Based on the above fact and the opportunity to explore the interesting features of these organotin compounds, in the present work, we report the comparative study on the antifungal activity of di- and tributyltin(IV) carboxylate compounds.

2. Experiment

2.1 Chemicals Required

All reagents were of reagent grades. Dibutyltin(IV) dichlorides ($[(C_4H_9)_2Cl_2]$), tributyltin(IV) chloride ($[(C_4H_9)_3Cl]$), carboxylic acids, dimethylsulfoxide (DMSO), sodium hydroxide (NaOH), methanol (CH_3OH) were either Sigma or JT Baker products and were used without further purification.

2.2 Experimental Procedure

The preparation of the organotin(IV) carboxylates, for this work and similar compounds with different carboxylate ligands have previously been reported (Hadi et al., 2007; Hadi et al., 2008) and the procedure used was adapted from Szorcik et al. (2002). An example procedure in the preparation of dibutyltin(IV) dicarboxylates is as follows:

2.2.1 Preparation of $[(n\text{-C}_4\text{H}_9)_2\text{Sn}(\text{OH})_2]$ (**2**)

To 3.0383 g (0.01 mol) $[(n\text{-C}_4\text{H}_9)_2\text{SnCl}_2]$ in 50 mL dry methanol was added with 0.8 g (0.02 mol) NaOH and the reaction mixtures were stirred for about 45 minutes. Compound **2** was precipitated out as white solid, filtered off and dried *in vacuo* till they are ready for IR and for further reaction. The yield in average was 2.3508 g (95 %)

2.2.2 Preparation of $[(n\text{-C}_4\text{H}_9)_2\text{Sn}(\text{OOCR})_2]$

To 0.37338 g (1.5 mmol) compound **2** in 50 mL dry methanol was added with 2 mole equivalents of carboxylic acids and was refluxed for 4 hours at 60 – 70°C. The product compounds $[(n\text{-C}_4\text{H}_9)_2\text{Sn}(\text{OOCR})_2]$ were obtained after removal of the solvent by rotary evaporator and dry *in vacuo* until they are ready for IR spectroscopy and used further for antifungal test. The average yield was more than ~ 90 %.

The similar procedure was used to prepare tributyltin(IV) carboxylates, $[(n\text{-C}_4\text{H}_9)_3\text{Sn}(\text{OOCR})]$, where in this reaction the carboxylic acids added was 1 mole equivalent.

2.3 The Antifungal Activity Test

The procedure of the antifungal activity test undertaken based on the procedure reported previously (Hadi et al., 2007; Hadi et al., 2008) and as follows:

1. The *F. oxysporum* and *A. niger* isolates are available in the botany laboratory, the University of Lampung.
2. The fungi isolates were taken from their pure culture and transferred to PDA (*Potatoes Dextrose Agar*) media to get their optimum growth.
3. The activity test of organotin(IV) compounds was performed with (1) the *disk diffusion test method* and (2) *dilution method*.

2.3.1 Disk diffusion test method

This method was done as follows: transferred the pure culture of the fungi which has grown optimum by cutting the colony of the fungi at the edge of their culture growth in 1 x 1 cm size. This colony agar blocks is put at the middle of PDA. It is incubated at 25 °C for 1-2 day to ensure its growth. When the growth of the fungi was seen clearly, three *filter disk papers*, which have been kept in the solution containing the organotin(IV) compound tested in DMSO was placed in surround of the inoculums aseptically. The media test was then incubated further at 25°C for 7 consecutive days and was daily checked. The observation was monitored by looking at the inhibition zone. If the inhibition zone was formed (the area where the fungi was unable to grow), then it indicated the compound tested showed the antifungal activity. If there is no any inhibition zone then the organotin used is inactive or the concentration used may be less than required.

2.3.2 Dilution test method

This method was done as follows: the organotin compound being used is dissolved in DMSO using the concentration which was the most effective from the disk diffusion test method. The compound is then mixed with 25 mL of agar media with the volume variation of 0.5; 1; 1.5; 2; and 2.5 mL. The inoculums block of the fungus is placed in the middle of the PDA media at 25°C for 10 consecutive days and was daily checked. The minimum inhibition concentration is then calculated based on the smallest concentration of the compound used which maximally inhibits the growth of the fungi.

Based on the results of the inhibition zone obtained from disk diffusion test and the smallest concentration used in dilution test, tributyltin(IV) carboxylates are in general more active three times than those of any analogous compound of dibutyltin(IV) carboxylates.

3. Results and Discussion

The preparations of dibutyltin(IV) dicarboxylates, $[(n\text{-C}_4\text{H}_9)_2\text{Sn}(\text{OOCR})_2]$ (**3-5**) and tributyltin(IV) carboxylates, $[(n\text{-C}_4\text{H}_9)_3\text{Sn}(\text{OOCR})]$ (**6-8**), were successfully done from their chlorides $[(n\text{-C}_4\text{H}_9)_2\text{SnCl}_2]$ (**1a**) and $[(n\text{-C}_4\text{H}_9)_3\text{SnCl}]$ (**1b**), respectively. To maximize the product obtained, the reactions in all cases were done *via* $[(n\text{-C}_4\text{H}_9)_2\text{SnO}]$ (**2a**) and $[\{(n\text{-C}_4\text{H}_9)_3\text{Sn}\}_2\text{O}]$ (**2b**) respectively similar to those previously reported (Hadi et al., 2007; Hadi et al., 2008). The antifungal activities of compounds **3** and **4** have previously been reported (Hadi et al., 2008), and included here to compare their activity values to the respective tributyltin(IV) compounds. The reaction occurred in each step for dibutyltin(IV) dicarboxylates, for example, is shown in Scheme 1. The microanalytical data of all compounds prepared are very good and all values obtained are close to the theoretical values as shown in Table 1.

The characterization of the products synthesized was confirmed mainly by analyzing them with FT-IR spectroscopy in the frequency range of $4000 - 250 \text{ cm}^{-1}$ and the results are presented in Table 2. The characteristic band of the starting materials (**1a,b**) is the appearance of strong stretching band of Sn - Cl bond at $390 - 310 \text{ cm}^{-1}$, and in the spectrum of **1a**, this bond appeared at frequency of 334.2 cm^{-1} . The other characteristic bands of this compound appear as stretching band from butyl ligands at 1069 cm^{-1} , and bending vibration of C-H aliphatic stretch of the butyl at frequency of $2956 - 2865 \text{ cm}^{-1}$.

When compound **1a** is converted to compound **2a**, the main stretching band of Sn - Cl disappeared and a new strong band at frequency of 417.4 cm^{-1} appeared as one of the main stretching band. This band is characteristic for Sn - O bond in compound $[(n\text{-C}_4\text{H}_9)_2\text{SnO}]$ (**2a**). The stretching band due to the butyls and their bending vibrations are still appeared as expected although the frequencies have little bit moved. The formation of dibutyltin (IV) dicarboxylate compounds, $[(n\text{-C}_4\text{H}_9)_2\text{Sn}(\text{RCOO})_2]$, (**3 - 5**) is confirmed by the strong asymmetric stretching bands of the carboxylates which occurred at *ca.* 1400 cm^{-1} and the symmetric stretch at *ca.* 1600 cm^{-1} , confirming the success of the substitution reaction (Hadi et al., 2008).

The UV-vis spectroscopy analyses have also been taken for all the compounds used. The λ_{max} of all the compounds is summarized in Table 3. The data obtained from Table 3 are clear that there was a shifting change in the λ_{max} for each compound in any steps of the reaction. For example, the compound **1a** has λ_{max} of 210.7 nm , while compound **2a** has λ_{max} of 202.9 nm . This information gave an indication that there was a shift to a shorter λ maximum when the conversion of compound **1a** to **2a** taken place. The wave length shift to a shorter λ_{max} could be occurred due to either the solvent used or the effect of auxochrome. However in this study, this can not be due to the effect of solvent as the solvent used for all measurements is the same, which is methanol. This change must be due to the auxochrome effect. In case of compound **1a** and **2a** can be closely looked at that in compound **2a** there is oxide group which has electron drawing effect bigger than that of chloride group in **1a**, as a result in **2a**, the electron transition is hard to occur, thus the λ_{max} measured is getting shorter (Sudjadi, 1985). The similar observations are also observed for other changes as can be seen from the Table 3. In compound **3**, for example, the electron drawing effect of $\text{o-C}_6\text{H}_4(\text{OH})\text{COOH}$ is less than chloride in **1a**, so the electron transition in its molecule will be easier (the energy required is less), thus producing longer λ_{max} , 307.8 nm .

The antifungal activity of salicylic acid and its derivative has long been known (Coates et al., 1957). However, compare to the organotin compounds used in the present study, the free salicylic acid and other carboxylic acids presented weaker antifungal activity against the tested fungi (see Table 4). Table 4 clearly illustrated that the Minimum Inhibition Concentration (MIC) values of the organotin(IV) salicylates (compounds **3** and **6**), in general, are smaller than other organotin(IV) carboxylate compounds, the derivatives of acetylsalicylate (**4**, **7**) and benzoate (**6**, **8**). These data agreed to those previously reported (Hadi et al., 2008). This indicates that the presence of the metal ions plays an important role in the increased antifungal activity when the acids are coordinated. In this respect, our results are consistent with a well-known fact that many biologically active compounds become more active upon complexation than in their uncomplexed forms (Gershon, 1974). The fact that the organotin(IV) carboxylates are more active against the tested fungi than their parent organotin(IV) compounds (the organotin(IV) chloride), the intermediate products, and the carboxylic acids suggests that the carboxylate groups play a role in the fungi toxicities of these compounds. According to Crowe (1989), the actual biological activity of diorganotin compounds of the type $\text{RR}'\text{SnXY}$ (R and R' = alkyl or aryl; X and Y = anions) is determined solely by the $\text{RR}'\text{Sn}^{2+}$ moiety.

Consequently the group X and Y would only influence the delivery of the active $\text{RR}'\text{Sn}^{2+}$ ion to the cell. The higher activities of the organotin(IV) carboxylates relative to their parent organotin(IV) compounds (the organotin(IV) chlorides), the intermediate products, and the carboxylic acids appear to be an additive (not a synergistic) effect of the metal ions and the carboxylate groups, with the possibility of a common mode of action. In this regard, the hypothesis that relates the toxicity and nontoxicity of metal complexes to the penetration and nonpenetration of the fungus by the toxicant is of interest (Crowe, 1989). Therefore the free carboxylic acids show some explanation for our results. The groups like acetylsalicylate and $(n\text{-C}_4\text{H}_9)_2\text{Sn}^{2+}$ considerably change the molecular parameter that influence the orientation of the molecule on biological receptor and facilitate penetration into the cell membranes (Bonire et al., 1998).

The observation that the tributyltin(IV) carboxylate compounds are more active than their dibutyltin(IV) is in line with the notion that the number of carbon atoms in the organotin moiety affects its activity (Crowe, 1989). In tributyltin(IV) derivatives optimal activity has been associated with 12 carbon atoms and this may be the case in the present work, where the dibutyltin(IV) derivatives contain only 8 carbon atom (Chohan and Rauf, 1996). These data are also in agreement with our previous result where in general, the derivative of triphenyltin(IV) carboxylate which contain 18 carbon atoms has smallest MIC values in the series (Hadi et al., 2008). As an example, the triphenyltin(IV) salicylate, $[(n\text{-C}_6\text{H}_5)_3\text{Sn}(\text{o-C}_6\text{H}_4(\text{OH})\text{COO})]$ has MIC value of 0.61 mM .

4. Conclusion

The results presented in the present study clearly have again indicated that the organotin(IV) carboxylates synthesized and described in this work showed strong antifungal activities. The MIC values obtained for tributyltin(IV) carboxylate compound are smaller than respective dibutyltin(IV) carboxylates compound. However, the MIC values of tributyltin(IV) compound are higher compared to their respective triphenyltin(IV) carboxylate. This observation does agree to the fact that the number of carbon atoms in the organotin moiety affects its activity against fungi tested.

Acknowledgments

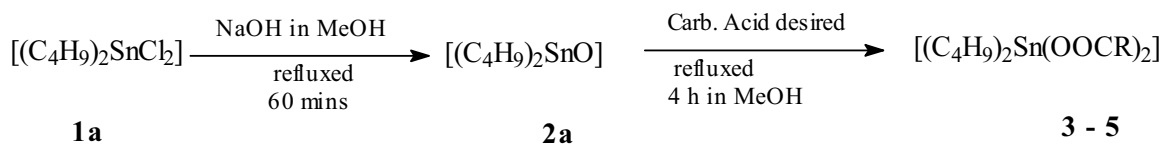
The authors would like to thank to The Directorate of Research and Services, Directorate General of Higher Education, The Ministry of Cultural and Education of Republic of Indonesia that provide fund for this project to be undertaken through Hibah Bersaing XVI/1 Research Grant Scheme 2008 with contract number of 010/SP2H/PP/DP2M/III/2008, 6 March 2008. Thank also goes to Prof. Bohari M. Yamin, Universiti Kebangsaan Malaysia for helping in doing microanalysis; as well as Desy Anggraini, Chandra Rini P. and Arif Dwi R. who help us in the preparation of the samples.

References

- Bhatti, M.H., Ali, S., Huma, F., Shahzadi, S. (2005). Organotin(IV) Derivatives of N-Maleoylamino Acids: Their Synthesis and Structural Elucidation, *Turkish Journal of Chemistry*, 29, 463-476.
- Blunden, S.J. and Hill, R. (1990). Bis(tributyltin) oxide as a wood preservative: Its conversion to tributyltin carboxylates in *Pinus sylvestris*. *Applied Organometallic Chemistry*, 4: 63 - 68.
- Bonire, J.J., Ayoko, G.A., Olurinola, P.F., Ehinmidu, J.O., Jalil, N.S.N. and Omachi, A.A. (1998). Syntheses and Antifungal Activity of some organotin(IV)carboxylates. *Metal-Based Drugs*. 5 (4), 233 - 236 and references therein.
- Chohan, Z.H. and Rauf, A. (1996). Some Biologically Active Mixed Ligand Complexes of Co(II), Cu(II) and Ni(II) with ONO, NNO and SNO Donor Nicotinoylhydrazine-Derived Ligands. *Synthesis and Reactivity in Inorganic and Metal-Organic Chemistry*. 6, 591-604.
- Coates, L.V., Brain, D.J., Kerridge, K.H., Marcus, F.J., and Tattershall, K. (1957). *Journal of Pharmacy and Pharmacology*, 9, 855.
- Crowe, A.J. (1989) The antitumour activity of tin compounds In *Metal-based Drugs*. Gielen, M. (Ed.). Freund Publishing House, Freund. 1, 103 - 149.
- de Vos, D., Willem, R., Gielen, M., van Wingerden, K.E. and Nooter, K. (1998). The Development of Novel Organotin Anti-Tumor Drugs: Structure and Activity. *Metal-Based Drugs*. 5 (4), 179 - 188.
- Gershon, H. (1974). Antifungal Activity of Bischelates of 5-, 7-, and 5,7-halogenated 8-quinols with copper(II). Determination of the long and short axes of the pores in the fungal spore wall. *Journal of Medicinal Chemistry*. 17, 824-827.
- Gielen, M. (2003). An Overview of Forty Years Organotin Chemistry Developed at the Free Universities of Brussels ULB and VUB, *Journal of the Brazilian Chemical Society*, 14 (6), 870-877.
- Hadi, S. and Irawan, B. (2007). Synthesis, Characterization and The Antifungal Activity Test of Diphenyltin(IV) Complexes. Proceeding of International Conference on Chemical Sciences, Gadjah Mada University, 24 - 26 May 2007, pp. 21-216 (Life Sciences Section)
- Hadi, S., Irawan, B., Efri. (2008). The Antifungal Activity Test of Some Organotin(IV) Carboxylates. Accepted for Publication at *Journal of Applied Sciences Research*. **In Press**.
- Mahmood, S., Ali, S., Bhatti, M.H., Mazhar, M., Iqbal, R. (2003). Synthesis, Characterization and Biological Applications of Organotin(IV) Derivatives of 2-(2-Fluoro-4-biphenyl)propanoic Acid, *Turkish Journal of Chemistry*, 27, 657-666.
- Pellerito, L. and Nagy, L. (2002). Organotin(IV)ⁿ⁺ complexes formed with biologically active ligands: equilibrium and structural studies, and some biological aspects, *Coordination Chemical Reviews* 224, 111 - 150 and references therein
- Ruzika, A., Dostal, L., Jambor, R., Butcha, V., Brus, J., Cisarova, I., Holcapek, M., and Holeccek, J. (2002). Structure and in vitro antifungal activity of [2,6-bis(dimethyl-minomethyl)phenyl]diphenyltin(IV) compounds, *Applied Organometallic Chemistry*, 16(6), 315 - 322.
- Shahid, K., Ali, S., Shahzadi, S., Akhtar, Z. (2003). Organotin(IV) Complexes on Aniline Derivatives Part-II-Synthesis and Spectroscopic Characterization of Organotin(IV) Derivatives of 2-[4-Bromoaniline]carboxyl]benzoic Acid, *Turkish Journal of Chemistry*, 27, 209-215.
- Sudjadi, (1985). Penentuan Struktur Senyawa Organik. Ghalia. Indonesia, 327p.

Szorcsik, A., Nagy, L., Gadjia-Schranz, K., Pellerito, L., Nagy, E. and Edelmann, E.T. (2002). Structural studies on organotin(IV) complexes formed with ligands containing {S, N, O} donor atoms, *Journal of Radioanalytical Nuclear Chemistry*, 252 (3), 523 – 530.

Tiekink, E.R.T. (1991) Structural Chemistry of Organotin Carboxylates: a Review of the Crystallographic Literature, *Applied Organometallic Chemistry*, 5, 1-30.



Scheme 1. The preparative route of $[(C_4H_9)_2Sn(OOCR)_2]$

Table 1. The microanalytical data of the organotin(IV) compounds synthesized

No.	Compound	Elemental analyses found (calculated)	
		C	H
3	$[(n-C_4H_9)_2Sn(o-C_6H_4(OH)COO^-)_2]$	55.98 (57.04)	3.26 (3.32)
4	$[(n-C_4H_9)_2Sn(o-C_6H_4(O_2CCH_3)COO^-)_2]$	56.23 (57.05)	3.76 (3.8)
5	$[(n-C_4H_9)_2Sn(C_6H_5COO^-)_2]$	54.39 (55.58)	5.94 (5.89)
6	$[(n-C_4H_9)_3Sn(o-C_6H_4(OH)COO^-)]$	55.04 (55.47)	7.90 (7.79)
7	$[(n-C_4H_9)_3Sn(o-C_6H_4(O_2CCH_3)COO^-)]$	53.0 (53.4)	7.37 (7.49)
8	$[(n-C_4H_9)_3Sn(C_6H_5COO^-)_2]$	61.47 (61.61)	7.18 (7.25)

Table 2. The characteristic and important IR bands of the organotin(IV) compounds (cm^{-1}) synthesized

Compound	3	4	5	6	7	8	References
Sn-O	434.5	435.7	491.8	464.2	444.1	456.2	600-400
Sn-O-C	1029.9	1028.1	1027.3	1030.8	1023.8	1029.4	1050-900
Sn-Bu	674.8	678.3	709.4	698.5	678.9	684.2	740-660
CO ₂ asym	1419.6	1418.2	1452.1	1483.9	1458.8	1462.3	1500-1400
CO ₂ sym	1558.7	1560.7	1589.3	1658.3	1648.7	1638.6	1660-1550
C-H aliphatic	2955 – 2862	2955 – 2866	2956-2865	2924-2856	2957-2855	2944-2855	2960 – 2850

Table 3. The λ_{maximum} of the UV spectra of the organotin(IV) compounds

Compound	λ_{maximum} (nm)
$[(n\text{-C}_4\text{H}_9)_2\text{SnCl}]$ (1a)	210.7
$[(n\text{-C}_4\text{H}_9)_2\text{SnO}]$ (2a)	202.9
$[(n\text{-C}_4\text{H}_9)_2\text{Sn}(\text{o-C}_6\text{H}_4(\text{OH})\text{COO}^-)_2]$ (3)	307.8
$[(n\text{-C}_4\text{H}_9)_2\text{Sn}(\text{o-C}_6\text{H}_4(\text{O}_2\text{CCH}_3)\text{COO}^-)_2]$ (4)	305.7
$[(n\text{-C}_4\text{H}_9)_2\text{Sn}(\text{C}_6\text{H}_5\text{COO}^-)_2]$ (5)	287.7
$[(n\text{-C}_4\text{H}_9)_3\text{Sn}(\text{o-C}_6\text{H}_4(\text{OH})\text{COO}^-)]$ (6)	308.9
$[(n\text{-C}_4\text{H}_9)_3\text{Sn}(\text{o-C}_6\text{H}_4(\text{O}_2\text{CCH}_3)\text{COO}^-)]$ (7)	302.3
$[(n\text{-C}_4\text{H}_9)_3\text{Sn}(\text{C}_6\text{H}_5\text{COO}^-)_2]$ (8)	282.4

Table 4. The Minimum Inhibition Concentration (MIC) of starting materials and organotin(IV) carboxylates

Compounds	<i>F. oxysporum</i> (mM)	<i>A. Niger</i> (mM)
Salicylic acid	18.7	18.5
Acetylsalicylic acid	13.7	13.9
$[(n\text{-C}_4\text{H}_9)_2\text{SnCl}_2]$ (1a)	16.5	16.0
$[(n\text{-C}_4\text{H}_9)_3\text{SnCl}]$ (1b)	12.2	11.8
$[(n\text{-C}_4\text{H}_9)_2\text{SnO}]$ (2a)	19.0	18.5
$[(n\text{-C}_4\text{H}_9)_3\text{O}]$ (2b)	9.4	9.2
$[(n\text{-C}_4\text{H}_9)_2\text{Sn}(\text{o-C}_6\text{H}_4(\text{OH})\text{COO}^-)_2]$	6.4	6.6
$[(n\text{-C}_4\text{H}_9)_2\text{Sn}(\text{o-C}_6\text{H}_4(\text{O}_2\text{CCH}_3)\text{COO}^-)_2]$	6.1	6.2
$[(n\text{-C}_4\text{H}_9)_2\text{Sn}(\text{C}_6\text{H}_5\text{COO}^-)_2]$	7.3	7.1
$[(n\text{-C}_4\text{H}_9)_3\text{Sn}(\text{o-C}_6\text{H}_4(\text{OH})\text{COO}^-)]$	2.61	2.62
$[(n\text{-C}_4\text{H}_9)_3\text{Sn}(\text{o-C}_6\text{H}_4(\text{O}_2\text{CCH}_3)\text{COO}^-)]$	2.54	2.56
$[(n\text{-C}_4\text{H}_9)_3\text{Sn}(\text{C}_6\text{H}_5\text{COO}^-)_2]$	2.98	3.14



Web Service with Chinese Language in Great Toronto Area

Feng Ding & Yanzhang Wang

Institute of Information and Decision Technology of DUT

Dalian 116023, China

E-mail: dingff@gmail.com; yzwang@dlut.edu.cn

This work was partially supported by the National Graduate Student Program of Building World-Class Universities (Grant No.[2007]3020)

Abstract

This article shows the importance of Chinese language in the websites of the Great Toronto Area(GTA) by analyzing the data from Alexa.com. Websites with Chinese in Toronto is growing up steadily. It will benefit more by adding a Chinese version to Canadian official websites for the needs of Canadian Chinese.

Keywords: Web Service, Chinese Language, GTA, Alexa

1. Preface

As a developed country, the cities of Canada are covered by high speed internet and the communication costs less than most of the developing countries. With the effective promotion by Canada government, many of the public services for the daily life of the people have formed complete integrated online business process. And the services are provided by some websites, such as canada.gc.ca, toronto.ca, and youth.gc.ca, and each of them serves lots of people everyday. Many new websites are integrated step by step to satisfy the public demand. The language using in the portals is English or French. These user-centered websites provide different entrances for the public to choose, such as the entrances for citizens, enterprises, and non-citizens.

Based on the statistics made by the government Canada, between 2001 and 2005, the top four visible minority groups in Toronto were Chinese (259,710 or 10.6%), South Asian (253,920 or 10.3 %), Black (204,075 or 8.3%) and Filipino (86,460 or 3.5 %). "Visible minority" is defined by Statistics Canada as "persons, other than Aboriginal peoples, who are non-Caucasian in race or non-white in color". Chinese Canadians are Canadians of Chinese descent and constitute the second-largest visible minority group in Canada, standing at 1,346,510 which comprise 4.3% of the population in 2006. Out of those 1,346,510 people, 211,145 people were of Chinese and one other heritage. Chinese is the top one visible minority group in Toronto. And also there are more and more Chinese moving to Toronto with the immigrations rising up. The Chinese language has become the third language used in Toronto besides English and French.

This article tried to discover the status of the Chinese websites in Toronto area and the visitors' preference by comparing 5 famous websites selected in Toronto. The 5 websites are 51.ca, Yorkbbs.ca, Anpopo.com, Toronto.com and Toronto.ca.

All of the charts and the figures in tables were from Alexa.com (Alexa).

2. Introduction about the selected websites

51.ca is a Chinese website set up in Toronto, 28 July 2001. It focuses on providing the daily life information for Chinese immigrants. There are mainly 3 parts of websites: flea market, yellow pages and forum.

Yorkbbs.ca was shown to the public at May, 2002 with Chinese language service. Now it has formed a forum which attracts a big number of Chinese everyday. News, jobs, house renting and other daily life information are provided to the visitors for free.

Anpopo.com is a kind of portal website. It was formally released on 10 Nov, 2007. As a Chinese website newly comes up, anpopo.com focuses on providing a service platform for the Chinese in Toronto.

Toronto.ca is an official integrated portal of Toronto. The four community home pages are Living in Toronto, Doing Business, Visiting Toronto and Accessing City Hall. It only provides English version.

Toronto.com offers comprehensive and searchable business, event and entertainment related information, as well as unique, expert editorial content. This website currently serves more than 900,000 unique visitors a month and continues to grow.

3. Explanation about the index

3.1 Reach

Reach measures the number of users. Reach is typically expressed as the percentage of all internet users who visit a given site. The three-month change is determined by comparing a site's current reach with its values from three months ago.

3.2 Traffic Ranking

The traffic ranking is based on three months of aggregated historical traffic data from millions of Alexa Toolbar users and data obtained from other, diverse traffic data sources, and is a combined measure of page views and users (reach). The three-month change is determined by comparing the site's current ranking with its ranking from three months ago.

3.3 Daily Traffic Ranking Trend

The daily traffic ranking reflects the traffic to the site based on data for a single day. In contrast, the main traffic ranking shown in the Alexa Toolbar and elsewhere in the service is calculated from three months of aggregate traffic data.

3.4 Daily Page views (Percent)

Page views measure the number of pages viewed by site visitors. Multiple page views of the same page made by the same user on the same day are counted only once. The page views per user numbers are the average numbers of unique pages viewed per user per day by the visitors to the site. The three-month change is determined by comparing a site's current page view numbers with those from three months ago.

4. Data Analysis

Chart 1 shows that the daily reach to the websites are stable except yorkbbs.ca. 51.ca and Toronto.ca have a higher daily reach than other 3 sites and Anpopo.com is on the bottom of the chart. It also reflects that Chinese visitors to 51.ca are more than the visitors to Toronto.ca and Toronto.com.

The daily traffic ranking trend of the 5 websites is shown in chart 2. The ranking of 51.ca, Toronto.ca and Toronto.com are relatively stable and 51.ca is on top of the others. But the ranking of Yorkbbs.ca and Anpopo.com changes frequently. Still at most of the time, from the chart we can see, Anpopo.com is on the bottom of the chart.

Shown in chart 3, Yorkbbs.ca is far beyond in the daily page views, though its ranking is up and down all the time. 51.ca is also ahead of the other 3 websites. Anpopo.ca, Toronto.ca and Toronto.com have no significant difference from each other. It seems that the Chinese visitors are more interested in the contents provided by yorkbbs.ca.

We can also see some details about the ranking of each website through the figure in table 1. Because of their comprehensive contents, 51.ca and Toronto.ca get a rising amount of visitors and their ranking is climbing up. But the amount of visitors to the other 3 websites is decreasing and ranking is dropping down more or less. In table 1, we observed that the users and ranking of Anpopo.com is decreasing a lot, but its page views is increasing fast in the recent 3 month. This shows that when Anpopo.com losing some visitors it has also gained some loyal visitors who have the similar interests.

In order to show the locations of the visitors and the traffic ranking of the 5 websites in Canada, we also collect the data from Alexa.com to form table 2. From this table we can see that most of the visitors to the 5 websites are from Canada, and all of the websites have a good ranking in Canada. The location of the visitors and ranking of the websites can stand the main trend and preference of the visitors in Canada.

5. Conclusion

- (1) Chinese in Toronto area still rely on Chinese websites strongly, though they live in an English or French environment.
- (2) Chinese websites in Toronto is growing up steadily. They have gained a big amount of visitors and a stable ranking in Canada.
- (3) It will be much better to add a Chinese version to Canadian official websites for needs of Canadian Chinese.

6. Acknowledgement

This work was partially supported by the National Graduate Student Program of Building World-Class Universities (Grant No. [2007]3020)

7. References

Wikipedia, "Visible minority," Visible minority, en.wikipedia.org, 28 June 2008. [online]. Available: http://en.wikipedia.org/wiki/Visible_minority. [Accessed: 29 June 2008].

City of Toronto, "Toronto's racial diversity," City of Toronto: Toronto Facts, toronto.ca, Jan 2007. [online]. Available: http://www.toronto.ca/toronto_facts/diversity.htm. [Accessed: 29 June 2008].

Alexa Internet, Inc., "About the Alexa Traffic Rankings," Alexa Web Search - Help, alexa.com, June 2008. [online]. Available: http://www.alexa.com/site/help/traffic_learn_more. [Accessed: 11 June 2008].

City of Toronto, "Welcome to the official Web site of the City of Toronto," The City of Toronto: Welcome to the official Web site of the City of Toronto, toronto.ca, 10 June 2008. [online]. Available: http://www.toronto.ca/get_connected/welcome.htm. [Accessed: 11 June 2008].

toronto.com, "About toronto.com," About toronto.com, toronto.com, 14 June 2008. [online]. Available: <http://www.toronto.com/article/500725>. [Accessed: 24 June 2008].

51.ca, "About us," About us- 51.ca, 51.ca, 14 June 2008. [online]. Available: <http://www.51.ca/aboutus.php>. [Accessed: 24 June 2008].

Table 1. Websites status















Name	Percent of global Internet users		Traffic ranking based on a combined measure of page views and users		The number of unique pages viewed per user per day	
	3 mos. Avg.	3 mos. Change	3 mos. Avg.	3 mos. Change	3 mos. Avg.	3 mos. Change
51.ca	0.01230%	 10%	6929	 944	10.39	No Change
yorkbbs.ca	0.00921%	 23%	7654	 1860	26.60	 3%
anpopo.com	0.00228%	 58%	36462	 19024	12.20	 146%
toronto.ca	0.01010%	 11%	11434	 1491	3.83	 1%
toronto.com	0.00545%	 8%	22957	 2082	3.14	 8%

Table 2. Website ranking in Canada

Name	Users from Canada	Traffic ranking in Canada
51.ca	84.8%	73
yorkbbs.ca	84.6%	193
anpopo.com	71.1%	1022
toronto.ca	85.4%	211
toronto.com	83.5%	489

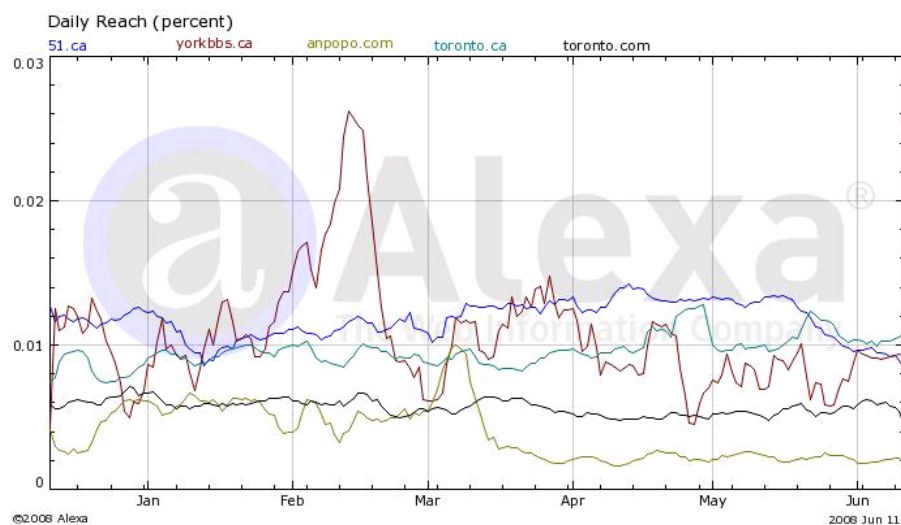


Chart 1. Daily reach (percent)

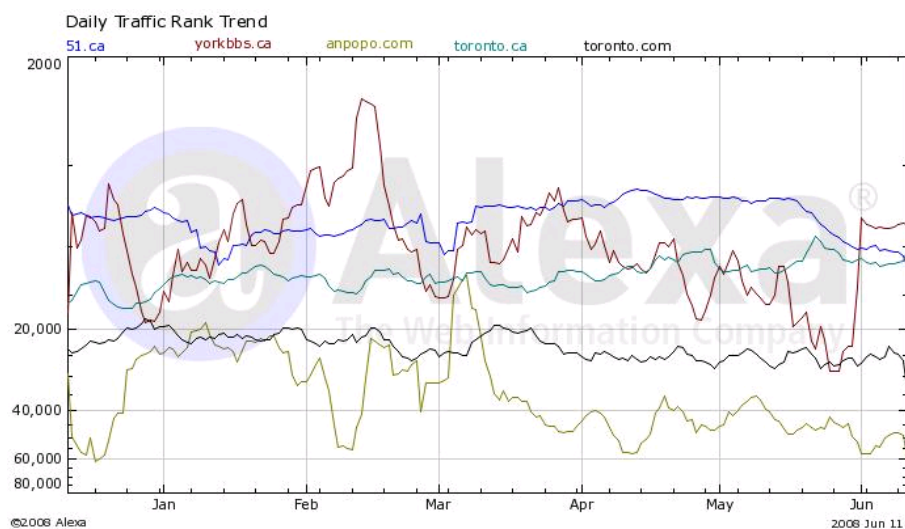


Chart 2. Daily traffic ranking trend

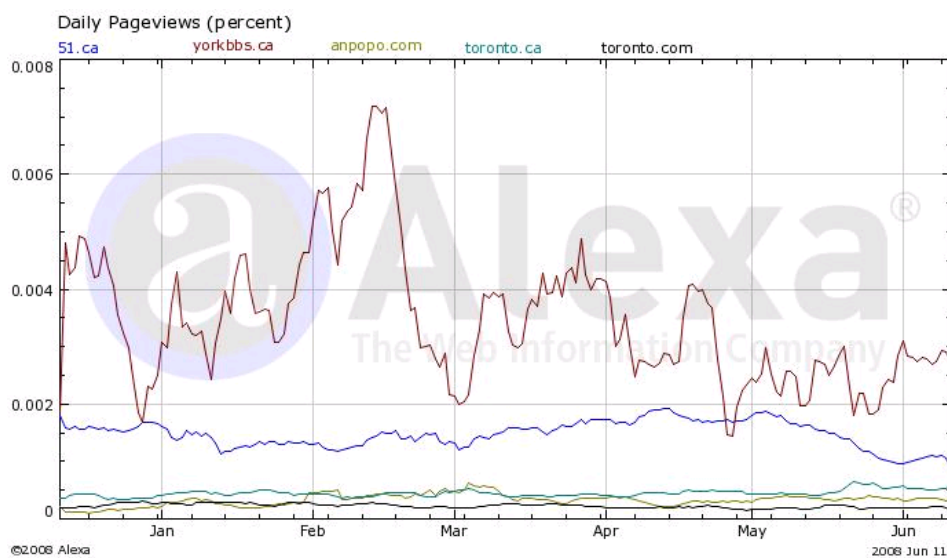


Chart 3. Daily page views (percent)



Free Convection over a Vertical Plate in a Micropolar Fluid

Subjected to a Step Change in Surface Temperature

Azizah Mohd. Rohni

Physical Science, College of Arts and Sciences

Universiti Utara Malaysia

06010 UUM, Kedah, Malaysia

Tel: 60-4-928-6980 E-mail: r.azizah@uum.edu.my

Zurni Omar (Corresponding author)

Physical Science, College of Arts and Sciences

Universiti Utara Malaysia

06010 UUM, Kedah, Malaysia

Tel: 60-4-928-6917 E-mail: zurni@uum.edu.my

Adyda Ibrahim

Physical Science, College of Arts and Sciences

Universiti Utara Malaysia

06010 UUM, Kedah, Malaysia

Tel: 60-4-928-6956 E-mail: adyda@uum.edu.my

Abstract

The Keller box method has been employed for free convection over a vertical plate subjected to a step change in surface temperature in micropolar fluid. Numerical results presented include the reduced angular velocity profiles, development of wall shear stress or skin friction and development of the rate of change of the gyration component at the wall for various values of Prandtl numbers and temperature ratios. The study shows that the present results obtained in micropolar fluids, when temperature ratio $\theta_{w2} = 1$, agree very well with the previous study without temperature change.

Keywords: Keller box, Free convection, Vertical plate, Step change, Micropolar fluid

1. Introduction

Free convection or (natural convection) is a process whereby the fluid motion is induced by buoyancy forces within the fluid. The mechanism of free or natural convection flow is a buoyancy-induced motion due to the presence of a fluid density gradient and a body force that is proportional to density. The phenomenon is of great importance in industries and the environment, such as materials processing and solar energy system.

Since the first successful experimental and theoretical study of a flat plate with uniform wall temperature by Schmidt and Beckmann, free convection heat transfer from a vertical flat plate in a quiescent medium has been studied by many investigators (Lee & Yovanovich, 1987a). Ostrach (1953) solved laminar boundary layer equations through similarity methods for the case of uniform wall temperature for various Prandtl numbers. Similarity solutions to boundary layer equations have been further extended by Sparrow and Gregg (1958). They have documented the results for the cases of surface temperature variations of the power-law and exponential form.

The above cited literature and many others deal with similarity problems with continuous and well-behaved boundary conditions at the wall. However, most practical problems in application often involve wall conditions that are arbitrary and unknown. The study of non-similar free convection heat transfer from a vertical flat plate with arbitrarily varying thermal conditions at the wall is a tedious investigation. The problem has attracted a great deal of interest over the past

years in several technological applications, particularly in the thermal design of microelectronic circuit boards and in the consideration of system behaviour under conditions where the usual mode of heat transfer fails.

To understand and solve problems involving general non-similar conditions at the wall, it is useful to investigate problems subjected to a step change in wall temperature (Lee & Yovanovich, 1987b). The problems impose a mathematical singularity and severe non-similar conditions at the wall.

2. Governing Equations

We consider a semi-infinite vertical heated plate with a discontinuous temperature variation immersed in a micropolar fluid. It is well known that the full equations governing the steady laminar free convection flow of an incompressible micropolar fluid subject to Boussinesq approximation may be written in the form

$$\frac{\partial \bar{u}}{\partial \bar{x}} + \frac{\partial \bar{v}}{\partial \bar{y}} = 0, \quad (1)$$

$$\rho \left(\bar{u} \frac{\partial \bar{u}}{\partial \bar{x}} + \bar{v} \frac{\partial \bar{u}}{\partial \bar{y}} \right) = -\frac{\partial \bar{p}}{\partial \bar{x}} + (\mu + \kappa) \left(\frac{\partial^2 \bar{u}}{\partial \bar{x}^2} + \frac{\partial^2 \bar{u}}{\partial \bar{y}^2} \right) + \rho g \beta (T - T_\infty) + \kappa \frac{\partial \bar{N}}{\partial \bar{y}}, \quad (2)$$

$$\rho \left(\bar{u} \frac{\partial \bar{v}}{\partial \bar{x}} + \bar{v} \frac{\partial \bar{v}}{\partial \bar{y}} \right) = -\frac{\partial \bar{p}}{\partial \bar{y}} + (\mu + \kappa) \left(\frac{\partial^2 \bar{v}}{\partial \bar{x}^2} + \frac{\partial^2 \bar{v}}{\partial \bar{y}^2} \right) - \kappa \frac{\partial \bar{N}}{\partial \bar{x}}, \quad (3)$$

$$\rho j \left(\bar{u} \frac{\partial \bar{N}}{\partial \bar{x}} + \bar{v} \frac{\partial \bar{N}}{\partial \bar{y}} \right) = -2\kappa \bar{N} + \kappa \left(\frac{\partial \bar{v}}{\partial \bar{x}} - \frac{\partial \bar{u}}{\partial \bar{y}} \right) + \gamma \left(\frac{\partial^2 \bar{N}}{\partial \bar{x}^2} + \frac{\partial^2 \bar{N}}{\partial \bar{y}^2} \right), \quad (4)$$

$$\bar{u} \frac{\partial T}{\partial \bar{x}} + \bar{v} \frac{\partial T}{\partial \bar{y}} = \alpha \left(\frac{\partial^2 T}{\partial \bar{x}^2} + \frac{\partial^2 T}{\partial \bar{y}^2} \right), \quad (5)$$

where (\bar{u}, \bar{v}) are the velocity components along the (\bar{x}, \bar{y}) axes; T , \bar{p} and \bar{N} are the temperature, pressure and the component of the gyration vector normal to the (x, y) - plane; g is the acceleration due to gravity; ρ, μ, α and β are the fluid density, viscosity, thermal diffusivity and coefficient of cubical expansion of the fluid; j, κ and γ are the micro inertia density, vortex viscosity and spin gradient viscosity. Also, $\nu = \frac{\mu}{\rho}$ is the kinematic viscosity. The spin gradient viscosity is given by the constant

$$\gamma = (\mu + \kappa/2)j. \quad (6)$$

The governing equations are subject to the following boundary conditions:

$$\begin{aligned} \bar{y} = 0 : \quad \bar{u} = \bar{v} = 0, \quad \bar{N} = -n \frac{\partial \bar{u}}{\partial \bar{y}}, \\ T = T_{w1} \text{ for } \bar{x} \leq \bar{x}_0 \text{ and } T = T_{w2} \text{ for } \bar{x} > \bar{x}_0, \\ \bar{y} \rightarrow \infty : \quad \bar{u} \rightarrow 0, \quad \bar{v} \rightarrow 0, \quad \bar{N} \rightarrow 0, \quad T \rightarrow T_\infty. \end{aligned} \quad (7)$$

It is worth mentioning that in (7), we have followed [1] for temperature condition.

Equations 1-5 may be written dimensionless by introducing the non-dimensional variables:

$$\begin{aligned} (\bar{u}, \bar{v}) &= (g\beta\Delta T l)^{\frac{1}{2}} (u, v), \quad (\bar{x}, \bar{y}) = l(x, y) \\ \bar{p} &= (g\beta\Delta T l) \rho p, \quad T = T_\infty + \Delta T \theta, \quad \bar{N} = (g\beta\Delta T l)^{\frac{1}{2}} N, \end{aligned} \quad (8)$$

where $j = l^2$ is the length scale for l and $\Delta T = T_w - T_\infty$.

So, the governing equations 1-5, after being rendered dimensionless are as follows

$$\frac{\partial u}{\partial x} + \frac{\partial v}{\partial y} = 0, \quad (9)$$

$$u \frac{\partial u}{\partial x} + v \frac{\partial u}{\partial y} = -\frac{\partial p}{\partial x} + \left(\frac{1+K}{Gr^{\frac{1}{2}}} \right) \left(\frac{\partial^2 u}{\partial x^2} + \frac{\partial^2 u}{\partial y^2} \right) + \theta + \frac{K}{Gr^{\frac{1}{2}}} \frac{\partial N}{\partial y}, \quad (10)$$

$$u \frac{\partial v}{\partial x} + v \frac{\partial v}{\partial y} = -\frac{\partial p}{\partial y} + \left(\frac{1+K}{Gr^{\frac{1}{2}}} \right) \left(\frac{\partial^2 v}{\partial x^2} + \frac{\partial^2 v}{\partial y^2} \right) - \frac{K}{Gr^{\frac{1}{2}}} \frac{\partial N}{\partial x}, \quad (11)$$

$$u \frac{\partial N}{\partial x} + v \frac{\partial N}{\partial y} = -2 \frac{K}{Gr^{\frac{1}{2}}} N + \frac{K}{Gr^{\frac{1}{2}}} \left(\frac{\partial v}{\partial x} - \frac{\partial u}{\partial y} \right) + \left(\frac{1+\frac{1}{2}K}{Gr^{\frac{1}{2}}} \right) \left(\frac{\partial^2 N}{\partial x^2} + \frac{\partial^2 N}{\partial y^2} \right), \quad (12)$$

$$u \frac{\partial \theta}{\partial x} + v \frac{\partial \theta}{\partial y} = \frac{1}{Pr Gr^{\frac{1}{2}}} \left(\frac{\partial^2 \theta}{\partial x^2} + \frac{\partial^2 \theta}{\partial y^2} \right), \quad (13)$$

where $K = \frac{\kappa}{\mu}$ is the material parameter, $Gr = \frac{g\beta\Delta T l^3}{\nu^2}$ is the Grashof number and $Pr = \frac{\nu}{\alpha}$ is the Prandtl number.

The dimensionless governing equations are subjected to the following boundary conditions:

$$\begin{aligned} y=0 : \quad & u=1, v=0, N=-n \frac{\partial u}{\partial y}, \\ & \theta=1 \text{ for } x \leq x_0 \text{ and } \theta=\theta_{w2} \text{ for } x > x_0, \\ y \rightarrow \infty : \quad & u \rightarrow 0, v \rightarrow 0, N \rightarrow 0, \theta \rightarrow 0. \end{aligned} \quad (14)$$

Next, we set the boundary layer variables

$$x = Gr^{\frac{1}{2}} \hat{x}, \quad y = \hat{y}, \quad u = Gr^{\frac{1}{2}} \frac{\partial \psi}{\partial \hat{y}}, \quad v = -Gr^{\frac{1}{2}} \frac{\partial \psi}{\partial \hat{x}}, \quad \text{and } N = Gr^{\frac{1}{2}} \hat{N}. \quad (15)$$

where ψ is the stream function defined in such a way that equation (9) is identically satisfied.

Hence, we substitute the variables in (15) into equations 10-13 and formally let the Grashof number become asymptotically large ($Gr \rightarrow \infty$).

The set of governing equation, after introducing the boundary layer variables is

$$\frac{\partial \psi}{\partial \hat{y}} \frac{\partial^2 \psi}{\partial \hat{y} \partial \hat{x}} - \frac{\partial \psi}{\partial \hat{x}} \frac{\partial^2 \psi}{\partial \hat{y}^2} = (1+K) \frac{\partial^3 \psi}{\partial \hat{y}^3} + \theta + K \frac{\partial \hat{N}}{\partial \hat{y}}, \quad (16)$$

$$\frac{\partial \psi}{\partial \hat{y}} \frac{\partial \hat{N}}{\partial \hat{x}} - \frac{\partial \psi}{\partial \hat{x}} \frac{\partial \hat{N}}{\partial \hat{y}} = -2K\hat{N} - K \frac{\partial^2 \psi}{\partial \hat{y}^2} + \left(1 + \frac{1}{2}K \right) \frac{\partial^2 \hat{N}}{\partial \hat{y}^2}, \quad (17)$$

$$\frac{\partial \psi}{\partial \hat{y}} \frac{\partial \theta}{\partial \hat{x}} - \frac{\partial \psi}{\partial \hat{x}} \frac{\partial \theta}{\partial \hat{y}} = \frac{1}{Pr} \frac{\partial^2 \theta}{\partial \hat{y}^2}, \quad (18)$$

subjected to the boundary conditions in (14) that have been reduced to

$$\begin{aligned} \hat{y}=0 : \quad & \psi = \frac{\partial \psi}{\partial \hat{y}} = 0, \quad \hat{N} = -n \frac{\partial^2 \psi}{\partial \hat{y}^2}, \\ & \theta = 1 \text{ for } \hat{x} \leq \hat{x}_0 \text{ and } \theta = \theta_{w2} \text{ for } \hat{x} > \hat{x}_0, \\ \hat{y} \rightarrow \infty : \quad & \frac{\partial \psi}{\partial \hat{y}} \rightarrow 0, \quad \hat{N} \rightarrow 0, \quad \theta \rightarrow 0. \end{aligned} \quad (19)$$

The standard similarity form of Polhausen (1921) may be used to derive the non-similar boundary-layer equations. Therefore, we set

$$\psi = \xi^{\frac{3}{4}} f(\xi, \eta), \quad \theta = g(\xi, \eta), \quad \hat{N} = \xi^{\frac{1}{4}} h(\xi, \eta), \quad \xi = \hat{x}, \quad \eta = \frac{\hat{y}}{\hat{x}^{\frac{1}{4}}}. \quad (20)$$

Thus, the governing equations for boundary-layer flows become

$$(1+K) \frac{\partial^3 f}{\partial \eta^3} - \frac{1}{2} \left(\frac{\partial f}{\partial \eta} \right)^2 + K \frac{\partial h}{\partial \eta} + \frac{3}{4} f \frac{\partial^2 f}{\partial \eta^2} + g = \xi \left(\frac{\partial f}{\partial \eta} \frac{\partial^2 f}{\partial \xi \partial \eta} - \frac{\partial f}{\partial \xi} \frac{\partial^2 f}{\partial \eta^2} \right), \quad (21)$$

$$\left(1 + \frac{1}{2} K \right) \left(\frac{\partial^2 h}{\partial \eta^2} \right) + \frac{3}{4} f \frac{\partial h}{\partial \eta} - \frac{1}{4} h \frac{\partial f}{\partial \eta} = \xi \left(\frac{\partial f}{\partial \eta} \frac{\partial h}{\partial \xi} - \frac{\partial f}{\partial \xi} \frac{\partial h}{\partial \eta} \right) + K \xi^{\frac{1}{2}} \left(2h + \frac{\partial^2 f}{\partial \eta^2} \right), \quad (22)$$

$$\frac{1}{\text{Pr}} \frac{\partial^2 g}{\partial \eta^2} + \frac{3}{4} f \frac{\partial g}{\partial \eta} - = \xi \left(\frac{\partial f}{\partial \eta} \frac{\partial g}{\partial \xi} - \frac{\partial f}{\partial \xi} \frac{\partial g}{\partial \eta} \right), \quad (23)$$

with the boundary conditions

$$\begin{aligned} \eta = 0 : \quad f = \frac{\partial f}{\partial \eta} = 0, \quad h + n \frac{\partial^2 f}{\partial \eta^2} = 0, \\ g = 1 \text{ for } x \leq x_0 \text{ and } g = g_{w2} \text{ for } x > x_0, \\ \eta \rightarrow \infty : \quad \frac{\partial f}{\partial \eta} \rightarrow 0, \quad h \rightarrow 0, \quad g \rightarrow 0. \end{aligned} \quad (24)$$

Equations 21-23 subject to (24) should be solved for different values of ξ with n in the range of $0 \leq n \leq 1$ using the Keller-Box scheme. Before that, we need to introduce $X = \xi^{\frac{1}{2}}$, so that the equations can be written as

$$(1+K) \frac{\partial^3 f}{\partial \eta^3} - \frac{1}{2} \left(\frac{\partial f}{\partial \eta} \right)^2 + K \frac{\partial h}{\partial \eta} + \frac{3}{4} f \frac{\partial^2 f}{\partial \eta^2} + g = \frac{1}{2} X \left(\frac{\partial f}{\partial \eta} \frac{\partial^2 f}{\partial X \partial \eta} - \frac{\partial f}{\partial X} \frac{\partial^2 f}{\partial \eta^2} \right), \quad (25)$$

$$\left(1 + \frac{1}{2} K \right) \left(\frac{\partial^2 h}{\partial \eta^2} \right) + \frac{3}{4} f \frac{\partial h}{\partial \eta} - \frac{1}{4} h \frac{\partial f}{\partial \eta} = \frac{1}{2} X \left(\frac{\partial f}{\partial \eta} \frac{\partial h}{\partial X} - \frac{\partial f}{\partial X} \frac{\partial h}{\partial \eta} \right) + K X \left(2h + \frac{\partial^2 f}{\partial \eta^2} \right), \quad (26)$$

$$\frac{1}{\text{Pr}} \frac{\partial^2 g}{\partial \eta^2} + \frac{3}{4} f \frac{\partial g}{\partial \eta} - = \frac{1}{2} X \left(\frac{\partial f}{\partial \eta} \frac{\partial g}{\partial X} - \frac{\partial f}{\partial X} \frac{\partial g}{\partial \eta} \right). \quad (27)$$

The reason is that the factor $\xi^{\frac{1}{2}}$ will cause large errors at the beginning of computation.

Boundary layer equations 25-27 subject to the boundary conditions (24) are solved numerically using the Keller-box method. In this method, the governing equations are first reduced to first order equation. We use the Newton's method to linearise the resulting nonlinear equations and finally, we obtain the solution using the block elimination methods

3. Numerical Solution

The results obtained by using Keller box method for the problem considered are presented here in. Comparison between present results and the existing solution in the literature is also included. The new results obtained by using Keller box method include the reduced angular velocity profiles, development of wall shear stress or skin friction and development of the rate of change of the gyration component at the wall for various values of θ_{w2} . To assess the accuracy of the present results, comparisons between the present results and previously published data reported by Rees & Pop (1997) are made.

4. Conclusion

From this study we can draw the following conclusions:

- In the cases of fixed K and n , the reduced angular velocity increases then decreases with increasing Prandtl number and eventually tends to zero.

- For fixed K and n , wall shear stress decreases then increases and eventually tends to zero with an increase in Prandtl number.
- For fixed K and n the rate of heat transfer increases then decreases and increases again and eventually tends to zero with an increase in Prandtl number.

References

- Kelleher, M. (1971). Free Convection From A Vertical Plate With Discontinuous Wall Temperature. *Trans. ASME*, 93, 349-356.
- Lee, S. & Yovanovich, M.M. (1987a). Laminar Natural Convection From A Vertical Plate With Variations In Wall Temperature. *Journal of Heat Transfer*, 113, 111-119.
- Lee, S. & Yovanovich, M.M. (1987b). Laminar Natural Convection From A Vertical Plate With A Step Change In Wall Temperature. *Journal of Heat Transfer*, 113, 501-504.
- Ostrach, S. (1953). An Analysis of Laminar Free-Convection Flow and Heat Transfer about a Flat Plate Parallel to the Direction of the Generating Body Forces. *NACA TR*, 1111.
- Rees, D.A.S & Pop. I. (1997). Free Convection Boundary Layer Flow of a Micropolar Fluid From a Vertical Flat Plate. *Journal of Applied Mathematics*, 61, 179-197
- Sparrow, E.M. and Gregg, J.L. (1958). Similar Solutions for Free Convection From a Nonisothermal Vertical Plate, *Trans. ASME.*, 80, 379-386.

Table 1. Comparison between Rees & Pop (1998) and the present method for variation of $h(0)$, $h'(0)$ and $g'(0)$

Pr	$h(0)$		$h'(0)$		$g'(0)$	
	Rees & Pop (1998)	Current	Rees & Pop (1998)	Current	Rees & Pop (1998)	Current
0.1	- 1.21505	- 1.21511	0.71152	0.71160	- 0.16274	- 0.16272
0.2	- 1.13288	- 1.13301	0.63528	0.63542	- 0.21772	- 0.21771
0.5	- 1.00855	- 1.00866	0.52277	0.52282	- 0.31195	- 0.31195
0.7	- 0.96012	- 0.96022	0.48000	0.48007	- 0.35321	- 0.35321
1.0	- 0.90819	- 0.90827	0.43495	0.43501	- 0.40103	- 0.40105
2.0	- 0.80789	- 0.80794	0.35117	0.35121	- 0.50662	- 0.50666
5.0	- 0.68135	- 0.68140	0.25424	0.25427	- 0.67458	- 0.67470
6.7	- 0.64312	- 0.64316	0.22741	0.22745	- 0.73597	- 0.73613
10.0	- 0.59283	- 0.59287	0.19411	0.19415	- 0.82684	- 0.82709

Table 1 shows that the solution obtained using the present method is remarkably close to the existing solution by Rees & Pop (1997).

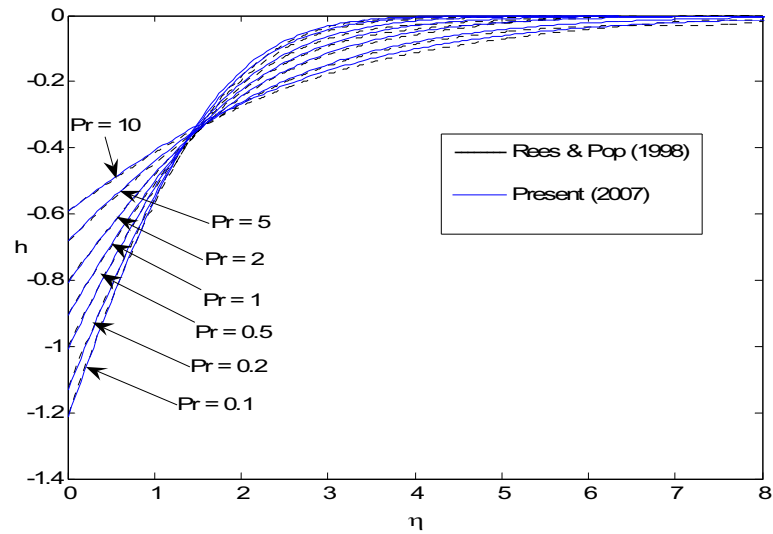


Figure 1. Comparison between Rees & Pop (1998) and the present method for profiles of the reduced angular velocity h as a function of η for different values of Pr when $K=0$ and $n=1$.

As we can see from the Figure 1, it is shown that the agreement between present results and those obtained by Rees & Pop are very good. Therefore, we confident that the present results are accurate. Hence, this is an encouragement to further study this problem.

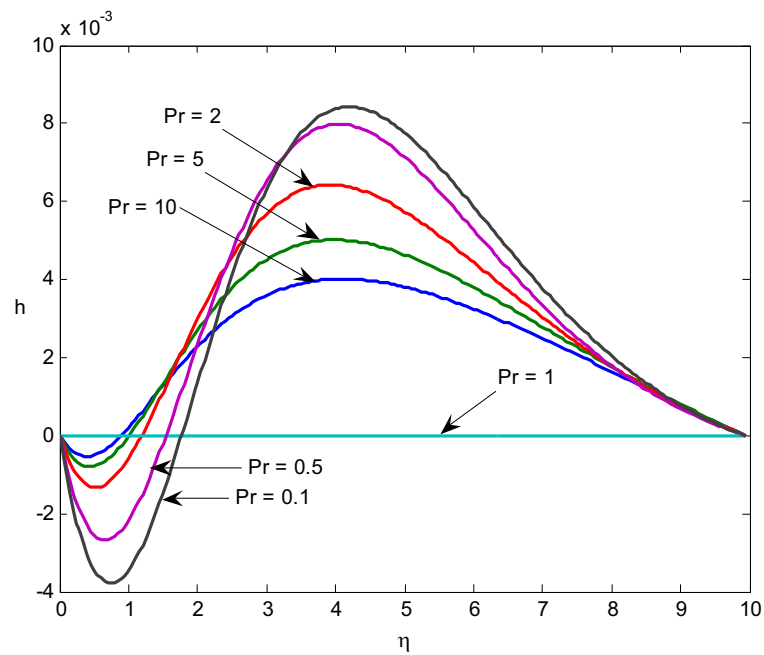


Figure 2. Profiles of the reduced angular velocity h as a function of η for different values of Pr when $K=1$, $n=0$ and $\theta_{w2}=0.5$.

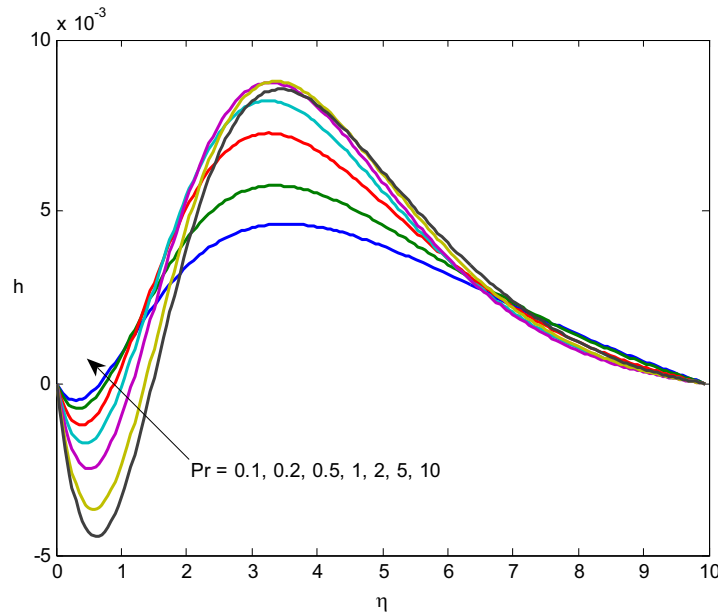


Figure 3. Profiles of the reduced angular velocity h as a function of η for different values of Pr when $K=1$, $n=0$ and $\theta_{w2}=2$.

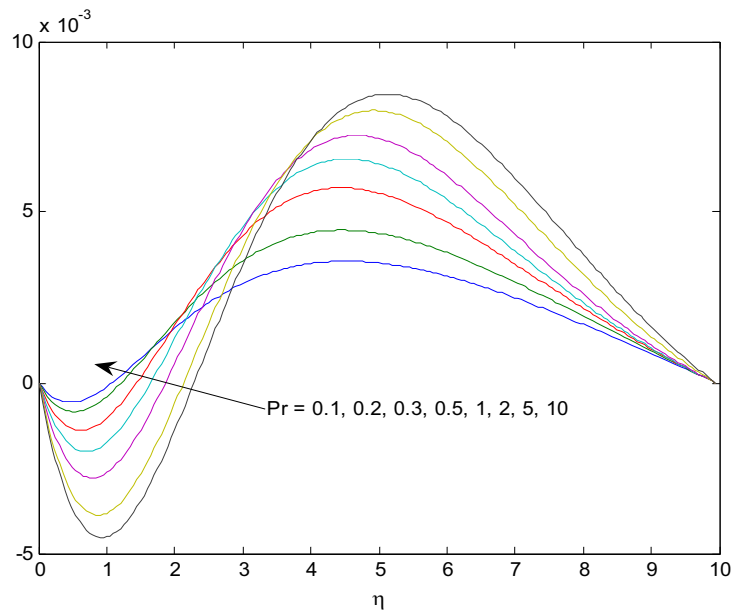


Figure 4. Profiles of the reduced angular velocity h as a function of η for different values of Pr when $K=1$, $n=0$ and $\theta_{w2}=0$.

In Figures 2-4, we have shown some graphs of the characteristics of angular velocity profile as a function of η at different streamwise locations for $\theta_{w2} = 0.5, 2$ and 0 . Figures 2-4 show that h initially increases then decreases and eventually tends to zero with an increase in Pr .

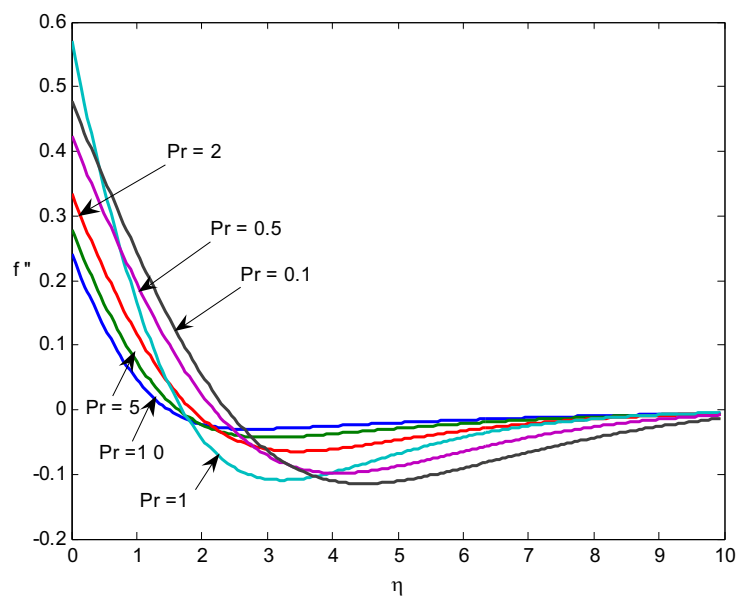


Figure 5. Profiles of the shear stress f'' as a function of η for different values of Pr when $K=1$, $n=0$ and $\theta_{w2}=0.5$.

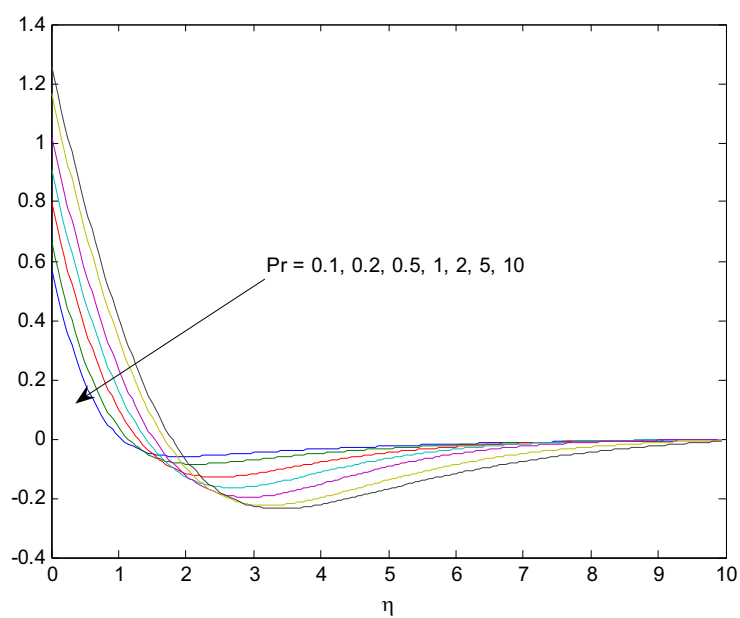


Figure 6. Profiles of the shear stress f'' as a function of η for different values of Pr when $K=1$, $n=0$ and $\theta_{w2}=2$.

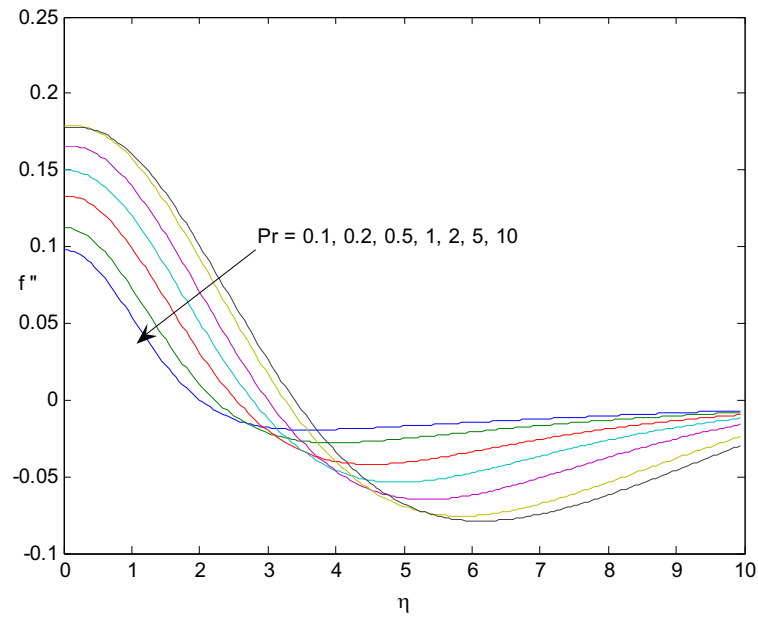


Figure 7. Profiles of the shear stress f'' as a function of η for different values of Pr when $K=1$, $n=0$ and $\theta_{w2}=0$.

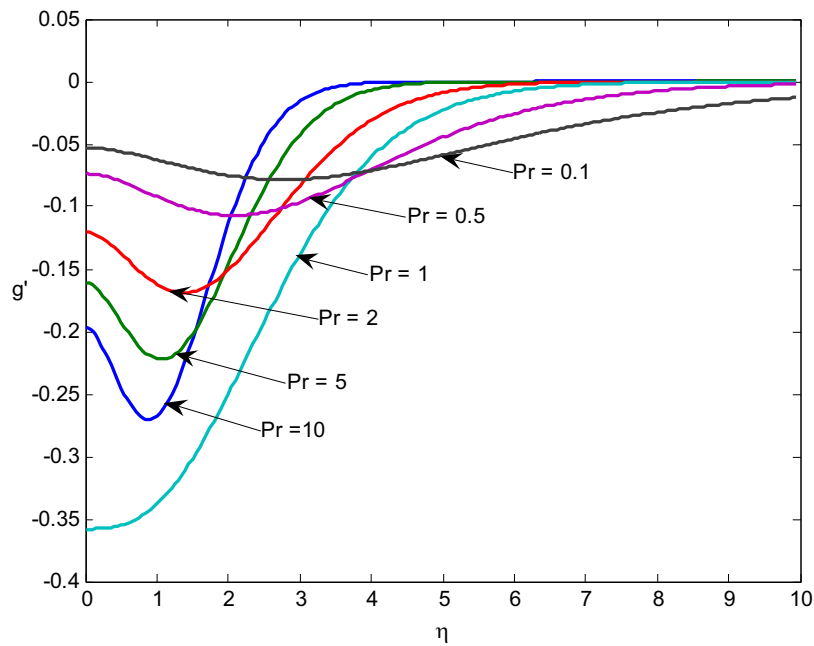


Figure 8. Profiles of rate of heat transfer g' as a function of η for different values of Pr when $K=1$, $n=0$ and $\theta_{w2}=0.5$.

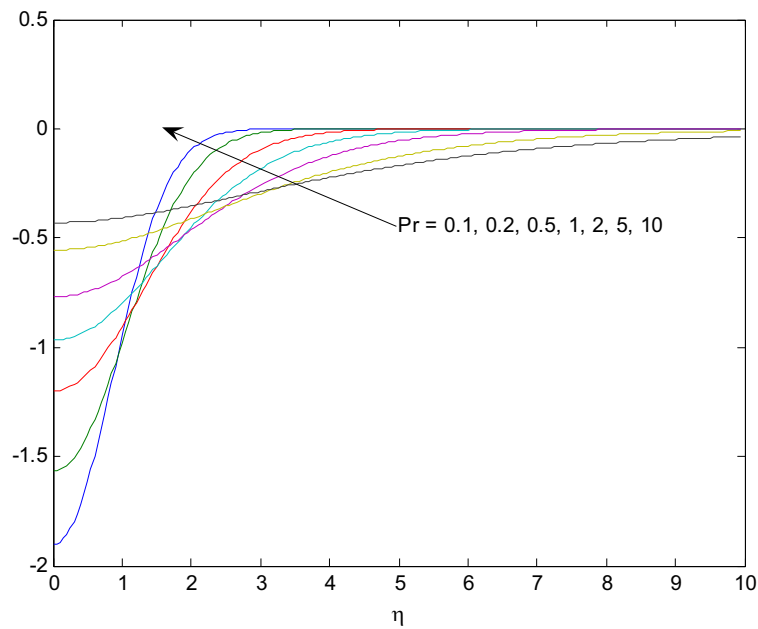


Figure 9. Profiles of rate of heat transfer g' as a function of η for different values of Pr when $K=1$, $n=0$ and $\theta_{w2}=2$.

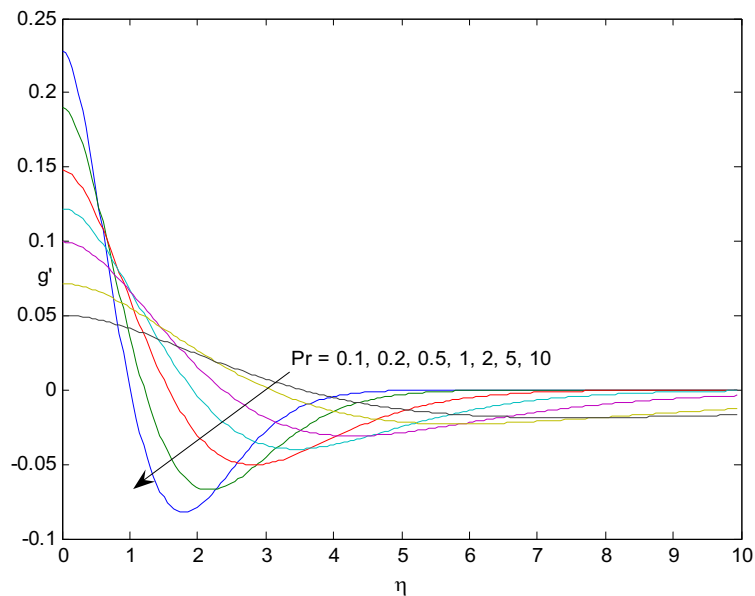


Figure 10. Profiles of rate of heat transfer g' as a function of η for different values of Pr when $K=1$, $n=0$ and $\theta_{w2}=0$.

From Figures 5-10, we now consider the variation of the shear stress (or skin friction) and the rate of change of gyration component at the solid boundary with η . From Figure 4 and Figure 7, we show f'' as a function of η at different streamwise locations for $\theta_{w2}=0.5, 2$ and 0 . Figures 4-7 show that f'' decreases then increases and eventually tends to zero with an increase in Pr . Otherwise, Figures 8-10 show g' increases then decreases and increases again and eventually tends to zero.



Study on Characteristics of Sound Absorption of Underwater Visco-elastic Coated Compound Structures

Zhihong Liu & Meiping Sheng

College of Marine

Northwestern Polytechnical University

Xi'an 710072, China

E-mail: liuzh_nwpu@126.com

Abstract

Visco-elastic damping materials containing kinds of air-filled, fluid-filled microspheres or cylindrical cavities have been widely used in various areas involving the coating of water-borne structure to reduce acoustic echoes to active sonar systems. As a special damping material, rubber has attracted great interest in the field of vibration and noise for its low Young's modulus and high strain recovery features. Based on wave transfer propagation theory in infinite layered medium, sound absorption performance for underwater compound damping structures is investigated using transfer matrix method.

A new anechoic coating containing different varying sectional cavities is proposed. Simulation results show that the new anechoic coating keeps good absorption performance in high frequency and its sound absorption coefficient is increased notably in low frequency. Simulations also show that the property of rubber material influences structural sound absorption greatly. Soft rubber as well as those with large loss factor may improve sound absorption performance of the whole structure remarkably. New anechoic coating containing varying sectional cavities have great advantages over the uniform compound structures. It's a good way to make different varying sectional cavities inside multi-layered rubber compound structures for improving sound absorption property. The sound absorption coefficient can be modulated by changing the thickness of the three different varying sectional cavities, and not the more the cavities are, the better sound absorption will achieve. As a new kind of complex multilayered rubber compound structures, compound structure containing varying sectional cavities has better sound absorption property than rubber interlayer with cylindrical cavities compound structure and homogeneous rubber compound structure.

Keywords: Visco-elastic material, Sound absorption, Compound structure, Varying sectional cavities

1. Introduction

Visco-elastic damping materials have been widely used in many areas involving the coating of water-borne structure to reduce the acoustic echoes to avoid active sonar systems. As a particular kind of damping material, rubber has lower Young's modulus and better strain recovery ability compared to metal material, and so it can prevent structure from noise transmission more effectively. In this paper, the study of sound absorption performance of underwater compound damping structures with varying sectional cavities is carried out, which can provide a guidance for underwater structure sound absorption research and engineering applications.

There are four important analysis methods for sound absorption: Transfer matrix method, FEM, BEM and statistical energy analysis (SEA). Transfer matrix method is a classical approach to solve sound absorption, which is adopted in literatures. The results of literatures show that there are some differences between predicted values and measuring ones in low frequency range because the infinite plate theory does not consider the influence of geometrical dimensions. But the limitation can be modified in a certain extent by considering structure finite sizes. SEA method in literature can simplify complex vibration-acoustic damping system and change its energy transmission to a set of linear equations' solution. But in general, SEA is commonly applied to calculate for the problem of high frequencies and it is also limited when solving non-resonance problems of sound and energy. Numerical method referred in literature is not restricted by structure geometrical dimensions and material properties, and can be applied to solve non-linear problems. But when the frequency increases, the necessary divided mesh number manifolds rapidly, calculating the highest frequency is then confined. To break the limitations of single approaches, combination of two kinds of methods is considered. For instance, FEM together with BEM is used to treat with low frequency diffusing field of double-wall sound barriers with elastic porous linings in literature; while the combination of FEM and SEA is used to dispose of multilayered panels in

literature. Nevertheless there are some problems in the combinations. Comparatively, Transfer matrix method is the better method, which has a long investigation history and mature theory analysis.

Therefore, based on wave transfer theory of infinite layered medium in literature, Transfer matrix method is adopted as a theoretical analysis method. In condition of normal incidence, the sound absorption properties of homogeneous underwater coatings and underwater coatings containing uniform cylindrical cavities are researched and their shortages of frequency response properties are pointed out in our early studies. Secondly, on the basis of the studies mentioned, a new type of underwater sound absorption coatings is proposed, whose sound absorption performances are also investigated and compared with the cylindrical cavities compound structure and homogeneous rubber compound structure. The theoretical formulation and results are described in Sec.2, the results obtained with different structures are shown and discussed in Sec.3, and finally summarized in Sec.4.

For reading conciseness, homogeneous rubber compound structure is simplified to HRCS rubber with cylindrical cavities compound structure is simplified to RWCCS, and rubber with varying sectional cavities compound structure is simplified to RVWCCS.

2. Theoretical Formulation and Solution

When plane wave transmits from one medium to another in normal incidence, two kinds of sound wave are produced because of the impedance difference between the two media. One is the reflection wave, the other is the transmission wave. At the interface of the two kinds of media, it satisfies: (1) pressure is continuous; and (2) particle vibration velocity in vertical direction is also continuous. Formulations of multi-layered HRCS and multi-layered RWCCS have been given in our early researches, so here only the formulation of multi-layered RVWCCS is given.

RVWCCS is a special multi-layered HRCS. This paper puts forward the kind of new coating structure on the basis of HRCS and RWCCS structure, and brings it into underwater noise control field and discusses its sound absorption performance in condition of normal incidence.

New varying sectional coating's structure in the paper is constituted of different sectional structures among rubber layers. A whole RVWCCS includes the surface layer, varying sectional layers and the bottom layer. In this way, varying sectional rubber layer is made up of three different rubber varying sectional layer, which is catenary shape structure, taper shape structure, and exponential shape structure layer. The RVWCCS sketch is illustrated in Figure 1. Hence, it is a five-layer structure. Underwater non-homogeneous compound structure illustrated in this paper is to add RVWCCS onto double-layer shells, which is a compound sound absorption structure composed by eight layers, seen in Figure 2.

The governing equation of sound in non-homogeneous layered rubbers containing varying sectional cavities is written as follows

$$\frac{\partial^2 p}{\partial x^2} + \left(\frac{\partial \ln s}{\partial x} \right) \frac{\partial p}{\partial x} = \frac{1}{c_0^2} \frac{\partial^2 p}{\partial t^2} \quad (1)$$

Let $p = p(x)e^{j\omega t}$ be the solution of the above equation. It is simplified to

$$\frac{d^2 p(x)}{dx^2} + \frac{s'}{s} \frac{dp(x)}{dx} + k^2 p(x) = 0 \quad (2)$$

Where $s' = \frac{ds}{dx}$, $k = \frac{\omega}{c_i}$, when $s(x)$ satisfies $\frac{(\sqrt{s})''}{\sqrt{s}} = \mu^2$

$$p(x) = \frac{1}{\sqrt{s}} \psi(x) \quad (3)$$

Apply Eq.(3) to Eq.(2), Eq.(4) is yielded

$$\frac{d^2 \psi(x)}{dx^2} + K^2 \psi(x) = 0 \quad (4)$$

Where $K^2 = k^2 - \mu^2$.

Apply Eq.(3) to Eq.(4), the solution of Eq.(4) is shown as

$$p(x) = \frac{1}{\sqrt{s(x)}} \left(p_{ia} e^{-j\sqrt{k^2 - \mu^2}x} + p_{ra} e^{j\sqrt{k^2 - \mu^2}x} \right) \quad (5)$$

Total pressures and particle velocity in unit sections of non-homogeneous layers are formulated as

$$F(x) = s(x)p(x) = -\rho c^2 s(x) \frac{\partial p}{\partial x} \quad (6)$$

$$v(x) = j\omega p(x) \quad (7)$$

Where $s(x) = \begin{cases} s_0 e^{2\mu x} \\ s_0 \cos^2 h(\mu x) \\ s_0 (1 + \beta x)^2 \end{cases}$, s_0 represents the initial area of varying sectional structure, μ represents the

parameter which determines the change of sectional area, β represents the extend slope ratio.

The underwater non-homogeneous compound structure is the model shown in Figure 2. It models the underwater large sample experiment environment. Transfer matrices of the sound wave in Multi-layered structures are denoted as when $x = 0$

$$\begin{bmatrix} F_1 \\ v_1 \end{bmatrix} = \begin{bmatrix} s_1 & s_1 \\ \frac{1}{z_1} & -\frac{1}{z_1} \end{bmatrix} \begin{bmatrix} p_{1ia} \\ p_{1ra} \end{bmatrix} \quad (8)$$

when $x = d_1$

$$\begin{bmatrix} e^{-jk_1 d_1} \times s_1 & e^{jk_1 d_1} \times s_1 \\ \frac{e^{-jk_1 d_1}}{z_1} & -\frac{e^{jk_1 d_1}}{z_1} \end{bmatrix} \begin{bmatrix} p_{1ia} \\ p_{1ra} \end{bmatrix} = \begin{bmatrix} e^{-jk_1 d_1} \times s_1 \times (-z_1 \times c_1) \times \left[\left(s^{-\frac{1}{2}} \right)' \Big|_{x=d_1} + s^{-\frac{1}{2}} \Big|_{x=d_1} \times (-jK) \right] \\ \frac{e^{-jk_1 d_1} \times j\omega}{\sqrt{s_1}} \\ e^{jk_1 d_1} \times s_1 \times (-z_1 \times c_1) \times \left[\left(s^{-\frac{1}{2}} \right)' \Big|_{x=d_1} + s^{-\frac{1}{2}} \Big|_{x=d_1} \times (jK) \right] \\ \frac{e^{jk_1 d_1} \times j\omega}{\sqrt{s_1}} \end{bmatrix} \begin{bmatrix} p_{2ia} \\ p_{ra} \end{bmatrix} \quad (9)$$

When $x = d_2$

$$\begin{bmatrix} e^{-jk_2 d_2} \times s_2 \times (-z_1 \times c_1) \times \left[\left(s^{-\frac{1}{2}} \right)' \Big|_{x=d_2} + s^{-\frac{1}{2}} \Big|_{x=d_2} \times (-jK) \right] \\ \frac{e^{-jk_2 d_2} \times j\omega}{\sqrt{s_2}} \\ e^{jk_2 d_2} \times s_1 \times (-z_1 \times c_1) \times \left[\left(s^{-\frac{1}{2}} \right)' \Big|_{x=d_2} + s^{-\frac{1}{2}} \Big|_{x=d_2} \times (jK) \right] \\ \frac{e^{jk_2 d_2} \times j\omega}{\sqrt{s_2}} \end{bmatrix} \begin{bmatrix} p_{2ia} \\ p_{ra} \end{bmatrix} = \begin{bmatrix} e^{-jk_1 d_2} \times s_2 & e^{jk_1 d_2} \times s_2 \\ \frac{e^{-jk_1 d_2}}{z_1} & -\frac{e^{jk_1 d_2}}{z_1} \end{bmatrix} \begin{bmatrix} p_{3ia} \\ p_{3ra} \end{bmatrix} \quad (10)$$

when $x = d_3$

$$\begin{bmatrix} e^{-jk_1 d_3} \times s_2 & e^{-jk_1 d_3} \times s_2 \\ \frac{e^{-jk_1 d_3}}{z_1} & -\frac{e^{jk_1 d_3}}{z_1} \end{bmatrix} \begin{bmatrix} p_{3ia} \\ p_{3ra} \end{bmatrix} = \begin{bmatrix} e^{-jk_2 d_3} \times s & e^{jk_2 d_3} \times s \\ \frac{e^{-jk_2 d_3}}{z_2} & -\frac{e^{jk_2 d_3}}{z_2} \end{bmatrix} \begin{bmatrix} p_{4ia} \\ p_{4ra} \end{bmatrix} \quad (11)$$

When $x = d_4$

$$\begin{bmatrix} e^{-jk_2 d_4} \times s & e^{jk_2 d_4} \times s \\ \frac{e^{-jk_2 d_4}}{z_2} & -\frac{e^{jk_2 d_4}}{z_2} \end{bmatrix} \begin{bmatrix} p_{4ia} \\ p_{4ra} \end{bmatrix} = e^{-jk_0 d_4} \begin{bmatrix} F_2 \\ v_2 \end{bmatrix} \quad (12)$$

So the Transfer matrices of multi-layered RVWCCS which is made up of n rubber layers can be expressed as follows

$$\begin{bmatrix} F_1 \\ v_1 \end{bmatrix} = A_1 A_2^{-1} A_3 A_4^{-1} A_5 A_6^{-1} \cdots A_{2n-1} A_{2n}^{-1} e^{-jk_0 d_n} \begin{bmatrix} F_{n+1} \\ v_{n+1} \end{bmatrix} \quad (13)$$

Where $K = \sqrt{k^2 - \mu^2}$ is the wave number of non-homogeneous multi-layered RVWCCS. And then it can be obtained that

$$\begin{bmatrix} (p_{ia} + p_{ra}) \times s \\ \frac{p_{ia}}{z_0} - \frac{p_{ra}}{z_0} \end{bmatrix} = \begin{bmatrix} c_{11} \times p_{ia} \times e^{-jk_0 d_4} \times s + \frac{c_{12} \times p_{ia} \times e^{-jk_0 d_4} \times s}{z_0} \\ c_{21} \times p_{ia} \times e^{-jk_0 d_4} \times s + \frac{c_{22} \times p_{ia} \times e^{-jk_0 d_4} \times s}{z_0} \end{bmatrix} \quad (14)$$

Ultimately, the sound pressure coefficient of transmission, reflection and absorption can be written respectively as

$$t_p = \frac{p_{ia}}{p_{ia}} = \frac{2}{c_{11} + \frac{c_{12}}{z_0 \times s} + c_{21} \times z_0 \times s + c_{22}} \quad (15)$$

$$r_p = \frac{p_{ia}}{p_{ra}} = \frac{c_{11} + \frac{c_{12}}{z_0 \times s} - c_{21} \times z_0 \times s - c_{22}}{c_{11} + \frac{c_{12}}{z_0 \times s} + c_{21} \times z_0 \times s + c_{22}} \quad (16)$$

$$\alpha = 1 - t_p^2 - r_p^2 \quad (17)$$

where k_0 is the water wave number, z_0 is the characteristic impedance of water.

3. Numerical simulation analysis

In order to understand the rules of the influences of material property and panel's thickness of coating on sound absorption performance, a hypothesis about the parameters of the material which will be used in the analysis is given below:

The thickness of steel shell 1 and steel shell 2 is 10mm and 30mm, respectively. The density of steel plate is 7800 kg/m^3 , Young's modulus is $21.6 \times 10^{10} \text{ Pa}$, Poisson ratio is 0.28. The density of sea water is 1026 kg/m^3 , the thickness of water-layer is 0.3m, and the sound speed in water is 1500 m/s .

The rubber layer is made of certain damping material as in literature. Its density is 1100 kg/m^3 , and its Poisson's ratio is 0.49. Its Young's modulus and corresponding loss factor properties, which depend upon the frequency and temperature. The temperature is equal to 20°C .

Influence of the thickness of surface layer on sound absorption coefficient is illustrated in Fig.3. The figure shows that the absorption peak value moves to low frequency with the increasing of thickness of surface layer, and absorption performance in low frequency is improved significantly, but the sound absorption coefficient becomes surged in about 2kHz frequency range. When the thickness increases, the absorption performance in high frequency range changes less than that in other frequency range. If the thickness of the surface layer increases too much, there will be a great effect on the absorption performance, especially in about such a frequency range from 1kHz to 2kHz.

Figure 4 shows the curve of sound absorption coefficient versus frequency, when the thickness of catenary layer is altered. With the increasing of the thickness of catenary layer, the absorption peak value remains constant before 630Hz frequency, and the sound absorption coefficient isn't improved yet. On the contrary, the sound absorption coefficient decreases with the increasing of the thickness of the catenary layer in the 10~630Hz frequency range. In the frequency band between 630Hz and 8kHz, sound absorption coefficient increases while the thickness of the catenary layer become thicker. And beyond 8kHz frequency, the influence on absorption performance is not notable with the increasing of the thickness of the catenary layer. Therefore, the thickness of the catenary layer depends on the frequency range which is concerned in the practical engineering problems.

Figure 5 shows the sound absorption coefficient curve verses frequency, while the thickness of the taper layer is altered. It is seen from the figure, the sound absorption coefficient in low frequency doesn't increase with the thickness of the taper layer, and there will be an optimal value, which can improve the sound absorption coefficient greatly in low frequency range, it is not necessary to increase the total thickness of anechoic coating for getting the optimal design. The higher the frequency, the smaller the influence on absorption performance, especially beyond 5kHz.

It is seen from figure 6 that the influence on sound absorption coefficient by the thickness of the exponential layer is small before 400Hz frequency. With the increasing of the frequency and the thickness of the exponential layer, the

sound absorption coefficient increases also in about such a frequency range from 400Hz to 2kHz. But compared to the extent that the thickness of the exponential layer, the sound absorption coefficient doesn't increase remarkably. And there is almost no influence on sound absorption coefficient in high frequency range (beyond 5kHz) with the increasing of the thickness of the exponential layer.

Influence of the thickness of bottom layer on sound absorption coefficient is given in figure 7. As is shown in the figure, there is almost no effect on sound absorption coefficient before 400Hz with the increasing of the thickness of the bottom layer. With the increasing of the thickness of the bottom layer, sound absorption coefficient increases accordingly in about such a frequency range from 400Hz to 3kHz. But influence on sound absorption performance isn't great in high frequency, especially beyond 7kHz.

Figure 8 shows that the frequency-response curve of sound absorption coefficient, when the perforation ratio is altered. It is seen from figure 8 that there is almost no effect on sound absorption coefficient with the change of the perforation ratio in such a frequency range from 1kHz to 20kHz. But influence on sound absorption coefficient is notable before 1kHz frequency. In addition, there will be an optimal perforation ratio value which can improve the sound absorption coefficient greatly in low frequency range.

Figure 9 shows the sound absorption coefficient curve versus frequency, while the loss factor is altered. It can be seen from the figure that the sound absorption coefficient increases with the increasing of the loss factor of rubber material. It also can be seen from the figure that there is almost no effect on peak value of the frequency of sound absorption coefficient, but influence on peak value of sound absorption coefficient is notable. From the figure, we can see that sound absorption coefficient will be decreased beyond 2kHz frequency range when loss factor becomes too large. Hence, there will be an optimal value for loss factor.

When the Young's modulus is altered, the sound absorption coefficient curve versus frequency is shown in Figure 10. It can be seen from the figure 10 that the sound absorption coefficient decreases if the Young's modulus is too large. It is because that if the Young's modulus becomes too large, impedance of rubber layer will not match the impedance of water well. It is also found that when the Young's modulus becomes small, sound absorption coefficient improves greatly in low frequency. Similarly, there will be an optimal value for Young's modulus.

Figure 11 shows the sound absorption coefficient curve versus frequency, while the thickness of the water layer is altered. It is seen from the figure that there is almost no effect on the form of the sound absorption coefficient, when the thickness of the water layer is changed. When the thickness of the water layer increases, peak value of sound absorption coefficient moves to low frequency. It is because that the sound speed diminishes in water, and at the same time the thickness of the water increases, and therefore the resonance phenomena occurs in water layer.

Figure 12 shows the sound absorption coefficient curve versus frequency with three different coating structures. As a particular kind of complex multilayered rubber compound structures, compound structure containing varying sectional cavities has better sound absorption property than rubber with cylindrical cavities compound structure and homogeneous rubber compound structure.

4. Conclusions

In condition of normal incidence, sound absorption performance of multi-layered RVWCCS is analyzed by the transfer matrices method in the manuscript. For multi-layered RVWCCS, the influence on sound absorption performance by rubber material properties and the thickness of varying sectional compound structure is mainly investigated. The sound absorption effect on different anechoic coating is also discussed. The following results can be obtained by the above investigations.

- (1). The properties of rubber material have a large influence on sound absorption coefficient of the structure. Rubber with small Young's modulus and large loss factor is adopted in order to improve sound absorption coefficient obviously. Sound absorption coefficient of RVWCCS develops with the increasing of rubber thickness, but there is limitation on increasing sound absorption coefficient of RVWCCS at the cost of increasing the thickness of rubber.
- (2). Multilayered RVWCCS can combine advantages of HRCS, and achieve better sound absorption effect. It is of advantageous improving sound absorption performance by perforation on inside rubber. But not the larger perforation ratio of inside rubber is, the better sound absorption performance will be achieved.
- (3). Because of complex inner topology, with the same thickness of these structures, sound absorption performance of RVWCCS is much better than that of both RWCCS and HRCS.

References

- Alberto Di Meglio, Lian Sheng Wang. (2000), A variational method for identification of viscoelastic parameters from experimental data, *JASA*, 108(6), p2746-2753.
- Brekhovski L M, *Waves in Layered Media*, 2nd Edition, New York, Academic Press, 1980.

- Craik RJM, Nightingale TR, Steel JA (1997), Sound transmission through a double leaf partition with edge flanking, *JASA*, , 101(2), p964-969.
- Du, gonghuan, Zhu, zhemin, Gong, xiufen. (2003), Acoustic Foundation, Pressed in Nan Jing University, (in Chinese).
- Liu, Zhihong, Sheng, MeiPing. (2006), Analysis of Absorption Characteristics of an Oblique Incidence Plane Wave on Isotropic Symmetric Plate, *Noise and Vibration*, 26(2), p58-61. (in Chinese).
- Liu, Zhihong, Sheng, MeiPing. (2005), Analysis of Absorption Characteristics of a Normal Incidence Plane Wave on Isotropic Symmetric Plate in Water, *Noise and Vibration Control*, 25(2), p11-13. (in Chinese).
- Liu, Zhihong, Sheng, MeiPing. (2005), Study on Absorption Characteristics of visco-elastic multi-layered compound structure. *Acoustic Technica.*, (p), p11-15(in Chinese).
- Michael El-Raheb. (1997), Frequency response of a two-dimensional trusslike periodic panel, *JASA*, 101(6), p3457-3465.
- Panneton R, Atalla N. (1996), Numerical prediction of sound transmission through finite multilayer systems with poroelastic materials, *JASA*, 100(1), p346-354.
- Sgard FC, Atalla N, Nicolas J. (2000), A numerical model for the low frequency diffuse field sound transmission loss of double-wall sound barriers with elastic porous linings, *JASA*, 108(6), p2865-2872.
- Steel JA, Craik RJM. (1994), Statistical energy analysis of structure-borne sound transmission by finite element methods, *Journal of Sound Vibration*, 178(4), p553-561.
- Wang, Man. (2004). Theoretical and Experimental Study of Underwater Anechoic Coating[D], Harbin Engineering University. (in Chinese).
- Wang, Man, He, ZuoYong. (1996). Theory study on absorption performance of water non-homogeneous structure, *Apply Acoustic*, 15(5), p. (in Chinese).

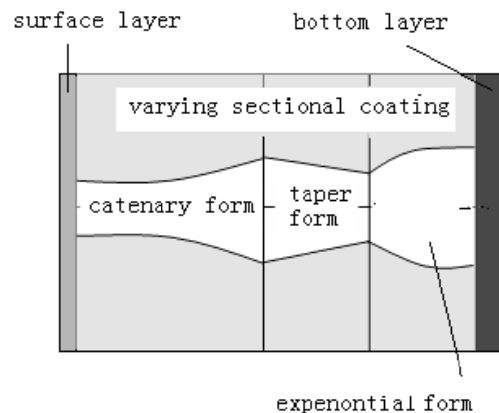


Figure 1. model of RVWCCS

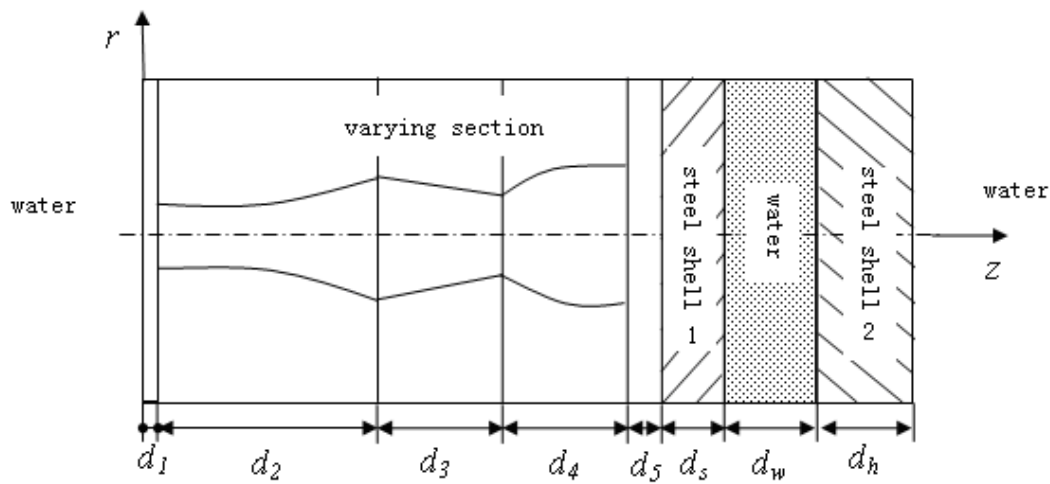


Figure 2. Sound absorption model of multi-layered RVWCCS in normal incidence.

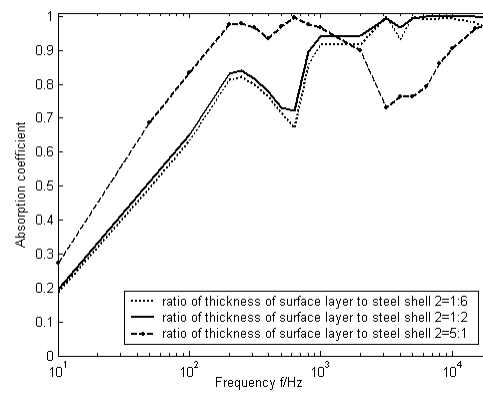


Figure 3. Sound absorption coefficient versus frequency for thickness of surface layer

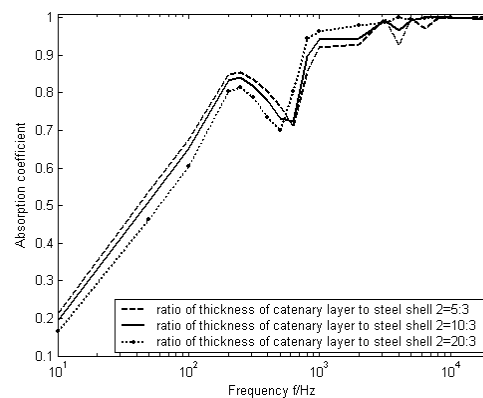


Figure 4. Influence on sound absorption coefficient of thickness of catenary layer

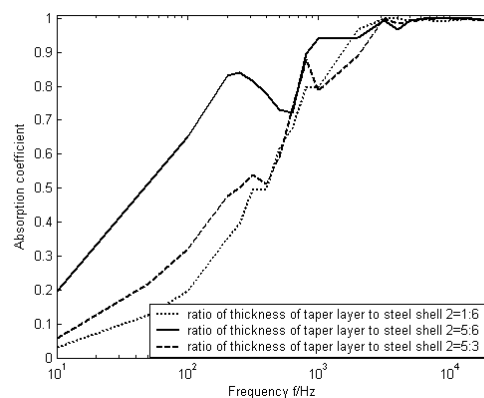


Figure 5. Influence on sound absorption coefficient of thickness of taper layer

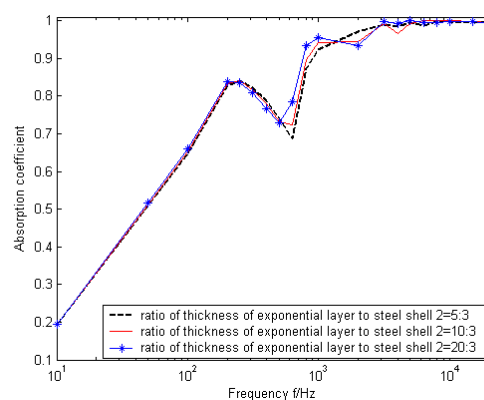


Figure 6. Influence on absorption performance by the thickness of the exponential layer

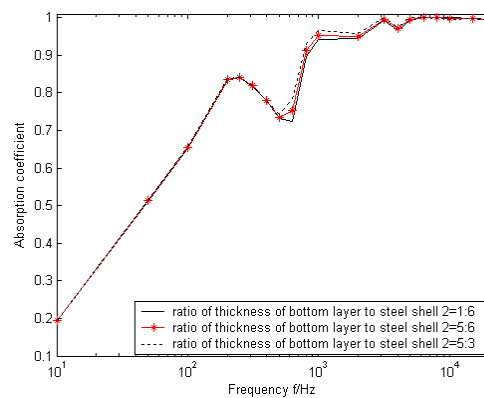


Figure 7. Influence on absorption performance by the thickness of the bottom layer

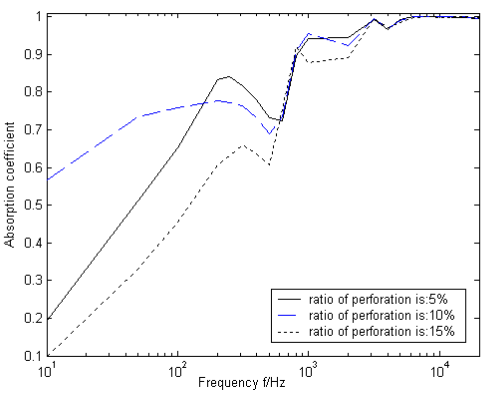


Figure 8. Influence on sound absorption coefficient of perforation ratio

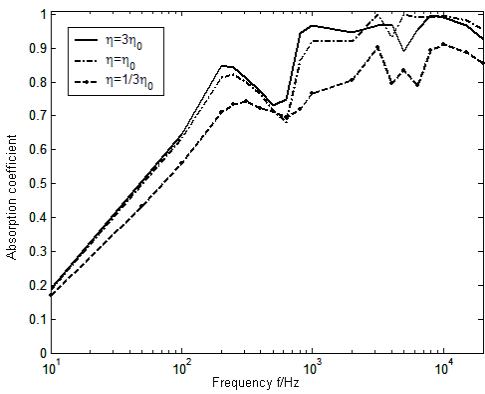


Figure 9. Influence on sound absorption coefficient of loss factor

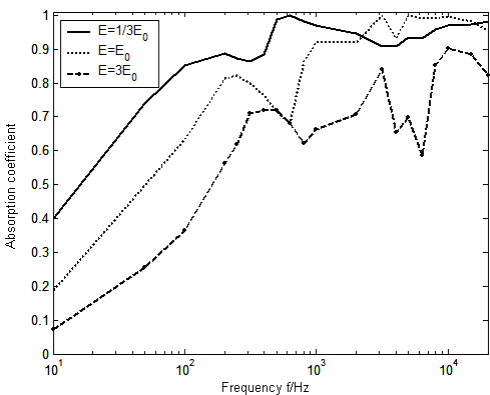
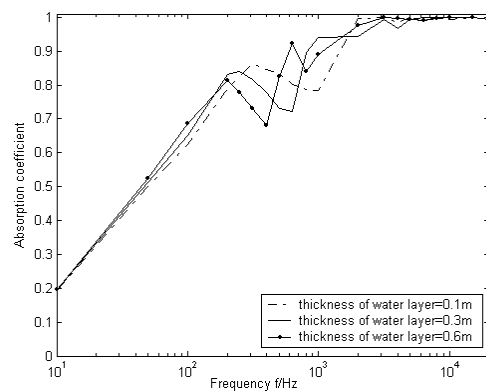


Figure 10. Influence on sound absorption coefficient of Young's modulus



..

Figure 11. Influence on sound absorption coefficient of the thickness of the water layer

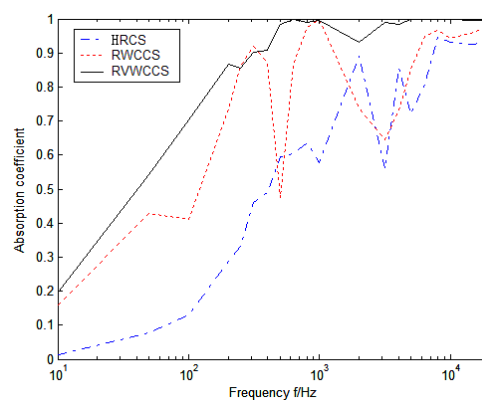


Figure 12. Influence on sound absorption coefficient of the different multi-layered coating structure



Mapping and Quantification of Land Area and Cover Types with LandsatTM in Carey Island, Selangor, Malaysia

Hj. Kamaruzaman, J (Corresponding author)

Yale University, Yale's School of Forestry & Environmental Studies

205 Prospect St, New Haven, CT 06511

Tel: 20-3-432-1384 E-mail: jusoff.kamaruzaman@yale.edu

Mohd Hasmadi, I

Department of Forest Production, Faculty of Forestry

Universiti Putra Malaysia, 43400 UPM, Serdang, Selangor, Malaysia

Tel: 60-3-8946-7220 E-mail: mhasmadi@hotmail.com

Abstract

Information about current land cover type is essential at a certain level to ensure the optimum use of the land resources. Several approaches can be used to estimate land cover area, where remote sensing and Geographic Information System (GIS) is among the method. Therefore, this study was undertaken to evaluate how reliable these technologies in preparing information about land cover in Carey Island, Selangor of Peninsular Malaysia. Erdas Imagine 9.1 was used in digital image processing. A primary data of Landsat TM, with spatial resolution of 30 m was acquired from scene 127/58 on July 2007. Area estimate was calculated using direct expansion method from samples proportion of each segments of land cover type (1 km by 1 km sample size). In this study, four classes of land cover type have been identified and the areas were oil palm, mangrove, water bodies and urban/bare land area. The area estimate for all classes are 11039.28 ha (oil palm), 5242.86 ha (mangrove), 4894.92 ha (water bodies), and 4751.96 ha (urban/bare land), respectively. The overall classification accuracy obtained for this study is 96%. The results showed that the use of direct expansion method for estimating land cover type area is practical to be used with remote sensing approaches.

Keywords: Land covers mapping, Satellite-based sensing, Direct expansion method

1. Introduction

Knowledge of land cover and land use is significant for management and planning activities concerned with the parcel of the earth. Land use is one of the essential tools for nearly all land development. Information about land cover type is essential to be gathered due to it important to understand the landscape process and generally refer to the functional character of an area with value to the occupations and culture. In traditional way, classification of land cover type and estimate their area requires a relatively time consuming and very costly. However, area estimation survey is very important in managing our land parcel and natural resources because it can facilitate land manager in land use planning. Most of time it is difficult to estimate land cover types when dealing with large area and result is requires in short time. Nowadays, remote sensing is one of the technology tools to provide advance complete information about land circumstance and human activities. The importance of remote sensing has been proved through the time serve as a useful tool in management of many types of natural resources. Land use managers planners are increasingly using remote sensing demanding that information for the decision making process (Junior and Simonett, 1976). In the beginning, the use of panchromatic, medium scale aerial photographs to map land use and land cover has been accepted practice since 1940s. Later on, small scale aerial photographs and satellite images have been utilized for land use and cover mapping of large areas (Lillesand and Kiefer, 1994).

Malaysia has started using remote sensing data such as SPOT and Landsat TM imageries for land cover mapping and land use change detection since early 1980's (Fook *et. al.*, 1994). These space borne data mainly serve as the basis for further improvement of existing procedures for land use data collection in the department of agriculture. In fact, according to Kamaruzaman and Souza (1997) the use of remote sensing data was started in 1961 by using extensive aerial photography for demarcated the upper altitudinal limit of forest land suitability for inclusion in forest state production. A black and white aerial photograph was use widely in forest resource survey in Peninsular Malaysia in 1962 which involved the systematic assessment for management purposes. Remote sensing is a less costly over large area and a more rapid means of data collection than field observation and some detail verification data are essential to its effective use. On the other

hand, remote sensing is a practical solution when area estimation is conducted using direct expansion method. Crucial needs for land cover inventory in many developing countries have already prompted the use of remote sensing and GIS to provide up-to-date information (Luney and Dill, 1970). Thus, remote sensing is often the most commercial and valuable source of current land cover and land use planning. Previously land cover area estimate by integration of sampling techniques and satellite images has been performed with high accuracy (Taylor et al., 1997; Ferencz et al.(2004).

The methodology utilized in this study is based on the use of remote sensing data and direct expansion method. Remote sensing can be valuable tools for land cover area estimate when area frame are used. Typically remote sensing helps in the definition of sampling unit and can be exploited to optimize the sample allocation and size of sampling units. In area estimation, classified remotely sensed images are used as auxiliary variables in a direct expansion estimator. This effort was demonstrated for classification and land cover statistics (Mohd Hasmadi and Kamaruzaman, 2007).

The aim of the study is to investigate the usefulness of remote sensing data for estimating land cover types at Carey Island, Peninsular Malaysia using direct expansion method, therefore the specific objectives of the study are to classify and map land cover types of the island using Landsat TM image.

2. Methodology

2.1 Description of study area

<<Figure 1. Location of the study area>>

2.2 Data acquisition and equipments

Data acquisition involved the satellite data and secondary data. Primary data was Landsat TM which taken on July 2007 for 127/58 (path / row) and acquired with spatial resolution of 30 m. Satellite imagery was obtained from Malaysia Center for Remote Sensing (MACRES). The secondary data such as 1:50000 scaled topographical map from Department of Mapping Malaysia, dated 1990 was used as reference to conduct ground verification and image interpretation process. Other equipments were used such as the Digital Planimeter (Koizumi KP 90N) to measure the area on topographical map, digital camera, and Global Positioning System (GPSmap 60CSx) for navigate point location during ground verification. The image processing and analysis was carried out using Erdas Imagine software version 9.1, while ArcView Version 3.3 was used for the GIS analysis.

2.3 Methods

Basically several steps were carried out in order to prepare satellite imagery to be used for classify and estimate area coverage of land cover types. Figure 2 illustrated the flow chart of the research process.

<<Figure 2: The flow chart of the study>>

Preprocessing involved on the imagery was geometric and radiometric correction. In geometric correction the Malaysia Rectified Skew Orthomorphic(MRSO) projection type (Spheroid name:Modified Everest and Datum name:Kertau 1948) with 30m pixels using a cubic convolution was used as a grid base system. Utilizing 8 ground control points, the final projected imagery accurate to RMSE of the registration was less than 1.0 m. De-stripping technique was done to remove radiometric problem on the image, thus improved the quality of the image for further interpretation and analysis.

Image enhancement was performed to edit the original image data by improving quality of the data for visual interpretation for creating 'new' image. Technically, image enhancement operations distort the original digital values of image data to more effectively display. Modifying contrast and brightness level to 55 and 58 percent was adequate to enhance the quality of the data for ease information extraction. However, there is no ideal or best image enhancement because the results are ultimately evaluated by humans, who make subjective judgments as to whether a given images enhancement is useful (Jensen, 1996). The original spectral band and artificial spectral band are used to create another value to the image to create different composite effects and increased information on land cover. For this study, enhancement image from 5-4-3 (R-G-B) band was the best to be used for visual interpretation and digital image classification. Image classification is the process of assigning the individual pixels of various spectral signatures to categories based on the reflectance of spectral characteristic. In this study unsupervised classification was chosen instead of supervised classification technique. At the beginning, the numbers of classes assigned for the unsupervised classification were 7 classes. Amalgamation was done to reduce the class number to 4. During the process, the maximum iterations were set to 60 times.

Ground verification was performed to verify features retrieved from the satellite images to the features on the ground. It was conducted for 2 days on 12 -13 September 2007. A total of 52 locations were visited randomly. GPS was used to assist in navigate the point location. Photographs were taken and parameters related to land cover types were recorded. All collected data obtain from ground verification were used to determine the accuracy of mapping. The data were organized in a confusion or error matrix from which both the overall classification accuracy on the individual classes can be calculated. Kappa coefficient (K) measurement was used to assess the accuracy of the classification. Kappa analysis is discrete multivariate technique of use in accuracy assessment (Congalton and Mead, 1983). It was calculated by

multiplying the total number of pixels in all the ground verification classes (N) by the sum of the confusion matrix diagonals ($\sum X_{kk}$), subtracting the sum of the ground verification pixels in a class times the sum of the classified pixels in that class summed over all classes ($\sum X_{k\Sigma} X_{\Sigma k}$), and dividing by the total number of pixels squared minus the sum of the ground verification pixels in that class times the sum of the classified pixels in that class summed over all class. The calculation of kappa statistic is as follow.

$$\kappa = \frac{\theta_1 - \theta_2}{1 - \theta_2}$$

where,

$$\theta_1 = \frac{\sum_{i=1}^r x_{ii}}{N}$$

$$\theta_2 = \frac{\sum_{i=1}^r x_{i+} x_{+i}}{N^2}$$

x_{ij} = number of counts in the ij th cell of the confusion matrix

N = total number of counts in the confusion matrix

x_{i+} = marginal total of row i

x_{+i} = marginal total of column i

Calculation of the variance of Kappa:

$$\text{var}(\kappa) = \frac{1}{N} \left[\frac{\theta_1(1-\theta_1)}{(1-\theta_2)^2} + \frac{2(1-\theta_1)(2\theta_1\theta_2 - \theta_3)}{(1-\theta_2)^3} + \frac{(1-\theta_1)^2(\theta_4 - 4\theta_2^2)}{(1-\theta_2)^4} \right]$$

where,

$$\theta_1 = \frac{\sum_{i=1}^r x_{ii}}{N}$$

$$\theta_2 = \frac{\sum_{i=1}^r x_{i+} + x_{+i}}{N^2}$$

$$\theta_3 = \frac{\sum_{i=1}^r x_{ii}(x_{i+} + x_{+i})}{N^2}$$

$$\theta_4 = \frac{\sum_{i=1, j=1}^r x_{ij}(x_{j+} + x_{+i})^2}{N^3}$$

x_{j+} = marginal total of row j

3. Sampling design and direct expansion method

Systematic random sampling was selected for sampling design where sample plots were distributed evenly to all parts of the target area. A total of 39 sample segments were selected using systematic sampling with 2 km by 2 km of size and the size of sample is about 1 km by 1 km. Later on, from sample segments a total of 39 sample unit were selected randomly. Each sample point represented an area corresponding to the size of the grid cell of the sample layout. For example, when sample points were selected randomly from a square systematic grid with 1000 meters distance between the points, each sample point represents an area of 1 km by 1 km. The percentage of sample proportion obtained from samples unit was 4.6 percent. Figure 2 illustrated the sample segment and sample unit of the study area. The value from each digitized of sample unit in each sample segment were then calculated using direct expansion equation to produce the estimate of the land cover area.

<<Figure 3. A systematic random design for 39 samples and unit segments over Carey Island.>>

Calculation of the area estimates has been done by proportions rather than as absolute areas because the proportion is automatically takes account of errors resulting from small localized variations in the segment scale and digitizing errors (Taylor et al., 1997; Mohd Hasmadi and Kamaruzaman, 2007). The unbiased estimate of land cover proportion of land area covered by class c is given by the equation:

$$\bar{y}_c = \frac{1}{n} \sum_{i=1}^n y_i$$

$$\text{with variance } \text{Var}(\bar{y}_c) = \left(1 - \frac{n}{N}\right) \frac{1}{n(n-1)} \sum_{i=1}^n (y_i - \bar{y}_c)^2$$

where: y_i is the proportion of segment i covered by class c ; N = total number of segments in the region, n = number of segments in the sample. The proportion of the study region sampled $\left(\frac{n}{N}\right)$ is referred to as the sample fraction. When this is less than 5%, the correction factor for a finite population $\left(1 - \frac{n}{N}\right)$ can be omitted from the above formula (Cochran, 1977). The estimate of the class area is:

$$\hat{Z}_c = D \bar{y}_c$$

$$\text{with variance: } \text{Var}(\hat{Z}_c) = D^2 \text{Var}(\bar{y}_c)$$

where, D is the area of the region.

The standard error or accuracy of \hat{Z}_c is estimated by calculating the 95% confidence interval as follows:

$$\hat{Z}_c \pm 1.96 \sqrt{\text{var}(\hat{Z}_c)}$$

4. Result and discussion

4.1 Image classification

In this classification, the land cover type was classified and divided into several classes based on natural grouping of the original Landsat TM data. The result of unsupervised classification technique from composite image of 5-4-3 (R-G-B) band produced four land cover classes namely oil palm, mangrove, water bodies and urban/bare land, respectively. The unsupervised classification image was shown in Figure 4.

<<Figure 4. Land covers type within the Carey Island using unsupervised technique>>

4.2 Area estimate calculation

Using the direct expansion equation, the land cover area estimates were calculated. Area proportion and total area estimate of each land cover class was shown in Table 1. The table includes standard error, coefficient of variation and 95% confidence interval. From the table it showed that area estimation results are as follows; oil palm (11039.28 ha.), mangrove (5242.86 ha), water bodies (4894.92 ha), and urban/bare land (4751.96 ha). Meanwhile, Figure 5 showing the extent of the area estimates in hectare and percent.

<<Table 1. Area proportion and total area estimate of each class by direct expansion method>>

<<Figure 5. Estimated land cover area (in ha and %) of Carey Island>>

4.3 Accuracy assessment

During accuracy assessment process a total of 52 random sampling points were selected in order to determine the accuracy for image classification output (Figure 6). The result of confusion matrix was expressed in tabular form as shown in Table 2. The overall accuracy achieve was 96.97% which is higher than qualification accuracy of a digital classified image of 80% using optical data suggested by Paul (1995). From the table most of the land cover types were classified correctly, but oil palm was confused with mangrove and urban/bare land. In Kappa analysis, kappa coefficient result is 0.95. Table 3 showed the producers and users accuracy of classified image of Carey Island, where the highest producer's accuracy was oil palm (100.00%) and followed by other land cover class with water bodies (96.30%), mangrove (95.65%), and urban/bare land (87.50%). Meanwhile, mangrove and water bodies classes were the highest of the user's accuracy (100.00%), oil palm (94.74%) and urban/bare land had the lowest accuracy (93.33%) due to false classification during classification process.

<<Figure 6: Selected ground verification points in Carey Island (fillet black)>>

<< Table 2. Confusion matrix of the classification image of Carey Island>>

<< Table 3. Producer's and user's accuracy of the classification image of Carey Island>>

5. Conclusion

Applying remote sensing data and for land cover classification and direct expansion method for area estimation revealed the benefit for managing land resources. This study concluded that remote sensing and GIS technique is a powerful tool for generating land cover types and estimate land cover area in Carey Island. False color composite of Landsat TM band 5-4-3 (R-G-B) has showed the best combination for image interpretation. Image classification result by unsupervised technique showed that 96% of the land cover mapping is correct. The result of using direct expansion method for area estimation is reliable and produced result in short time. The highest land cover proportion was oil palm (11039.28 ha or 43%), followed by mangrove (5242.86 ha or 20%), water bodies (4894.92 ha or 19%) and the lowest percentage was urban/bare land type (4751.96 ha or 18%), respectively. Further studies are recommended to integrate remote sensing data and GIS in developing land cover data base system for efficient management of natural resources and it changes over time. Area estimation studies should be tested with different resolution of optical data and cost effectiveness of the methodologies also should be investigated.

Acknowledgements

The authors would like to thank Mr. Khairudin Hashim, the Director of Golden Hope Research Sdn. Bhd for his permission to conduct this research in Carey Island. Special thanks also go to Malaysian Centre for Remote Sensing (MACRES) for providing satellite data for this work.

References

- Cochran, W.G., (1997). *Sampling Techniques*. 3rd Edition. John Wiley and Sons, 413p.
- Congalton, R.G. and Mead, R.A., (1983). A Quantitative Method to Test for Consistency and Correctness in Photointerpretation. *Photogrammetric Engineering and Remote Sensing*, 49 (1): 60-74.
- Ference, C., Bogner, P., Lichtenberger, J., Hamar, T., Tarcs, I.G., Timar, G., Molnar, G., Pasztor, R.S., Steinbach, P., Szekel, Y.B., Ference, O.E., and Ference-Arkos, I., (2004). Crop yield estimation by remote sensing. *International Journal of Remote sensing*, 25: 4113-4149.
- Fook, L.K., Ku Mohd and Laili, N., (1994). Complimentary Nature of SAR and Optical Data for Land Cover Mapping. Paper Presented at *The National Seminar for Decision Makers on 'Potential Applications of ERS-1 in Malaysia'*, 1 September 1994, Kuala Lumpur. 8 p.
- Jensen, J.R., (1996). *Introductory Digital Image Processing: A Remote Sensing Perspective*. Prentice-Hall, Inc. U.S.A. 318 p.
- Junior, J.L and Simonett, D.S., (1976). *Remote Sensing of Environment*. Addison-Wesley Publishing Company, Inc. USA. 694 p.
- Kamaruzaman Jusoff and Souza, G.D. (1997). Use of satellite remote sensing in Malaysia and its potential. *International Journal of Remote Sensing*, 18,(1): 57-70.
- Lillesand, T.M. and Kiefer, R.W., (1994). *Remote Sensing and Image Interpretation*. 3rd Edition. John Wiley and Sons, Inc. USA. 750 p.
- Luney, P.R and Dill, H.W., (1970). Uses, Potentialities, and Needs in Agriculture and Forestry. In *Remote Sensing with Special Reference to Agriculture and Forestry*. Nat. Acad. Of Sci. 1-34 p.
- Mohd Hasmadi, I., and Kamaruzaman, J., (2007). Estimating Forest Area Using Remote Sensing and Regression Estimator, *WSES Transaction on Signal Processing*. Greece. Issue 1, Volume 3, January 2007. ISSN 1790-5022 : 88-94
- Paul, M. (1995). *Guideline for the Use of Digital Imagery for Vegetation Mapping*, United State Dept. of Agriculture, Washington, D. C., U.S.A. 125 p.
- Taylor, J.C., Sannier, C., Delince, J. and Gallego, F.J. (1997). *Regional Crop Inventories in Europe Assisted by Remote Sensing: 1988-1993*. Published by European Commission (EUR 1719EN). 71p.

Table 1. Area proportion and total area estimate of each class by direct expansion method

No. of segment:39	Oil palm	Mangrove	Water bodies	Urban/bare land
$\sum y_{ic}$	23.154	6.077	4.593	5.508
Proportion (\bar{y}_c)	0.6093	0.2894	0.2702	0.2623
Area (Z_c)[ha]	11039.28	5242.86	4894.92	4751.96
Area (Z_c)[%]	43	20	19	18
Std.Error [ha]	0.0587	0.0754	0.0572	0.0943
C.V (%)	59.33	119.36	87.27	164.59
$Z_c+1.96SE$ [ha]	0.71	0.41	0.36	0.42
$Z_c-1.96SE$ [ha]	0.51	0.17	0.18	0.11

$C.V = \text{Coefficient of Variation (Std.Error/Expanded area)} * 100, \sum y_{ic} * 100$

Table 2. Confusion matrix of the classification image of Carey Island

REFERENCE DATA (Ground verification)						
		Urban/bare land	Oil palm	Mangrove	Water bodies	Total
CLASSIFICATION DATA	Urban/Bare Land	2	0	0	0	2
	Oil Palm	2	25	1	0	28
	Mangrove	0	0	4	0	4
	Water Bodies	0	0	0	18	18
	Total	4	25	5	18	52
Overall accuracy 96.97%						

Table 3. Producer's and user's accuracy of the classification image of Carey Island

	Producer's Accuracy (%)	User's Accuracy (%)	Kappa
Oil Palm	100.00	94.74	0.9043
Mangrove	95.65	100.00	1.0000
Urban / Bare Land	87.50	93.33	0.9231
Water Bodies	96.30	100.00	1.000
Overall Kappa Statistics			0.9514

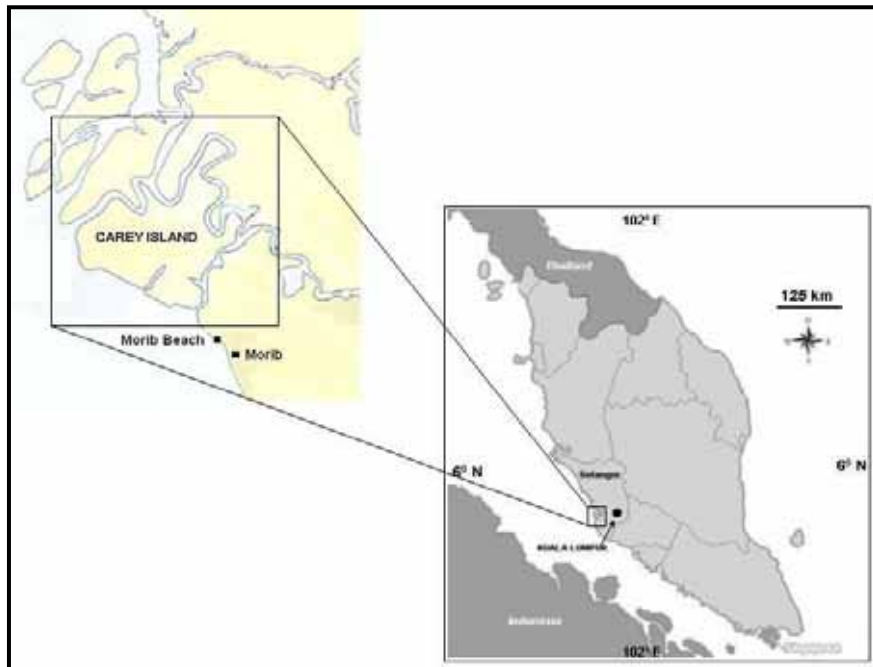


Figure 1. Location of the study area

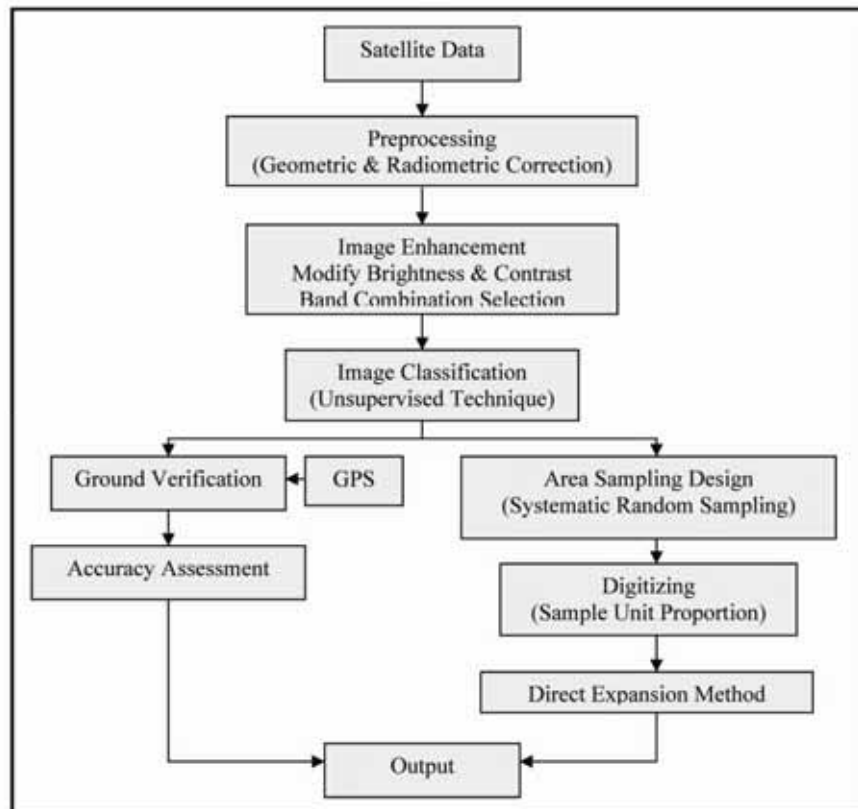


Figure 2. The flow chart of the study

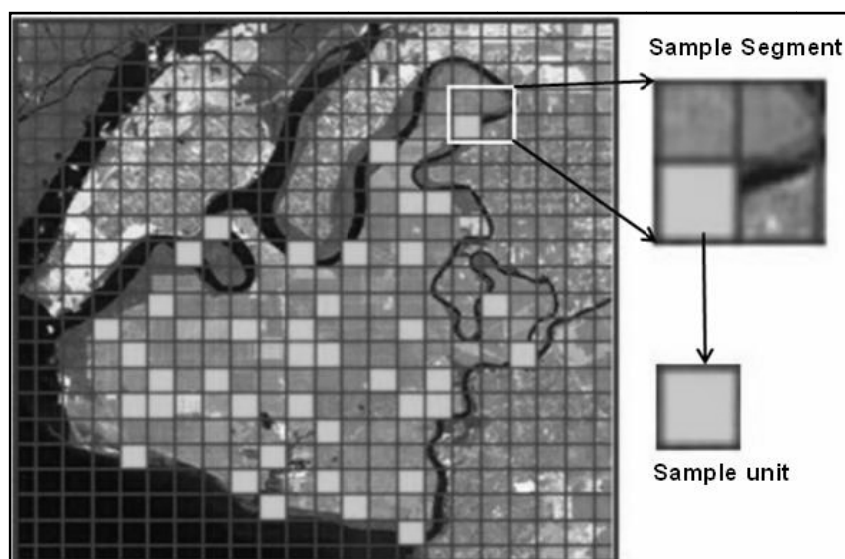


Figure 3. A systematic random design for 39 samples and unit segments over Carey Island

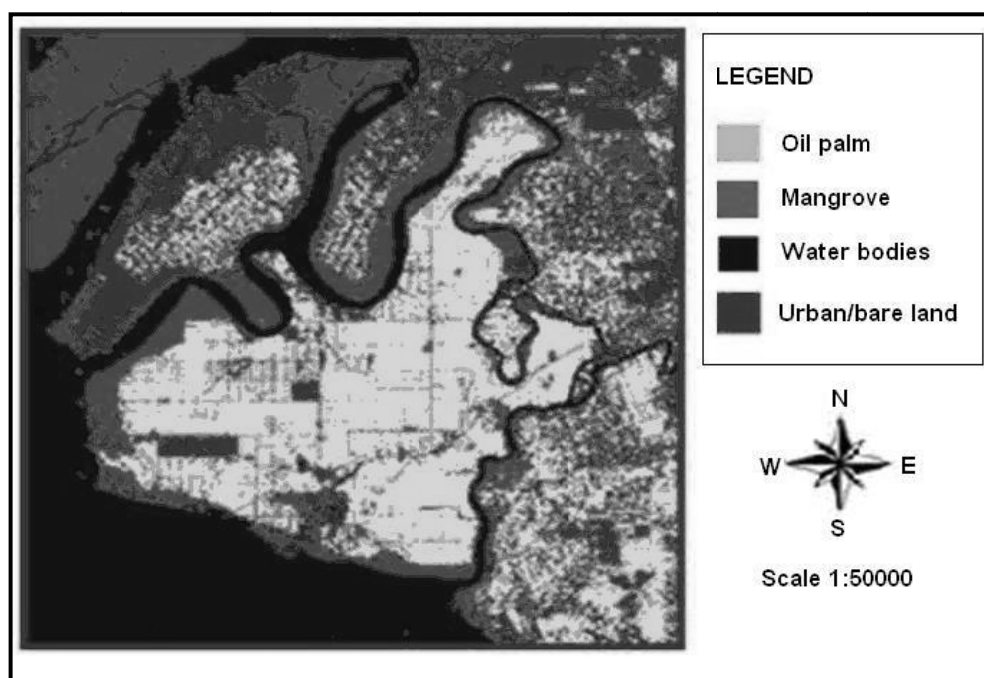


Figure 4. Land cover types within the Carey Island using unsupervised technique

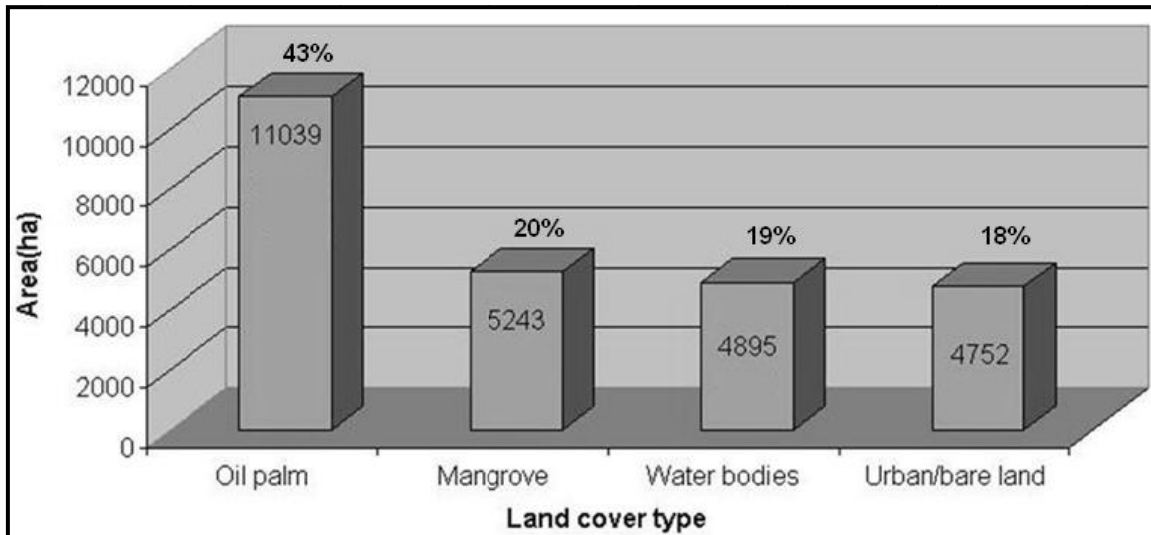


Figure 5. Estimated land cover area (in ha and %) of Carey Island

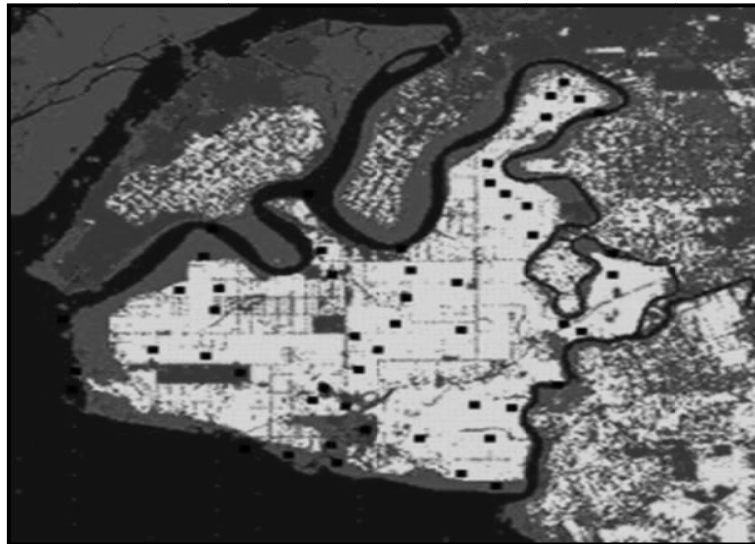


Figure 6. Selected ground verification points in Carey Island (fillet black)



Microwave Dielectric Characteristics of Single-walled Carbon Nanotubes

Xiaolai Liu & Qinghuai Li

Department of Physics and Electronic Science

Beijing University of Chemical Technology

Beijing 100029, China

Donglin Zhao

Education Ministry Key Laboratory of Science and Technology of Controllable Reactions

Institute of Carbon Fiber and Composites

Beijing 100029, China

E-mail: liuxl1@mail.buct.edu.cn

Abstract

In this article, we studied the microwave permittivity of the complex of the single-walled carbon nanotubes and paraffin in 2-18GHz. In the range, the dielectric loss of single-walled carbon nanotubes are higher, and the real part and the imaginary part of the dielectric constant decrease with the increase of frequency, and the dielectric constant possesses the property of dispersion frequency response. The ϵ' , ϵ'' and $\tan\delta$ of the complex of the single-walled carbon nanotubes and paraffin increase with the increase of the content of carbon tubes, and it presents good second-order function relationship with the volume fraction of carbon in certain range. The polarization dispersion dielectric response is the main reason that the single-walled nanotubes absorbs and wastes microwaves.

Keywords: Single-walled carbon nanotubes, Microwave permittivity, Microstructure, Microwave absorption

1. Introduction

Since Iijima found the carbon nanotubes in 1991 (S. Iijima, 1991, P.56), the carbon nanotubes have been broad concerned by people, and it has been the research hotspot in many scientific domains such as chemistry, physics, and material science. There are many methods such as graphite electric arc method (DC electric arc method), catalytic crack method, laser evaporation graphite rod method, pyrolytic polymer method, flame method, ion (electron beam) radiation method, electrolysis method and model carbonization method to be used to prepare nanotubes (G, Ya, Slepyan, 2001, P.121-123, Bachtold A, 2001, P.1317, Tans SJ, 1998, P.49, Wagner HD, 1998, P.188, Planeix JM, 2001, P.1447, Cheng HM, 2001, P.1317, Service RF, 1998, P.940, John W, 2003), and the method which takes Fe, Co, Ni and other metals as activators and catalyze and crack the hydrocarbon to prepare the carbon nanotubes make the industrialization production of carbon nanotubes possible. Various forms and structures of carbon nanotubes make the nanotubes possess many potential applied values, for example, it can be used in the strengthening of materials, one-dimensional quanta lead, semiconductor materials, activator carrier, molecule absorbent, tunnel scanning and the detector of the atom force microscope. The carbon nanotubes have many characters such as small tube diameter and big length-diameter ratio, and the diameter is in tens nanometers, and the axial length of the tube is on the level from micron to centimeter, and it is the thinnest fiber material, and this sort of special structure makes the carbon nanometer possess excellent mechanical performance and special electric performance, and the experiment shows that the Yong modulus of single multiple layers nanotubes averagely are 1.8TPa, and the curve intensity can achieve 14.2GPa (J, A, Roberts, 2004, P.4352-4356), and because the carbon nanotubes are the one-dimensional material with hollow structure, so we can utilize the capillary phenomenon of carbon nanotubes to fill some elements into the interior of the carbon nanotubes and make the one-dimensional quanta line with special performance (K, G, Ong, 2002, P.82, C, Bower, 2002, P.3820, Zhao D L, 2001, P.2471). In a word, the preparation and application of carbon nanotube shave been implemented for a long time, and in recent years, the research about the complex material of carbon nanotubes have been one hotspot of the carbon nanotubes applicaiton, and there are few researches about the microwave permittivity of carbon nanotubes, especial for the single-walled carbon nanotubes and the function relationship between the effective dielectric constant of single-walled carbon nanotubes and the volume fraction of carbon nanotubes. In this article, we study the change rule of the dielectric constant of single walled carbon nanotubes and paraffin complex with the volume fraction and frequency

of carbon nanotubes in 2-18GHz, which will offer references for the application of single-walled carbon nanotubes in the absorbing materials.

2. Experiment

The single-walled carbon nanotubes used in the experiment is made by Shenzhen Nanotech Port Co., Ltd, and the diameter of the single-walled carbon nanotubes are less than 2nm, and length is in 5-15 μ m, and the specific surface area is 450-600m²/g. We use the coaxial line method to measure the dielectric constant of the single-walled carbon nanotubes in the frequency range of 2-18GHz, and the type of the network analyzer is HP8722ES. The preparation process of the dielectric constant testing sample of single-walled carbon nanotubes are that putting the single-walled carbon nanotubes dispersed in the melting paraffin evenly, and casting the liquid compound of paraffin and single-walled carbon nanotubes into the copper loop standard flange, and testing the dielectric constants of the complex with the flange after solidification to eliminate the testing error induced by the gap between sample and flange. And the contents of single-walled carbon nanotubes respectively are 5wt%, 8wt%, 10wt%, 15wt% and 20wt%.

3. Results and discussions

The function between the microwave and the agglomeration matter can be described by the complex dielectric constant ϵ^* ($\epsilon^* = \epsilon' - i\epsilon''$, ϵ' is the real part of the dielectric constant, and ϵ'' is the imaginary part) and the complex electrical conductivity σ^* . And the relationship between the real part $\sigma'(\omega)$ of the electrical conductivity and the imaginary part $\epsilon''(\omega)$ of the complex dielectric constant is $\sigma'(\omega) = \omega \epsilon''(\omega)$, where, ω is the angle frequency of the electromagnetic wave (K, G, Ong, 2002, P.82, C, Bower, 2002, P.3820, Zhao D L, 2001, P.2471, A, K, Jonscher, 1983, P.138, P, Debye, 1945, P.257, E, Mouchon, 1996, P.323, Liu, Xiaolai, 2005, P.721, A, K, Jonscher, 1983, P.13). Most researchers mix the measured samples with the paraffin to test the electromagnetic parameters of the complex (Zhao D L, 2001, P.2471, A, K, Jonscher, 1983, P.138, P, Debye, 1945, P.257, E, Mouchon, 1996, P.323).

Because the specific surface area of the single-walled carbon nanotubes are very large, and it is hard to be compacted, so we can not exactly measure the microwave dielectric constant of the pure single-walled carbon nanotubes. In this article, we studied the change rule of the dielectric character of single-walled carbon nanotube and the paraffin with the content of the carbon nanotubes, and researched the dielectric character of the samples with five different contents (5wt%, 8wt%, 10wt%, 15wt% and 20wt%) in 2~18GHz, and the real part and imaginary part of the dielectric constant of the paraffin used in the experiment were constants, i.e. $\epsilon' = 2.26$ and $\epsilon'' = 0$. Figure 1, Figure 2 and Figure 3 respectively show the change curves of the dielectric constants of the complex with different single-walled carbon nanotubes and paraffin (ϵ' and ϵ'') and the dielectric waste angle tangent ($\tan\delta = \epsilon''/\epsilon'$) with the frequency. We can see that with the increase of the content of single-walled carbon nanotubes, the ϵ' , ϵ'' and $\tan\delta$ of the complex gradually increase, and with the increase of the frequency, ϵ' and ϵ'' gradually decrease, and it possesses obvious frequency response property, which is very beneficial to enhance the absorbing performance of absorbing materials in the wide frequency range.

The research about the complex electromagnetic property is an old and active topic (Liu, 2005, P.721, A, K, Jonscher, 1983, P.13, J, C, M, Gamett, 1904, P.385, J, C, M, Garnett, 1904, P.237, A, H, Sihvola, 1998, P.420, K, Bober, 1997, P.101, G, F, Dionne, 1976, P.1708), and J.C. Maxwell Garnett deduced the famous effective medium formula which was used to solve the complex dielectric constant in 1904, i.e. the Maxwell Garnett formula (A, K, Jonscher, 1983, P.13, J, C, M, Gamett, 1904, P.385). With the development of science and technology, many microwave apparatus, especially for the microwave absorbing materials developing from stealth technology, all need the materials with special electromagnetic property, but single material could not fulfill these special requirements, so we need prepare complex materials to implement these objectives, and though researches try to look for a sort of mathematical theoretical model to compute the microwave electromagnetic parameters of complex materials all along, but they could not establish a sort of general theoretical model (G, F, Dionne, 1976, P.1708).

The effective dielectric function of complex material is generally obtained by experiment and test or the establishment of proper mathematical model, and the later has important function in the material design, but up to now, there is not very satisfactory model, so researchers still try to find the optimal model all along. Bober et al (G, F, Dionne, 1976, P.1708) used Maxwell Garnett formula to respectively compute the complex dielectric constant and complex permeability for the complex materials which are respectively composed by resin with nickel zinc ferrite, mangan zinc ferrite, Sr ferric oxide and graphite in 10GHz, and they found the Maxwell Garnett effective medium formula could approximately compute ϵ' for the complex material of nickel zinc ferrite and resin, but obvious warp would occur in ϵ'' , μ' and μ'' , and ϵ' , ϵ'' , μ' and μ'' all had very large warps in other sorts of complex material. Boner's study result also indicated that the dielectric constant (ϵ' and ϵ'') and permeability (μ' and μ'') of the complex materials which are respectively composed by resin with nickel zinc ferrite, mangan zinc ferrite, Sr ferric oxide and graphite and the volume fractions of ferrite and graphite accorded with the second-order multinomial relationship (ϵ' , $\epsilon'' = Av^2 + Bv + C$). Dionne et al studied the dielectric constants of the complex of rutile ($\epsilon' = 100$), anatase ($\epsilon' = 48$) and paraffin, and found that the warp would occur between measured value with computation value of Maxwell Garnett formula. Above research results indicate the Maxwell Garnett effective medium formula is not fit to compute the dielectric constant and permeability of

the microwave complex materials.

From above discussions, we can see that we should look for other methods to compute the dielectric constant of the complex materials composed by single-walled carbon nanotubes with different materials in the frequency band of microwave. Our research indicated that the dielectric constant measured value of the complex materials with different single-walled carbon nanotubes contents had very good fitting relationship with the volume fraction of nanometer powder, and ϵ' and ϵ'' with the volume fraction of nanometer powder accord with the second-order multinomial relationship (ϵ' , $\epsilon''=Av^2+Bv+C$). Figure 4 and Figure 5 respectively are the second-order function curves of ϵ' and ϵ'' which are obtained by the fitting of dielectric constant measured value in 10GHz for the complex of single-walled carbon nanotubes with paraffin with the volume fraction of nanometer powder (v). From the figures, we can see that $\epsilon'=-39.444v^2+214.531v-7.717$, $r^2=0.9999$, $\epsilon''=2049.436v^2-283.591v+11.011$, $r^2=0.9929$, and they possess very good fitting relationship.

The researches also indicate that when the content of single-walled carbon nanotubes are in 5wt%-20wt%, and in the frequency range from 2GHz to 18GHz, for different frequency testing sites, good second-order function relationship among ϵ' , ϵ'' and v , and the coefficients A, B and C are different with the change of frequency. This research result is very important for the optimal design utilizing single-walled carbon nanotubes and their polymer complex for the single narrow frequency, multiple frequencies and wide frequency absorbing wave.

In the single-walled carbon nanotubes give priority to the sp^2 hybridization structure with carbon atom hexagonal close array, and the hybridization orbit presents electric moment, and the π electron bond energy is small, and its combination force with atom is weak, and the effective quality is small and it presents high speed move and super polarization property, and in the alternation electric field function of microwave, the turning polarization of electric moment forms, and with the increase of frequency, the turning polarization of electric moment gradually trails the change of the exterior field, so this sort of polarization will decrease with the increase of frequency. In the turning process of electric moment, the energy loss will occur because of the non-elasticity mutual function with surrounding particles, and the move will trail the electric field, so the polarization dispersion dielectric response is the main reason that the single-walled nanotubes absorb and waste microwaves.

4. Conclusions

(1) The dielectric loss of single-walled carbon nanotubes are higher in the microwave frequency range of 2-18GHz, and the real part and the imaginary part of the dielectric constant will decrease with the increase of the frequency, and the dielectric loss angle tangent increases with the increase of frequency, and it possesses the property of polarization dispersion dielectric response.

(2) In the single-walled carbon nanotubes give priority to the sp^2 hybridization structure with carbon atom hexagonal close array, and the hybridization orbit presents electric moment, and the π electron bond energy is small, and its combination force with atom is weak, and the effective quality is small and it presents high speed move and super polarization property, and in the alternation electric field function of microwave, the turning polarization of electric moment forms, and the polarization dispersion dielectric response is the main reason that the single-walled nanotubes absorb and waste microwaves.

(3) In the microwave frequency range of 2-18GHz, the ϵ' and ϵ'' of the complex of single-walled carbon nanotubes with paraffin have significant independence relationship with the content of single-walled carbon nanotubes, and in the 5%-15% of the single-walled carbon nanotube content, the ϵ' and ϵ'' have good second-order function fitting relationship with the volume fraction of single-walled carbon nanotube, i.e. ϵ' , $\epsilon''=Av^2+Bv+C$.

References

- A, H, Sihvola & J, A, Kong. (1998). IEEE Trans, Geosc, Remote Sensing. No.26. P.420.
- A, K, Jonscher. (1983). *Dielectric Relaxation in Solids*. (Chelsea Dielectric Press, London). P.13.
- A, K, Jonscher. (1983). *Dielectric Relaxation in Solids* (Chelsea Dielectric Press, London). P.138.
- Bachtold A, Hadley P & Nakanishi T. (2001). *Science*. No.294. P.1317.
- C, Bower, W, Zhu, D, Shalom, D, Lopez, P, L, Gammel, and S, Jin. (2002). *Appl, PhysLett*, 80, 3820.
- Cheng HM, Yand QH & Liu C. (2001). *Carbon*. No.294. P.1317.
- E, Mouchon & Ph, Colomban. (1996). *J, Mater, Sci*. No.31. P.323.
- G, F, Dionne, J, F, Fitzgerald, R, C, Aucoin. (1976). *J, Appl, Phys*. No.47. P.1708.
- G, Ya, Slepnyan, S, A, Maksimenko. (2001). *Synthetic Metals*. No.124. P.121-123.
- J, A, Roberts, T, Imholt, Z, Ye. (2004). *Journal of Applied Physics*. No.95. P.4352-4356.
- J, C, M, Garnett. (1904). *Philosoph, Trans, Roy, Soc, London*. No.203. P.237.

- J, C, M, Gamett. (1904). *Philosoph, Trans, Roy, Soc, London*. No.203. P.385.
- John W, Schultz, Rick L, Moore. (2003). *Mat, Res, Soc, Symp, Proc, 739 Materials Research Society*.
- K, Bober, R, H, Giles, J, Waldman. (1997). *Inter, J, Infr, Mill, Wav*. No.18. P.101.
- K, G, Ong, K, Zheng, and C, Grimes. (2002). *IEEE Sensors*. J,2,82.
- Liu Xiaolai. (2005). *Microwave Permittivity of Multi-walled Carbon Nanotube AICAM*. (in Chinese). P.721.
- P, Debye. (1945). *Polar Molecules* (Dover, New York). P.257.
- Planeix JM, Coustel N & COQ B. (2001). *J Am Carbon*. No.39. P.1447.
- Service RF. (1998). *Science*. No.281. P.940.
- S, Iijima. (1991). *Nature (London)*. No.354. P.56.
- Tans SJ, Verschueren AR & Dekker C. (1998). *Nature*. No.393. P.49.
- Wagner HD, Lourie O & Feldman Y. (1998). *Appl Phys Lett*. No.72. P.188.
- Zhao D L, Zhou W C, Wan W. (2001). *Acta Phys, Sin*. No.50. P.2471. *Acta Physica Sinica*. No.50. P.2471.

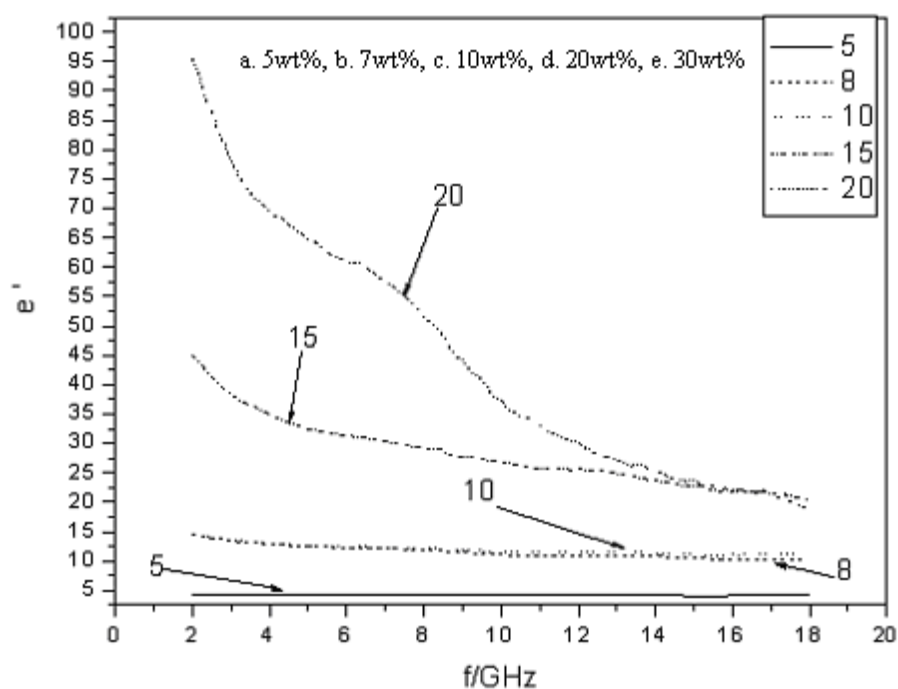
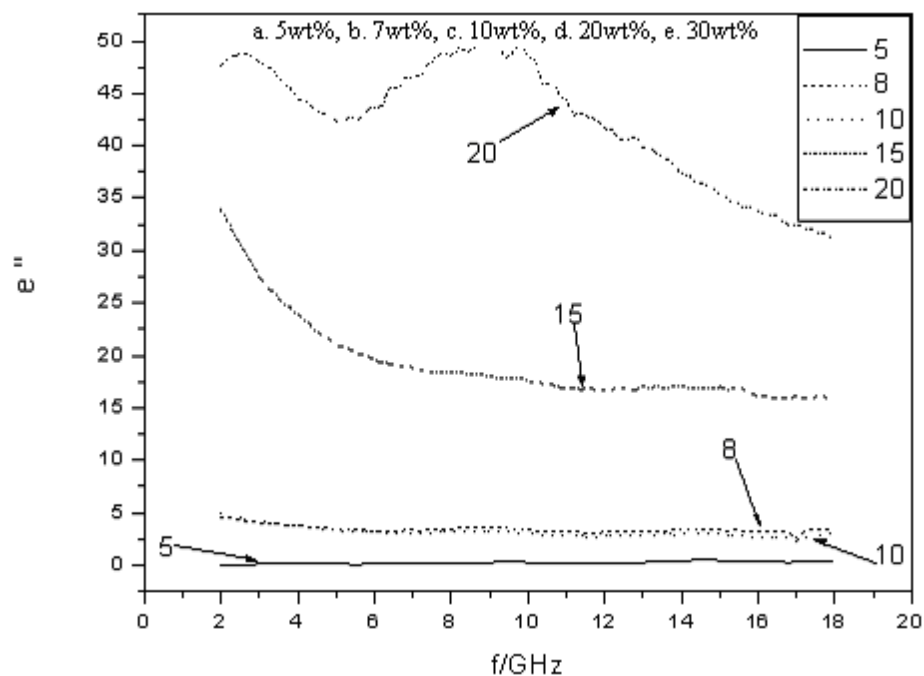
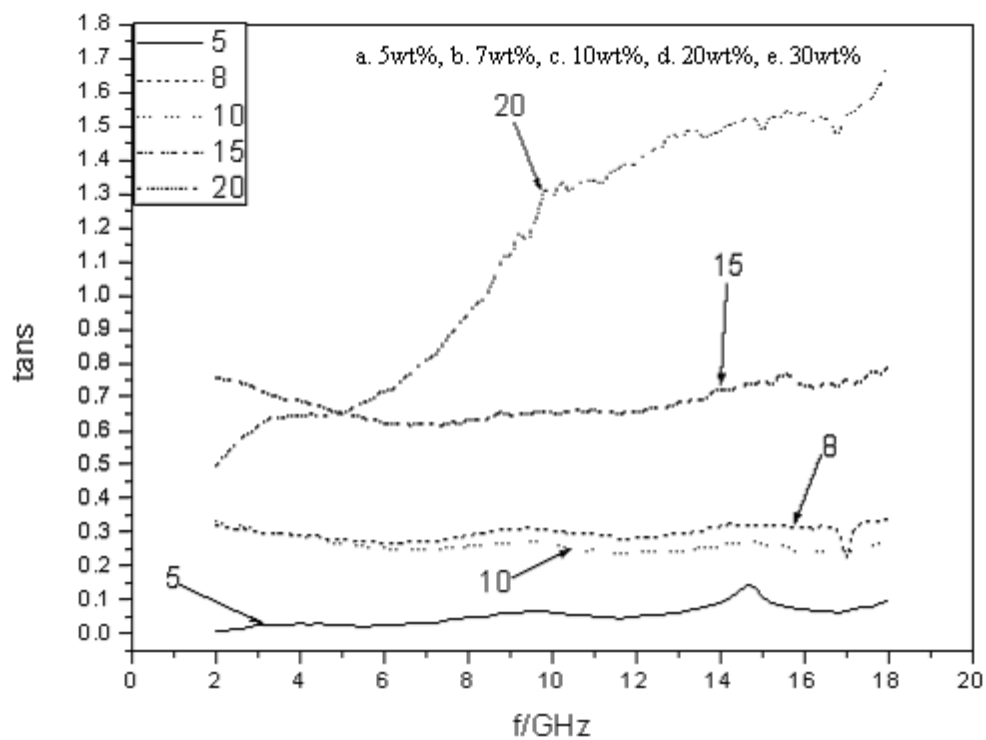


Figure 1. Relationship between ϵ' and frequency

Figure 2. Relationship between ϵ'' and frequencyFigure 3. Relationship between $\tan \delta$ and frequency

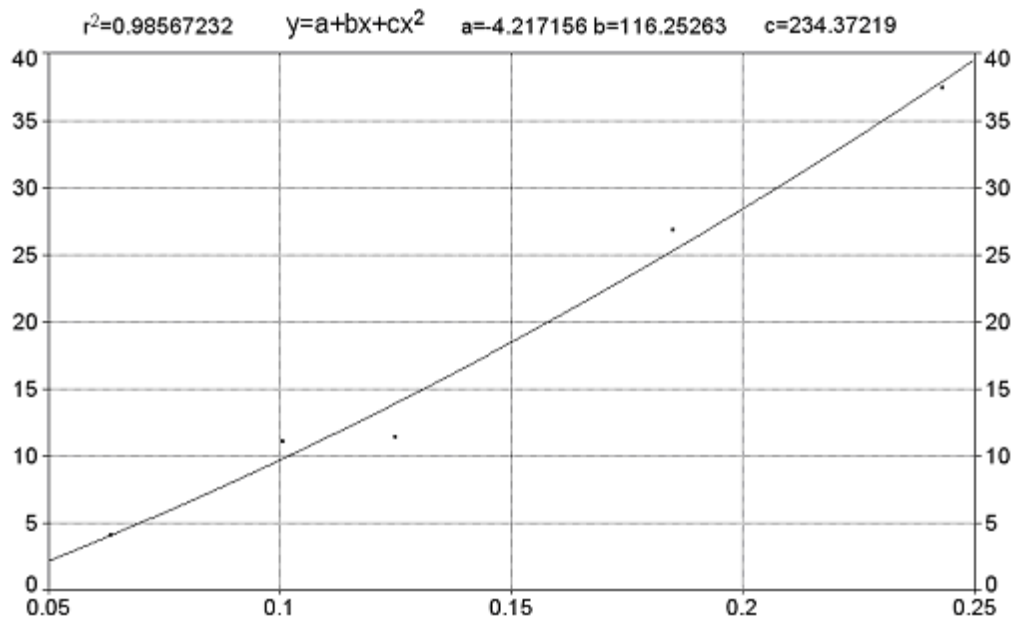


Figure 4. Relationship between ϵ' in 10GHz and nanometer power volume fraction (v)

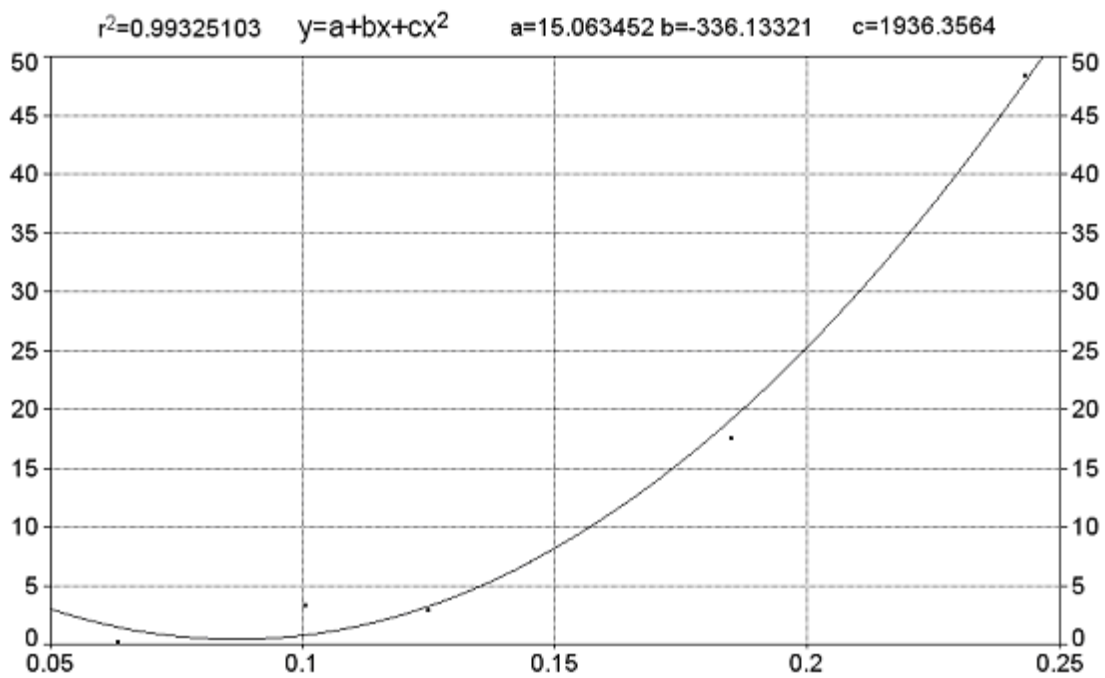


Figure 5. Relationship between ϵ'' in 10GHz and nanometer power volume fraction (v)



Laser Effects on Skin Melanin

Khalid M. Omar

Universiti Sains Malaysia, School of Physics

11800 Penang, Malaysia

E-mail: khalhadithi@yahoo.com

Khaled A. Al-Khaza'leh, M.S. Jaafar, Y. JIDIN & N. N. Bidi

Universiti Sains Malaysia, School of Physics

11800 Penang, Malaysia

Abstract

Melanin is investigated as a pigment that is responsible for colorization in human skin. The color of human skin varies from dark brown to nearly colorless "pinkish white". The amount of skin melanin in the individual skin depends on both genetic and environmental factors. This offers some protection against the damaging effects of ultraviolet radiation. For the studies of laser effects on the skin melanin, the suitable sample is chosen depends on the availability for getting the sample and also the existence of skin melanin on that sample. Therefore, the skin of laboratory rat is used as an experimental sample. Carbon dioxide laser is used as a source of radiation in this study because of its 10.6 μ m of wavelength which has an ability to penetrate effectively on soft tissue that contains 90% of water. The rat skin is exposed to carbon dioxide laser "CO₂ laser" radiation and any changes on the skin is observed and analyzed. After the exposure, the pieces of normal and exposed skin are preserved. In order to go through the sample, histological method is carried out to make the standard slides for examination under the compound light microscope. The images obtained on the both skin sample the normal and the exposed skin show that there are changes in both skin structures which can be seen clearly under the microscope lenses. These changes contributed by the interaction of the skin cells to the heat and energy produced by the carbon dioxide laser "CO₂ laser" during the exposure time.

Keywords: Laser application, Medical physics, Laser-tissue interaction

1. Introduction

The facts have shown that the theories in physics, chemistry, and mathematics are bonded together in the laser invention. The biological sciences also related to this invention due to the effect of laser beam to the environment. Furthermore, since the invention of the laser in 1960's [Blois, M.C., Quevedo, W.C. et al. (1969), Grossman, K. (2008)], The unusual properties of laser beam were all too obvious and yet it was not clear in how they could be put to practical use. More and more applications were discovered as the years passed and this attitude slowly changed year by year. There was scarcely an area of sciences and technology in which lasers are utilized for such diverse purposes as aiming missiles, for eyes surgery, for monitoring pollution, for welding, cutting and marking, for checking out goods at supermarket and also for light show entertainment [Blois, M.C., Quevedo, W.C. et al. (1969), Andrews, D.L. (1986)]. All application is taking the advantage of the wavelength of laser that can be used. Different wavelength of lasers will give the different effect on the target tissue. In such medical application, the laser is ordinarily used for treatment or therapy purpose such as cancer or tumor treatment. The use of high-intensity light can destroy the cancer cells. This technique is often used to relieve symptoms of cancer such as bleeding or obstruction, especially when the cancer cannot be cured by other treatments. Lasers can be used in two ways to treat cancer either by shrinking or destroying a tumor with heat, or by activating a chemical that destroys cancer cells [Parks, J. et al (2002)]. For this purpose, the laser that usually used is carbon dioxide laser or Nd:YAG laser which has the wavelength of 10.6 μ m and 1064nm respectively [C. Dierickx, C. et al (2004)]. Due to those wavelengths, they may be used with flexible endoscopes fitted with fiber optics, tubes that allow physicians to see into certain areas of the body. In medical application, laser is commonly used in surgery and treatment procedures on the skin. The most ordinary surgery are like hair removal [Parks, J. et al (2002), C. Dierickx, C. et al (2004), Aesthetic Laser Concepts (2007)], skin resurfacing, treating scars, treating tattoo pigment (tattoo removal) and treatment for tumor cells. The CO₂ laser emits spectral energy in the far infra red portion of the electromagnetic spectrum at "10,600 nm". At this wavelength, energy is heavily absorbed by water, which is the primary constituent and chromophore of cells in living tissue. Thus, the energy generated by this laser can be used for cutting or volume ablation by means of tissue vaporization [Lee, S. (2008)]. This unique characteristic

makes the CO₂ laser the most widely used medical laser today. This laser offers the advantages such as pain reduction, swelling reduction, control of infection and minimal surgical bleeding [Long Beach Animal Hospital (2007)].

2. Methodology

2.1 Interaction between CO₂ Laser and the Rat Skin

At “3% of PWM”, the average of power output generated by the laser is “2.96 W” and the power density is “30.77 W/cm²”. At this power output level, the changes on the skin surface are clearly seen by naked eyes. Since the melanin is responsible on the skin coloration, there will be some effect on that soft tissue.

2.2 Measuring the thickness of dermis layer of the normal skin

The thickness of the dermis is measured automatically by the software provided for the compound light microscope. The dermis layer of rat skin with 40 times of magnification as shown in “Figure 1”. The measurement of the thickness of dermis layer is done on five different places. It gives the average thickness of dermis layer obtained from “Table 1” is “985.03µm”.

2.3 Measuring the thickness of epidermis layer of the normal skin

The epidermis thickness is measured from the upper of black layer to the lower one. This is automatically done by software provide with the light compound microscope. The part of epidermis layer that is being measured under the magnification of 100 times as shown in “Figure 2”. From “Table 2”, the average thickness of epidermis layer obtained is “44.80µm”.

3. Results and Discussion

The reaction of the skin to laser radiation depends on many factors. The color or amount of pigmentation in the skin is very important in determining the amount of damage that will be produced by a given laser pulse. The output characteristics of the laser, particularly the wavelength are also important. The reactions of the skin to laser radiation vary depending on the exact circumstances and the type of skin that is impossible to specify reactions of the skin exactly. Furthermore, the transmission of radiation through skin varies with the thickness of the different layers of the epidermis and therefore with location on the body. The loss of transmission is due to scattering by the optically discontinuous surfaces in the epidermis, reflection from the surface and the various pigments of the skin and absorption by protein, nucleic acids, carotenoid and hemoglobin pigments. Melanin granules contribute to the absorption and scattering of visible and infra red radiation as well as absorption by ultraviolet radiation. The stratum corneum which is in epidermis layer strongly absorbs far-infrared radiation. Melanin granules are small “1 µm diameter” and not only protect the dermis by absorption of ultraviolet radiation, but also by scattering optical radiation. Melanin scatters rather than absorbs radiation in the near-infrared region. For this and other reasons, near-infrared radiation penetrates deeply into the tissue. Since the index of refraction of the stratum corneum is about 1.5, the Fresnel reflective component is similar to the glass. Optical radiation incident on the skin at grazing angles of incidence is hardly absorbed at all. The relative effectiveness of optical radiation in penetrating the epidermis “and dermis” varies approximately as the cosine of the angle of incidence since light penetrates the outermost layers of the skin and undergoes multiple scattering, and some light is scattered back out of the skin. Since the carbon dioxide laser operates in the far infrared spectral region, it can be categorized as a non-ionizing radiation which has lower energy levels and longer wavelength. Visible light can be seen and feel the burning effects of infrared radiation. Non-ionizing radiation is strong enough to influence the atoms it contacts, but not strong enough to affect their structure.

The heating of skin by infrared radiation causing the water molecules in the skin vibrate, but the composition of the cells is not influenced. Far infrared rays have the ability to penetrate deeply “up to 1.5 inches” and permeate thoroughly into the hypodermic layer of skin. Thus, it is possible to revitalize cells and tissue by warming the body from the inside. Again, this warming is made possible by the heat energy transfer of the far-infrared radiation. In the far-infrared, however, all tissue absorbs heavily, not just melanin pigment granules.

The sample that was used to expose with CO₂ laser is the albino mouse which is a Wistar type, lack of melanin in its skin. Since the rat is albino type, it is failed to tan because a functional tyrosinase is absent from the fully developed epidermal melanin system. Then, the skin burns are the main effect to be considered. The carbon dioxide laser radiation is absorbed very strongly by the skin, with a high absorption coefficient. This means that carbon dioxide laser radiation is deposited in a localized depth of skin and therefore the temperature rises can be higher locally than for the case of visible laser radiation which is transmitted through greater depths of skin. The skin was assumed to be homogeneous, with the thermal properties of water. As the energy of laser increased, burns and damage tissue produced due to absorption of incident laser energy by the natural pigmented materials found in the skin, melanin and hemoglobin. Damage with high keratin content such as the palms was relatively less. The area of the spot of burning skin increased as well as the radiation time increased. The burning spot can be seen clearly as the brown spot and the burning spot spreading into the bigger area after several minutes. The reaction between the radiated tissue and the surrounding tissue

caused the burning area to spread out. This burning skin is known as the thermal radiation effect where the energy of laser ray is being absorbed and causing the raise on temperature of radiated skin. Chemical reactions always involve a change in energy. Energy is neither created nor destroyed. Energy is absorbed or released in chemical reactions which can be described as endothermic or exothermic reactions. Here, the chemical reactions in which laser energy is absorbed by skin are involved the endothermic process. Energy in the form of heat is required for the reaction to occur.

The normal rat skin (before exposed to laser radiation) at 40 times of magnification is shown in "Figure 3". The scale is "200 μ m", automatically done by the software based on the current magnification of microscope. This skin is cut at the normal cross section during the sectioning process which influenced by the orientation of sample during the embedding process. The epidermis layer of rat skin and the skin melanin is supposed to be in the innermost of epidermis layer. There are approximately six hair follicles with the sebaceous gland at the left side of hair follicles. Each hair follicle is surrounded by the tissue and there is the adipose tissue at the bottom area which is also called as a fat layer.

The exposed skin at 40 times of magnification is shown in "Figure 4". The scale is "200 μ m", also automatically done by the software based on the current magnification of microscope. The different in skin structure compared to before is caused by the different orientation of sample in sectioning. This sectioning is influenced by the orientation of sample during the embedding process. The epidermis layer of rat skin and the skin melanin is supposed to be in the innermost of epidermis layer. All the structure which is the big circle in shape is the hair follicles. Each hair follicle is surrounded by the tissue and there is the adipose tissue at the bottom area which is also called as a fat layer.

The heat effect of laser energy that was absorbed by the skin caused the expanding of empty space between the hair follicles and its surrounding tissue. This phenomenon occurs because of the skin tissue is shrunk as the laser energy being absorbed and heated the water molecules in skin being heated. This endothermic process caused the vaporization of water molecules in exposed skin.

The full view of the normal rat skin before the exposure to carbon dioxide laser radiation is shown in "Figure 5". There is an epidermis layer, a dermis layer and the hypodermis or subcutaneous layer of skin. All the structure in dermis layer "second layer" is the darker than surrounding tissue are the hair follicles. The third and fourth layers are the subcutaneous layer.

The full view of the rat skin after being exposed to carbon dioxide laser radiation is shown in "Figure 6". Besides the expanded of empty space between the hair follicles and its surrounding tissue, the thermal radiation effect also caused the dermis layer separated from the subcutaneous layer. This phenomenon also caused by the shrinkage tissue as the effect of vaporization of water molecules in skin structure.

In the overall view, the skin structure seems to be shrinking after the exposure to carbon dioxide laser. This shrinkage structure caused by the energy of laser absorbs on the soft tissue and makes the water in that tissue heats up and vaporizes. It is proved the fact that during lasing time, water in target tissue absorbs the laser energy, heats up, boils and vaporizes, taking the surrounding tissue with it.

Since the carbon dioxide operates in the far infra red spectral region, it may have the properties of far infrared radiation. A far infrared wave has an ability to remove toxins. Toxic gases may be encapsulated by clusters of water. When a 10 micron far infrared wave is applied to these large water molecules, the water begins to vibrate, which reduces the ion bonds of the atoms which are holding together the molecules of water. As the breakdown of the water molecules occurs, encapsulated gases and other toxic materials are released. Interaction of far infrared radiation with the body also produces nitric oxide gas "NO" by the reaction of the photons of the far infrared on the enzymes, which is useful for body immunization and faster wound healing.

4. Conclusion

This paper studied the laser effects on skin melanin. The main objective is to know the effectiveness of laser radiation on the skin melanin. The best way to determine the result is on the facts about the skin and also the expected results according to the published paper that discussed on the studies of radiation and skin. Subsequently, it is closely related with the application of laser in medical field. During preparing this paper, the experiment is carried out to determine the effect of laser radiation on the skin melanin. The type of laser which is selected to be used is depends on the wavelength of output laser which is related to the absorption of that wavelength on the target tissue. It also depends on which laser is available at the school. Then, the sample to be used is decided based on the experiment by other researchers. The color of the sample is changed due to the dose of radiation, time exposure and also the pigment or melanin contains on that sample. Furthermore, the exposed sample is examined on many ways. Therefore, this gives a hint for us to select the way on how to examine the results for data analysis and results.

References

Aesthetic Laser Concepts. Available from World Wide Web: <http://www.aestheticlaserconcepts.com/about.html>, (July 22, 2007).

Andrews, D.L, Lasers in Chemistry (1986) (New York: Springer-Verlag), pp.15-18 and p.p. 31-35.

Blois, M.C., Quevedo, W.C. et al. (1969), The Biological Effects of Ultraviolet Radiation. (Oxford: Pergamon Press), pp. 325-326 .

C. Dierickx, C. et al, (2004), You're Looking Great. Available from World Wide Web: http://youre-looking-great.com/effective_paper.htm, (July 22, 2007).

Grossman, K. Epidermis Anatomy-Skin & Beauty, Available from World Wide Web:http://dermatology.about.com/od/anatomy/ss/epidermis_2.htm, (July 22, 2007).

Lee, S. Lasers, General Principles and Physics – e-Medicine. Available from World Wide Web: <http://www.emedicine.com/ent/topic40.htm>, (January 20, 2008) .

Long Beach Animal Hospital. (2007). Available from World Wide web:<http://www.lbah.com/laser.htm>, (March 24 2008).

Parks, J. et al, (2002), Effectively Treating Ethnic Skin -Skin & Aging, Available from World Wide Web: <http://www.skinandaging.com/article/576>, (July 22, 2007).

Table 1. The Thickness of Dermis Layer

No.	Horizontal distance (μm)
1	979.04
2	997.01
3	1004.49
4	967.07
5	977.54
Average	985.03

Table 2. Thickness of epidermis layer

No.	Thickness (μm)
1	48.58
2	57.61
3	43.52
4	46.98
5	33.64
6	42.18
7	34.17
8	51.71
Average	44.80



Figure 1. Dermis layer, 40 x

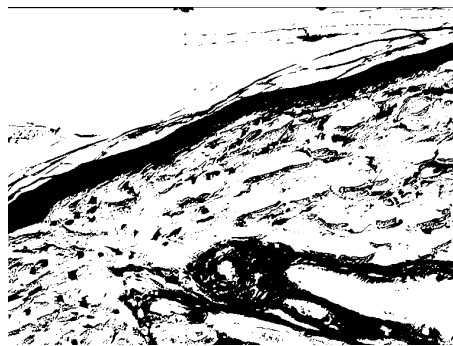


Figure 2. Epidermis layer, 100 x.



Figure 3. Normal Skin, 40 x.

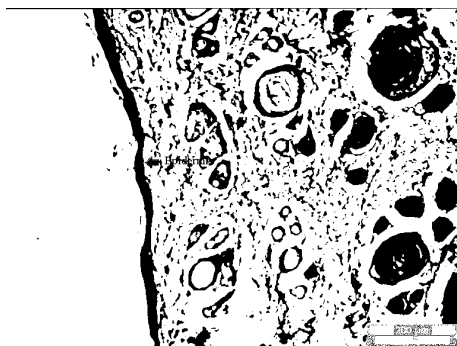


Figure 4. After exposure to CO₂ Laser, 40x.



Figure 5. The full view of the normal rat skin

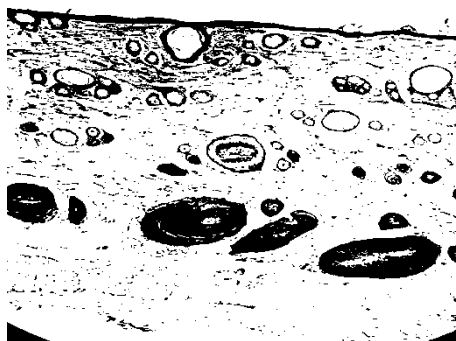


Figure 6. The full view of the exposed rat skin



Damage Analysis of 3D Frame Structure under Impulsive Load

Wenzhao Fan & Julin Wang

Institute of Building Structures

Shanxi Architectural Technical College

Taiyuan 030006, China

Tel: 86-351-743-2632 E-mail: wangjl_tj@163.com

Liming Gao

Department of Civil Engineering

Siegen University

Sigen D-57076, Germany

E-mail: gaolm_ty@126.com

Shougao Tang

School of Aerospace Engineering and Applied Mechanics

Tongji University

Shanghai 200092, China

Tel: 86-21-6513-1712 E-mail: tangshougao@yahoo.com

Abstract

In this article, we utilized the lumped damage mechanics method to implement the damage analysis to the 3D frame structure under impulsive load. First, take the damage parameters as the interior variable of the system, and based on the finite unit, combine continuum mechanics, fracture mechanics and plastic hinge to analyze the mechanical behaviors of the structure, and finally implement numerical simulation analysis to the frame structure with two layers, and compare the result with the computation result of ABAQUS to validate the feasibility.

Keywords: Lumped damage mechanics, Impulsive load, Damage

1. Introduction

Since the twin towers of the World Trade Center were stroke by terrorists, the nonlinear analysis and damage computation of structure under sudden impulsive loads are more and more concerned by people. The relative researches can not only establish more reasonable structure design theory, but offer necessary theoretic base for the reliability evaluation and reinforce design of damaged structure.

In recent years, many deep researches about the reaction analysis and damage mechanism of structure under sudden impulsive loads occur and some reasonable methods are put forward one by one (Fabio F, 1991, Xue, 1999, P.334-342, Zhu, 1991, P.21-30, G. Bolzon, 1996, P.1481-1491, Cipollina, A, 1995, P.1113-1126, Marante, 2002, P.1141-1152, Mazza, 1998, Perera, 2000, P.293-302). Based on former researches, we utilize the method of lumped damage mechanics to directly solve the damage of 3D frame structure under the impulsive loads, and implement numerical simulation analysis to one frame structure with two layers, and compare the result with the computation result of ABAQUS to validate the feasibility.

2. The dynamic equation of 3D structure

Suppose there are m frame members and n nodes, and the dynamic equation in the time range of $[0, T]$ is

$$\sum_{e=1}^m [B]_e^T [M]_e + \sum_{e=1}^m [m]_e \left\{ \dot{U} \right\} = \{P\} \quad \forall \left\{ \dot{U}^* \right\} \quad (1)$$

Where, the matrix $[B]$ is the node displacement function, and the concrete form is

$$[B] = \begin{bmatrix} -\frac{m_1}{L} & -\frac{m_2}{L} & -\frac{m_3}{L} & n_1 & n_2 & n_3 & \frac{m_1}{L} & \frac{m_2}{L} & \frac{m_3}{L} & 0 & 0 & 0 \\ -\frac{m_1}{L} & -\frac{m_2}{L} & -\frac{m_3}{L} & 0 & 0 & 0 & \frac{m_1}{L} & \frac{m_2}{L} & \frac{m_3}{L} & n_1 & n_2 & n_3 \\ -t_1 & -t_2 & -t_3 & 0 & 0 & 0 & t_1 & t_2 & t_3 & 0 & 0 & 0 \\ \frac{n_1}{L} & \frac{n_2}{L} & \frac{n_3}{L} & m_1 & m_2 & m_3 & -\frac{n_1}{L} & -\frac{n_2}{L} & -\frac{n_3}{L} & 0 & 0 & 0 \\ \frac{n_1}{L} & \frac{n_2}{L} & \frac{n_3}{L} & 0 & 0 & 0 & -\frac{n_1}{L} & -\frac{n_2}{L} & -\frac{n_3}{L} & m_1 & m_2 & m_3 \\ 0 & 0 & 0 & -t_1 & -t_2 & -t_3 & 0 & 0 & 0 & t_1 & t_2 & t_3 \end{bmatrix} \quad (2)$$

Where, t , m and n respectively are the unit vectors of x , y and z axis, and L is the length of the frame member.

M_e^T is the interior force of the unit e, $M_e^T = (m_{iy}, m_{jy}, N, m_{iz}, m_{jz}, m_x)$.

Where, N is the axial force, m_x is the torque, m_{iy} and m_{jy} are the flexural moments of i and j ports in the face of xz , m_{iz} and m_{jz} are the flexural moments of i and j ports in the face of xy (seen in Figure 1).

$\{U\}^T$ is the displacement matrix of the whole structure, $\{U\}^T = (\{u\}_1, \{u\}_2, \dots, \{u\}_n)$.

$\{P\}$ is the node exterior force of the structure.

3. Model of lumped damage mechanics

3.1 The damage constitutive equation (Maria, 2003, P.5109-5123)

For the lumped damage mechanics model, the unit is composed by one elastic girder and two plastic hinges on two ends (seen in Figure 2), and suppose the dissipation of all energies is centralized on the plastic hinges.

Suppose the distortion of the hinge is composed by the plastic distortion and the distortion induced by the damage, i.e.

$$\{\Phi^h\} = \{\Phi^p\} + \{\Phi^d\} \quad (3)$$

Where, Φ^p denotes the plastic distortion of the hinge and Φ^d denotes the distortion induced by the damage.

$$\{\Phi^p\} = (\phi_{iy}^p, \phi_{jy}^p, \delta^p, \phi_{iz}^p, \phi_{jz}^p, \phi_x^p)^T \quad (4)$$

In the frame structure of RC, the plastic corner is mainly induced by the reinforcing steel bar yield, and the fracture of the concrete can be described by following two damage matrixes.

$$\{D^+\} = (d_{iy}^+, d_{jy}^+, d_{iz}^+, d_{jz}^+) \quad (5)$$

$$\{D^-\} = (d_{iy}^-, d_{jy}^-, d_{iz}^-, d_{jz}^-) \quad (6)$$

Where, $+$ and $-$ respectively denote the damages induced by positive and negative flexural moments (seen in Figure 3).

The constitutive equation of the plastic hinge is

$$\{\Phi - \Phi^p\}_e = [F(D^+)]_e [M]_{e,+} + [F(D^-)]_e [M]_e \quad (7)$$

Where, $+$ and $-$ respectively denote the damages induced by positive and negative flexural moments, $[F(D)]$ denotes the flexibility matrix of the damage unit, and the concrete expressions are

$$F(D^+) = F^0 + C(D^+) \quad (8)$$

$$F(D^-) = F^0 + C(D^-) \quad (9)$$

In the equation (8) and equation (9), F^0 denotes the flexibility matrix of the unit in the flexible stage, $C(D^+)$ and $C(D^-)$ denotes the flexibility matrix induced by the damage of concrete, and the concrete expressions are

$$[C(D^+)] = \begin{bmatrix} \frac{d_{iy}^+ F_{11}^0}{1-d_{iy}^+} & 0 & 0 & 0 & 0 & 0 \\ 0 & \frac{d_{jy}^+ F_{22}^0}{1-d_{jy}^+} & 0 & 0 & 0 & 0 \\ 0 & 0 & 0 & 0 & 0 & 0 \\ 0 & 0 & 0 & \frac{d_{iz}^+ F_{44}^0}{1-d_{iz}^+} & 0 & 0 \\ 0 & 0 & 0 & 0 & \frac{d_{jz}^+ F_{55}^0}{1-d_{jz}^+} & 0 \\ 0 & 0 & 0 & 0 & 0 & 0 \end{bmatrix} \quad (10)$$

$$[C(D^-)] = \begin{bmatrix} \frac{d_{iy}^- F_{11}^0}{1-d_{iy}^-} & 0 & 0 & 0 & 0 & 0 \\ 0 & \frac{d_{jy}^- F_{22}^0}{1-d_{jy}^-} & 0 & 0 & 0 & 0 \\ 0 & 0 & 0 & 0 & 0 & 0 \\ 0 & 0 & 0 & \frac{d_{iz}^- F_{44}^0}{1-d_{iz}^-} & 0 & 0 \\ 0 & 0 & 0 & 0 & \frac{d_{jz}^- F_{55}^0}{1-d_{jz}^-} & 0 \\ 0 & 0 & 0 & 0 & 0 & 0 \end{bmatrix} \quad (11)$$

3.2 Damage evolvement rate (Marante, 2002, P.1141-1152)

Marante regarded the damage rule of Rankine as the function of the plastic hinge energy release rate, and Figure 4 explains the rule.

From the figure, we can see that the undamaged is confirmed by the following equations.

$$\begin{aligned} G_{iy}^+ &= R_{iy}^+(d_{iy}^+; N, m_x) \quad ; \quad G_{iy}^- = R_{iy}^-(d_{iy}^-; N, m_x) \\ G_{iz}^+ &= R_{iz}^+(d_{iz}^+; N, m_x) \quad ; \quad G_{iz}^- = R_{iz}^-(d_{iz}^-; N, m_x) \end{aligned} \quad (12)$$

The function of $R(\quad)$ is used to describe the anti-cracking ability of the plastic hinge i , and it is related with the axial force, torque and damage parameters, and it can be confirmed in the experiment. Cipollina et al obtained the expression of $R(\quad)$ according to the experiment.

$$R = G_{cr}(N, m_x) + q(N, m_x) \frac{\ln(1-d)}{1-d} \quad (13)$$

Where, G_{cr} and q respectively denote the anti-cracking parameters before and after the crack occurs, and both parameters are related with the axial force and torque, and they are confirmed by the following formulas.

$$G_{cr} = \frac{1}{2} F_0 m_{cr}^2(N, m_x) \quad (14)$$

$$\begin{aligned} \frac{F_0 m_u^2(N, m_x)}{2} &= (1-d_u)^2 G_{cr} + q(1-d_u) \ln(1-d_u) \\ &- 2(1-d_u) G_{cr} + q[\ln(1-d_u) + 1] = 0 \end{aligned} \quad (15)$$

In above two formulas, m_{cr} denotes the flexural moment when the crack occurs, m_u denotes the maximum flexural moment, and d_u denotes the maximum damage value.

3.3 Yield function

The effective flexural moments of the plastic hinge, \bar{m}_{iy} and \bar{m}_{iz} are

$$\bar{m}_{iy} = \begin{cases} \frac{m_{iy}}{1-d_{iy}^+} & d_{iy}^+ > 0 \\ \frac{m_{iy}}{1-d_{iy}^-} & d_{iy}^- > 0 \end{cases} \quad (16)$$

$$\bar{m}_{iz} = \begin{cases} \frac{m_{iz}}{1-d_{iz}^+} & d_{iz}^+ > 0 \\ \frac{m_{iz}}{1-d_{iz}^-} & d_{iz}^- > 0 \end{cases} \quad (17)$$

Replace the actual flexural moment by the effective flexural moment, and the yield function of the plastic hinge i is

$$f_i = f_i(\bar{m}_{iy}, \bar{m}_{iz}, m_x, N, \phi_{iy}^p, \phi_{iz}^p, \delta_i^p) \quad (18)$$

So the plastic distortion evolvement rate of the plastic hinge is

$$\begin{aligned} \dot{\phi}_{iy}^p &= \dot{\lambda}_i \frac{\partial f_i}{\partial m_{iy}} ; & \dot{\phi}_{iz}^p &= \dot{\lambda}_i \frac{\partial f_i}{\partial m_{iz}} \\ \dot{\phi}_x^p &= \dot{\lambda}_i \frac{\partial f_i}{\partial m_x} ; & \dot{\delta}_i^p &= \dot{\lambda}_i \frac{\partial f_i}{\partial N} \end{aligned} \quad (19)$$

And the axial plastic distortion evolvement rate and the plastic corner evolvement rate of the unit are

$$\dot{\delta}_x^p = \dot{\lambda}_i \frac{\partial f_i}{\partial N} + \dot{\lambda}_j \frac{\partial f_j}{\partial N} \quad (20)$$

$$\dot{\phi}_x^p = \dot{\lambda}_i \frac{\partial f_i}{\partial m_x} + \dot{\lambda}_j \frac{\partial f_j}{\partial m_x} \quad (21)$$

4. Numerical computation of the example

4.1 Description of the example

The example is one single span RC frame structure with two layers. The span is 3.5m, the height of the layer is 2m, the Poisson ratio is 0.3, the elastic modules is 2.633GPa and the density is 2.5t/m³. When the pole section is 0.3×0.3m, the reinforcement assembly is 4Φ10, and when the girder section is 0.4×0.4m, the reinforcement assembly is 4Φ12. The top suffers the impulsive load, which is seen in Figure 5.

In 1ms, the pressure will increase from zero to the max. 700KN, and then the pressure will keep at the constant in 9ms, and in the later 10ms, the pressure will reduce to zero. And the pressure will keep at zero in later analysis (seen in Figure 6).

4.2 Numerical analysis (Anil K. Chopra, 2005)

The time interval $[0, T]$ is dispersed into a series of discontinuous time $(0, t_1, t_2 \dots, T)$, and we use the finite difference method and the Newmark method to denote the node displacement acceleration by the node displacement, and structure can be analyzed in $[0, T]$. In the appointed time t_s , the equation (1) can be wrote as

$$\{L(U)\} = \sum_{e=1}^m [B]_e^T [M]_e + \sum_{e=1}^m [m]_e \left\{ \ddot{U} \right\} - \{P\} = 0 \quad (22)$$

To obtain the displacement at the time t_s , we can solve it by the following equation.

$$\{L(U)\} \cong \{L(U_0)\} + \left[\frac{\partial L}{\partial U} \right]_{\{U\}=\{U_0\}} \{U - U_0\} = 0 \quad (23)$$

Where, $\{U_0\}$ denotes the displace matrix obtained by the computation before the time t_s , and $\{U\}$ denotes the displace matrix of the time t_s which we want to beg.

We utilize the center difference method to implement explicit time integral to the above motion equation, and offer the

acceleration which can fulfill the dynamical balance condition when the increment step begins. To obtain the acceleration, we explicitly deduce the speed and displacement on time. The computation of the unit includes confirming the constitutive relation between unit strain and applied materials and the unit stress, and further computing the interior force and obtaining the damage value of the unit finally. The concrete approaches include

- (1) According to the strain rate $\dot{\varepsilon}$, compute the unit strain increment $d\varepsilon$.
- (2) According to the constitutive relation, compute the stress σ .

$$\sigma_{(t+\Delta t)} = f(\sigma_{(t)}, d\varepsilon) \quad (24)$$

- (3) Integrating node internal force $I_{(t+\Delta t)}$.
- (4) Computing the damage value of the unit.

4.3 Parameter setting

Take the time increment as $3.0 \times 10^{-5} s$. According the design principle of RC, compute and obtain the flexural moment of the girder and pole in various stages.

Pole: $m_{cr} = 0.28 \times 10^5 KN mm$, $m_u = 1.61 \times 10^5 KN mm$.

Girder: $m_{cr} = 0.69 \times 10^5 KN mm$, $m_u = 2.53 \times 10^5 KN mm$.

4.4 Computation and analysis

Take the sub-module VUMAT of ABAQUS as the interface, adopt Fortran to compile and define the above model of the lumped damage mechanics, and run the program, and the computation result is seen in Figure 7. Use the fixed subprogram EXPLICIT modeling and compute the example, the result is seen in Figure 8.

From Figure 7 and Figure 8, both the method in the article and the commercial software ABAQUS can compute the damage of structure under the impulsive load, but the obvious difference is that the method can compute the damage values of the two ends of the frame member, but ABAQUS can compute the damage value of the whole unit. In fact, the place that damage easily occurs in RC is the joint among frame members, i.e. the end part of the frame members. So, the method in the article more accords with the requirement of the actual engineering.

For the computation of the damage value, because of different damage meanings both express, so we can not directly compare, but it is consistent to judge whether the frame member is damaged and the damage degree. For example, for the frame member AB, comparing with other pole members, the damage values computed by two sorts of method are maximum values, and for the frame member DK, the former computation results are 0.06 and 0.09, and the later computation results are 0.09, which indicates the frame member DK is not damaged basically.

5. Conclusions

From above analysis, we can obtain two conclusions.

First, because the method in the article can be used to directly analyze the damage value of the two ends of the frame member, it can be extensively applied in diagnosing the damages because of earthquake or other sudden loads or evaluation the surplus credibility.

Second, the mature interface of the finite unit commercial software can be utilized to realize the mechanical model in the method and develop applied program conveniently.

References

- Anil K. Chopra. (2005). Dynamics of structures (Theory and applications to Earthquake Engineering). 2005.5.
- Cipollina, A. López-Inojosa and J. Flórez-López. (1995). A simplified damage mechanics approach to nonlinear analysis of frames. *Comput. Struct.* No.546. P.1113–1126.
- Fabio F. Taucer. Earico Spacone. (1991). A fiber beam-column element for seismic response analysis of reinforced concrete structures. *Earthquake engineering research center*.
- G. Bolzon. (1996). An approximate method for fatigue-life prediction of framed structures. *Fatigue Fract. Engng Mater. Struct.* P.1481–1491.
- Marante and Flórez-López, M.E. Marante and J. Flórez-López. (2002). Model of damage for RC elements subjected to biaxial bending. *Engng Struct.* No.249. P.1141–1152.
- Marante, M.E, Flórez-López.J. (2002). Model of damage for RC elements subjected to biaxial bending. *Engng Struct.* No.24(9). P.1141–1152.

Maria Eugenia Marante, Julio Flórez-López. (2003). Three-dimensional analysis of reinforced concrete frames based on lumped damage mechanics. *International Journal of Solids and Structures*. No.40. P.5109-5123.

Mazza & Mazza, F. (1998). Modelli di danneggiamento nell'analisi sismica non lineare di strutture intelaiate in C.A. (in Italian). Tesis, Università degli Studi della Calabria Cosenza, Italy.

Perera, A. Carnicero, E. Alarcón and S. Gómez. (2000). A fatigue damage model for seismic response of RC structures. *Comput. Struct.* No.78. P.293-302.

Xue, Weichen & Zhang, Zhitie. (1999). Nonlinear full range analysis methods of steel concrete structures and its application. *Chinese Journal of Computational Mechanics*. No.16(3). P.334-342.

Zhu Bolong & Yu Andong. (1991). Nonlinear full-range analysis of R.C. frames. *Journal of tongji university*. No.83(3). P.21-30.

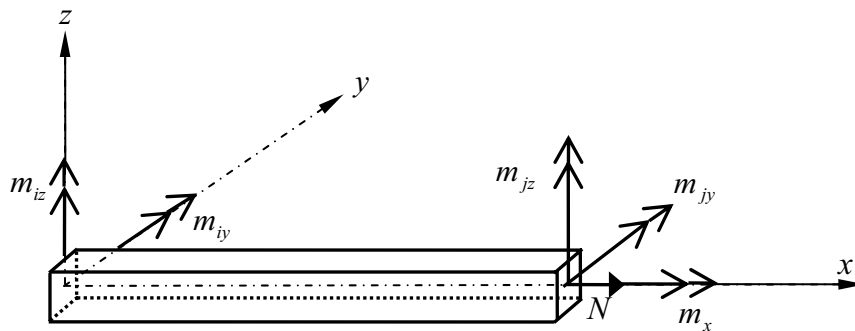


Figure 1. Generalized Stresses in a Frame Member

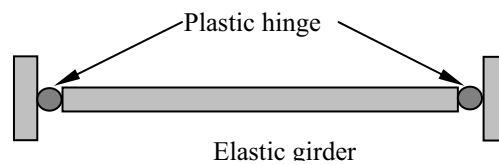


Figure 2. Inelastic Hinges in Frame Member

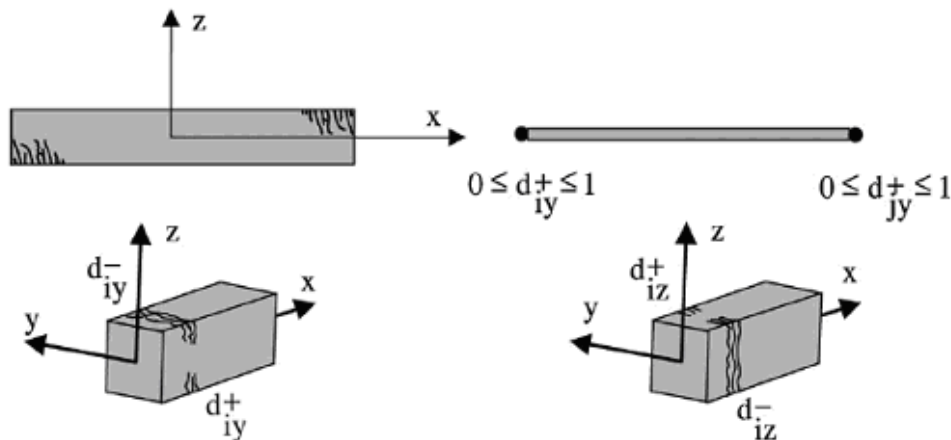


Figure 3. Cracking in a RC Frame Member via Damage Variables

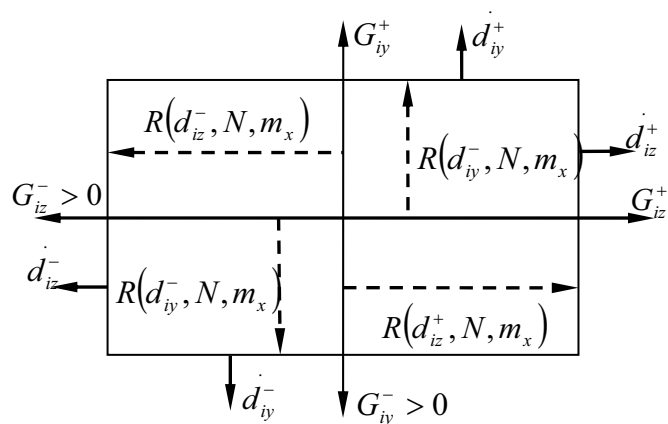


Figure 4. Damage Criterion in the Energy Release Rate Space

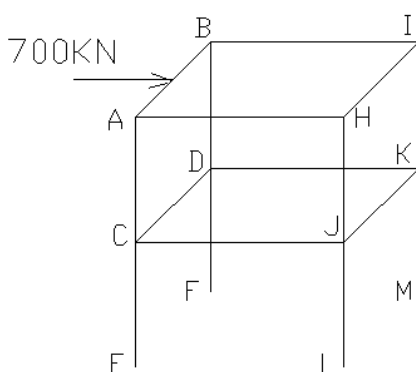


Figure 5. Finite Element Model of the Frame Structure

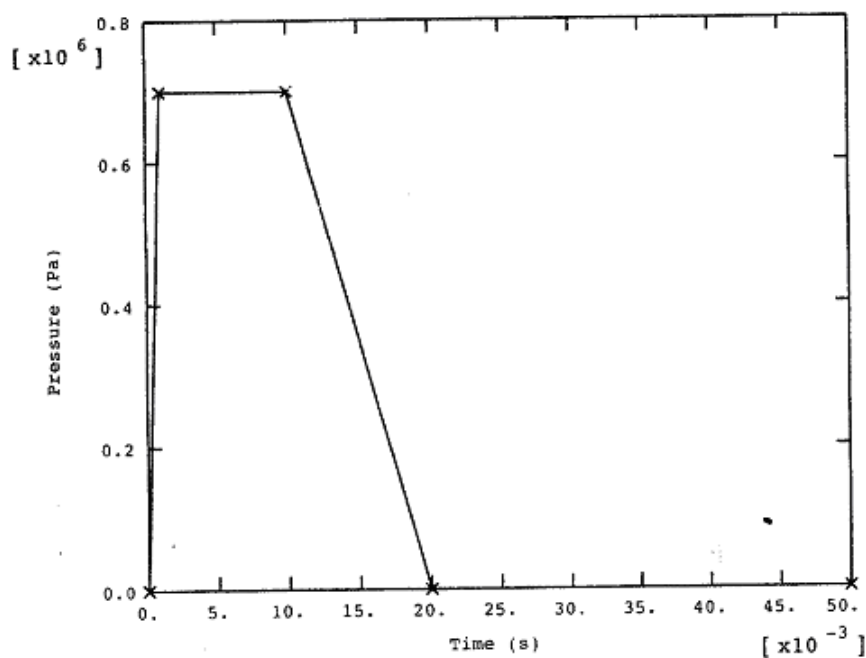


Figure 6. The Impulsive Load as the Function of Time

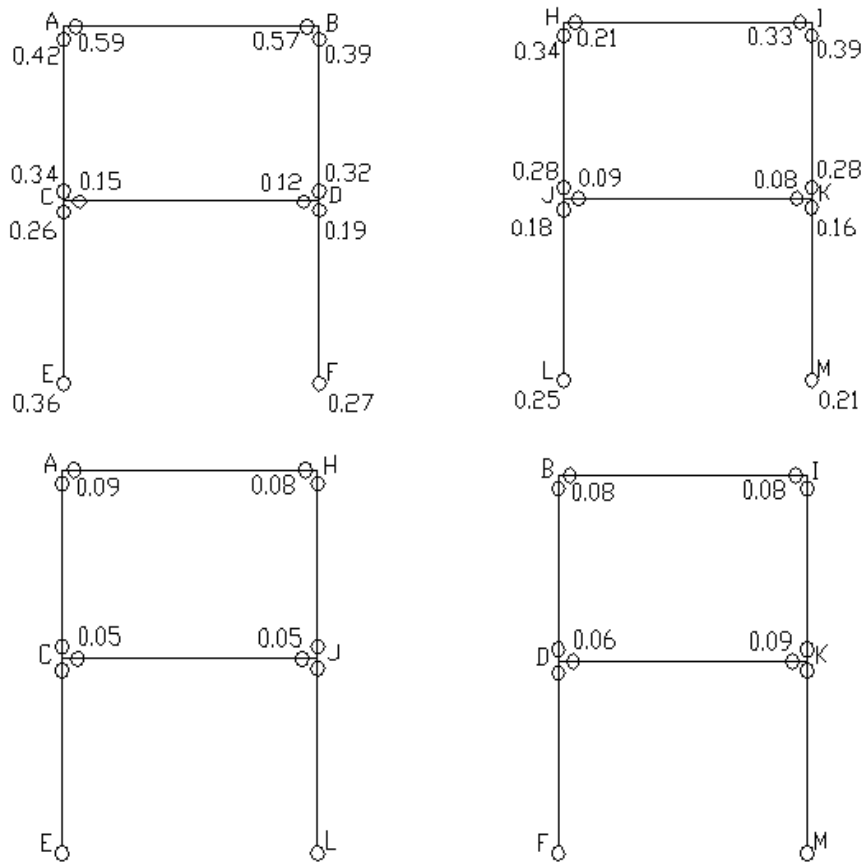


Figure 7. Result of Lumped Damage Mechanics

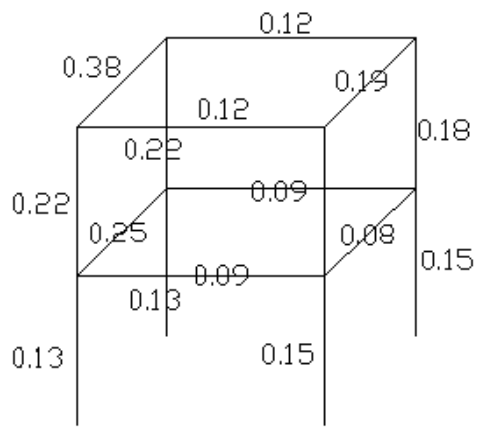


Figure 8. Result of EXPLICIT



Study on Public Agricultural Insurance in China

——Based on Xinjiang Mode

Yu Zheng

School of Management

Xi'an Polytechnic University

19 Jinhua South Road, Xi'an 710048, China

Tel: 86-29-8233-0193 E-mail: zyki2003@163.com

Juan Zhang

Applied Technology College

Xi'an Polytechnic University

19 Jinhua South Road, Xi'an 710048, China

Wangxi Wang

China Flight Test Establishment

8 Shifeiyuanlu Road, Xi'an 710089, China

The research is financed by the foundation of Xi'an Polytechnic University. No. 2008XG54

Abstract

Presently, China, which has set up four agricultural insurance companies, emphasizes the work in experimental units of agricultural policy insurance, and enlarges the area of experimental units. Through these experimental units explore different modes of China's agricultural insurance, as well as establish policies to encourage commercial insurance companies participate in agricultural insurance. Based on Xinjiang mode, public agriculture insurance is a suitable mode for agricultural insurance in China.

Keywords: Public Agricultural insurance, Experience, Mode

Agricultural insurance is always a hot subject in the domain of insurance and agronomics. Firstly, it is because the risk carriers are farmers, whose economical capability is relatively low in most countries. Due to the fundamentality of agriculture in the economy, stable production and subsistence in the sector are significant to national economic development. Secondly, agricultural risks derive from natural, social and economic, especially nature. In other words, agricultural insurance needs to cover risks which insurability are relative low and affected range is widespread. Above reasons show the speciality of agricultural insurance. So, establish a suitable agricultural insurance mode for a country is very important for national economic development.

1. Public Agricultural Insurance

Public agricultural insurance, also called governmental agricultural insurance, may take a number of forms. First, there may be public insurance institutions competing freely with private companies. Such institutions are reported to have existed in Germany and Denmark as early as the 17th century. There was, for instance, a public fire insurance institution in Schleswig-Holstein, and another managed by the city of Copenhagen. The second type of public insurance institution consists of those which have a legal or virtual monopoly of insurance although the insurance is voluntary, e.g. the United States Federal Crop Insurance, crop and livestock insurance in Brazil, and coffee insurance in Puerto Rico. Public insurance institutions of the third type comprise those where insurance is compulsory. There are three different categories of compulsory public insurance. First, there is the obligatory public insurance from which private competition is completely excluded. In the second category of compulsory insurance under State monopoly the competition of private companies is excluded only from the minimum of cover available under it but they may engage in the business for values above the minimum. The third category of compulsory public insurance is the "optional

application of compulsory insurance” that is, where compulsory public insurance may be introduced only when people have decided in its favor by vote in a commune or district.

2. The Situation of China's Agricultural Insurance

The China's insurance system was almost totally destroyed during the Cultural Revolution. In 80s, it began to be gradually recovered. The development of Chinese agricultural insurance over the past 30 years, and it can be divided into two stages Recovery and Fluctuation Stage. Since 1982, civil administration departments, agriculture departments and insurance companies issued agricultural insurances one after the other, it presented fast uptrend. The income of agricultural insurance premium was 561 million yuan in 1993. At the same time, loss ratio increased largely, the loss ratio of agricultural insurance reached 116.04% .

Three-Nong Problems have been paid more and more attention recent years, as well as China entered WTO, the sheltering effect of agricultural insurance for agriculture, countryside and farmers becomes prominent, and agricultural policy insurance has been paid attention to. In 2004, the China Insurance Regulatory Commission (CIRC) has launched agricultural insurance experimental units in 9 provinces and cities, e.g., Shanghai, Heilongjiang, Jilin etc. The agricultural insurance premium has increased obviously, and the loss ratio has shown a sharp decrease in 2005(fig.1).

3. Analyzing the Mode of Xinjiang Agriculture Insurance

3.1 Characteristics of Xinjiang mode

In 1986, Xinjiang Production and Construction Corps set up the first policy agricultural insurance company which called Xinjiang Production and Construction Corps Farming and Grazing Production Company. The name has been changed to Xinjiang Corps Property Insurance Company in 1989. In 2002, the name has been changed again to China United Property Insurance Company Limited (CIC). In 2006, as CIC finished its system reform, all the insurance organizations in Xinjiang completely realized the shareholding system. Each company gradually built the modern enterprise system from the reform of structure and management system to the operation system, perfecting the structure of inner management, resulting in a great change of the operation idea, bettering the level of management, creating a new situation for the reform and development of Xinjiang insurance industry.

Xinjiang mode has some unique characteristics. Firstly, it is compulsory insurance, means every one has to cover. According to Document No.12 made by Xinjiang Crops, all of the crop productions and livestock breeding which undertake by farming and grazing organizations, home farms and contractors should be covered. The loss has to bear by itself, if the ones do not cover. Contrarily, there is some preferential policy concerning the premium and financial affairs, if the ones participate in agricultural insurance.

Secondly, CIC follows the direction which is that the agricultural insurance should be always served for farms and farmers, and the guiding ideology - pulling together in times of trouble, integrating prevention with compensation, undertaking risks together, and pooling-of-interest. In addition, agricultural insurance also uses individual account, and surplus keeps as local agricultural insurance fund.

Thirdly, CIC constitutes clear executive methods as follows: (1) Establishing collegiums for agriculture policy insurance in every division of corps which exam the operation of agriculture policy insurance once a year. (2) Setting up agricultural insurance fund. If there is surplus in a year, set up agricultural insurance fund in both division and regiment with the proportion of 30% and 70%. Insurance fund managed by insurance company, accumulated step by step, in order to prepare for catastrophe. (3)CIC uses premium and unused insurance fund over the years to compensate, when farms suffer from calamities and damages within their insurance coverage. If the premium and unused insurance fund are not enough to pay for the indemnity, CIC will take out 30% from the profit of commercial insurance to support it. (4)The unused agricultural insurance fund has two purposes. First, surplus keeps as agricultural insurance fund. Second, when unused agricultural insurance fund is more than premium income of the same year, take out 30% from premium balance of the year to improve urgent need items, hazard resistant items, as well as scientific experiments.

3.2 Effect of Xinjiang mode

Generally speaking, agricultural insurance in Xinjiang is very successful. Because it is a kind of public agricultural insurance, it gets great support from government continuously. In addition, due to its compulsoriness and speciality, not only insureds get guarantee for their production and life, but also the size and strength of insurance companies get increase. It realizes “Two Win” in both insureds and insurers. Agricultural insurance has experienced a remarkable development in Xinjiang. In 2007, the agricultural insurance premium income was 757 Million yuan, increased by 167.3% and continuously ranked 1st in China's agriculture insurance. The Property insurance depth was 0.78 percent, while the density was 121.68 yuan per person. The agricultural insurance premium income rises steadily year by year. We can see the statistics of agricultural insurance operation achievement of CIC from following figure (fig. 2).

3.3 Problems of Xinjiang mode

Although the agricultural insurance operates very satisfactory in Xinjiang, it still has some problems inevitably. Firstly,

the guarantee level of agricultural insurance is low in Xinjiang. The operational principle is low sum insured, low premium, and implement basic guarantee in Xinjiang. Because the sum insured is low, and most types of risk are deficit insurances. Insureds can not gain enough indemnity when they have been hit by calamities. To solve this problem, we suppose that government should increase its effect in agricultural insurance in Xinjiang, and leading enterprises can be brought into agricultural insurance, so that to set up a risk pooling mechanism, i.e. government supports, leading enterprises and farmers share premium together. By means of this method, it can reduce farmers' premium burden. Besides, with the help of the compensation effect of agricultural insurance, the basic links of leading enterprises' industry chain may become steadier. And what's more, it embodies pooling-of-interest and risk pooling mechanism between companies and insureds.

Secondly, the type of risk is simplex. The types of risk are centralized on crops in Xinjiang, especially cotton. There is no type of risk on forest and melon & fruit. Xinjiang is the second pasturing area in China, so that animal husbandry economy plays an important role in Xinjiang. Although the agricultural insurance increases steadily, breed aquatics insurance is still behindhand. A small quantity of milk cow and sheep insurances has been launched presently, but it is still in experimental stage. Government should increase the support in this field.

Thirdly, the loss ratio of agricultural insurance is still high (fig.2). According to the report from Statistic Bureau of Xinjiang, the average loss ratio of agricultural insurance was 72.5% from 1985 to 2006. Some years even exceed 100%, and it was higher than agricultural insurance breakeven point 70% which is generally accepted internationally. Loss ratio is related to the profit of a company intimately. If the loss ratio is too high, it will bring deficit for a company. A vulgate method to solve this problem in international is that offer policy allowance for reinsurance business of catastrophe risks through legislative form.

4. Successful Experience of Xinjiang Mode

4.1 Remarkably improving the external developing environment of insurance industry.

Firstly, the local governments put more emphasis and supports on insurance industry. In 2006, the local government's printed and distributed the document <Decision on Speeding up the Reform and Development of Insurance in Xinjiang>. The government held an insurance conference to carry out the spirits of the document No.23 from the State Council and arranged some work related to the insurance, put the insurance on the government's agenda in the next period, researched and deployed it.

Secondly, the social circles focused more on the insurance industry. Under the powerful supports of the local related departments, the insurance industry widely started some activities such as "Enter schools, enter communities, enter farming and pasture areas", and reinforced the universal education of insurance knowledge to make more people know insurance, take out insurance and support insurance so that a sound social environment has been built.

4.2 Strengthening the force of supervision and gradually making the market order better.

Firstly, the thought of "Stress supervision and promote development" was getting clearer day by day. CIRC Xinjiang Bureau summed up the experiences constantly in terms of the economic growth pattern and the features of social development. They were: vigorously developed insurance market of the minority as the focus of promoting the harmonious development of Xinjiang, enhanced the capacity and infiltrated degree of serving the construction of new industrialization in Xinjiang as the main direction of supporting and protected local economical construction, vigorously pushed forward the experimental spot project of agricultural insurance, expanded the coverage of agricultural insurance as the major measures for the construction of a new socialist countryside.

Secondly, the regulatory force of market conducts was constantly reinforced. CIRC Xinjiang Bureau emphasized on the wicked price competition, dishonesty and misleading, and invasion of the consumers' interests, organized special examination in the truth of business, finance and statistical data, and special treatment to the conduct of misleading risks, concentrated on punishing the irregular problems. Moreover, they strengthened the regulatory system of insurance intermediary market, and earnestly carried out the cleaning work against commercial bribes, organizing the self-examination and self-correction in business policy-making, financial management, inner controlled system and business operation throughout the insurance industry.

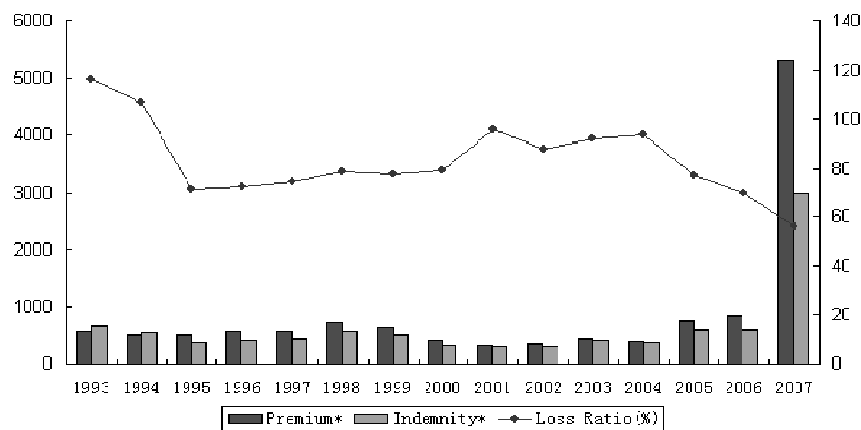
5. Conclusion

Based on Xinjiang mode, this article discusses effect on boosting public agriculture insurance. In the aspects of serving agriculture, rural areas and farmers and boosting the construction of socialist new village, CIRC pushed forward the development of agricultural insurance energetically, worked out "the program of the experiment for policy-related agricultural insurance" and tried to win the support from the governments in all provinces. For example, the governments in Hebei province, Jilin province and Sichuan province, etc. issued documents to boost the development of agricultural insurance. The regions and products of agricultural insurance for the experiments have been enlarged constantly and insurance businesses for corn, rice, pig and milk cow as well as breeding insurance have been opened

successively. 145 million acres of crops and 246 live pigs have been covered in the recent three years.

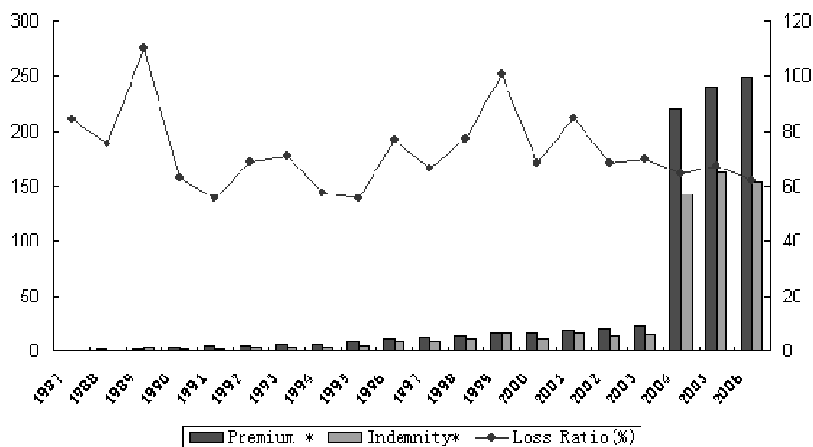
References

- Yankun Du(2005). The Basic Thought to Construct Agriculture Policy Insurance System. *Economic Information Daily*. 17 September 2005.
- Danli Chen and Lie Zhou(2006). Empirical Study on the Situation of Agricultural Insurance's Development in China. Southeast University. 12-18.
- Shengting Xiao and Jingyu Zhang(2007). Research on Agricultural Insurance Modes in China. University of Skovde. 13-19.
- Jianhua Yuan (2008). Study on Models of Policy-rated Agricultural Insurance Company. *Modern Finance & Economics*. No. 2, 2008, 32-36.
- CIRC(2007). *Yearbook of China's Insurance 2007*. 986-987.
- Yu Zheng, Juan Zhang and Wangxi Wang(2008). Suggestion on Promoting Agricultural Insurance in China. *International Journal of Business and Management*. Vol. 3, No. 12, 2008, 57-59.



Unite: Million yuan

Figure 1. China's Agricultural Insurance Premiums and Indemnity, 1993-2007



Unite: Million yuan

Figure 2. Statistics of Agricultural Insurance Operation Achievement of CIC, 1987-2006



Fabrication of LaNiO_3 Porous Hollow Nanofibers via an Electrospinning Technique

Xiangting Dong (Corresponding author), Jinxian Wang, Qizheng Cui, Guixia Liu & Wensheng Yu

School of Chemistry and Environmental Engineering

Changchun University of Science and Technology

Changchun 130022, China

Tel: 86-431-8558-2574 E-mail: dongxiangting888@yahoo.com.cn

This work was financially supported by the Science and Technology Development Planning Project of Jilin Province (Grant Nos. 20040125, 20060504, 20070402), the Scientific Research Planning Project of the Education Department of Jilin Province (Under grant Nos. 200224, 2005109, 2007-45)

Abstract

Polyvinyl Pyrrolidone(PVP)/[$\text{La}(\text{NO}_3)_3 + \text{Ni}(\text{CH}_3\text{COO})_2$] composite nanofibers were fabricated via an electrospinning technique. SEM micrographs indicated that the surface of the prepared composite fibers was smooth, and the diameters of the nanofibers were in the range of 1-3 μm . XRD analysis revealed that the composite nanofibers were amorphous in structure. LaNiO_3 nanofibers were fabricated by calcination of the PVP/[$\text{La}(\text{NO}_3)_3 + \text{Ni}(\text{CH}_3\text{COO})_2$] composite fibers. The diameters of LaNiO_3 nanofibers were smaller than those of the relevant composite fibers. The surface of the LaNiO_3 nanofibers became coarse with the increase of calcination temperatures. LaNiO_3 porous hollow nanofibers formed by nanoparticles were acquired when firing temperature was 600-900°C. SEM images indicated that the diameters of the synthesized LaNiO_3 nanofibers ranged from 500 to 800nm, and their lengths were greater than 100 μm . XRD analysis revealed that LaNiO_3 nanofibers were trigonal in structure with space group $R\bar{3}m$. Possible formation mechanism for LaNiO_3 nanofibers was preliminarily proposed.

Keywords: LaNiO_3 , Lanthanum, Nickel, Nanofibers, Electrospinning

1. Introduction

The science and technology of nanostructured materials is advancing at a rapid pace. Over the past decade, the preparation and functionalization of one-dimensional nanostructured materials has become one of the most highly energized research fields. One-dimensional nanostructured materials, such as nanowires, nanorods, nanowhiskers and nanofibers, have stimulated great interest due to their importance in basic scientific research and potential technological applications. They are expected to play an important role as both interconnects and functional components in the fabrication of nanoscale electronic and optoelectronic devices. In order to obtain these materials, various preparation methods have been developed including arc discharge, laser ablation, template, precursor thermal decomposition, and other methods. Electrospinning technique is widely applied to prepare polymers nanofibers. Recently, some inorganic compounds nanofibers have been prepared by electrospinning technique using electrospun fibers of polymer/inorganic composite as the precursor. This processing involved the following three steps: (1) Preparation of a gel with suitable inorganic precursor and proper polymer, and achieving the right rheology for electrospinning process; (2) Electrospinning of the gel to obtain fibers of polymer/inorganic precursors composite; (3) Calcinations of the composite fibers to obtain final oxide fibers. It is important, however, to control all of the above three steps in order to obtain high quality fibers with the desired final properties. LaNiO_3 has attracted much interest recently due to their specific electrical and catalytic properties. A few methods on the preparation of LaNiO_3 nanocrystalline materials were reported. However, to the best of our knowledge, there have been no reports on the preparation of LaNiO_3 nanofibers by electrospinning. In this paper, LaNiO_3 nanofibers were fabricated by calcination of the electrospun fibers of PVP/(lanthanum nitrate and nickel acetate) composite, and some new results were obtained.

2. Experimental section

2.1 Chemicals

Polyvinyl pyrrolidone(PVP)($M_r \approx 10000$) and nickel acetate tetrahydrate[$\text{Ni}(\text{CH}_3\text{COO})_2 \cdot 4\text{H}_2\text{O}$] were purchased from Tianjin Kermel Chemical Reagents Development Center. Lanthanum nitrate hexahydrate[$\text{La}(\text{NO}_3)_3 \cdot 6\text{H}_2\text{O}$] was obtained

from Tianjin Guangfu Institute of Fine Chemicals. All chemicals were analytically pure and directly used as received without further purification. Distilled water was used as solvent.

2.2 Preparation of PVP/[La(NO₃)₃+Ni(CH₃COO)₂] composite gel

PVP/[La(NO₃)₃+Ni(CH₃COO)₂] composite solution was prepared by dissolving 29.9700g of PVP powders, 5.6213g of La(NO₃)₃·6H₂O and 3.2306g of Ni(CH₃COO)₂·4H₂O in 26.33g of distilled water, and stirring for 10h, then remaining motionlessly for 2h. Thus, a viscous gel of PVP/[La(NO₃)₃+ Ni(CH₃COO)₂] composite containing 46%(wt%) PVP, 10%(wt%) metallic salts, 44%(wt%) H₂O, and the molar ratio 1:1 of La³⁺ to Ni²⁺ were obtained for electrospinning processing.

2.3 Fabrication of PVP/[La(NO₃)₃+Ni(CH₃COO)₂] composite fibers and LaNiO₃ nanofibers

The setup used for electrospinning was indicated in Fig. 1. The above composite gel of PVP, La(NO₃)₃, Ni(CH₃COO)₂ and H₂O mixture was contained in a plastic syringe with a stainless steel needle on its top. A copper wire connected to a DC high-voltage generator was placed in the gel, and the gel was kept in the syringe by adjusting the angle between syringe and the fixing bar. A grounded aluminum foil served as counter electrode and collector plate. A voltage of 18 kV was applied to the composite gel and a sprayed dense web of fibers was collected on the aluminum foil. The collected fibers were PVP/[La(NO₃)₃+Ni(CH₃COO)₂] composite fibers. The prepared composite fibers were dried initially at 70°C for 12h under vacuum, and then calcined at a heating rate of 120°C/h and remained for 10h at 300°C, 600°C and 900°C, respectively. Thus, LaNiO₃ nanofibers were obtained when calcinations temperature is 600-900°C.

2.4 Characterization methods

XRD analysis was performed with a Holland Philips Analytical PW1710 BASED X-ray diffractometer using Cu Kα₁ radiation, the working current and voltage were 30mA and 40kV, respectively. Scans were made from 10° to 80° at the speed of 3°/min, and step was 0.05°. The morphology and size of the fibers were observed with a S-4200 scanning electron microscope made by Japanese Hitachi company. FTIR spectra of the samples were recorded on BRUKER Vertex 70 Fourier transform infrared spectrophotometer made by Germany Bruker company, and the specimen for the measurement was prepared by mixing the sample with KBr powders and then the mixture was pressed into pellets, the spectrum was acquired in a wave number range from 4000cm⁻¹ to 400cm⁻¹ with a resolution of 4cm⁻¹.

3. Results and discussion

3.1 XRD patterns

In order to investigate the lowest crystallizing temperature and the variety of phases, the PVP/[(La(NO₃)₃+Ni(CH₃COO)₂] composite fibers and samples obtained by calcining the composite fibers at different temperatures for 10h were characterized by XRD, as indicated in Fig. 2. The results showed that the PVP/[La(NO₃)₃+Ni(CH₃COO)₂] composite fibers were amorphous in structure, only a broad peak was located around 20°, it was the typical peak of the amorphous polymer, indicating that the composite fibers were amorphous in structure. LaNiO₃ was not formed at 300°C, and the sample was the mixture of metallic oxides. The polycrystalline LaNiO₃ nanofibers with single phase were synthesized when calcination temperature was in the range of 600-900°C, the d(spacing between crystallographic plane) values and relative intensities of LaNiO₃ diffraction peaks were consistent with those of JCPDS standard card(34-1181), the crystal structure of the prepared LaNiO₃ was trigonal system in structure with space group is R $\bar{3}m$.

3.2 SEM images

In order to study the morphology and size of the as-synthesized fibers, the prepared fibers were investigated by SEM, as shown in Fig. 3. As seen from Fig. 3, the morphology and size of the fibers varied strongly with the increase of calcination temperatures. The surface of the PVP/[La(NO₃)₃+ Ni(CH₃COO)₂] composite fibers was very smooth, and the diameter of the composite fibers was in the range of 1μm-3μm. The morphology and size of the fibers at 300°C were almost the same as those of the composite fibers. The surface morphology of LaNiO₃ nanofibers became coarse with the increase of calcinations temperatures. LaNiO₃ porous hollow nanofibers formed by nanoparticles were acquired at 600°C-900°C. SEM analysis indicated that the diameters of the synthesized LaNiO₃ nanofibers were in the range of 500nm-800nm, and their lengths were greater than 100μm. The diameters of LaNiO₃ nanofibers were smaller than those of the PVP/[La(NO₃)₃+Ni(CH₃COO)₂] composite fibers owing to the decomposition and evaporation of PVP, NO₃⁻ and CH₃COO⁻.

3.3 FTIR spectra analysis

Pure PVP, PVP/[La(NO₃)₃+Ni(CH₃COO)₂] composite fibers and LaNiO₃ nanofibers(obtained by calcination of the PVP/[La(NO₃)₃+Ni(CH₃COO)₂] composite fibers at 900°C for 10h) were analyzed by FTIR, as shown in Fig. 4. As seen from Fig.4, PVP(Fig.4a) and PVP/[La(NO₃)₃+Ni(CH₃COO)₂] composite fibers(Fig.4b) had the identical spectra, but absorption peaks intensity of spectrum for PVP/[La(NO₃)₃+Ni(CH₃COO)₂] composite fibers was lower than those of spectrum for pure PVP. This resulted from the lower content of PVP in the PVP/[La(NO₃)₃+Ni(CH₃COO)₂] composite

fibers. All absorption peaks were attributed to PVP at 3445cm^{-1} , 2955cm^{-1} , 1668cm^{-1} , 1424cm^{-1} , and 1289cm^{-1} , corresponding to the stretching vibrations of hydroxyl group($\nu_{\text{O-H}}$), C-H bond($\nu_{\text{C-H}}$), carbonyl group($\nu_{\text{C=O}}$), C-H bond($\nu_{\text{C-H}}$), and C-N bond or C-O bond($\nu_{\text{C-N}}$ or $\nu_{\text{C-O}}$), respectively. It was seen from Fig. 4c that all peaks of PVP disappeared, and at low wave number range, new absorption peaks at 601 , 563 , 428cm^{-1} appeared. The new absorption peaks were ascribed to the vibration of metal-oxygen bonds, indicating that LaNiO_3 was formed. The results of FTIR analysis were in good agreement with XRD results.

3.4 Possible formation mechanism of LaNiO_3 porous hollow nanofibers

Possible formation mechanism of LaNiO_3 porous and hollow nanofibers was described as follows. $\text{La}(\text{NO}_3)_3 \cdot 6\text{H}_2\text{O}$, $\text{Ni}(\text{CH}_3\text{COO})_2 \cdot 4\text{H}_2\text{O}$ and PVP were mixed with distilled water to form gel with certain viscosity. PVP acted as template during the formation processing of LaNiO_3 nanofibers. La^{3+} , Ni^{2+} , NO_3^- and CH_3COO^- were mixed with or absorbed onto PVP molecules to fabricate PVP/ $[\text{La}(\text{NO}_3)_3 + \text{Ni}(\text{CH}_3\text{COO})_2]$ composite fibers under electrospinning. During calcination treatment of the composite fibers, solvent water containing La^{3+} , Ni^{2+} , NO_3^- and CH_3COO^- ions in the composite fibers would remove to the surface of the PVP/ $[\text{La}(\text{NO}_3)_3 + \text{Ni}(\text{CH}_3\text{COO})_2]$ composite fibers and eventually evaporated from the composite fibers. Thus, La^{3+} , Ni^{2+} , NO_3^- and CH_3COO^- ions would also remove to the surface of the composite fibers brought by removed water. With the increasing in calcination temperature, PVP, NO_3^- and CH_3COO^- would oxidize and volatilize rapidly, La^{3+} and Ni^{2+} were oxidized into LaNiO_3 crystallites, and many crystallites were combined to form small LaNiO_3 nanoparticles, and these nanoparticles were mutually connected to generate hollow-centered and porous LaNiO_3 nanofibers. It was found from experiments that the average molecular weight of PVP and PVP content in the starting mixed gel had important impact on the formation of LaNiO_3 porous hollow nanofibers. Further work is under way.

4. Conclusions

4.1 PVP/ $[\text{La}(\text{NO}_3)_3 + \text{Ni}(\text{CH}_3\text{COO})_2]$ composite fibers were fabricated by electrospinning. Polycrystalline LaNiO_3 nanofibers were synthesized by calcining the relevant composite fibers at $600\text{--}900^\circ\text{C}$.

4.2 XRD analysis revealed that the composite fibers were amorphous in structure. The crystal structure of LaNiO_3 nanofibers was trigonal system in structure with space group $R\bar{3}m$.

4.3 SEM micrographs indicated that the surface of the prepared composite fibres was smooth, and the diameters of the composite fibres were in the range of $1\text{--}3\mu\text{m}$. The diameters of LaNiO_3 nanofibers were smaller than those of the composite fibers. The surface of the LaNiO_3 nanofibers became coarse with the increase of calcination temperatures. LaNiO_3 porous and hollow nanofibers formed by nanoparticles were acquired when calcining temperature was $600\text{--}900^\circ\text{C}$. The diameters of LaNiO_3 nanofibers were in the range of $500\text{nm--}800\text{nm}$, and their lengths were greater than $100\mu\text{m}$.

References

- Duan, X. F., Huang, Y., Agarwal, R., Lieber, C. M. (2003). Single-nanowire electrically driven lasers. *Nature*, 421, 241-245.
- Hu, X. K., Qian, Y. T., Song, Z. T., et al. (2008). Comparative study on MoO_3 and H_xMoO_3 nanobelts: structure and electric transport. *J. Chem. Mater.*, 20(4), 1527-1533.
- Huynh, W. U., Dittmer, J. J., Alivisatos, A. P. (2002). Hybrid nanorod-polymer solar cells. *Science*, 295, 2425-2427.
- Iijima, S. (1991). Helical microtubules of graphitic carbon. *Nature*, 354, 56-58.
- Kar, S., Chaudhuri, S. (2006). Shape selective growth of CdS one-dimensional nano-structures by a thermal evaporation process. *J. Phys. Chem. B*, 110(10), 4542-4547.
- Li, A. D., Ge, C. Z., Di, P. L., et al. (1997). Fabrication and Electrical properties of sol-gel derived BaTiO_3 films with metallic LaNiO_3 electrode. *Appl. Phys. Lett.*, 70(12), 1616-1618.
- Li, D., Xia, Y. N. (2004). Direct Fabrication of Composite and Ceramic Hollow Nanofibers by Electrospinning. *Nano Lett.*, 4(5), 933-938.
- Li, D., Xia, Y. N. (2004). Electrospinning of Nanofibers: Reinventing the Wheel? *Adv. Mater.*, 16(14), 1151-1170.
- Liang, X. Y., Ma, Z., Bai, Z. C., et al. (2002). Properties and sonochemical preparation of nanostructured LaNiO_3 . *Acta Physico-Chimica Sinica*, 18(6), 567-571.
- Mohapatra, S. K., Misra, M., Mahajan, V. K., et al. (2008). Synthesis of Y-branched TiO_2 nanotubes. *Materials Letters*, 62, 1772-1774.
- Morales, A. M., Lieber, C. M. (1998). A laser ablation method for the synthesis of crystalline semiconductor nanowires. *Science*, 279, 208-211.
- Pan, Z. W., Dai, Z. R., Wang, E. L. (2001). Nanobelts of semiconducting oxides. *Science*, 291, 1947-1949.

Shao, C. L., Guan, H. Y., Liu, Y. C., et al. (2004). A novel method for making ZrO_2 nanofibres via an electrospinning technique. *J. Crystal Growth*, 267, 380-384.

Shi, W. S., Zheng, Y. F., Wang, N., et al. (2001). A general synthetic route to III-V compound semiconductor nanowires. *Adv. Mater.*, 13, 591-594.

Wang, Y. P., Zhu, J. W., Yang, X. J., et al. (2006). Preparation and characterization of LaNiO_3 nanocrystals. *Mater. Res. Bull.*, 41(8), 1565-1570.

Yang, Q. H., Fu, X. X. (2003). Analysis of photocatalytic oxidation activity of nano- LaMO_3 (M=Cr Mn, Ni, Co) compounds. *J. Chin. Ceram. Soc.*, 31(3), 254-256.

Zhang, S. H., Dong, X. T., Xu, S. Z., et al. (2007). Preparation and characterization of $\text{TiO}_2/\text{SiO}_2$ submicron-scaled coaxial cables via a static electricity spinning technique. *Acta Chimica Sinica*, 65(23), 2675-2679.

Zhang, S. H., Dong, X. T., Xu, S. Z., et al. (2008). Preparation and characterization of $\text{TiO}_2/\text{SiO}_2$ composite hollow nanofibers via an electrospinning technique. *Acta Materiae Compositae Sinica*, 25(3), 138-143.

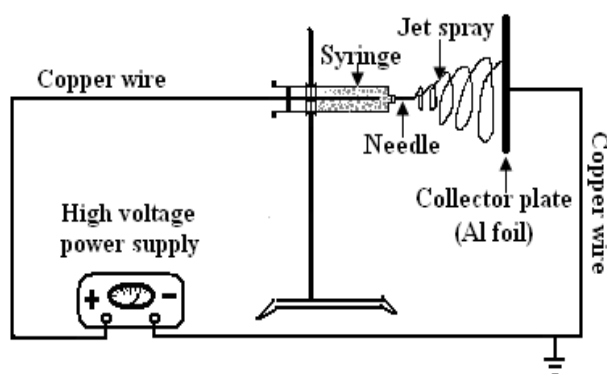


Figure 1. Schematic diagram of electrospinning setup

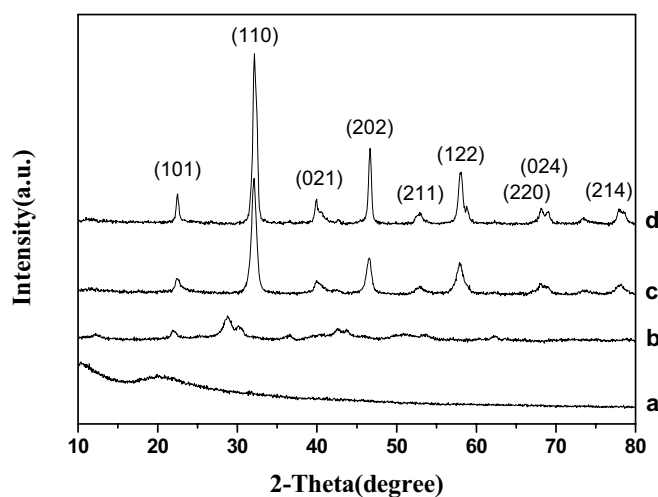


Figure 2. XRD patterns of samples

a. PVP/ $[\text{La}(\text{NO}_3)_3 + \text{Ni}(\text{CH}_3\text{COO})_2]$ composite fibers b. 300°C c. 600°C d. 900°C

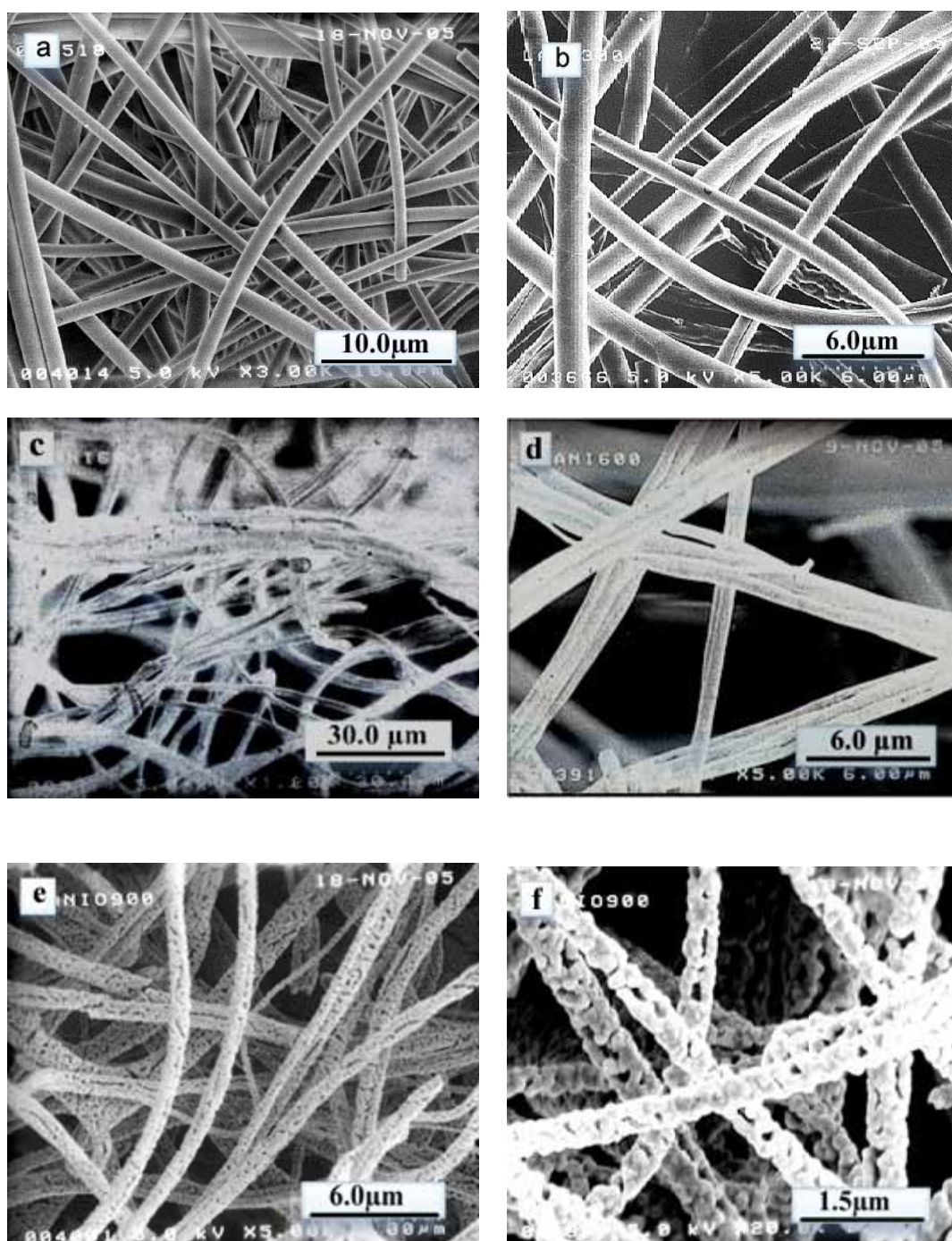


Figure 3. SEM micrographs of the fibers obtained at different temperatures

- a. PVP/[La(NO₃)₃+Ni(CH₃COO)₂] composite fibers b. 300°C c. 600°C(Low magnification)
 d. 600°C(High magnification) e. 900°C(Low magnification) f. 900°C(High magnification)

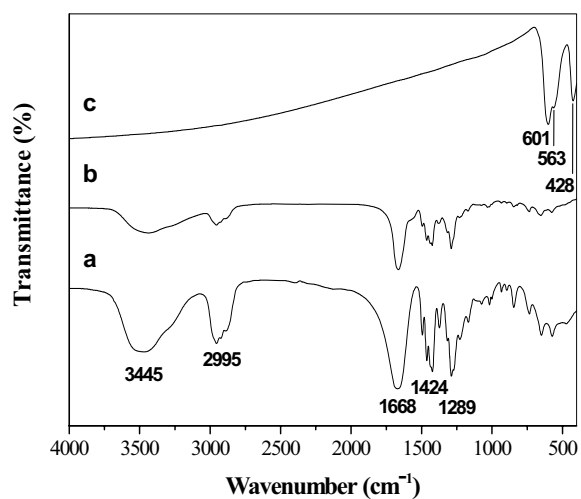


Figure 4. FTIR spectra of the samples

a: PVP b: PVP/[La(NO₃)₃+Ni(CH₃COO)₂] composite fibers c: LaNiO₃ nanofibers



Investigation of Differences of Topographical Map and GIS-derived Spatial Map with Actual Ground Data in Peninsular Malaysia

Mohd Hasmadi Ismail (Corresponding author)

Survey and Engineering Laboratory, Department of Forest Production

Faculty of Forestry, Universiti Putra Malaysia, 43400 UPM, Serdang, Selangor, Malaysia

Tel: 60-3-8946-7220, Fax: 603-89432514

E-mail: mhasmadi@putra.upm.edu.my

Taylor, J.C.

Cranfield Centre for Geographical Information Management

National Soil Resources Institute, Cranfield University, Silsoe, Bedford

MK45 4DT, United Kingdom

Tel: 44-1525 863064

E-mail: j.c.taylor@cranfield.ac.uk

Abstract

In a geographical information system (GIS), digital maps usually used to show multiple views of geographical objects either through two-dimensional or three-dimensional, which topographical parameters are digitally generated. Digital maps are often used in extensively environmental application without quantifying the effect of their errors. This study was carried out to investigate the difference of elevation and slope of topographical map and GIS-derived spatial map with actual ground data. The analyses of differences were quantified from interpolation process, sampling and measurement in the field. The RMSE of the DEM creation for the test site was 0.62. The result was based on the 10 m DEM resolutions and 20 m contour interval. From the analysis of differences (elevation and slope) of topographical map and actual ground data, it's showed that the difference is only about 2 % and 28%, respectively. The great differences on slope may be due to error during data collection by different enumerators and also inconsistent reading of slope measurement and target. Despite the difficulty occurs during ground data collection, estimation method was applied and this relatively simple procedure but appears acceptable in regard to sufficient data sets at nominal map scale 1:50000.

Keywords: Peninsular Malaysia, DEM analysis, Validation, Elevation and slope differences

1. Introduction

A fundamental for natural resources survey whether at local, regional or global scales is availability of map with high quality, reliable and up to date information. An additional consideration is the increasing use of satellite remote sensing data combine with global positioning system (GPS) in natural resources surveys Kardoulas et al. (1996). Topographical maps at any scale are beneficial to be used as a baseline data for designing ground survey (Thomas et al., 2000). These maps are usually used to determine the range of an area, shows a comprehensive information and logistic about certain area. It is also represents the earth surface as digital elevation data (DEM) that has been specified mathematically and is illustrated upon identified scale. Most usually, a map is a two-dimensional, geometrically accurate representation of a three-dimensional space. Previously, people used the topographical maps to know the place by looking at the geographic feature in the paper map. With the advancement of technologies, the topographical map was digitized into GIS system and they called GIS map or digital map. In the beginning era of digital maps there were only exclusive use of digital data, and the data were assumed to ready precisely. However, all maps are always inherent errors that

constituent uncertainty. According to Helen (2003) uncertainty need not be excised as a flaw, but needs to be managed and accepted as an intrinsic part of complex knowledge.

Digital maps data are often used in analyses without quantifying the effects of these errors. In addition, elevation data in a particular grid cell is often based on sample elevation points. If the sampling scheme is inefficient, the resulting grid may be biased. It is a practical impossibility to obtain information on the exact source and amount of error in a particular digital topographical map. The underlying assumption of this research is that specific error within digital topographical map cannot be known and therefore the map is remaining question with uncertainty. Many digital topographical maps are generated from paper topographic maps. The grid location on the ground may vary and most likely will not correspond directly with the co-located value in a digital map. However, issues on the data errors or uncertainty are become a critical in GIS especially when users are taking this thing as an important key in decision making. According to Blakemore (1985) the main concern is being expressed within the geographic information science to effectively deal with uncertainty and manage the quality of information outputs. The basic scientific requirement of being able to describe how close their information is to the truth it represents. Meanwhile Stoms (1987) discussed knowledge-based approaches which employ various methods of reasoning under uncertainty for specific applications. Many studies has been carried out for calculating topographical parameter related to DEM, and each method were produced with different results (Skidmore, 1989; Ryder and Voyadgis, 1996; Suzanne and Chales, 2006; Qiming et al., 2006). Thus, more research needs to be done in this area to verify the uncertainty of topographical used in many environmental and resources analysis. Therefore, the intent of this study is to investigate the differences of digital topographical map in geographical information system (GIS) with reference to elevation and slope compared to actual ground survey data.

2. Methodology

2.1 Quantifying of DEM accuracy

The topographical map was acquired from the Department of Survey and Mapping Malaysia. The map is scaled 1: 50000, based on aerial photograph/photogrammetric restitution (Figure 1). The selected test site is at the northeast Jerantut region in Pahang State, Peninsular Malaysia. The topographical isolines contours are 20 m intervals and were digitised into GIS. The contour lines were assigned an attribute value according to their height in meters above sea level. The resulting dataset was then used to produce a DEM using Arc View software with the 3D extension analyst. Height value were added to the existing contour line used previously in generating the DEM. Adding the height information to the contour lines was the most time consuming stage of the process to generate a DEM.

The methodology to quantify DEM accuracy is the Root Mean Square Error (RMSE). It measures the dispersion of the frequency distribution of deviations between the known or measured elevation and the interpolated elevation (DEM surface). Based on the study by Gao (1997), the accuracy of a raster DEM is related to the contour density and the DEM resolution was derived as follows:

$$\text{DEM accuracy [RMSE (m)]} = \frac{(7.274 + 1.666 S) D}{1000 + \varepsilon}$$

where, S stand for resolution in meters; D stands for contour density expressed as km km^{-2} ; ε is an error term related to D. Contour density was calculated by dividing the total length of contour by the size of the study area. The accuracy of terrain representation was evaluated against root-mean-square-error (RMSE) of elevation residual at 50 selected check points, mathematically expressed as:

$$\text{RMSE} = \sqrt{\frac{1}{n} \sum_{i=1}^n (Z_i - z_i)^2}$$

where n is number of check points; z_i stands for the interpolated elevation; Z_i is the elevation read directly from measured elevation at the same position. In particular, the RMSE for the study area was based on the 10 DEM resolutions and 20 m contour interval (m). The contour density in this area is 25.82 km km^{-2} , thus the RMSE of the DEM creation for the study area is 0.62.

2.2 Validation of the slope and elevation

Ground surfaces potentially have an infinite number of points that can be measured. However, it is impossible to record every point; consequently a sampling method must be used to extract representative points to build an elevation model that approximates the actual surface. The choice of data collection strategy and techniques is critical for the quality of the results. Field data should represent adequate information in the modelling. Since field data tend to be very important, the survey of terrain surface characteristics is adapted to provide accurate information about the slope and elevation. However, as this particular collection technique is relatively time consuming, the limited small sampling area is used as a representation of a whole study area.

Slope and elevation samples were collected from two different approaches, (i) On road tracking using GPS and (ii) Off road sampling. On selected site, a five linear transect was designed in the forest with the distance interval of 50 m for each transect. In the second method by GPS tracking, two existing forest roads were taken as a sample track. To test the "fitness" of the two data sets in representing the ground surface a regression analysis was performed. A linear regression technique was used to regress both ground slope and elevation data against the corresponding slope and elevation and from the contour spatial map. Correlation and regression analyses will be performed in order to correlate the "fitness" of slope and elevation obtained from digital elevation model and field data for the entire test site. Measured and estimated data values were considered as x and y data points respectively. If there was 1:1 correspondence between x and y values, the regression coefficient and the intercept of regression line in y-axis would have the following equation:

$$y = a + bx$$

where,

y = estimated data (from map)

x = measured data in field

A test of significance can be made by comparing the ideal data of $a = 0.0$ and $b = 1.0$ with the best-fit and chosen significance limit values of a and b from the fitted linear regression. The letter r is the correlation coefficient that when it approaches value 1.0, it gives an indication of close association between two data points. A total of 108 sample measurements were collected for calibration and validation. The calibration data set was used to establish the coefficient in the regression equation. The predictive ability of the calibration equation was assessed using the coefficient of multiple determinations (r^2).

2.3 On road tracking using GPS

The GPS was placed on the vehicle while the tracking was carried out. On the road where a slope break or 'breakline' is observed (breaklines are lines in the topography where grade changes exist, such as tops and toes of slopes), measurements were taken to estimate the 'original' of the slope and elevation due to cut and fill work during the road construction. Figure 2 illustrated the example of road cross section, cut and fill and slope breakline profile, while Figure 3 illustrated the sample track.

Geo Explorer 3 is functioning as rover was used to collect road data. The data base was created by Data Dictionary Editor was opened in Geo Explorer 3. After all data were collected, the data was first transferred into a computer. Several pieces of equipment were required such as cable from GeoExplorer 3 to desktop PC and platform to hold the GPS. The transferred data were then opened and displayed in the Pathfinder Office software. This software provides a step-by-step guide to the data transferred. The data has been saved as a Pathfinder Office format (*.ssf) format. The differential correction was implemented to correct the data. The correction was performed using the base reading, which was obtained from the reference map. The coordinated system was set up and the value of latitude and longitude were recorded. The extension of a base format created in .dat. format. The procedure to transfer the data from GPS into computer was the same as transferring the field data into computer. The final file of the road maps was converted to the .shp format to allow this data to be displayed in the Arc View GIS.

2.4 Off-road sampling

Line transect sampling describes a class of methods and estimations which have been developed (and mostly applied) in environmental surveys to estimate population size. The best known line transect method is known as distance sampling. The methods are specifically intended to deal with the problem of undercount or incomplete detection, which is widespread in environmental surveys but also occurs in other surveys. The method used for this survey is the line-transect sampling method: Five lines transect 600 m long, carried out in a deep forest and the elevation and slope measured within a constant interval of 60 meter. The point sample of slope, elevation and distance were recorded at every interval. Layout of the slope and elevation sampling is shown in Figure 4. Altogether were five transects or 3000 meters.

3. Results and discussions

3.1 Evaluation of DEM and slope

Most of the elevation data in this region of study range from 400 m to 800 m. There is very little high area that is more than 900 meters. In fact, a DEM model that generated at the 20-meter contour interval revealed that a ground surface from this contour interval is suitable for road planning purposes. Evaluation of elevation and slope was made by the regression analysis of acquired data from field and GIS spatial maps. The good result and success of the evaluation depended upon the size, location of sample collected and consistency in data recorded by enumerators. From the data collected for off road and on road sampling, the coefficients of determination for regression analysis are presented in the next section.

3.2 Evaluation on off-road sampling.

The graphs show that r^2 for slope and elevation range from 0.5047 to 0.9871(slope) and 0.0327 to 0.9816(elevation). From the total of the samples (Transect 1-5) in Figure 5, it reveals that elevation and slope data that are created in the GIS as a spatial map are more accurate compared to slope maps, whereas r^2 of elevation is 0.9547 and slope is only 0.6813. Therefore, it is important to note that the final results of spatial map produced have their limitations or random errors. Random error can result from mistakes such as inaccurate validation survey or improper recording of slope and elevation data will remain.

3.3 Evaluation of on road tracking by GPS

Slope and elevation measurements which were taken from existing forest roads with the aid of GPS revealed improvement in the regression analysis (Figure 6). The r^2 for slope data were 0.6296 and 0.8486, while r^2 for elevation data was 0.997 and 0.9889, respectively. Meanwhile, the regression analysis of all data (Road 1 and 2) revealed a higher result of r^2 with 0.7462(slope) and 0.9928 (elevation). The result of linear regression showed that the elevation and slope created in the GIS from topographical map and data recorded from the field from off-road and on road were correlated with the topographical map.

Figure 7a and Figure 7b presents a plot of this regression analysis from ground data and estimated data from the spatial map of both methods. This graph representing regression analysis shows the relationship between slope and elevation in the ground as represented on the X-axis, and slope and elevation that derives from spatial information map in GIS on the Y-axis. Over 220 sample locations were used and measured in the analysis that contained the length of 9139 m. The coefficient of determination for all collected data from both methods in this analysis is 0.7207(slope) and 0.9889(elevation), significant at the .05 levels. This result implies that approximately 72% of the appraisal data of the slope and 98% of the elevation data were attribute to variations on the ground surfaces and spatial data that are present in spatial information.

The scattergram showed that most of the slope measurements were distributed and far away from the regression line. Those patterns are probably due to the error of data collection by different enumerators and also a different shoot of slope target during the field survey. It can be stated that the regression is only efficient if the coefficient of determination is high, which suggests that small errors occurred during the data collection and the regression relationship must be linear with the equation slope around one.

4. Conclusions

This paper addressed the DEM accuracy and differences of digital topographical map derived from GIS with actual ground data with emphasised on elevation and slope parameters. As a result, the contour density in this area is 25.82km km^{-2} , thus the RMSE of the DEM accuracy creation for the test site is 0.62. Greater difference are exist in slope than elevation but less or similar in the flat surface. The differences of both methods are less than 30 % for slope ($r^2 = 0.72$); and less than 5 % for elevation ($r^2 = 0.98$). The great differences on slope were due to error of data collection by different enumerators and also inconsistent reading of slope measurement and target during field survey. It can be stated that the regression is only efficient if the coefficient of determination is high, which suggests that small errors occurred during the data collection. It is recommended that, future studies should be carried out using difference sampling design and statistical approaches. Comparison studies on difference map scale (e.g. 1:10000, 1:20000 and 1:50000) are also recommended in order to reveal the uncertainty and its effect on topographical parameters.

5. Acknowledgements

This work was carried out under collaboration project between Faculty of Forestry University Putra Malaysia (UPM) and Pahang State Forestry Department. This research article is a part of the Ph.D thesis completed in the Cranfield University, Silsoe at the United Kingdom. To Dr. Graham Thomas and Mr. Tim Brewer at Cranfield University thank for giving an invaluable discussion in this work. The authors are also grateful for the comments provided by the referees that helped to enhance this article. Above all, I wish to thank all Forest Rangers and Foresters who are involves in this work, especially during field work in the forest.

References

- Blakemore M. (1985). High or low resolution? conflicts of accuracy, cost, quality and application in computer mapping. *Computers & Geosciences*, 11. 345-348.
- Gao J. (1997). Resolution and accuracy of terrain representation by grid DEM at a microscale. *International Journal of Geographic Information Systems*, 11. 199-212.
- Helen C. (2003). The certainty of uncertainty: GIS and the limits of geographic knowledge. *Transaction GIS*, 7. 165-175.

- Kardoulas N G Bird A C and Lowan A L. (1996). Geometric correction of Spot and Landsat imagery: A comparison of map and GPS derived control points. *Photogrammetry Engineering & Remote Sensing*, 62. 1173-77.
- Qiming Z Xuejun L and Yizhong S. (2006). Terrain complexity and uncertainties in grid-based digital terrain analysis. *International Journal of GIS*, 20. 1137-1147.
- Ryder W and Voyadgis D. (1996). Measuring the performance of algorithms for generating ground slope *Proceeding at the 2nd International Symposium on Spatial Accuracy Assessment in Natural Resources and Environmental Sciences*, 21-23, May, 1996. Fort Collins Colorado U S A pp 208-216.
- Skidmore A. (1989). A comparison of technique for calculating gradient and aspect from a gridded digital elevation model. *International Journal of GIS*, 3. 323-334.
- Stoms D M Davis F W and Cogan C B, (1992). Sensitivity of wildlife habitat models to uncertainties in GIS data. *Photogrammetric Engineering & Remote Sensing*, 58. 843-850.
- Suzanne P W and Chales N K. (2006). Quantifying DEM uncertainty and its effect on topographic parameter. *Photogrammetric Engineering & Remote Sensing*, 72. 1081-1090.
- Thomas G Cristophe S and Taylor J C. (2000). Mapping systems and GIS: A case study using the Ghana national grid. *The Geographical Journal*, 166. 306-311.

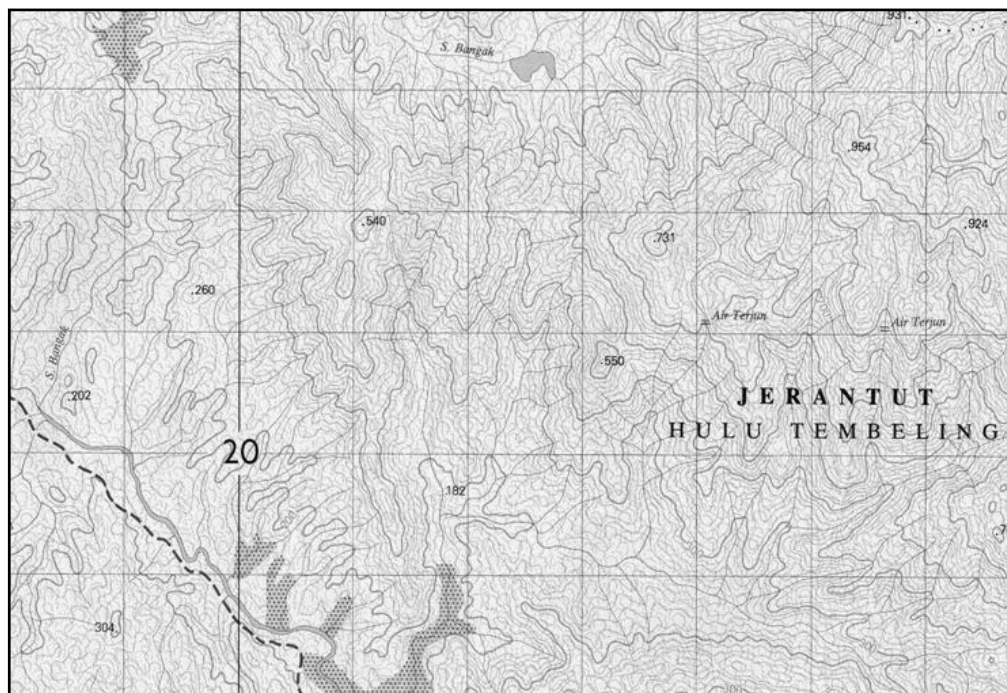


Figure 1. A 1:50000 scale topographical map of the study area

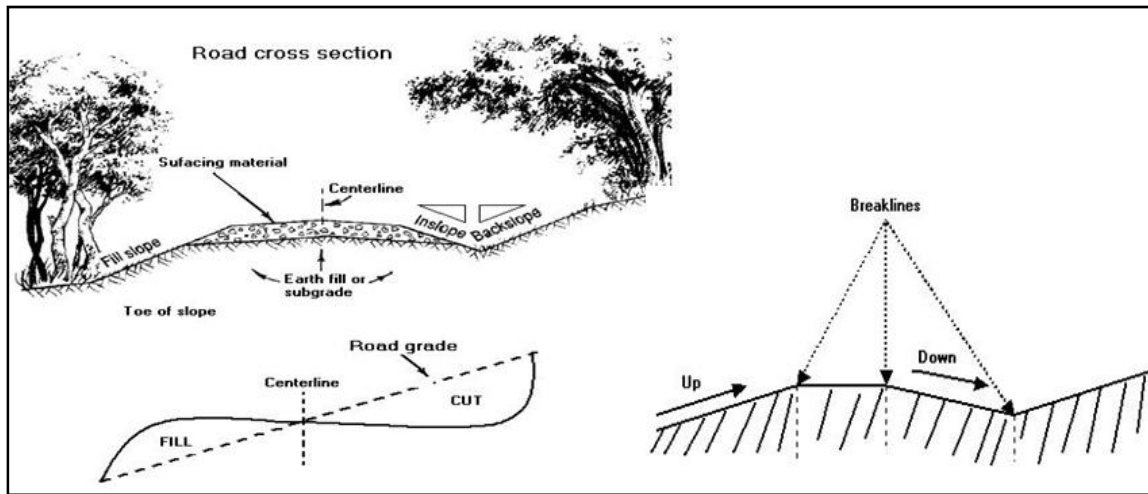


Figure 2. Illustration of road cross section, cut and fill and slope breakline profile.

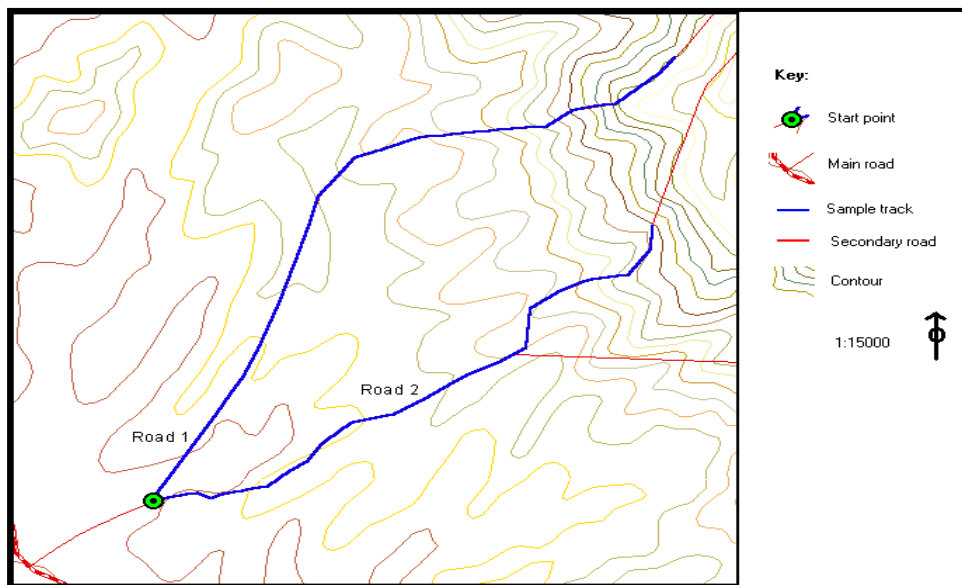


Figure 3. The selected sample tracks in the study area

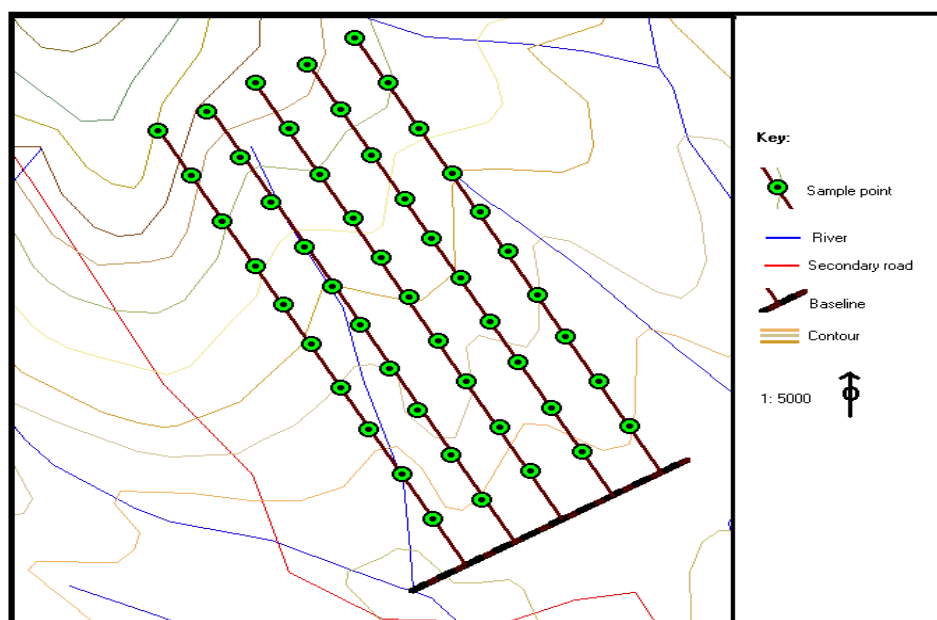


Figure 4. Layout sampling site for off road survey (elevation and slope)

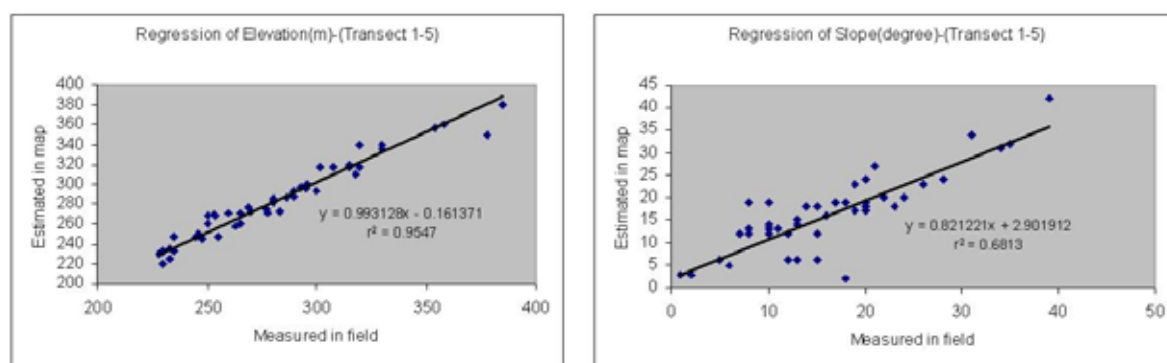


Figure 5. Relationship of measured and estimated elevation and slope from all transect data.

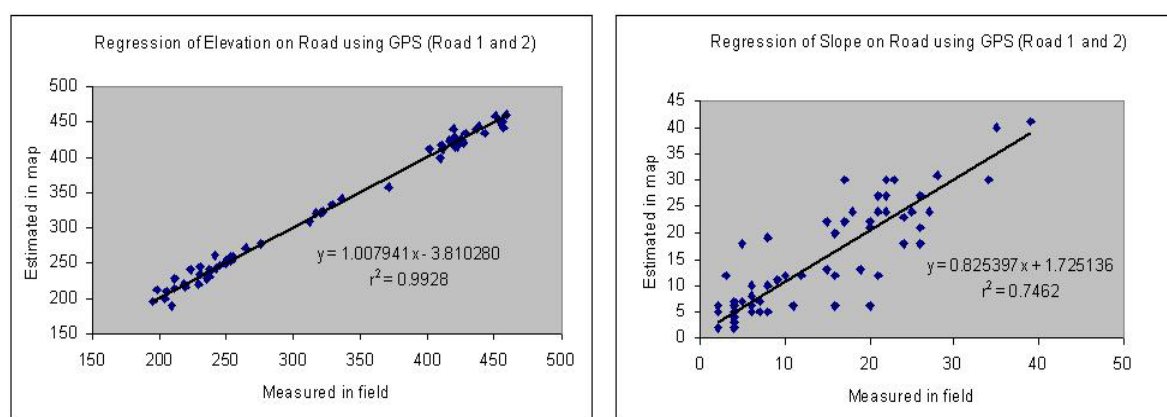


Figure 6. Relationship of measured and estimated elevation and slope from all sampling data.

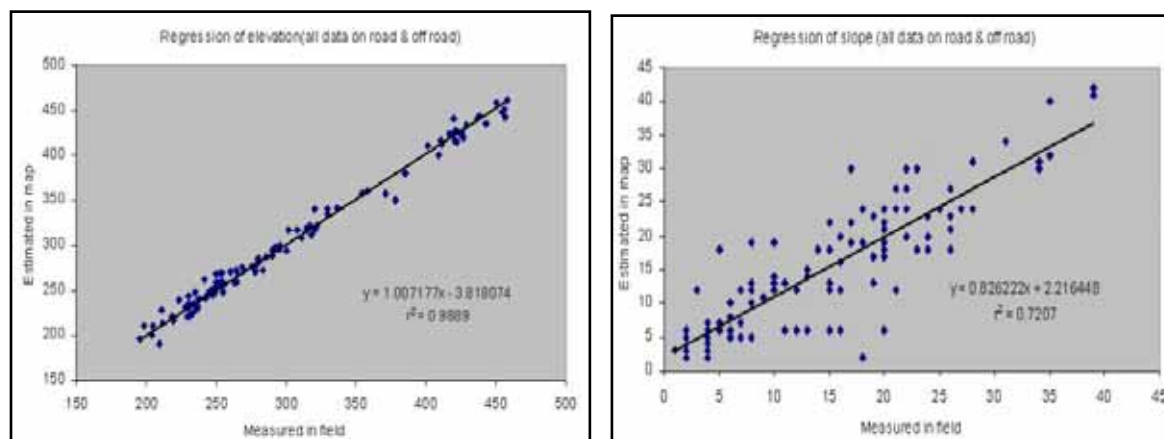


Figure 7. A regression plot derived from the slope analysis of both methods.



Application of Nano-ZnO on Antistatic Finishing to the Polyester Fabric

Fan Zhang & Junling Yang

School of Material Science and Chemical Engineer

Tianjin Polytechnic University

Tianjin 300160, China

Abstract

Settlement experiment was employed to estimate the dispersion of nano-ZnO in aqueous solution, which was surface modified with different surfactants, through the deposition time. And suitable surfactant was selected to improve the dispersion effect. Antistatic finishing agent, which was compounded with nano-ZnO, was applied to polyester fabric by pad-dry-cure process and the optimal processing conditions were obtained by orthogonal test: the concentration of finishing agent was 1.0%, soaking time was 5 min, curing temperature and time were 180°C and 3 min respectively. By the static test, the results showed that the antistatic property of the treated fabric was better.

Keywords: Nano-ZnO, Surfactants, Polyester fabric, Antistatic finishing, Orthogonal test

1. Introduction

Zinc oxide powders are materials for a wide range of applications, because it possesses unique photocatalytic, electrical, optical and antibacterial properties and is a biofriendly absorber (Chen, 2006, p.434; Alessio, 2007). In recent years, nano-ZnO, which shows special physical and chemical properties to bulk particles, becomes a new solid material (Alessio, 2007; Chen, 2006, p.434; Zhu, 2007). ZnO nanoparticles are prepared by different synthesis approaches, including hydrothermal, mechanochemical, sonochemical, chemical precipitation, sol-gel, spray-pyrolysis, microemulsion, solution combustion, solid state reaction and laser induced chemical methods (Chen, 2006, p.434; Wang, 2006, p.40). But direct precipitation method is widely used, owing to the advantages of easy operation, low require to the equipment, high purity product and lower cost (Liao, 2003, p.22). Currently, the application of nanotechnology in the textile industry has increased rapidly. The fabrics are treated with the nanoparticles as finishing agent, that result in textile materials producing different performances (Alessio, 2007). In this paper, the surface treatments of nano-ZnO were carried out with different surfactants to improve the dispersion of nano-ZnO in aqueous solution and prepare antistatic finishing agent. In order to evaluate the antistatic performance of the treated textiles, then nanometer antistatic finishing agent, which was prepared with nano-ZnO, was applied to polyester fabric (Alessio, 2007).

2. Experimental

2.1 Materials

Nano-ZnO was prepared according to the literature (Liao, 2003, pp.22-23). Surfactants and 106 binder were obtained from market and were used without any further purification. The mass per unit surface was 150 g/m² for white polyester fabric, which was used as received (Alessio, 2007).

2.2 Method

2.2.1 The choice of surfactants (Cui, 2001)

Different amount of cationic surfactant A, anionic surfactant B, nonionic surfactant C and amphoteric surfactant D were added into the aqueous of nano-ZnO, respectively. With the ultrasonic vibration, the solution was dispersed uniformly, which was placed at colorimetric tube and kept to observe the deposition time of nano-ZnO in aqueous solution.

2.2.2 The preparation of nanometer antistatic finishing agent

A certain amount of nano-ZnO, surfactant and binder were added into distilled water, and then the mixture was mixed well under stirring, that was the nanometer antistatic finishing agent with a certain concentration (Li, 2006, p.265).

2.2.3 Fabric treatments

Two dipping and rolling → drying (80°C, 1 min) → curing.

2.2.4 The Orthogonal design

The polyester fabric was finished with antistatic finishing agent, which was compounded with nano-ZnO, its main

factors: solution concentration, soaking time, curing temperature and time. The four factors four levels orthogonal test table L16 (45) was adopted to obtain the optimal finishing process. The factor levels of orthogonal test are shown in table 1 (Zhang, 2006, p.15).

2.3 Measurements

2.3.1 TEM of nano-ZnO

The morphology and size of the ZnO products were characterized by a Hitachi Model H-7650 transmission electron microscope (TEM) (Tang, 2006, p.548).

2.3.2 The fabric static test

The charge density of the untreated and treated fabric was measured according to a standard method (Professional Standards of the People's Republic of China ZB W 04008-89) (Alessio, 2007).

2.3.3 The fabric whiteness test

The whiteness of the untreated and treated fabric was performed by a WSD—3U fluorescent whiteness meter.

3. Results and discussion

3.1 TEM analysis of nano-ZnO

Small dimension, large surface area and high surface energy of nano-ZnO result in agglomeration, especially when the synthesis is carried out in an aqueous medium (Luo, 2003, p.27; Alessio, 2007). Therefore, in order to improve the dispersion of nano-ZnO in aqueous solution, the reaction conditions of nano-ZnO preparation were discussed and the optimal reaction conditions were obtained. TEM image of the nano-ZnO that was prepared with the optimal reaction conditions is shown in Fig. 5. Nanoparticles with good dispersion were nearly spherical and their diameters were between 20 and 40 nm.

3.2 The impact of different surfactants on the dispersion of nano-ZnO in aqueous solution

Nanoparticles easy to agglomeration, that due to their properties of small dimension, large specific surface area, and high surface activity (Luo, 2003, p.27). Surfactants added into aqueous solution will decrease contact angle of solid particles that are dispersed in aqueous solution, be beneficial to the particle swarm fragmentation and increase the energy barrier of particles to prevent reagglomeration of the dispersed particles (Xia, 1997, p.107). Particle's settling velocity in dispersion medium is related to size and quality of the particle. The larger the particle, the higher settling velocity it is (Ni, 2006). Therefore, the changes of aggregation degree, the dispersion state and the aggregation of the modified nano-ZnO in aqueous solution were qualitatively detected through the deposition time. The results show that the deposition time is longer, the dispersion is better and the agglomeration among particles is harder (Cui, 2001, p.99).

(1) The deposition time of aqueous solution containing nano-ZnO is 10 days by adding cationic surfactant A, but which will not be applied to practical application because the results are unstable.

(2) With the increase of addition amount of the anionic surfactant B, the deposition time of nano-ZnO in aqueous solution present a trend of first increase then decrease, which is shown in Fig. 2. When its adding amount is 40 drops, the dispersion of nano-ZnO in aqueous solution is significantly improved that the deposition time is 218 h.

(3) The deposition time of 18 h means the stability of nano-ZnO in aqueous solution is not improved obviously when the nonionic surfactant C is added.

(4) With the increasing of amphoteric surfactant D added into aqueous solution containing nano-ZnO, nano-ZnO can be completely dissolved that result in forming thermodynamic stable and isotropic transparent solution, which owns stable character even placed for long time.

By comparing the effects of the four kinds of surfactants on the dispersion of nano-ZnO in aqueous solution, the choice was amphoteric surfactant D. This is because the micellar solubilization of amphoteric surfactant D on the nano-ZnO in aqueous solution (Xia, 1997, p.109) is convenient for the application of nanometer antistatic finishing agent in fabric finishing.

3.3 The orthogonal test results of functional finishing of the fabric

3.3.1 Fabric antistatic property

The charge density of the fabrics, which are finished according to the factors and levels of orthogonal test, are shown in table 2.

Orthogonal test analysis shows that the greater the range, the greater the impact of the factor on the experimental index (Zhang, 2006, p.15). The concentration of finishing agent has the most influential effect on the charge density, other ranked as follows: Soaking time, baking temperature and baking time, which are shown in table 2. The comparison among the average of various level index reflects influence effect of the level on the index, that means the k_n is smaller,

the level is better (Zhang, 2006, p.15). When the concentration of finishing agent is 0.5%, the charge density of the treated fabric is smaller based on the comparison of K_n^A . However, in this case, a caking phenomenon of the binder is occurred in the finishing agent, that has an adverse effect on practical application. Considering the K_n and application, the optimal finishing process was obtained: the concentration of finishing agent 1.0%, soaking time 5 min, baking temperature 180 °C and baking time 3 min.

3.3.2 The fabric whiteness

As can be seen from table 3, the hunter whiteness of the treated fabric with different treatment is slightly increased in comparison with the original piece, but the change is not obvious. This is because the properties of the surfactant and adhesion agent in finishing agent have no change via pad-dry-cure process, and the transparent and compact film, which doesn't generate virtual effect on the optical properties of the fabric, is formed on the surface of the fabric (Xu, 2005, p.68).

4. Conclusions

To nano-ZnO, amphoteric surfactant D owing micelle solubilization as dispersing agent is used to prepare nanometer antistatic finishing agent. And the best processing conditions of polyester fabric treated with the finishing agent that are the concentration of finishing agent 1.0%, soaking time 5 min, curing temperature 180°C and curing time 3 min are obtained by orthogonal test.

References

- Alessio, B., Maximilian, D., Pierandrea, L. N., & Piero, B. (2007). Synthesis and characterization of zinc oxide nanoparticles: application to textiles as UV-absorbers. *J Nanopart Res.*
- Chen, W. F., Li, F. S., Yu, J. Y., & Li, Y. X. (2006). Novel salt-assisted combustion synthesis of high surface area ceria nanopowders by an ethylene glycol-nitrate combustion process. *Journal of Rare Earths*, 24, 434-439.
- Cui, A. L., Wang, T. J., He, H., & Jin, Y. (2001). Dispersion behavior of ultrafine titanium dioxide particles in aqueous solution. *The Chinese Journal of Process Engineering*, 99-101.
- Liao, L. L., Liu, J. P., & Xu, D. Y. (2003). Studies on synthesis and effects on smoke suppression of nano-oxides. *Chinese Journal of Colloid & polymer*, 22-24.
- Li, Y. H., Lin, H. M., Yu, Z. C., & Chen, W. G. (2006). Study on the application of nano-scaled antistatic finishing agent to the PET ornamental Fabric. *Journal of Zhejiang Sci-Tech University*, 264-267.
- Luo, Y. X., Wang, X., Lu, L. D., Yang, X. J., & Liu, X. H. (2003). Progress of preparation and applications of nanocrystalline CuO. *Shanghai Chemical Industry*, 24-28.
- Ni, X. Y., Shen, J., & Zhang, Z. H. (2006). *The physicochemical properties and application of nano-materials*. Beijing: Chemical Industry Press.
- Tang, X. L., Ren, L., Sun, L. N., Tian, W. G., Cao, M. H., & Hu, C. W. (2006). A solvothermal route to Cu_2O nanocubes and Cu nanoparticles. *Chem. Res. Chinese U.*, 22(5), 547-551.
- Wang, Z. X., Zheng, D. M., Li, J. M., Fan, M., Liu, M., & Zhuang, Y. K. (2006). Study on producing of nanometer ZnO by direct precipitation method. *Inorganic Chemicals Industry*, 40-42.
- Xu, P., Wang, W., & Chen, S. L. (2005). Application of nanosol on the antistatic property of polyester. *Melliand China*, 66-68,70.
- Xia, J. D., & Ni, Y. Q. (1997). *Chemistry and Technology of surfactants and detergents*. Beijing: China Light Industry Press.
- Zhu, X. B., Yang, D., Chang, X. J., Cui, Y. M., Hu, Z., & Zou, X. J. (2007). Selective solid-phase extraction of trace Fe(III) from biological and natural water samples using nanometer SiO_2 modified with acetylsalicylic acid. *Microchimica Acta*.
- Zhang, W., Wang, B. H., Zhang, W. B., & Fan, F. R. (2006). Experiment study on preparing magnesia nanopowder by homogeneous precipitation method. *Henan Chemical Industry*, 14-16.

Table 1. The factor levels of orthogonal test

Levels	Concentration of nano-ZnO (A)	Soaking time (B) /min	Curing temperature (C) /°C	Curing time (D) /min
1	0.5%	5	120	0.5
2	1.0%	15	140	1.5
3	1.5%	30	160	3
4	3.0%	40	180	4

Table 2. Orthogonal test table and analytical results of charge density

Factors	A	B	C	D	Charge density $\times 10^{-8}/\text{C}\cdot\text{m}^{-2}$
1	1	1	1	1	5.2
2	1	2	2	2	3.5
3	1	3	3	3	9.5
4	1	4	4	4	15
5	2	1	2	3	38
6	2	2	1	4	41
7	2	3	4	1	50
8	2	4	3	2	22
9	3	1	3	4	77
10	3	2	4	3	61
11	3	3	1	2	160
12	3	4	2	1	130
13	4	1	4	2	170
14	4	2	3	1	280
15	4	3	2	4	250
16	4	4	1	3	230
k1	8.3	72.6	109.1	116.3	
k2	37.8	96.4	105.4	88.9	
k3	107	117.4	97.1	84.6	
k4	232.5	99.3	74	95.8	
R	224.2	44.8	35.1	31.7	

Table 3. Hunter whiteness of the different samples and their relative change percentage

Samples	Hunter whiteness /Wh	Relative change percentage
1	85.45	1.05%
2	86.05	1.76%
3	87.25	3.18%
4	86.97	2.85%
5	86.04	1.75%
6	85.32	0.90%
7	86.87	2.73%
8	86.84	2.70%
9	86.25	2.00%
10	88.71	4.91%
11	84.77	0.25%
12	84.75	0.22%
13	88.65	4.84%
14	86.09	1.81%
15	85.83	1.50%
16	86.06	1.77%
Original piece	84.56	

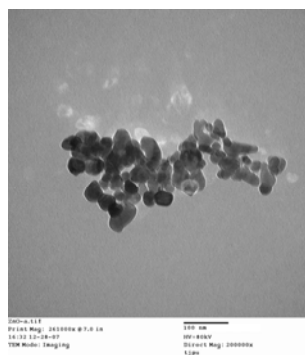


Figure 1. TEM photograph of nano-ZnO

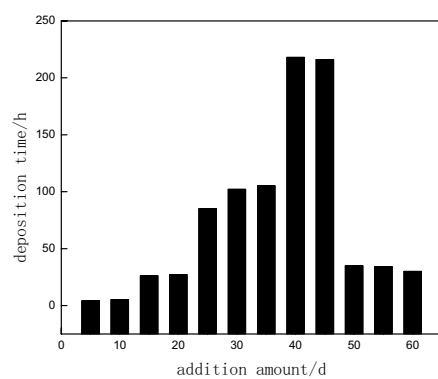


Figure 2. Effect of addition amount of the anionic surfactant B on nano-ZnO deposition time



A Proposed Technique for Analyzing Experiments Of Type $2^p 3^m$

Abbas F. M. Alkarkhi (Corresponding author)

Environmental Technology Division

School of Industrial Technology

Universiti Sains Malaysia

11800 Penang, Malaysia

Tel.: 60-4-653-2107 E-mail: alkarkhi@yahoo.com

H. C. Low

School of Mathematical Sciences

Universiti Sains Malaysia

11800 Penang, Malaysia

Tel: 60-4-653-3641 E-mail: hclow@cs.usm.my

Abstract

This paper deals with the experiments of type $2^p 3^m$. Fitting a response surface model to this type of experiments was studied using a new technique. This technique depends on partitioning the whole experiment into two experiments and analyzes each experiment separately. In addition to the proposed technique, the least squares method was studied and a comparison is made between the proposed technique and the least squares method. The results showed that the proposed technique and least squares method gave the same results. This indicates that partitioning the whole experiment does not affect the results of fitting the response surface model. This paper proposes an easy technique for analyzing this type of experiments. The results showed that the new technique is easier to use than the least squares method. Simple calculations and substitutions in fixed formulae are used to get the results directly. On the contrary, the least squares method requires complicated calculations to get the results.

Keywords: Response surface, Contrast, Least squares method

1. Introduction

Experiments are performed by investigators in virtually all fields of inquiry, usually to discover something about a particular process or system. Factorial designs are widely used in experiments involving several factors where it is necessary to study the joint effects of the factors on the response.

Experiments of type $2^p 3^m$ have been used in many disciplines, especially in industry where there are several factors; some of the factors are at two levels, and others at three levels. This type of experiment consists of $p + m$ factors, where p factors have two levels, and m factor have three levels (Montgomery, 2002). Margolin (1967) proposed a new procedure for analyzing this type of experiments $2^p 3^m$, how to calculate the effects, sum of squares and fitting a response surface model. The technique is based on the two procedures presented by Yates (1964) for two and three levels. In this paper, the factors are denoted by capital letters A, B, ..., and the levels are denoted by -1 if the factor is at the low level and 1 if the factor is at the high level in the case of two levels, and for factors with three levels -1 if the factor is at the low level, 0 if the factor is at the intermediate level, and 1 if the factor is at the high level. The objective of this study is to provide an alternative technique for fitting a response surface model to the experiments of type $2^p 3^m$.

2. Fitting a response surface model to an experiment of type $2^p 3^m$

Consider the following response surface model for an experiment of type $2^p 3^m$

$$Y = \beta_0 + \sum_{j=1}^p \beta_j X_j + \sum_{l=1}^m \gamma_l Z_l + \sum_{l=1}^m \gamma_{ll} Z_{ll}^2 + \sum_{j < i} X_i X_j + \sum_{l < q} \gamma_{lq} Z_l Z_q + \sum_{j=1}^p \sum_{l=1}^m \delta_{jl} X_j Z_l$$

where

X_j represents factors with two levels, and Z_l represents factors with three levels.

The technique of least squares is used to estimate the parameters of the model. In this technique, we minimize the sum of the squared differences of the actual Y values and the values of Y predicted by the regression equation. The computation can be complicated and difficult if the number of factors included in the model is large.

2.1 The proposed technique

The proposed technique depends on partitioning the whole experiment $2^p 3^m$ into two experiments. To fit a response surface model to this type of experiment, the following steps are used:

(1) The first step is to partition the experiment ($2^p 3^m$) into two experiments according to the number of levels, one experiment with factors at three levels 3^m and the other with factors at two levels 2^p .

(2) Analyze each experiment separately:

For two levels, the procedure given by Abbas et al., (2000) is used as follows:

$$b_j = \frac{\text{Contrast for } A_j}{4n}, \quad b_{ji} = \frac{\text{Contrast for } A_j A_i}{4n}, \quad j < i$$

And for three levels, the procedure given by Abbas et al., (2001) is used as follows:

$$\gamma_l = \frac{\text{Linear contrast for } A_l}{2n}, \quad \gamma_{ll} = \frac{\text{Quadratic contrast for } A_l}{2n}$$

$$\gamma_{lq} = \frac{\text{Linear contrast for } A_l A_q}{4n}, \quad l < q$$

(3) For this step, $C_1^p C_1^m$ experiments of the form $2^1 3^1$ are constructed to find the interaction between factors that have three levels and factors that have two levels.

To fit a response surface model to the experimental results, the formulae in step 2 are used, and for the joint coefficients, the following formula shall be used:

$$\delta_{jl} = \frac{CL}{2(n_1 + n_2)} = \frac{CL}{4n}, \quad (n_1 = n_2 = n), \quad j = 1, 2, \dots, p, \quad l = 1, 2, \dots, m$$

where

δ_{il} represents the regression coefficient for factor l which has three levels and factor q which has two levels,

n_1 represents the number of replicates at the low level for the factor at two levels,

n_2 represents the number of replicates at the high level for the factor at two levels, and

(4) represents the distance between the high and low levels of the three level factor.

Also,

$$CL = d_{+1} - d_{-1}, \text{ where}$$

d_{+1} represents the joint contrast between the factor at three levels and the high level for the factor at two levels, and

d_{-1} represents the joint contrast between the factor at three levels and the low level for the factor at two levels.

Furthermore, the joint coefficient can be found by using the following formula:

$$\delta_{jl} = \frac{CL}{n \sum C_{jl}^2} = \frac{CL}{4n}, \quad l = 1, 2, \dots, p, \quad l = 1, 2, \dots, m$$

where

$\sum C_{jl}^2$ represents the sum of squares of the joint contrast coefficients,

and CL represents the linear contrast, and

n represents the number of replicates

(5) To find the sum of squares, the following formula is used:

$$\text{S.S.} = \frac{CL^2}{2(n_1 + n_2)} = \frac{CL^2}{4n}, \quad (n_1 = n_2 = n)$$

2.2 Proof for the $2^p 3^m$ experiments

Consider the following model:

$$Y = \beta_0 + \sum_{j=1}^p \beta_j X_j + \sum_{l=1}^m \gamma_l Z_l + \sum_{l=1}^m \gamma_{ll} Z_l^2 + \sum_{j < i} X_i X_j + \sum_{l < q} \gamma_{lq} Z_l Z_q + \sum_{j=1}^p \sum_{l=1}^m \delta_{jl} X_j Z_l \quad (1)$$

subjected to the following constraints:

2.2.1 For the factors at two levels:

$$\sum_{i=1}^k X_i = 0, \quad \sum_{i < j} X_i X_j = 0, \quad \sum_{i < j} X_i^2 X_j = 0, \quad \sum_{i < j} X_i X_j^2 = 0$$

$$\sum_{i=1}^k X_i^2 = k, \quad \sum_{i < j} (X_i X_j)^2 = k \quad (2)$$

These constraints come from factor levels related to the factors having two levels.

2.2.2 For factors at three levels

$$\sum_{i=1}^k Z_i = 0, \quad \sum_{i < j} Z_i Z_j = 0, \quad \sum_{i < j} Z_i Z_j^2 = 0, \quad \sum_{i=1}^k Z_i^4 = \sum_{i=1}^k Z_i^2 = 2 \times 3^{m-1},$$

$$\sum_{i < j} (Z_i Z_j)^2 = \sum_{i < j} (Z_i Z_j)^2 = 4 \times 3^{m-2}, \quad (3)$$

These constraints come from factor levels related to the factors having three levels.

2.2.3 Constraints related with mixed factors, some factors have two levels and others have three levels

$$\sum_{i=1}^k (Z_i X_i)^2 = 4 \times (3^{m-1} \times 2^{p-1}), \quad \sum_{i=1}^k X_i Z_i = \sum_{i=1}^k X_i^2 Z_i = \sum_{i=1}^k X_i Z_i^2 = 0,$$

$$\sum_{i < j < w} X_i X_j Z_w = \sum_{i < j < w} Z_i Z_j X_w = 0. \quad (4)$$

These constraints come from the mixed factors.

To illustrate the procedure, consider a $2^2 3^2$ experiment.

Suppose there are four factors: Z_1, Z_2 at three levels and X_1, X_2 at two levels (Table 1). The model for this experiment is:

$$Y = b_0 + b_1 X_1 + b_2 X_2 + b_{12} X_1 X_2 + \gamma_1 Z_1 + \gamma_2 Z_2 + \gamma_{11} Z_1^2 + \gamma_{22} Z_2^2 + \gamma_{12} Z_1 Z_2 + \delta_{11} Z_1 X_1 + \delta_{12} Z_1 X_2$$

$$+ \delta_{21} Z_2 X_1 + \delta_{22} Z_2 X_2 \quad (5)$$

For the linear and quadratic coefficients and the linear interaction for 3^k , we obtain the same results that we obtained previously. The same results are also obtained for 2^p .

Procedure:

(1) First, partition this experiment into two experiments as follows:

- a. Experiments where the factors have three levels.
- b. Experiments where the factors have two levels.

(2) Analyze each experiment separately as mentioned in section 2.1.

The formula for the interaction coefficient between a factor at two levels and a factor at three levels is given below:

If equation (5) is multiplied by $Z_1 X_1$, and sum over i , then

$$\sum Z_1 X_1 Y = \delta_{11} \sum (Z_1 X_1)^2$$

$$\delta_{11} = \frac{\sum Z_1 X_1 Y}{\sum (Z_1 X_1)^2}$$

Similarly, for δ_{12}, δ_{21} and δ_{22}

In general, the formula is given by:

$$\delta_{jl} = \frac{\sum Z_l X_j Y}{\sum (Z_l X_j)^2}$$

Consider the formula for δ_{11} :

$$\delta_{11} = \frac{\sum Z_1 X_1 Y}{\sum (Z_1 X_1)^2} \quad (6)$$

The denominator

$\sum (Z_1 X_1)^2 = 4 \times (3^{m-1} \times 2^{p-1}) = 4 \times (3^{2-1} \times 2^{2-1}) = 4 \times 6 = 24$, This is equal to 4×6 , where 6 represents the number of replicates at each joint level.

The numerator

$$\begin{aligned} \sum_{i=1}^{36} Z_{1i} X_{1i} Y_i &= (-1)(-1)Y_1 + (0)(1)Y_2 + (1)(1)Y_3 + \dots + (-1)(1)Y_{16} + (0)(1)Y_{17} + (1)(1)Y_{18} + \\ &\quad (-1)(1)Y_{19} + (0)(1)Y_{20} + (1)(1)Y_{21} + \dots + (-1)(1)Y + (0)(1)Y + (1)(1)Y_{36} \\ &= (Y_1 + Y_4 + Y_7 + Y_{10} + Y_{13} + Y_{16} + Y_{21} + Y_{24} + Y_{27} + Y_{30} + Y_{33} + Y_{36}) + \\ &\quad (0)(Y_2 + Y_5 + Y_8 + Y_{11} + Y_{14} + Y_{17} + Y_{20} + Y_{23} + Y_{26} + Y_{29} + Y_{32} + Y_{35}) - \\ &\quad (Y_3 + Y_6 + Y_9 + Y_{12} + Y_{15} + Y_{18} + Y_{19} + Y_{22} + Y_{25} + Y_{28} + Y_{31} + Y_{34}) \end{aligned}$$

(3) In the third step, consider experiments where one factor has three levels and the other has two levels (Table 2), and then sum the observations in the cells, which have the same joint level, before doing anything. For instance,

from Table 2, it can be seen that

$$\begin{aligned} d_{-1} &= (-1)(-1)(Y_1 + Y_{10} + Y_4 + Y_{13} + Y_7 + Y_{16}) + (0)(-1)(Y_2 + Y_{11} + Y_5 + Y_{14} + Y_8 + Y_{17}) + \\ &\quad (1)(-1)(Y_3 + Y_{12} + Y_6 + Y_{15} + Y_9 + Y_{18}) \end{aligned}$$

and

$$\begin{aligned} d_{+1} &= (-1)(1)(Y_{19} + Y_{28} + Y_{22} + Y_{31} + Y_{25} + Y_{34}) + (0)(1)(Y_{20} + Y_{29} + Y_{23} + Y_{32} + Y_{26} + Y_{35}) + \\ &\quad (1)(1)(Y_{21} + Y_{30} + Y_{24} + Y_{33} + Y_{27} + Y_{36}) \end{aligned}$$

$$\therefore CL = d_{+1} - d_{-1}$$

$$\begin{aligned} &= (Y_1 + Y_4 + Y_7 + Y_{10} + Y_{13} + Y_{16} + Y_{21} + Y_{24} + Y_{27} + Y_{30} + Y_{33} + Y_{36}) + \\ &\quad (0)(Y_2 + Y_5 + Y_8 + Y_{11} + Y_{14} + Y_{17} + Y_{20} + Y_{23} + Y_{26} + Y_{29} + Y_{32} + Y_{35}) - \end{aligned}$$

$$(Y_3 + Y_6 + Y_9 + Y_{12} + Y_{15} + Y_{18} + Y_{19} + Y_{22} + Y_{25} + Y_{28} + Y_{31} + Y_{34}) = \sum Z_1 X_1 Y$$

This is equal to the numerator of equation (6).

The joint contrast can also be found by using the contrast directly, as follows:

$$\begin{aligned} CL = & (-1)(-1)(Y_1 + Y_{10} + Y_4 + Y_{13} + Y_7 + Y_{16}) + (-1)(1)(Y_{19} + Y_{28} + Y_{22} + Y_{31} + Y_{25} + Y_{34}) + \\ & (0)(-1)(Y_2 + Y_{11} + Y_5 + Y_{14} + Y_8 + Y_{17}) + (0)(1)(Y_{20} + Y_{29} + Y_{23} + Y_{32} + Y_{26} + Y_{35}) + \\ & (1)(-1)(Y_3 + Y_{12} + Y_6 + Y_{15} + Y_9 + Y_{18}) + (1)(1)(Y_{21} + Y_{30} + Y_{24} + Y_{33} + Y_{27} + Y_{36}) = \sum Z_1 X_1 Y \end{aligned}$$

Thus,

$$\delta_{11} = \frac{\text{Linear contrast for } Z_1 X_1}{4 \times 6} = \frac{\text{Linear contrast for } Z_1 X_1}{4 \times n} \quad (\text{Here } n=6)$$

Note that 6 represent the number of replicates.

Similarly for δ_{12}, δ_{21} and δ_{22} .

In general, if we let n represent the number of replicates, the formula becomes:

$$\delta_{jl} = \frac{\text{Linear contrast for } A_j A_l}{4 \times n}, \quad j = 1, 2, \dots, p, \quad l = 1, 2, \dots, m$$

3. Application

Suppose the situation where there are three factors with two of them having two levels and the other factor having three levels (Margolin, 1967). Table 3 presents three factors: X_1 and X_2 with two levels, and Z_1 with three levels.

The least squares method and the new procedure will be used to fit a response surface model to the experiment:

3.1 The least squares method

SPSS version 11 was used to obtain the results as shown below:

$$\hat{Y} = 20 - 9X_1 + 10X_2 + 4X_1X_2 + 8X_3 + 15X_3^2 - 5X_3X_1 + 7X_3X_2$$

3.2 The proposed technique

Use the procedure explained in Section 2.1 for analyzing this experiment and then compares the results with the least squares method. The following gives the procedure step by step:

Step 1. Analysis of the 3^1 experiment (Table 3.a):

Linear contrast,

$$CL = (-1)108 + 0(80) + (1)172 = 64$$

To find the coefficient of regression, γ_1 , the following formula was used

$$\gamma_1 = \frac{CL}{2n} = \frac{64}{2(4)} = 8$$

Quadratic contrast,

$$CQ = (1)108 + (-2)80 + (1)172 = 120$$

To find the coefficient of regression, γ_{11} , The following formula was used

$$\gamma_{11} = \frac{CQ}{2n} = \frac{120}{2(4)} = 15$$

Step 2. Analysis of the 2^2 experiment (Table 3.b):

Let $X_1 = A$, $X_2 = B$, then

$$A = (a-1)(b+1) = 105 + 21 - 99 - 135 = -108$$

$$b_1 = \frac{\text{Contrast for } A}{4n} = \frac{-108}{4 \times 3} = -9$$

$$B = (a+1)(b-1) = 105 + 135 - 21 - 99 = 120$$

$$\therefore b_2 = \frac{\text{Contrast for } B}{4n} = \frac{120}{4 \times 3} = 10$$

$$AB = (a-1)(b-1) = 105 + 99 - 135 - 21 = 48$$

$$b_{12} = \frac{\text{contrast for } AB}{4n} = \frac{84}{4 \times 3} = 4$$

Step 3. Analysis of the $3^1 2^1$ experiments (Table 3.c and Table 3.d):

The contrast between the factor at three levels and the lower level for the factor at two levels was found as follows:

$$d_{-1} = (-1) 64 + (0) 54 + (1) 116 = 52$$

Next, the contrast between the factor at three levels and the higher level for the factor at two levels is given below:

$$d_{+1} = (-1)(44) + (0)26 + (1) 56 = 12$$

The linear contrast is equal to:

$$CL = d_{+1} - d_{-1} = 12 - 52 = -40$$

$$\delta_{11} = \frac{CL}{2(n_1 + n_2)} = \frac{CL}{4n} = \frac{-40}{4(2)} = -5, \quad 4n = 4 \times (3^{m-1} \times 2^{p-1}) = 4 \times (3^{1-1} \times 2^{2-1}) = 4 \times 2 = 8$$

Or by using the alternative formula:

$$\delta_{31} = \frac{CL}{n \sum C_{ij}^2} = \frac{CL}{4n}$$

$$CL = (0) (0) (64) + (0) (1) (44) + \dots + (2) (1) 56 = -40$$

$$\delta_{31} = \frac{-40}{4(2)} = -5$$

For δ_{21} ,

$$d_{-1} = -42 + 0 + 46 = 4,$$

$$d_{+1} = -66 + 0 + 126 = 60$$

$$CL = 60 - 4 = 56$$

$$\delta_{21} = \frac{CL}{4n} = \frac{56}{4(2)} = 7$$

Or by using the formula:

$$\delta_{21} = \frac{CL}{n \sum C_{ij}^2} = \frac{CL}{4n}$$

$$CL = (0) (0) (42) + \dots + (2) (1) (126) = 56$$

$$\delta_{21} = \frac{56}{4(2)} = 7$$

$$b_0 = \bar{Y} - b_{33} \bar{X}_3^2 = \frac{360}{12} - 15 \frac{8}{12} = 30 - 10 = 20$$

Comparing the results obtained by least squares and the new procedure (Table 4), it can be seen that the results obtained by the proposed technique and the least squares method are the same.

4. Conclusion

It can be concluded that the least squares method and the proposed technique gave the same values for the coefficients of the model. It may also be concluded that partitioning an experiment of type $2^p 3^m$ into two-experiment does not affect the results. The new technique is easier to use than the least squares method, as the results can be obtained directly from simple calculations and substitutions in fixed formulae. On the contrary, the least squares method requires complicated calculations to get the results.

References

- Abbas F. M. A., Low, H. C. and Quah, S. H., (2000). A New Method For Analyzing Experiment of Type 2^p . National Conference on Management Science/ Operations Research, November (2000). Malaysia. pp 123-130.
- Abbas F. M. A., Low, H. C. and Quah, S. H., (2001). A New Procedure for Fitting a Response Surface Model To Experiments of Type 3^m . International Conference on Recent Developments in Statistics and its Applications, Malaysia. pp 1-8.
- Draper N.R & smith, H., (1998). *Applied regression Analysis* 3rd edition. Wiley.
- Margolin, B. H. (1967). "Systematic Methods of Analysis 2^k Factorial Experiments with Applications." *Technometrics*, Vol. 9, pp. 245-260.
- Montgomery, D. C. (2002). *Design and Analysis of Experiments*. 5th edition, New York: John Wiley & Sons, Inc.
- Yates, F. (1964). *The design and Analysis of Factorial Experiments*. 5th edition, Harpenden, England: Publisher (Rothmasted Experimental Station). Technical Communication, No. 35 of the Commonwealth Bureau of Soils.

Table 1. A design with four factors where Z_1, Z_2 have three levels each, and X_1, X_2 have three levels each

Z_1	Z_2	X_1	-1	-1
		X_2	1	1
			-1	1
			-1	1
-1	-1		Y_1	Y_{10}
0	-1		Y_{19}	Y_{28}
1	-1		Y_2	Y_{11}
-1	0		Y_{20}	Y_{29}
0	0		Y_3	Y_{12}
1	0		Y_{21}	Y_{30}
-1	1		Y_4	Y_{13}
0	1		Y_{22}	Y_{31}
1	1		Y_5	Y_{14}
			Y_{23}	Y_{32}
			Y_6	Y_{15}
			Y_{24}	Y_{33}
			Y_7	Y_{16}
			Y_{25}	Y_{34}
			Y_8	Y_{17}
			Y_{26}	Y_{35}
			Y_9	Y_{18}
			Y_{27}	Y_{36}

Table 2. The results for factors Z_1 at three levels and X_1 at two levels

X_1	-1	1
Z_1		
-1	$Y_1+Y_{10}+Y_4+Y_{13}+Y_7+Y_{16}$	$Y_{19}+Y_{28}+Y_{22}+Y_{31}+Y_{25}+Y_{34}$
0	$Y_2+Y_{11}+Y_5+Y_{14}+Y_8+Y_{17}$	$Y_{20}+Y_{29}+Y_{23}+Y_{32}+Y_{26}+Y_{35}$
1	$Y_3+Y_{12}+Y_6+Y_{15}+Y_9+Y_{18}$	$Y_{21}+Y_{30}+Y_{24}+Y_{33}+Y_{27}+Y_{36}$

Table 3. The design matrix and results for the $2^2 3^1$ experiment

	X_1	-1	-1	1	1
Z_1	X_2	-1	1	-1	1
-1		28	36	14	30
0		27	27	5	21
1		44	72	2	54

Table 3 a. The results for factor X_3 at three levels

Z_1 Levels	Response	L	Q
-1	108	-1	1
0	80	0	-2
1	172	1	1

Table 3 b. The results for factors X_1 and X_2 , each at two levels

	X_2	-1	1
X_1			
-1		99	135
1		21	105

Table 3 c. The results for factor X_1 at two levels and factor Z_1 at three levels

	X_1	-1	1	L
Z_1				
-1		64	44	-1
0		54	26	0
1		116	56	1

Table 3 d. The results for factors X_2 at two levels and factor Z_1 at three levels

	X_2	-1	1	L
Z_1				
-1		42	66	-1
0		32	48	0
1		42	126	1

Table 4. Results for the two methods

Coefficient	Least squares	Proposed Procedure
b_0	20	20
b_1	-9	-9
b_2	10	10
b_{12}	8	8
γ_1	15	15
γ_{11}	-5	-5
δ_{11}	7	7
δ_{21}	4	4



Application Study of Xylo-oligosaccharide in Layer Production

Enku Zhou & Xiaoliang Pan

Institute of Animal Science and Technology

Shi Hezi University

Xinjiang 832003, China

Xiuzhi Tian

College of Animal Science and Technology

China Agriculture University

Beijing 100193, China

E-mail: zek7550@yahoo.com.cn

Abstract

Xylo-oligosaccharide (XO) is a kind of functional oligosaccharide, a kind of safe and health additive. Because of its unique properties, XO has been used in food, medicine and health care widely. As additives for functional foods, XO impels economy to create a great deal of nutrimental substance and presents prebiotic action. But its application in animal husbandry in China has just started. The research progress of xylo-oligosaccharide's physical-chemical properties, value and application in layer production is introduced in this article especially.

Keywords: Xylo-oligosaccharide, Layer, property, Value, Application perspective

1. Introduction

Xylo-oligosaccharides (XO) are sugar oligomers showing potential for practical applications in a variety of fields, including pharmaceuticals, feed formulation, agricultural purposes and food applications (Va'zquez, M.J. et al, 2001, 387-393). As additive for functional foods, XO present prebiotic action (Fooks, L.J. et al, 2002, 67-75), showing positive biological effects such as improvement of the intestinal function by increasing the number of healthy Bifidobacteria (Izumi, Y. et al, 2003, Patent 2003048901). Additionally, XO show an ability for suppressing the growth of Clostridium and bacteriostatic action against *Vibrio anguillarum* (Izumi, K. et al, 2001, Patent 2001226409). Commercial developments have been focused on the XO utilization as suitable components of synbiotic compositions. In 1993, Suntory company manufactured the functional food which contains xylo-oligosaccharide, bifidobacteria, mineral and tea extracts for the first time (Va'zquez, M.J. et al, 2000, 387-393).

Xylo-oligosaccharide's act as a new kind oligosaccharide additive, first throw up to market by Suntory group in Japan in 1989. Xylo-oligosaccharide largely is mixture of disaccharide and trisaccharide which are hydrolyzed from xylan. Xylan is hydrolyzed by interior contact xylanase at β -1,4 glucosidic bond.

The safe and green livestock and poultry product has become a kind consume trend, the remaining problem of harmful materials in the product has become a key factor which hold-up the development of domestic livestock breeding. The animal feed additive is one of the main reasons which cause vestigial of harmful material in livestock and poultry product, so brought about researches upsurge in nuisanceless feed additive in recent years. Xylo-oligosaccharide in the same way as a kind of neotype, high performance and nuisanceless feed additive which not only can prevent disease and antidisease but also can elevate cultivational yield and quality.

2. Characteristic of Xylo-oligosaccharide

2.1 Physicochemical property

Xylo-oligosaccharide is one of the Oligosaccharide which is combined with 2-7 xylopyranoses through β -1,4 glycosidic bond. The main composition of its product is xylopyranose, xylobiose, trisaccharide and other oligosaccharides. Xylo-oligosaccharide's acid Stability and thermal stability are both better (Bhat M K., 1998, 787-802), when heated at pH4.0, 80-150°C for 20min still keep 100% integrity, and at 120 °C for 1h still stable. Xylo-oligosaccharide's storage

stability is also very good, at pH 2.5-8.0, 37 °C deposit 3 months, it almost didn't break with loss. Digestion test in vitro showed that its digestion residual rate Gastric in Juice, pancreatic juice and small intestinal mucosa enzyme juice is 99.9%, 99.8% and 99.6% respectively.

2.2 Physiology property

Xylo-oligosaccharide is physiology functionality oligosaccharide, which was confirmed by long term and widely research. It can be used by intestinal available bacteria bifidobacterium but not intestinal harmful bacteria clostridium perfringens. Its main physiology function be concluded as follows.

2.2.1 mediate the intestinal microflora

Health protection of xylo-oligosaccharide is mostly based on its differential effect on pathogens and probiotic. Xylo-oligosaccharide has strict selectivity proliferative effect on bifidobacterium and lactobacillus (Jeong K.J., 1998, 113-118), but has obvious restrain function on escherichia, enterococcus and clostridium. In vitro experiment showed that bifidobacterium could utilize xylobiose, trisaccharide and other oligosaccharides (Suwa Y. et al, 1999), lactobacillus and other probiotic also can ferment xylo-oligosaccharide, but not escherichia, enterococcus and clostridium (Crittenden R. et al, 2002, 781-789). In vivo study on rats showed that xylo-oligosaccharide had strict selectivity proliferative effect on bifidobacterium, not only proliferate quantity, but also prolonged life time (Yuan X. et al, 2005, 225-229). The mechanism xylo-oligosaccharide multiplying probiotic is that it affords carbon for probiotic (Crittenden R. et al, 2002, 781-789). Xylo-oligosaccharide is a kind of nondigestible oligosaccharide, it can't be capitulated by gastric acid and digestive enzyme and not absorbed by intestinal mucosa. After taking xylo-oligosaccharide 24h, it can't be checked in the dejection and urine, indicating that it has been metabolised by intestinal microflora (Okazaki M. et al, 1991, 41-44). Otherwise, it also indicated xylo-oligosaccharide could knock-down intestinal deoxycholic acid, taking health products that contain xylo-oligosaccharide can significantly reduce the risk of colon cancer (Rull P. S. et al, 2006, 1 614 357).

2.2.2 Improving immunity function of animal

Functional oligosaccharide can improve the development of external beneficial bacteria, form biological barrier, inhibit harmful bacteria. Normal flora has extensive immunogenicity, which can stimulate and promote a animal generating immunity function, promote to produce interferon, activate macrophage and lymphocyte B and T, increase natural killing cells ability, induce antibody's producement, enhance immunity ability. Be also likely to low the assistance Th-2 (the T lymphoid cell) reactions combine to build up Th1, regulate Th1/Th2 of unbalance appearance. Study indicated that for infant who is devoided of breast milk, bifidobacterium proliferation can prominently improve the immunity ability, moreover, guard against and cure illness induced by immunity function lowlihead (Stahl B et al, Patent WO 2,005,039,597; 2005.).

2.2.3 Ferment the carbohydrate in the food, prevent constipation

Xylo-oligosaccharide makes bifidobacterium proliferate. Bifidobacterium use acetic acid and lactic acid, which produced by functional oligosaccharide, to stimulate gut motion, increase feces moist degree and keep certainly osmotic pressure, in order to prevent constipation. The results showed that xylo-oligosaccharide significantly improved the symptoms of constipation after three weeks taking it according to 0.7g/d, for the water in the feces increased from 35% to 75% before and after taking it (Jian-xian Zheng et al, 2004, 181-182).

2.2.4 Synthesize vitamin

Functional oligosaccharide make bifidobacterium proliferate, bifidobacterium can synthesize vitamin B1, B2, B6, B12, nicotinic acid and folic acid and so on.

2.2.5 Participate in the digestion of food

Absorb of functional oligosaccharide can make bifidobacterium proliferative. Bifidobacterium can decompose all kinds of proteins to amino acid and peptide which can be easily absorbed, it also decompose cholesterol and lipid. Meanwhile in the acid environment, mineral solubility can increase, improve intestinal mucosa absorptivity.

2.2.6 Have parts of physiology functions of dietary fiber

Functional oligosaccharides belong to water-soluble dietary fiber, have parts of physiology functions of dietary fiber and cannot be easily absorbed. Functional oligosaccharides decrease cholesterol and triglycerides (GTO) in the blood and liver, urge blood lipid normalization, low the caloric value, won't induce blood glucose rise.

2.2.7 Xylo-oligosaccharide special physiology function

Xylo-oligosaccharide can satisfy probiotic which is a functional component that can't be absorbed in vivo. Probiotic can selectively stimulate and promote one or more external microorganism to develop, so that it can improve the host's health.

3. Value and applications of xylooligosaccharides in the layer production

Xylo-oligosaccharides have good physicochemical and physiological properties, so have following characteristics in the layer production.

3.1 Elevate brooding bred rate, laying period conserve rate and laying rate

In the production, xylo-oligosaccharides can boost organism immune function, so elevate brooding bred rate, laying period conserve rate. Shu-ying Han et al, found that brooding bred rate is 98.4% and 97.2% respectively in two batches roman chickens in 2003, and one of the batches laying period death and culling rate is 4.5%. Wang Hua added 0.05% xylo-oligosaccharides in animal feeds and elevated laying rate 4%-5% significantly (Hua Wang, 2005, 23-24). Besides, it shows that the yield and the weight of eggs rose respectively 2.0%~4.0% and 4.5%~6.3%, and the ratio between eggs and feed rose 3.6%~5.7% when the dosage of xylo-oligosaccharides was 0.007% (g/g feed) (Yong Xu et al, 2005, 56-59).

3.2 Elevate the egg's quality, stability and thickness, convenient for coloring

Xylo-oligosaccharides can make the egg yolk bright-coloured and well-distributed, the egg albumen thickening (Guo-hua Dang et al, 2005, 29-36) divided 1260 newborn roman layer into 7 groups, added 0.01%, 0.015%, 0.02%, 0.025%, 0.03% xylooligosaccharides in the group 2, 3, 4, 5, 6 respectively, and the 7th group added 0.1% fructo-oligosaccharide as control. The results showed that adding 0.015% and 0.02% xylo-oligosaccharides could elevate layer daily mean laying rate and egg weight significantly ($p < 0.01$), and also 0.02% group could increase eggshell intensity, eggshell thickness and egg rate ($p < 0.01$), however had no effect on the egg shape index, egg yolk colorimetric, egg yolk rate and haugh unit.

Guo-hua Dang et al also found that adding 0.015% xylo-oligosaccharides in the day food could decrease crude fat more significantly than 0.020% group (Guo-hua Dang et al, 2003, 33-34), and two groups both cut down cholest notably, through 720 layers experiment. As the mechanism of oligosaccharide decrease fat, some investigate showed that it could promote intestinal bifidobacterium which can form bionic to hyperplasia. Bionic inhibits fat synthesis related hormone so as to depress lipopexia. There is report show that xylo-oligosaccharide can decrease more than 15% cholest. Study also considered that bacillus bifidus and lactobacillus could assimilate cholest, thus decrease cholest and fat. However the mechanism still needs more researches.

Yong Xu et al detected the egg quality and found that there was no difference on the egg shape, eggshell, essential amino acid and microelement before and after adding xylo-oligosaccharide, meanwhile they found that adding 0.007% xylo-oligosaccharide could make the eggshell bloom, so develop a new way in high quality viridis egg production.

3.3 Raise immunity

Xylo-oligosaccharide excites layer's immune system, enhance immunity and disease resistance, reduce disease incidence, so diminish the antibiotic addition that low the medication cost. After adding the xylo-oligosaccharide, intestinal disease and respiratory tract disease significantly decrease, also washy disappeared, moreover there was no adverse effect after epidemic prevention, dejecture shape and colour at equal pace. Feeding porcine with xylo-oligosaccharides, diarrhea rate reduce more than 60%, and Ig G, Ig M and Ig A in the serum boost notably, illuminating that xylooligosaccharide can improve the immunity markedly (Ji-cheng Wang et al, 2006, 3-7).

3.4 Improve the chicken house environment

In keep the chicken production, if there isn't enough airing, alkaline air will stir your nasal, especially in winter. After adding the xylo-oligosaccharide, nutrient substance absorb and use ratio can be elevated, there is less protein in dejecture so that alkaline air reduce and thus environment sanitation condition improved.

3.5 Improve feather sheen

Because of the fully absorption of nourishment material, strengthened the anti-disease ability of the layer, the layers feather color is shining, color and luster good, feather fluffy and sheen bad rarely seen.

3.6 Raise feed conversion rate

Xylo-oligosaccharide can improve animal intestinal microecology condition, inhibit pathogenic bacteria development, promote animal feed's digestion and absorption. Guohua Dang et al^[17], added 0.015% and 0.02% xylo-oligosaccharide into the diet and found that layer feed conversion increasing significantly ($p < 0.01$). Yong Xu et al reported that when xylo-oligosaccharide accounts for 0.007% of diet its growth promotion effect was best, so ratio of egg to feed can increase 3.6~5.7%. When xylo-oligosaccharide and calcium are absorbed in the meantime, it will promote calcium absorption, and stimulate organism to form many kinds nutrient substance, such as V_{BI} , V_{B2} , V_{B6} , V_{BI2} , V_{PP} and V_M . Xylo-oligosaccharide influences layer productive performance. And xylo-oligosaccharides significantly reduced the cholesterol content of eggs, and moreover elevate the layers resistance and descend the death rate, so boost the comprehend economic returns of layer breeding, even make the population risk of the layer descend about 70%. In

conclusion, xylo-oligosaccharide is green color environmental protection additives

4. Mechanism of action

At present, action mechanism of xylo-oligosaccharide still needs further researches. Proliferation test in vitro confirmed that xylo-oligosaccharide extracted from vegetable fibre using biotechnology could make layer intestinal tract bacillus bifidus proliferate effectively, so it brings out much effect on health and growth. Now four action mechanisms of xylo-oligosaccharide on layer explained as follows. First, antagonism, xylo-oligosaccharide offers carbon source to probiotics, make *Bacillus bifidus* and other beneficial bacterium proliferate greatly so as to competitively repel pathogenic bacteria field planting consolidation site and finally inhibit pathogenic bacteria. Second, improve animal intestinal microecology condition, inhibit pathogenic bacteria, elevates feeder digestion and absorption. Third, increase animal's non-specificity immunologic competence, enhance resistance of organism to pathogenic bacteria. Fourth, decompose noxious substance, form organic acid and other beneficial substance, less dejecture odour, improve breeding circumstance.

5. Xylo-oligosaccharide's application prospect

Many study indicated that adding xylo-oligosaccharide into feeder could increase layer productive performance. Xylo-oligosaccharide can promote layer to absorb nutrient substance and utilize feeder, make layer grow and produce, improve product quality. Among more than ten kinds oligosaccharides product, xylo-oligosaccharide is the most famous. Currently in the animal feed additive, because of its special advantage, such as it is a kind of natural sugar material, is safe and animal digestive enzyme system cannot decompose it, xylo-oligosaccharide has a wide perspective in layer production. Xylo-oligosaccharide can all arrive large intestine, and its stability and compatibility are both good, moreover promote layer to grow. Therefore, as feed additive, xylo-oligosaccharides is provided with capacious development space.

In our country, xylo-oligosaccharide still be placed in a research and exploited phase, haven't entered large-scale industrialization production. Therefore, we should begin from three aspects in the production. Firstly, consummate xylo-oligosaccharide enzymic method production process. Secondly, Development of xylanase and xylo-oligosaccharide has great potentialities and profound significance, so must enlarge application range. Thirdly, take further research on xylo-oligosaccharide action mechanism in layer production.

References

- Bhat, M.K. (1998). Oligosaccharides as functional food ingredients and their role in improving the nutritional quality of human food and health [R]. *Recent Res Dev Agric Food Chem*, 2, 787-802.
- Crittenden, R., Karppinen, S., and Ojanen, S. (2002). In vitro fermentation of cereal dietary fibre carbohydrates by probiotic and intestinal bacteria[J]. *J Sci Food Agric*, 82, 781-789.
- Fooks, L.J., and Gibson, G.R. (2002). In vitro investigations of the effect of probiotics and prebiotics on selected human intestinal pathogens. *FEMS Microbiol. Ecol*, 39, 67-75.
- Guo-hua, Dang., Wen-xing, Du., Tian Wang., and Han-jing Zhu. (2003). The effects of xylo-oligosaccharides on conventional components and cholesterol content in layer, 8, 33-34.
- Guo-hua, Dang., Wen-xing, Du., Xiao-chun Song., Tian, Wang., and Han-jing Zhu. (2005). The effects of xylo-oligosaccharides on laying performance and egg quality, 41(1), 29-36.
- Hua Wang. (2005). Study on the effect of xylo-oligosaccharides on laying performance, (7), 23-24.
- Izumi, K., Azumi, N., (2001). Xylooligosaccharide compositions useful as food and feed additives. *JP Patent* 2001226409.
- Izumi, Y., and Kojo, A., (2003). Long-chain xylooligosaccharide compositions with intestinal function-improving and hypolipemic activities, and their manufacture. *JP Patent* 2003048901.
- Jeong, K.J., Park, I.Y., and Kim, M.S. (1998). High-level expression of an endoxylanase gene from *Bacillus* sp. in *Bacillus subtilis* DB104 for the production of xylobiose from xylan[J]. *Appl. Microbiol. Biotechnol.* 50, 113-118.
- Jian-xian, Zheng., Hai-xia, Zhu., and Zhi-juan, Rao. (2004). *Functional oligosaccharide*. 181-182.
- Ji-cheng, Wang., Ling-hui, Pan., and Shu-yun, Li. (2006). Study on production performance, intestinal microflora and immunity level in weaned piglets of xylo-oligosaccharides, 33(5), 3-7.
- Okazaki, M., Koda, H. and Izumi, R. (1991). Effect of xylo-oligosaccharide on growth of intestinal bacteria and putrefaction products[R]. *J Jpn Soc Nutr Food Sci*, 44, 41-44.
- Rull, P.S. (2006). Dietary supplements comprising prebiotics and physiologically active fatty acids[P]. *Eur. Patent EP*. 1 614 357.

- Stahl, B, M'Rabet, L and Vos, AP. (2005). Immunomodulating oligosaccharides, and therapeutic use there of. Int. Patent WO 2, 005, 039, 597.
- Suwa, Y, Koga,K and Fujikawa, S. (1999). Bifidobacterium bifidum proliferation promoting composition containing xylooligosaccharide [P]. *USA Patent US*. 5939309.
- Va'zquez, M.J., Alonso, J.L. and Dom'ý nguez H. (2000). Xylooligosaccharides:manufacture and applications[R]. *Trends Food Sci Technol*, 11, 387-393.
- Va'zquez, M.J., Alonso, J.L., Domi'nguez, H. and Parajo', J.C. (2001). Xylooligosaccharides :manufacture and applications. *Trends Food Sci. Technol*, 11, 387–393.
- Yong, Xu., Yang, Gu., Mei, Chen.,and Shi-yuan, Xu.(2005). Study on the growth function and promoting growth mechanism in layer of xylo-oligosaccharides, 26(22), 56-59.
- Yuan,X., Wang, J., and Yao,H. (2005). Feruloyl oligosaccharides stimulate the growth of bifidobacterium [J]. *Bifidum Anaerobe*, 11, 225-229.



On the Comparison of Capacitance-Based Tomography Data

Normalization Methods for Multilayer Perceptron

Recognition of Gas-Oil Flow Patterns

Hafizah Talib

School of Electrical and Electronic Engineering

Universiti Sains Malaysia

14300 Nibong Tebal, Pulau Pinang, Malaysia

E-mail: fizah04@gmail.com

Junita Mohamad-Saleh

School of Electrical and Electronic Engineering

Universiti Sains Malaysia

14300 Nibong Tebal, Pulau Pinang, Malaysia

E-mail: jms@eng.usm.my

Khursiah Zainal-Mokhtar

School of Electrical and Electronic Engineering

Universiti Sains Malaysia

14300 Nibong Tebal, Pulau Pinang, Malaysia

E-mail: ven_conmigo1010@yahoo.com

Najwan Osman-Ali

School of Electrical and Electronic Engineering

Universiti Sains Malaysia

14300 Nibong Tebal, Pulau Pinang, Malaysia

E-mail: reeto_millenia@yahoo.com

The research is fully funded by the Ministry of Science, Technology and Innovation (MOSTI), Malaysia under eScienceFund grant.

Abstract

Normalization is important for Electrical Capacitance Tomography (ECT) data due to the very small capacitance values obtained either from the physical or simulated ECT system. Thus far, there are two commonly used normalization methods for ECT, but their suitability has not been investigated. This paper presents the work on comparing the performances of two Multilayer Perceptron (MLP) neural networks; one trained based on ECT data normalized using the conventional equation and the other normalized using the improved equation, to recognize gas-oil flow patterns. The correct pattern recognition percentages for both MLPs were calculated and compared. The results showed that the MLP trained with the conventional ECT normalization equation out-performed the ones trained with the improved normalization data for the task of gas-oil pattern recognition.

Keywords: Electrical Capacitance Tomography, Artificial Neural Networks, Quasi-Newton (QN), Levenberg-Marquardt (LM), Resilient-Back-propagation (RP), Pattern Recognition

1. Introduction

Recognition of flow regimes of gas-liquid flow is important in industrial process such as gas-oil industry. However, this

information cannot be easily determined since gas-oil flows are normally concealed within a pipe. One way to obtain such information is by employing the Electrical Capacitance Tomography (ECT) technique. ECT is a technique used to visualize the distribution of two dielectric components (Yang and Byars, 1999). It has been employed for industrial process containing different dielectric materials, such as gas/oil flows in oil pipeline. In an ECT sensor, several electrodes are mounted around the pipe vessel. It is said to be non-invasive and non-intrusive since the sensing electrodes are not physically in contact with the medium inside the pipe vessel. With N electrodes, the total number of M independence capacitance measurements is given by (Xie et al, 1992)

$$M = \frac{N(N-1)}{2} \quad (1)$$

The measured capacitances are usually normalized before being used for any application. There two versions of equations for normalizing the capacitance values, referred to in this paper as the conventional normalization and improved normalization methods. The conventional normalization approach assumes that the distribution of the two materials is in parallel and hence, the normalized capacitance is a linear function of the measured capacitance (Yang and Byars, 1999). The normalization equation is given by (Xie et al, 1992)

$$N_{ij}^{old} = \frac{C_{ij(p)}^{old} - C_{ij(e)}^{old}}{C_{ij(f)}^{old} - C_{ij(e)}^{old}} \quad (2)$$

where N_{ij}^{old} is the conventional normalized capacitance between a pair of electrodes i and j, $C_{ij(p)}^{old}$ is the measured capacitance, $C_{ij(e)}^{old}$ is the capacitance when the pipe is full of gas and $C_{ij(f)}^{old}$ is the capacitance when the pipe is full of the higher permittivity material than the permittivity of the gas, such as oil. An improved normalization approach is derived from a series sensor model by modeling the sensor capacitances as two capacitances in series and is given by the following equation (Yang and Byars, 1999)

$$N_{ij}^{new} = \frac{\frac{1}{C_{ij(p)}^{new}} - \frac{1}{C_{ij(e)}^{new}}}{\frac{1}{C_{ij(f)}^{new}} - \frac{1}{C_{ij(e)}^{new}}} \quad (3)$$

where N_{ij}^{new} is the improved normalized capacitance between a pair of electrodes i and j, $C_{ij(p)}^{new}$ is the measured capacitance, $C_{ij(e)}^{new}$ is the capacitance when the pipe is full of gas and $C_{ij(f)}^{new}$ is the capacitance when the pipe is full of the higher permittivity material than the permittivity of the gas.

For both equations, the normalized capacitance values for empty and full pipe are 0 and 1, respectively. This can be proven by substituting $C_{ij(p)} = C_{ij(e)}$ for empty and $C_{ij(p)} = C_{ij(f)}$ for full pipe. Therefore, ideally, the maximum and minimum values for normalized capacitances are 1 and 0, respectively. If the normalized capacitance value is higher than 1, the value is said to overshoot and if it is less than 0, the value is said to undershoot.

Until now, there has been no proper research to investigate which normalization method is the best for flow regime recognition using neural network. Thus, this paper presents the work on such investigation using the Multilayer Perceptron (MLP) neural network, the most commonly used neural network.

1.1 Multilayer Perceptron (MLP)

An Artificial Neural Network (ANN) or simply referred to as a 'neural network' is an intelligent system composed of simple processing elements which operate in parallel (Haykin, 1999). An MLP is a type of an ANN model. MLPs have been used in various different applications due to their ability to solve complex functions including pattern classification (Yan *et al*, 2004), function approximation (Lee *et al*, 2004), process control (Ren *et al*, 2000) and filtering tasks (Parlos, 2001).

Figure 1 shows the basic MLP supervised learning structure where pairs of input and target output are used to train the networks. The term 'supervised' refers to the involvement of target output that act as a 'teacher' during a neural network learning process. Typically, an MLP consists of neurons or nodes or processing elements arranged within an input layer, one or more hidden layers and an output layer. The input signal propagates through the network in a forward direction, on layer-by-layer basis. Figure 2 shows the architecture of an MLP (Haykin, 1999).

2. Methodology

Figure 3 shows schematic diagrams of flow regimes investigated in this work which are the empty flow, full flow, stratified, bubble, annular and core flows. The first stage of the work involved collection of ECT raw dataset using an

ECT simulator based on the finite element method (Spink, 1996). The simulated data were used because of two reasons. Firstly, the actual data of flow regimes are very difficult to obtain since some flow patterns are non-repeatable. Secondly, the actual plant data are constantly interrupted by noise and external interference and hence the data collected are not accurate. The dataset were obtained based on various geometrical flow patterns to give a variety of patterns for each flow regime. Since the number of electrodes used for the ECT sensor was 12, each ECT dataset consists of 66 capacitance values corresponding to the difference in capacitances between all possible pairs of electrodes (refer to equation 1). Table 1 shows the number of readings corresponding to their pairs of electrodes.

For each flow regime, all of the capacitances values were computed into normalized value before being randomly divided into three sets in the ratio of 8:1:1 for training, validation and test, respectively. For this investigation, the number of training set, validation set and testing set were 1140, 142 and 142, respectively. The training set was used for computing the gradient and updating the network weights and biases during ANN learning. The validation set was used to stop the training process. The testing set was used to verify the network's generalization performance.

The second stage is data analysis. As already mentioned, the ideal normalized capacitance values are within 0 and 1. This stage is performed to determine the differences in normalized capacitance values between the conventional and improved normalization in terms of how much their overshoot and undershoot values differ. Normalized capacitance values for one pattern from each flow regime, for both normalization methods were plotted on the same graph and their differences were calculated and discussed.

The third stage is an ANN learning or training process. In this stage, MLP were trained with three different kinds of back-propagation training algorithms; the Resilient Back-propagation (RP), Quasi-Newton (QN) and the Levenberg Marquardt (LM). These training algorithms are the most commonly used training algorithms for classification using MLP neural networks. The number of inputs used in an MLP was 66 (corresponding to 66 normalized values) and outputs was 6 (corresponding to 6 flow regimes to classify). The output class representations are as listed in Table 2. The number of hidden neurons was determined using the network growing approach by adding one neuron at a time to the hidden layer.

Suitable activation functions must be applied to the MLP hidden and output neurons. The logistic sigmoid activation function is the most commonly used activation function for back-propagation algorithm because it is differentiable (Demuth and Beale, 1998). Due to this fact, the activation function had been applied to hidden neurons during training. Since the output neurons could result in either 0 or 1, the activation function applied to these neurons was the logistic sigmoid.

To ensure that the MLP was not stuck at a local minimum, 30 runs were made for each number of hidden neurons. Each training process stopped when there was no improvement in the validation error after 5 consecutive training iterations. At completion, the MLP weights and biases at the minimum of the validation error were saved.

The last step was MLP performance assessment. This stage was carried out to investigate the performance of the MLPs based on the percentage of correct classification (CCP) of test data to determine the best normalization method. The CCP is calculated using,

$$CCP = \frac{\text{No. of correct classification}}{\text{Total no. of data}} \times 100\% \quad (4)$$

3. Results and Discussion

The results on data analysis of the normalized ECT data and the performances of the MLPs trained with the conventional and improved normalized data are discussed in the following subsections.

3.1 Data Analysis

Figures 4(a) to 4(d) show plots of capacitance values for a variety of flow pattern examples normalized based on the improved and conventional normalization equations. The number of reading (i.e. x-axis) corresponds to the electrode pairs as listed in Table 1. Table 3 shows the results of total shooting for the capacitance values based on the improved and conventional normalization equations. The table shows that the total undershooting for stratified flow normalized using the improved equation is higher than that normalized using the conventional normalization equation. On the other hand, its capacitance overshoot is higher when normalized using the conventional equation compared to the improved normalization. For bubble pattern, the overshoot value for both improved and conventional normalization methods is 0. However, the conventional normalization gives a slightly higher overshoot capacitance value of about 0.4%. The core example pattern gives 0 overshoot for both normalization methods, whilst the undershoot is higher when the improved normalization equation is used. The annular flow pattern for both, the improved and conventional normalization equations give 0 undershoot, whilst the conventional equation produces an undershoot value of about 0.2% higher than the improved equation. From the table, it shows that the improved normalization equation results in 38%

lower total overshoot value than the conventional normalization. However, the improved normalization equation results in 74% higher total undershoot value than the conventional normalization equation. Overall, the data analysis results have shown that the conventional normalization method has led to less total shooting compared to the improved normalization method.

3.2 Flow Regime Recognition

Figures 5, 6 and 7 shows the CCP plots of MLPs trained with the RP, QN and LM algorithms based on the improved and conventional normalization methods, respectively. From Figure 5, it is obvious that the MLP trained with the conventional normalized data produces higher CCP than the MLP trained with the improved normalized data. Also, it can be seen that the MLP trained with the improved normalized data give rather unstable CCP at different numbers of hidden neurons. Comparing the plots in Figure 6, it can be seen that the MLP trained with the conventional normalized data outperformed the MLP trained with the improved normalized data at 3 and more hidden neurons. The performances of the MLPs trained using the LM algorithm (see Figure 7) for both improved and conventional normalized data seems less competitive. However, it can be seen that the MLP trained with the improved normalized data is rather unstable in its CCP values for different numbers of hidden neurons. Although both MLPs produce the same maximum CCP, the MLP trained with the conventional normalized data reaches the maximum CCP earlier (at 6 hidden neurons) than the MLP trained with the improved normalized data.

Table 4 shows the comparison in the maximum performance of the MLPs trained with the improved and the conventional normalized data using various training algorithms as investigated. In the table, HN is the abbreviation for the number of hidden neurons. For the RP algorithm, the conventional normalization is better than the improved normalization in terms of the maximum CCP value. Also, its number of hidden neurons is less than the MLP trained with the improved normalized data. For the QN algorithm, the conventional normalization obtains its highest CCP at 98.6% with 11 hidden neurons whilst the improved normalization obtains its highest CCP at 96.5% with less number of hidden neurons. However, since the main concern for an MLP performance is the CCP value, it can be concluded that the conventional normalization is better than improved normalization. For the LM algorithm, even though both normalization methods obtain the same value of highest CCP with 99.3%, the conventional normalization has achieved its highest CCP with less number of hidden neurons compared to the improved normalization. Consequently, the conventional normalization method is better in terms of the number of hidden neurons, which results in smaller structure of the MLP. Thus, the network execution becomes faster.

The overall results demonstrate that it is better to use the conventional normalization for ECT data compared to the improved normalization method. However, it does not mean that the improved normalization method is of no value for other application. It has to be born in mind that this work focuses on flow regime recognition application. Perhaps, the improved ECT data normalization method might be of better used for other applications, such as image reconstruction.

4. Conclusion

An investigation had been carried out to determine the best normalization equation for ECT data for the task of flow regime recognition. For all the three training algorithms investigated, the results proved that the conventional equation was a better normalization equation for ECT data in the quest to train MLP neural networks.

5. References

- Demuth B. and Beale M. (1998). *Neural Network Toolbox User Guide Version3*. Natick: The Math Works Inc.
- Haykin S. (1999). *Neural Networks: A Comprehensive Foundation 2nd Edition*. Canada: Macmillan
- Lee E. W. M., Lim C.P., Yuen R. K. K. and Lo S. M. (2004). A Hybrid Neural Network Model for Noisy Data Regression. *IEEE Transactions on System, Man, and Cybernetic, Part B*, 34, 951-960.
- Parlos A. G. (2001). An Algorithm Approach to Adaptive State Filtering Using Recurrent Neural Network. *IEEE Transactions on Neural Network*, 12, 1411-1432.
- Ren Z., Chen J., Tang X. and Yan W. (2000). A Combined Method Based on Neural Network for Control System Fault Detection and Diagnosis. *Proceedings of the 2000 IEEE International Conference on Control Applications*, Anchorage, Alaska, USA, 104-108.
- Spink M. D. (1996). Direct Finite Element Solution for the Capacitance, Conductance or Inductance and Force in Linear Electrostatic and Magnetostatic Problem. *International Journal of Computation and Mathematics in Electrical and Electronic Engineering*, 15, 70-84.
- Xie C. G., Huang S. M., Hoyle B. S., Thorn R., Lenn C., Snowden and Beck M. S. (1992). Electrical Capacitance Tomography for Flow Imaging: System Model for Development of Image Reconstruction Algorithms and Design of Primary Sensors. *IEEE Proceedings-G*, 139, 89-98.

Yan H., Liu Y. H. and Liu C. T. (2004). Identification of Flow Regimes Using Back-Propagation Networks Trained on Simulated Data Based on Capacitance Tomography Sensor. *Measurement Science Technology*, 15, 432-436.

Yang W. Q. and Byars M. (1999). An Improved Normalisation Approach for Electrical Capacitance Tomography. *1st Congress on Industrial Process Tomography*, Buxton, UK, 215-218.

Table 1. Number of readings corresponding to electrode pairs

No. of reading	C _{ij}	
	i	j
1	1	2
2	1	3
3	1	4
4	1	5
5	1	6
6	1	7
7	1	8
8	1	9
9	1	10
10	1	11
11	1	12
12	2	3
13	2	4
14	2	5
15	2	6
16	2	7
17	2	8
18	2	9
19	2	10
20	2	11
21	2	12
22	3	4

No. of reading	C _{ij}	
	i	j
23	3	5
24	3	6
25	3	7
26	3	8
27	3	9
28	3	10
29	3	11
30	3	12
31	4	5
32	4	6
33	4	7
34	4	8
35	4	9
36	4	10
37	4	11
38	4	12
39	5	6
40	5	7
41	5	8
42	5	9
43	5	10
44	5	11

No. of reading	C _{ij}	
	i	j
45	5	12
46	6	7
47	6	8
48	6	9
49	6	10
50	6	11
51	6	12
52	7	8
53	7	9
54	7	10
55	7	11
56	7	12
57	8	9
58	8	10
59	8	11
60	8	12
61	9	10
62	9	11
63	9	12
64	10	11
65	10	12
66	11	12

Table 2. Output class representation for each flow regime

Flow regime	Target output
Full	1 0 0 0 0 0
Stratified	0 1 0 0 0 0
Bubble	0 0 1 0 0 0
Core	0 0 0 1 0 0
Annular	0 0 0 0 1 0
Empty	0 0 0 0 0 1

Table 3. Undershoot and overshoot values based on the improved and conventional normalization equations for examples of flow patterns

Flow regime	Improved Normalization		Conventional normalization	
	Total undershoots	Total overshoots	Total undershoots	Total overshoots
Stratified	4.937	1.334	1.561	3.932
Bubble	0.000	3.760	0.000	4.179
Core	4.051	0.000	1.717	0.000
Annular	0.000	0.150	0.000	0.349
Total shooting	14.233		11.738	

Table 4. A comparison of the MLP flow regime recognition performances based on different training algorithms for improved and conventional normalization methods

		Improved Normalization	Conventional Normalization
RP	CCP (%)	97.9	99.3
	HN	38	3
QN	CCP (%)	96.5	98.6
	HN	6	11
LM	CCP (%)	99.3	99.3
	HN	7	6

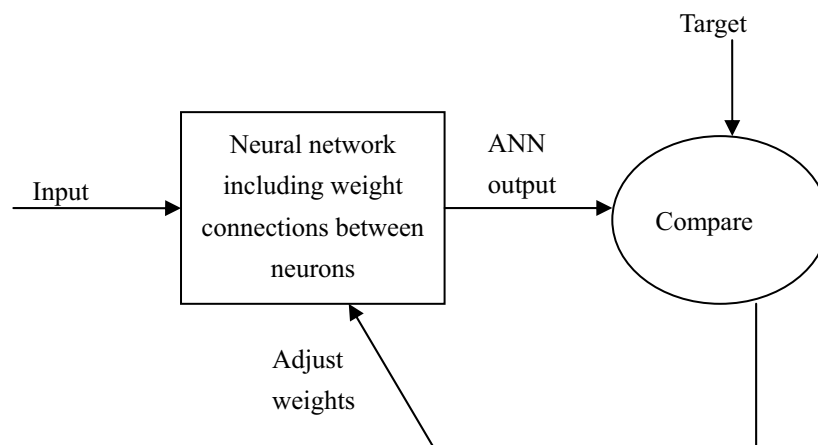


Figure 1. MLP supervised learning structure

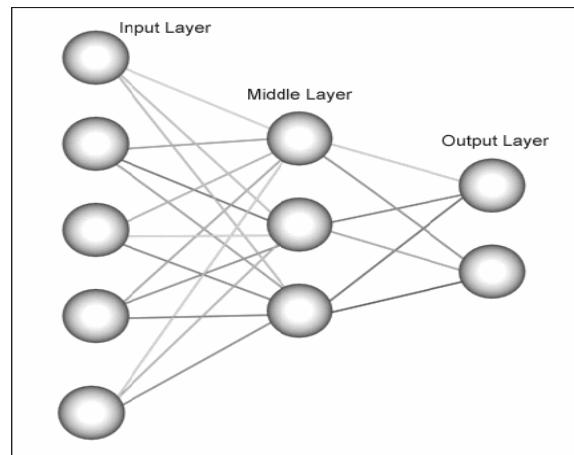
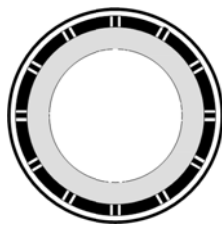


Figure 2. Schematic diagram of MLP architectural structure



(a) Empty



(b) Full



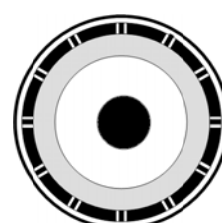
(c) Stratified



(d) Bubble

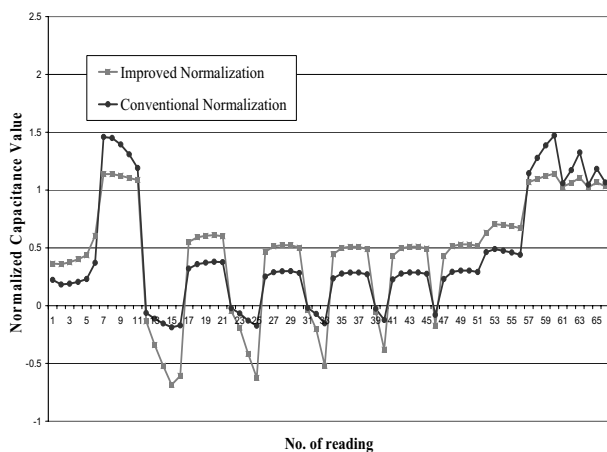


(e) Annular

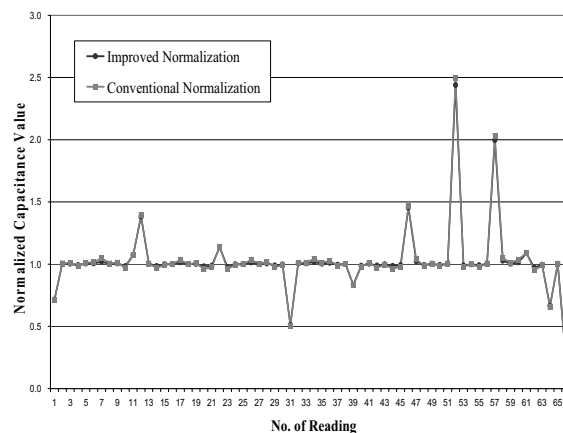


(f) Core

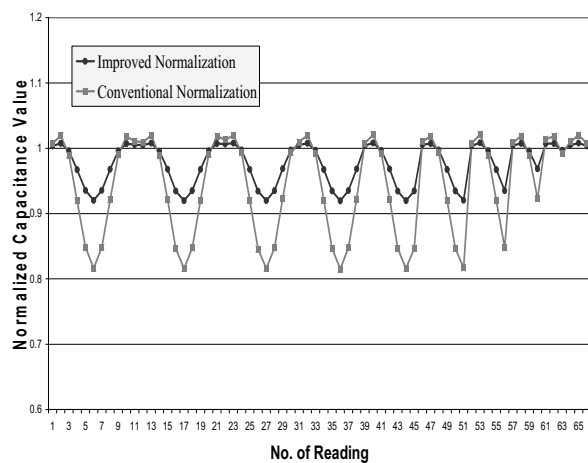
Figure 3. Schematic diagrams of (a) empty, (b) full, (c) stratified, (d) bubble, (e) annular and (f) core, flow regimes. The shaded area indicates oil and the white area indicates gas



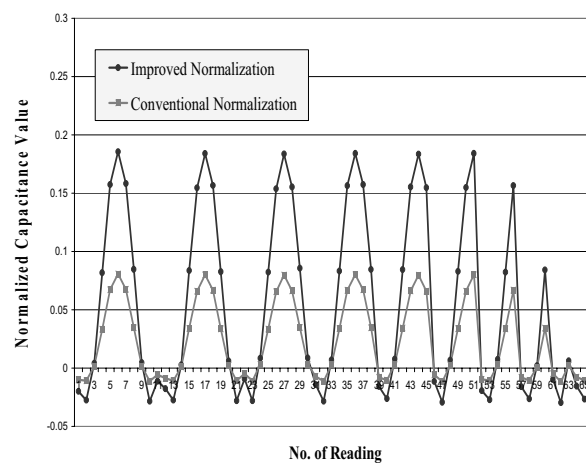
(a) Example of stratified flow



(b) Example of bubble flow



(c) Example of annular flow



(d) Example of core flow

Figure 4. Plots for capacitance values based on improved and conventional normalization method for examples of (a) stratified, (b) bubble, (c) annular and (d) core, flows

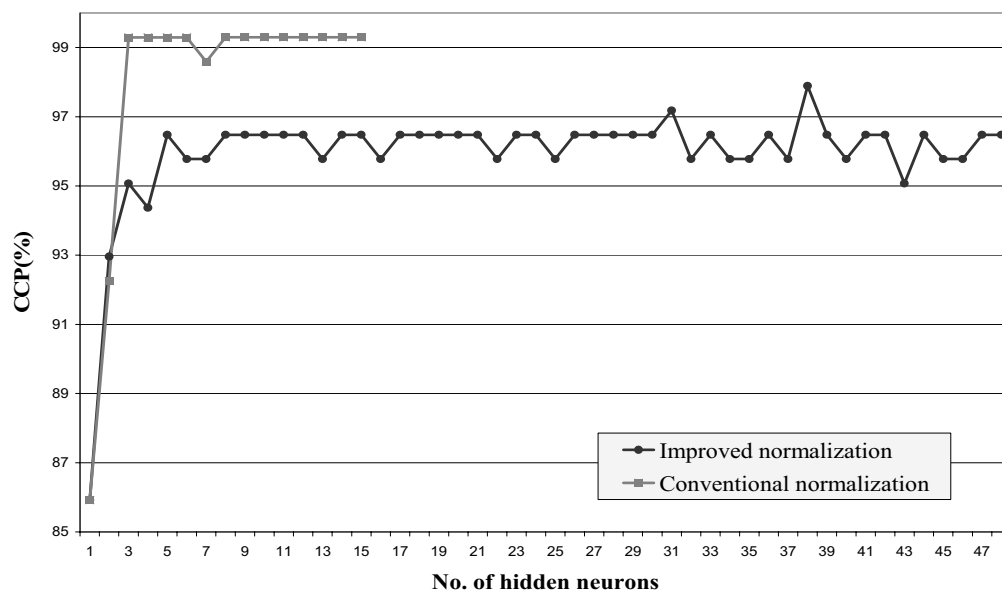


Figure 5. CCP of MLP trained with RP algorithm based on (a) improved and (b) conventional normalization methods

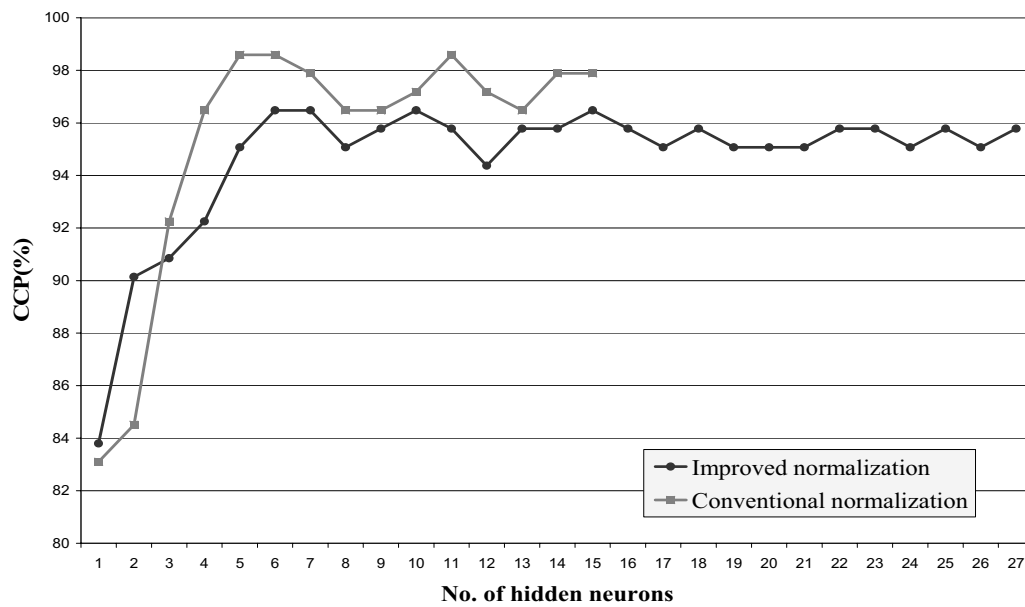


Figure 6. CCP of MLP trained with QN algorithm based on (a) improved and (b) conventional normalization methods

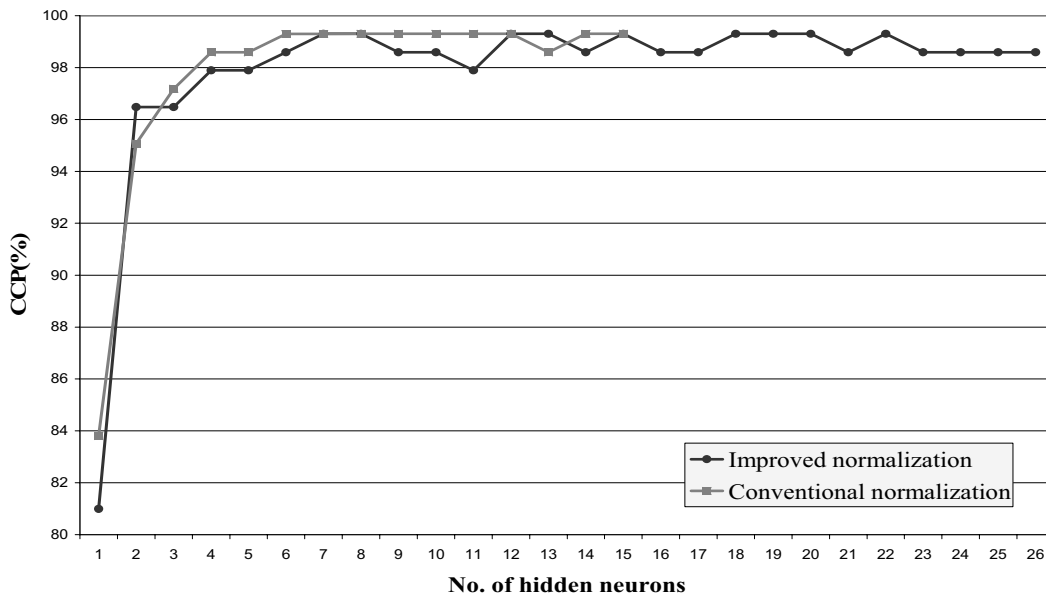


Figure 7. CCP of MLP trained with LM algorithm based on (a) improved and (b) conventional normalization methods



Analysis of Factors to Influence Yarn Dynamical Mechanical Property

Qian Wang, Jiankun Wang & Ling Cheng

School of Textiles

Tianjin Polytechnic University

Tianjin 300160, China

E-mail: yybbxjl@126.com

Abstract

The mechanical property of yarn influences the mechanical property and endurance of textiles to large extents. At present, the research and evaluation of yarn mechanical property mainly refer to some static testing indexes such as breaking strength and tensile strength at break of yarn mechanical property. However, these indexes can not comprehensively reflect the mechanical property of yarn in the spinning and using process. In this article, we adopt the CTT yarn property testing instrument made by US Lawson Company to test the dynamic strength of yarn, and analyze factors to influence the yarn dynamic strength, and more objectively evaluate the mechanical property of yarn.

Keywords: Mechanical property, Dynamic strength, CTT, Influencing factors

1. Introduction

The testing indexes of yarn mechanical property mainly include tensile breaking strength, relative strength, breaking elongation and tensile distortion. In these indexes, the yarn strength is the most important index to influence yarn property and reflect the interior quality of yarn, and it is the necessary condition to possess machining property and final purpose, and the technical parameter involved in various working procedures such as spinning and knitting.

The modern testing instrument of single yarn has been very advanced, and it can display breaking load, breaking elongation, breaking power and their variation coefficients. In the spinning, the information can offer directions of relative properties among yarns. However, the information can not completely predict the operation status of yarn, because it is not enough to only consider the static mechanical indexes of yarn. In the subsequent machining process, yarn will continually suffer tension and friction and always be in the dynamic status, but not in the static status. Therefore, it is more meaningful to research the mechanical property of yarn under the dynamic mechanical condition. The CTT yarn property testing instrument made by US Lawson Company can realize the strength testing of yarn under the dynamic condition.

2. Experiment instruments

The experiment instruments include CTT yarn property testing instrument and Y331A Twister.

2.1 Brief introduction of CTT

CTT (Constant Tension Transport) (seen in Figure 1) is the yarn property testing instrument made by US Lawson Company. The meaning of CTT is that under the draught of constant tension (1.96-735cN) exactly selected, the yarn can be transported by the selected speed, which is an important character. The instrument is the international advanced multi-function yarn property analysis and testing system, and it is composed by many testing modules such as EIB (electric imitation blackboard), YAS (yarn quality analysis), DET (dynamic extension testing), LGT (yarn down quality testing), DTT (dynamic friction coefficient testing) and YAT (abrasion resistant testing). It can not only implement yarn comprehensive property testing analysis and research the influences of physical mechanical property, structure and apparent characters of different yarns to performance of fabrics, but implement quality evaluation to the yarn according to the international standard. In this article, we mainly use the DET module to test the dynamic strength of yarn and analyze the factors influencing the dynamical strength of yarn.

2.2 Testing method of CTT

The basic parts of CTT are composed by input roller, output roller and tension sensors. The output roller runs by the constant speed (20-360m/min), and the speed of input roller is maintained on certain value with the set tension. The speed difference between input roller and output roller makes the tension endured by yarn in the operation process keep on the set value. When the dynamic testing is implemented, we can gradually increase the set tension to observe the operation of yarn, and once the breaking happens, so the set tension value here represents the dynamic breaking strength of the testing yarn, and the dynamic breaking elongation ratio of measured yarn can be computed according to the speed

difference between input roller and output roller, and though this method, we can also establish the relationship between yarn dynamic tension and yarn elongation. Otherwise, the average breaking strength and its variation coefficient of yarn and the average of dynamic running tension and its variation coefficient which is also very important to analyze the running status of yarn can be computed according to the testing tension value.

3. The experiments and analysis of factors to influence dynamic strength of yarn

The experiment environment: all experiments are implemented in the lab with the temperature of 25°C and the relative humidity of 65%.

The main factors to influence the yarn breaking strength include fiber length, fiber intention, fiber fineness and yarn twist. We will compare and analyze the factors to influence the yarn dynamic strength from flowing aspects.

3.1 Influence of yarn twist to yarn dynamic strength (experiment 1)

3.1.1 Experiment

(1) Sample: 20 pipes of 40^s pure cotton yarn.

(2) Testing: a. the twist. b. the dynamic strength under the running speeds of 100m/min, 200m/min and 360m/min, and the influences of twist to yarn dynamic strength.

3.1.2 Testing result and analysis

The testing results are seen in Table 1. The data in Table 1 can be described as following curves seen in Figure 2, Figure 3 and Figure 4.

From Figure 2, we can see that (1) the dynamic strength of yarn increases with the increase of twist, and when the twist achieves the certain value, i.e. 96.5 twists/10cm, the dynamic strength of yarn begins to reduce instead with the increase of twist, (2) the curve is smooth, and when the yarn running speed, $V=100\text{m/min}$, the change of its dynamic strength is stable with the change of twist, and there is not biggish fluctuation.

From Figure 3, we can see that (1) the dynamic strength of yarn increases with the increase of twist, and when the twist achieves the certain value, i.e. 96.5 twists/10cm, the dynamic strength of yarn begins to reduce instead with the increase of twist, which is same with the above figure, (2) the inflexion appears in the curve, which indicates that the change of yarn dynamic strength has certain fluctuation and it is not very stable.

From Figure 4, we can see that (1) the dynamic strength of yarn increases with the increase of twist, and when the twist achieves the certain value, the dynamic strength begin to reduce whereat increase, and when the twist achieves 98.0 twists/10cm, the dynamic strength reduces, (2) the fluctuation extent of the curve is large, which indicates that when the running speed $V=360\text{m/min}$, the change relationship of yarn dynamic strength is complex and unstable with the change of twist.

The reason is that the breaking always happens in the feeblest section under the pull for a length of yarn. To the short fiber yarn, there are two situations that it breaks because of the outside pull force, and one is that the breaking of fiber makes the yarn break, and the other is the surge among fibers makes the yarn break. The influence of twisting function to the yarn strength is decided by the integration of advantage factors and disadvantage factors. When the twist is small, the twisting function is mainly represented to improve the unevenness ratio of yarn strength and reduce the surge fiber amount of yarn breaking, so the yarn strength increases with the increase of twist. When the twist achieves certain value, the twisting function is mainly represented to increase the pre-stress of fiber in yarn and reduce the axes component force of fiber intension, so the yarn strength gradually reduces with the increase of twist. Three above curves all embody this rule, and with the increase of twist, the twist-dynamic strength curve of yarn fluctuates largely (Yao, 1993).

3.2 Influence of yarn running speed to yarn dynamic strength (experiment 2)

3.2.1 Experiment

(1) Sample: 20 pipes of 40^s pure cotton yarn, and their breaking strengths are close.

(2) Testing: change different running speeds, and respectively test the dynamic strengths of yarn when $V=100\text{m/min}$, $V=200\text{m/min}$ and $V=360\text{m/min}$, and analyze the influences of running speeds to dynamic strengths.

3.2.2 Testing result and analysis

The testing results are seen in Table 2. The data in Table 2 can be described as following curves seen in Figure 5, Figure 6 and Figure 7.

From Figure 5, we can see that (1) the values of yarn dynamic strength are mainly focused in 113-123cN, (2) the yarn dynamic strength presents normal school, and the rule closes to the static single yarn strength.

From Figure 6, we can see that (1) the values of yarn dynamic strength are mainly focused in 107-121cN, (2) the yarn dynamic strength frequently appears in the range of 99-103cN, which indicates the strength is relative low, (3) when the

running speed increases, the yarn dynamic strength goes to reduce.

From Figure 7, we can see that (1) the values of yarn dynamic strength are mainly focused in 107-121cN, (2) the yarn dynamic strength frequently appears in the range of 99-103cN, which indicates the strength is relative low, (3) when the running speed increases, the yarn dynamic strength goes to reduce.

From Figure 8, we can see that (1) when $V=100\text{m/min}$ and $V=200\text{m/min}$, the fluctuation extension of curve is small, and when $V=360\text{m/min}$, the fluctuation extension of curve is large, which indicates that when the running speed is lower, the yarn dynamic strength is relative stable, and when the running speed is higher, the yarn dynamic tension changes largely, and the tension is difficult to be controlled, (2) the curve of $V=100\text{m/min}$ goes up and the curve of $V=360\text{m/min}$ goes down, which indicates that under usual situation, the running speed of yarn is higher, its dynamic strength is smaller. The results also tell us that in the subsequent process, we can not make yarn exceed its dynamic tension, or else the breaking will happen, and the running speed of yarn should be controlled better, and the speed should not be higher to avoid the large extent fluctuation of yarn tension.

From Table 3, we can see that (1) the Δ (Δ =single yarn strength – dynamic strength) of the No. 8 yarn is maximal, and its single yarn strength and dynamic strength is very large, which indicates the twist influences the strength of yarn whether in static condition or in dynamic condition to some extents, (2) the Δ of the No. 9 yarn is minimum, and though its twist is very high, but its strength is very low, which indicates the twist is not the only factor to decide the yarn strength, and the yarn dynamic strength is influenced by other factors.

3.3 Influence of average fiber length to yarn dynamic strength (experiment 3)

3.3.1 Experiment

(1) Sample: the cotton yarns with the fineness of about 20tex, 1# yarn is the upland cotton with the length of 29mm, and 2# yarn is the long-staple cotton with the length of 37mm.

(2) Testing: respectively test the breaking strength and the dynamic strength of yarn, and analyze the influence of the average fiber length to the dynamic strength of yarn.

3.3.2 Testing result and analysis

The testing results are seen in Table 4. From Table 4, we can see that (1) the average length of cotton fiber is longer, its breaking strength and dynamic tension of yarn is higher, and the reason is that when the fiber length is long and the fineness is thin, the friction resistance among fibers in the yarn is large, and the surge hardly appears, so the yarn strength is high, (2) the difference between the breaking strength of yarn with the dynamic tension under the dynamic testing condition is large, which indicates that the amount of the weak loop in the yarn sample is plenty, and the tension of yarn has serious unevenness, and we should timely inspect and adjust it in the production process.

3.4 Influence of fiber type to yarn dynamic strength (experiment 4)

3.4.1 Experiment

(1) Sample: same 32^s pure cotton yarn and 40^s pure cotton yarn.

(2) Testing: test the breaking tension and dynamic tension, and analyze the influence of yarn fineness to dynamic tension.

3.4.2 Testing result and analysis

The testing results are seen in Table 5. From Table 5, we can see that the fineness of the yarn is higher and the breaking tension and dynamic tension is larger.

The reason is that the fiber is the unit to compose yarn, and the cross section of yarn must contain fibers with quite amount, it can possess certain tension. When the fibers are same in type but the number is different, the yarn is thinner, the fiber amount contained in the unit section is more and the strength is larger.

3.5 Influence of yarn type to yarn dynamic strength (experiment 5)

3.5.1 Experiment

(1) Sample: 32^s pure cotton yarn and 32^s terylene/cotton mixed yarn.

(2) Testing: test the breaking tension and dynamic tension, and analyze the difference of yarn dynamic strength of different sorts of yarn.

3.5.2 Testing result and analysis

The testing results are seen in Table 6. From Table 6, we can see that (1) the breaking strength CV value of the terylene/cotton mixed yarn is lower than the value of pure cotton yarn, which indicates the strength of mixed yarn is very stable, (2) the dynamic tension of the terylene/cotton mixed yarn is obviously higher than the tension of the pure cotton yarn.

The reason is that the strength of terylene fiber is higher than the strength of pure cotton, so the mixed yarn can enhance the dynamic strength of yarn.

4. Conclusions

The dynamic strength of yarn is tested under the running status, so the dynamic property of yarn more really reflect the behavior of yarn in the subsequent machining process to some extent, which offers important technical parameters in the future production process for us and can better control the running status to control the yarn. Secondly, all yarns in the dynamic testing process endure the tests, and all “weak sections” in the testing yarns are tested.

In the article, we analyze the factors to influence the yarn dynamic strength, and these factors including yarn running speed, twist, fineness, fiber length, sorts and mixed ratio all influence the yarn dynamic strength to certain extent, and it is meaningful to grasp and control these influencing factors for enhancing the strength in the spinning and knitting process.

CTT yarn property testing instrument is the most advanced comprehensive property testing and analysis instrument in the world, and the development of the various function of the instrument can not only help us deeply understand and analyze the level and character of foreign advanced spinning testing technology, but offer more direct references and helps to develop new product, adopt new technology, enhance quality and work efficiency, and control the quality of yarn.

References

- Hu, Wenxia. (1996). *Experiment of Textile Materials*. Beijing: Textile Industry Press.
- Li, Ziqiang. (2008). *Probability Theory and Mathematical Statistics Tutorial*. Beijing: Science Press.
- Wang, Hongbo. (2001). The Control and Testing of Yarn Tension. *Beijing Textile Journal*. No.22(5). p.17-20.
- Yaomu. (1993). *Science of Textile Material*. Beijing: Textile Industry Press.

Table 1. The twists and dynamic tension values of yarn under different velocities

No.	Twist (twist/10cm)	Dynamic strength (cN)		
		V=100m/min	V=200m/min	V=360m/min
1-1	97.0	112	110	111
1-2	98.2	120	117	125
2-1	94.4	98	105	107
2-2	97.4	114	125	94
3-1	93.4	114	111	122
3-2	96.5	133	130	112
4-1	95.0	119	116	107
4-2	95.3	118	117	123
5-1	95.0	106	99	119
5-2	95.3	108	113	110
6-1	98.0	98	100	95
6-2	99.2	113	103	95
7-1	94.9	119	111	112
7-2	98.3	113	118	115
8-1	102.1	107	114	94
8-2	96.5	114	103	108
9-1	99.6	120	115	111
9-2	98.8	110	120	117
10-1	95.7	122	113	120
10-2	98.8	112	114	95

Table 2. The dynamic breaking strength values and dynamic strength values under the velocities of 100m/min, 200m/min and 300m/min

Running velocity	V=100m/min		V=200m/min		V=360m/min	
strength	Breaking strength	Dynamic strength	Breaking strength	Dynamic strength	Breaking strength	Dynamic strength
1-1	137	112	144	110	139	111
1-2	169	120	162	117	158	125
2-1	130	98	132	105	134	107
2-2	169	114	161	125	129	94
3-1	140	114	151	111	152	122
3-2	167	133	159	130	155	112
4-1	151	119	150	116	149	107
4-2	147	118	150	117	156	123
5-1	140	106	123	99	148	119
5-2	148	108	137	113	138	110
6-1	134	98	136	100	144	95
6-2	141	113	129	103	130	95
7-1	148	119	139	111	140	112
7-2	156	113	147	118	146	115
8-1	147	107	144	114	139	94
8-2	146	114	129	103	136	108
9-1	139	110	147	115	142	117
9-2	150	120	148	120	152	111
10-1	153	122	160	113	150	120
10-2	139	112	143	114	144	95
Average	148	114	145	113	144	110
Max.	169	133	162	130	158	125
Min.	130	98	123	99	129	94
Level difference		35		31		31
Group distance		5		4.4		4.4

Table 3. Data of differences between single yarn strength and dynamic strength (Δ =single yarn strength – dynamic strength)

Yarn No.	1	2	3	4	5	6	7	8	9	10
Single yarn strength	222	217.5	230.9	224.8	219	216.1	216.1	223.5	213.1	219
Dynamic strength	116	106	123.5	118.5	107	106	116	110.5	115	117
Δ	106	111.5	107.4	106.3	112	110.1	110.1	113	98.1	102
Twist	97.6	95.8	94.9	94.3	95.2	98.6	96.6	99.9	99.2	97.3

Table 4. Experiment data between upland cotton and long-staple cotton

Fiber type	Length of fiber (mm)	Fineness (tex)	Twist (twist/10cm)	Breaking strength (cN)	Breaking strength CV (%)	Strength (cN/tex)	Dynamic strength (cN)
upland cotton	29	20.3	91.4	205.1	10.6	10.1	65
long-staple cotton	37	21.2	87.1	385.8	13.6	17.4	140

Table 5. Experiment data of 32^S yarn and 40^S yarn

Yarn type	Fineness (tex)	Twist (10cm)	Breaking strength (cN)	Breaking strength CV (%)	Strength (cN/tex)	Breaking tension (cN)	Dynamic strength (cN)
Pure cotton 40 ^S	14.4	97.3	167.7	16.15	11.6	128	100
Pure cotton 32 ^S	18.2	82.8	199.4	13.29	11	146	95

Table 6. Experiment data of 32^S pure yarn and 32^S terylene/cotton mixed spinning

Yarn type	Fineness (tex)	Twist (10cm)	Breaking strength (cN)	Breaking strength CV (%)	Strength (cN/tex)	Breaking tension (cN)	Dynamic strength (cN)
Pure cotton 40 ^S	18.2	82.8	199.4	13.29	11	146	95
Terylene/cotton 32 ^S	18.3	70.2	351.1	11.5	19.2	277.5	198.0

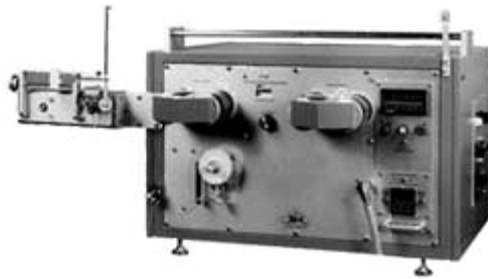


Figure 1. CTT Yarn Property Testing Instrument

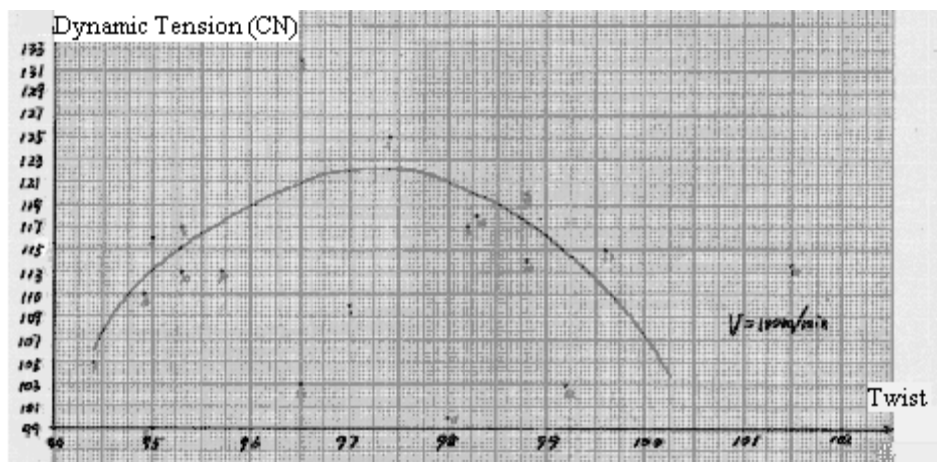


Figure 2. Twist-Dynamic Tension Curve (V=100m/min)

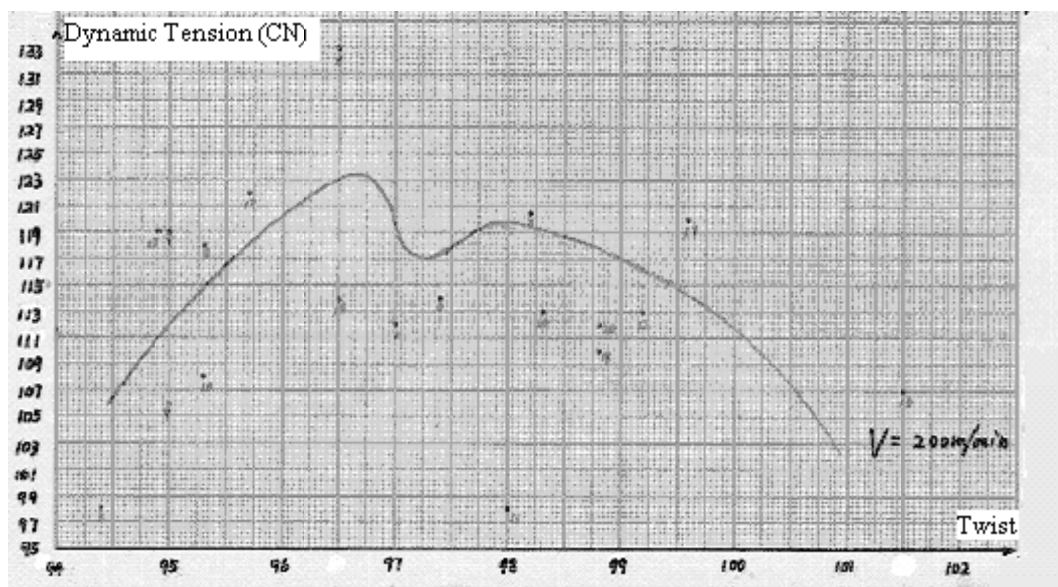


Figure 3. Twist-Dynamic Tension Curve (V=200m/min)

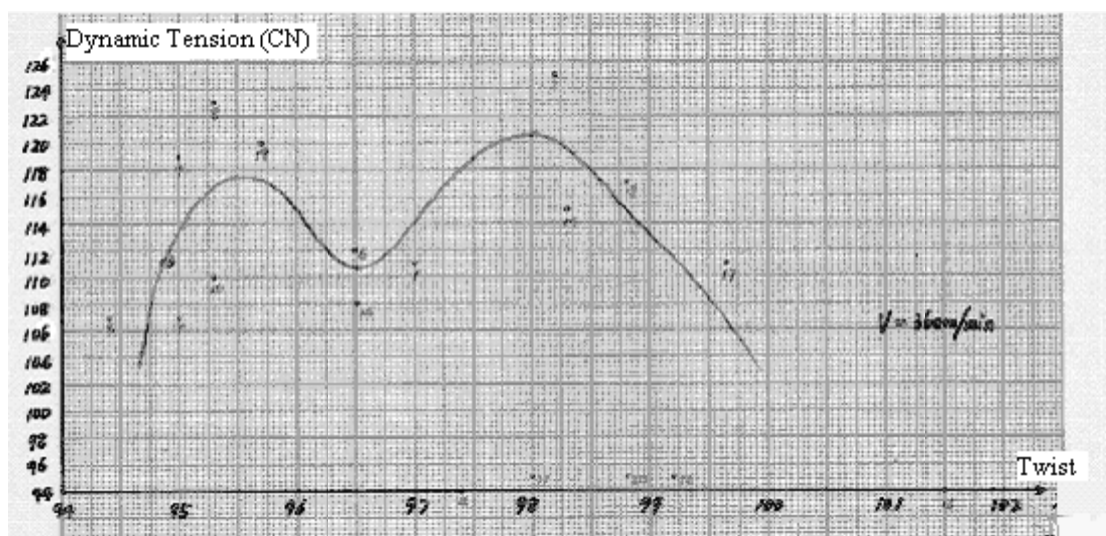


Figure 4. Twist-Dynamic Tension Curve (V=360m/min)

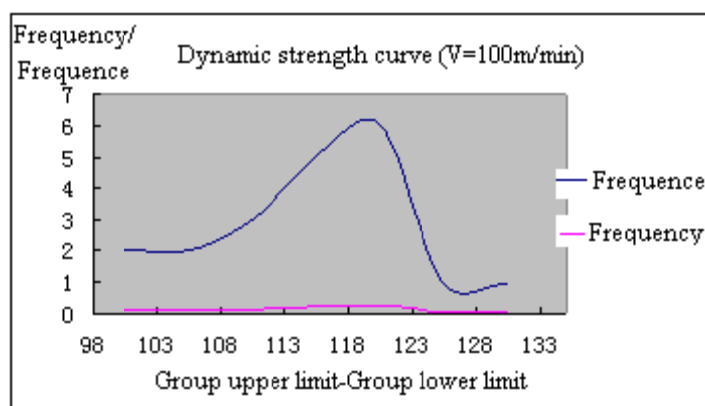


Figure 5. Dynamic Strength Curve (V=100m/min)

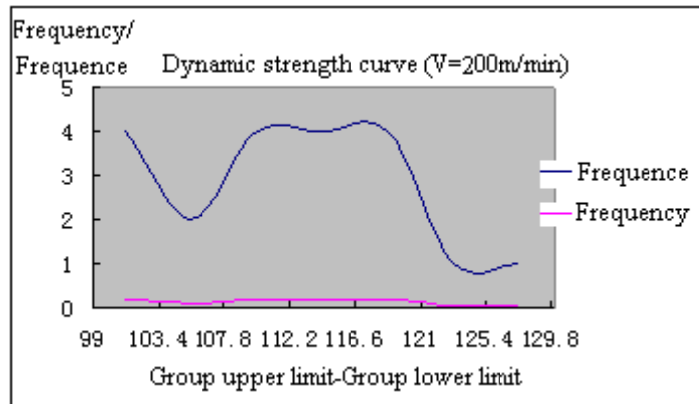


Figure 6. Dynamic Strength Curve (V=200m/min)

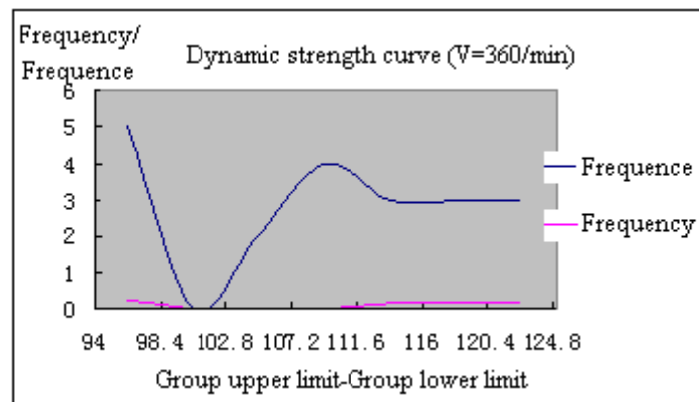


Figure 7. Dynamic Strength Curve (V=360m/min)

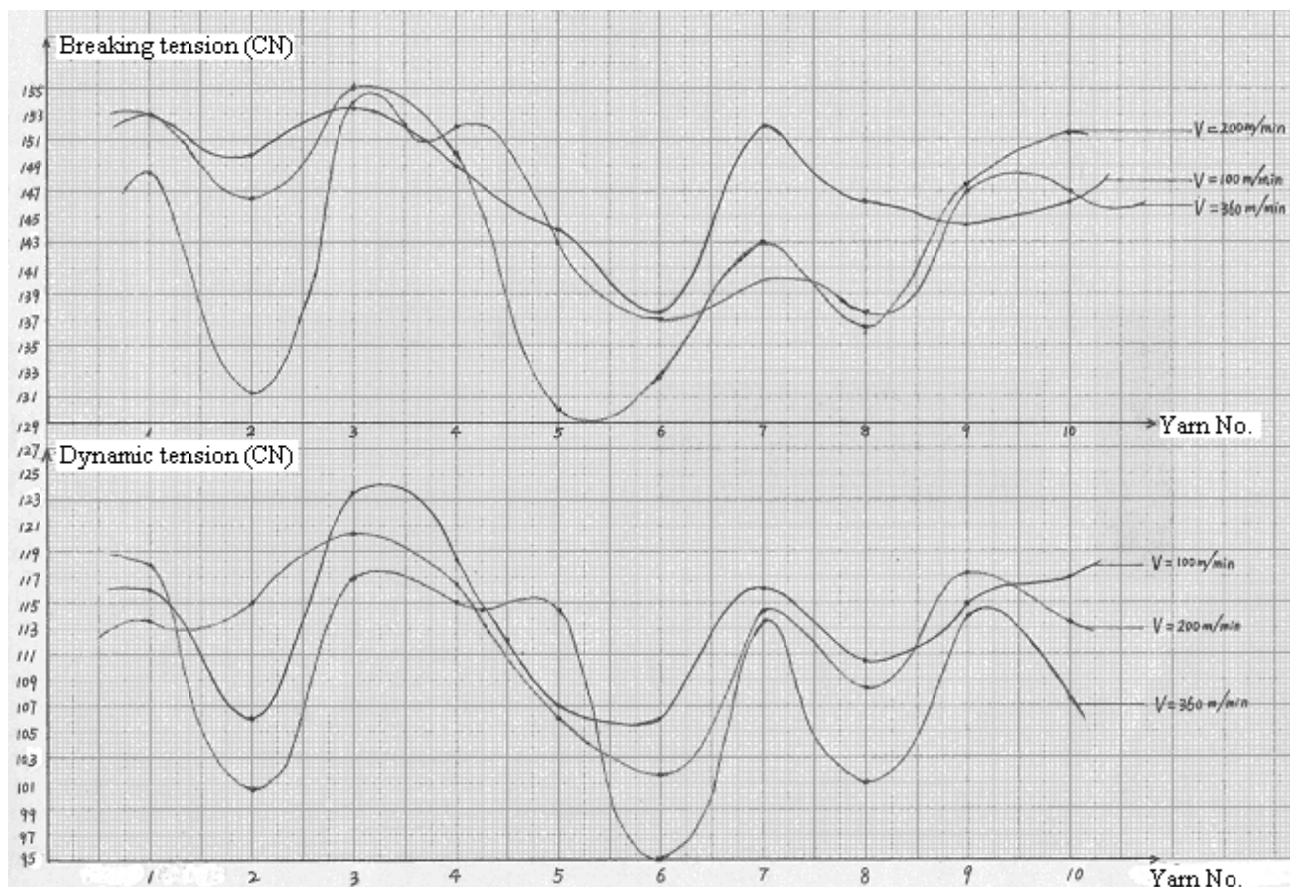


Figure 8. Breaking Tension Curve and Dynamic Tension Curve under Different Velocities



Natural Language Processing for Foreign Languages Learning as Computer-based Learning Tools

Ying Zhang & Junyan Liu

School of Foreign Studies

Jiangxi Science & Technology Normal University

Jiangxi 330013, China

Abstract

This paper outlines a framework to use computer and natural language techniques for various levels of learners to learn foreign languages in Computer-based Learning environment. We propose some ideas for using the computer as a practical tool for learning foreign language where the most of courseware is generated automatically. We then describe how to build Computer Based Learning tools, discuss its effectiveness, and conclude with some possibilities using on-line resources.

Keywords: Natural language, Computer-based Learning tools

1. Computer-based Learning Tool

Now, many computer-based learning (CBL) systems are designed as Web-based Training

(WBT) systems. As pointed by William Horton (2000), the most important features that are required for ideal learners are who:

- Learn independently and view learning positively
- Are self-disciplined, manage time well, and enjoying working alone
- Have a definite goal, such as certification, a degree, or the ability to perform a specific task
- Are moderately experienced in a field and already understand the basic concepts of that field

We in this paper will discuss how the language resources (e.g. machine-readable dictionaries (MRDs), large scale corpora, lexical databases, grammar books, etc.) can be used to build personal-based question-answering tools for learners to learn foreign languages such as English. In this research, we study how to employ various on-line linguistic resources to build CBL tools for training learners/learners to learn foreign languages, we in this paper limit our discussion to English. These tools will be embedded in a CBL system to improve learners' abilities in syntax and vocabulary. Unlike traditional classroom training and over disk-based computer-based training which are unable to corresponding to individual differences and needs efficiently, ours aims to provide a dynamic learning environment in which different learner will answer different questions and learn language knowledge by one pace.

(1) Linguistic knowledge is automatic extracted from on-line machine-readable dictionaries and thesaurus, lexical databases, plain corpora and annotated corpora, grammar books. From these resources, we can automatic extract collocations, co-occurrences, conceptual relations, semantic similarities, contextual similarities, selectional restrictions, the definition and real usage of vocabulary.

(2) Automatic question generation automatically/semi-automatically produce various types of questions and answers form online corpora or dictionaries. These questions will be stored in a question base. This topic will be discussed in Section 4 in detail.

(3) Error detections find and correct misspelling, word or phrase misusing, grammar misunderstanding, etc. and provide this information to learners.

(4) Tutorials for language, grammar, spelling and vocabulary deliver onscreen, sequential instruction that simulates the presentations instructors typically make to a whole class. In general they are self-paced, they are interactive, they provide some drill and practice, and they test learners learning periodically.

(5) Human interfaces are designed for learners, tutors and designers. For learners, they can evaluate these tools by their degrees of satisfaction, and give some suggestions that may be useful to improve the CBL system. For tutors or teachers,

they can check the question base and edit it, assign some important syntactic patterns, and select particular source(s) that is used of generate questions, answers, and explanations if possible. For designers, they can make the system friendlier to the users of the system and extend its applications to other areas or other language.

(6) Student models offer an efficient, time-saving method of keeping track of each learner's progress and record each learner with the items of tests' scores and his degree in learning. The student model of a learner can help the system to generate individual oriented courseware and organize individual learning sequences that let each learner accomplish his/her learning goals.

2. Natural language Processing for Computer-based Learning

Our goal is creating CBL system for learner mainly by drill and exercise learning. Here, we aim to build CBL environment to enrich learners' vocabulary, correct their errors both in syntax and vocabulary. Here, we acquire various kinds of information that is vital for designing our CBL tools. Here, we discuss below several most important cues helpful to realize our aims.

● Word Associations and Mutual Information

We use mutual information (church et al.1990) as a measurement to measure word association norms.

● Semantic Similarity

Semantic Similarity is vital to generate both questions and /or their answers for many types of questions. Here we use The WordNet as a tool that measures the semantic similarities between two words or phrases.

The WordNet is a lexical database organized on psycholinguistic principles (Miller 1990; Beckwith et al. 1991). It has a thesaurus-like structure in which lexical information about nouns, verbs, adjectives and adverbs is put in terms of word meanings, rather than word forms. Two words are considered to be similar if their distance in the WordNet is 0 (synonyms) or 1 in semantic relationships of antonyms (e.g., *man and woman*, *boy and girl*, *black and white*), IS-A (e.g., *red and color*, *man and human*), PART-OF (e.g., *head and body*, *China and Asia*).

● Selectional Restriction

Selectional restriction (SR) governs a semantic relation that occurs between or among the constituents in a phrase or sentence. It can be expressed as semantic constraints in the semantic interpretation process. SR is a semantic restriction imposed on lexical items when forming a sentence. We view SR as negative information, a constraint between two words. We acquire information on SRs from corpora: for a particular adjective and a particular noun, we try to find 'similar' words to them and then check if they co-occur in the corpora. If no co-occurrences are observed in the corpora, then we consider that there is a SR between two words.

Selectional restrictions are used as a semantic constraint when we generate questions.

3. Question Generation

In this section, we shall define five basic question forms for learning English, in which each question is automatically produced using on-line language resources. From these produced questions, instructors can choose and store them in question bases for different level learners, add explanation to the questions if necessary and sort the questions into a unit of a test or a lesson. The number of the question done by a learner and its result are also stored in the learner's student model.

3.1 Multiple-choice questions

Multiple-choice questions display a list of answers for learners to choose from. We generate multiple-choice questions from online linguistic resource such as a dictionary definition randomly selected from on-line machine-readable dictionaries (MRDs) or thesauri like Collins Cobuild English Dictionary, WordNet, etc. The word being defined has been blanked out from the definition. Each missing word is indicated by underline.

Example 1: Fill the missing word by choosing the right word listed.

When you make a _____, you choose what should be done or which is the best of various possible actions.

- (a) plan (b) selection (c) decision (d) adjustment

The candidate words excluding the correct answer (i.e., the missing word) are produced using the words that co-occur the key word(s) and their mutual information is larger than 0. In this example, the key word is *make*.

Multiple-choose questions are easy to construct and easy to understand. Unfortunately, some learners attempt to make a guess rather than think, however.

3.2 Answer-input questions

Answer-input questions demand the learner to type in the answer to a question. Typically, the answer is dependent to the context. Answer-input questions are produced by the similar way of multiple-choose questions that use definition of the

missing word or phrase on-line dictionaries.

Example 2: Can you guess what word or phrase is being defined?

Some people use _____ to call the partner of a married couple that they love each other very much.

Use answer-input questions to verify whether the learners have truly learnt the meanings of words or phrases. The answer may not be unique. Say, in some case, a word should be replaced by its synonyms.

3.3 Correct-misusage questions

Correct-misusage questions demand the learner to use a synonym to replace an underlined word or a phrase that is not suitable to the context. Typically, the answer is justified using the context and the listener's knowledge and/or experience. This kind of question of question is generated using the sentence from some corpus or online grammar book where the modifier is replaced by its similar word defined in WordNet and the mutual information between the replaced word and the word that is modified by it is great less than 0, which means that there is no modifier-modificant relation between the two words and there is a selectional restriction between them.

Example 3: Correct the miss in the following sentence:

His car was involved in a heavy accident. Input your answer: **big**

The system: The correct answer is **serious**, not **big**.

Correct-miss questions are helpful to building and checking learners' vocabulary efficient.

3.4 Fill-in-the-blanks questions

Fill-in-the-blanks questions require the learner to supply missing words in several places in a paragraph of text or a segment in a dialog. Fill-in-the-blanks questions are also called *cloze* questions. Such questions have a long history and are staples of education.

Example 4: Fill in the missing word in underline.

(1) _____ are you?

_____ am _____, Thank _____, and _____?

(2) Suddenly the spring _____, the bad _____ weather _____ gone. It _____ May 1945.

Fill-in-the-blanks questions can also be generated using corpora as the resourcers. What words can be missed, however, is quite difficulty. In many cases, the produced question should be checked by human tutors.

According to Horton, W. (2000), we can use fill-in-the-blanks questions to measure the learner's ability to "apply knowledge within a contextual matrix." That means that learners use a partial answer to figure out the complete answer. Use fill-in-the-blanks questions:

- **To test incremental knowledge.** Learners know part of a subject and apply what they know such as world knowledge and language knowledge to complete the answers.
- **Where context matters.** The correct answer could be inferred from surrounding text.
- **To measure ability to apply verbal knowledge in context.**

3.5 Pick-up-error questions

Pick-up-error questions are generated by choosing typical syntactic patterns from grammar books, corpus, or from instructors, and then replaced these patterns by change the number of verb and noun, the part of speech of a word, the tense of verb, and so on.

Example 5: Find the error in the following sentence and circle its mark.

(1) All of the newly elected council members introduced themselves to the audience.

(A) (B) (C) (D)

(2) John demanded Mary meeting his parents at the park as he was too busy to take a rest.

(A) (B) (C) (D)

3.6 Generate Questions for Individual Learner

To motivate each learner, the question producer should not produce questions too difficult or too easy to the learner. In the recent phase, we consider vocabulary as the standard for define learners' levels. Each learner will decide his/her level by choosing the vocabulary, for example, of three thousand words. In advanced course, the vocabulary will be more than ten thousand words. The CBL tools will sort words with their occurrences in some large scale corpus such as British Nation Corpus, and select the words which rank in the m th (here, m represents the number of words chosen by a

learner).

To activate and motivate learners, the CBL system provides two ways for learners: system-led learning and learner-led learning. The courses can shift from system-led to learner-led during the progress of the course. For example, if a learner has made too many errors, the system will ask if the learner to choose a lower level. To the contrary, if the learner thinks the questions are too easy to him/her, he/her can demand to a higher one.

When the learner's answer is wrong, the system will give the correct answer. If the learner needs more examples, the system will give multiple examples extracted from corpora and other on-line linguistic resources.

4. Discussion

Designing Computer-based Learning systems are normally laborious and also money-consuming work. It costs too much to design courseware and the framework of the system. In our proposal, the framework of the CBL system and courseware are built using natural language processing techniques that employ various machine-readable linguistic resources such as corpora, dictionaries, thesaurus, lexical database, grammar books, and employ various linguistic tools. We think our method is helpful to build CBL system for helping learners to learn foreign language like English. The CBL system ensures that learners can learn at their own pace, provides options for individualized exploration and control of the learning process.

Since there are more and more free or low-cost linguistic resources come to be usable, the CBL system has good extensibility.

References

- Alessi, S.M. & Trollip, S.R. (1991). *Computer-based Instruction: Methods and Development*. Englewood Cliffs: Prentice Hall, 1991.
- Church, K.W. & Hanks, P.: "Word Association Norms, Mutual Information, and Lexicography." *Computational Linguistics*, Vol.16, No.1, pp: 22-29.
- Horton, W. (2000). *Designing Web-based Training*. Robert Ipsen, 2000.
- Morgan, S.(1997). "Computers and Academic Development in English at South African Universities". Paper for SAAAD conference 1997.
- Turton, N.D., & Heaton, J.B.(2001). *Longman Dictionary of Common Errors*. Bilingual English/Japanese edition, 2001.



Treatment and Reuse of Tannery Waste Water by Embedded System

S.Krishnamoorthi (Corresponding author)

Dept. of Civil Engineering

Kongu Engineering College, Perundurai, India

Tel: 91-4294-226700 E-mail: sk_moor@yahoo.co.in

Dr.V.Sivakumar

Dept. of Chemical Engineering

Kongu Engineering College, Perundurai, India

Dr.K.Saravanan

Dept. of Chemical Engineering

Kongu Engineering College, Perundurai, India

E-mail: rumisivaesh@yahoo.com

T.V.Sriram Prabhu

Consultant /Akshay Water Tech.

Perundurai, India

Abstract

Due to scarcity of water problem in India especially southern part of India the large number small and medium scale industries are facing hectic loss in production. On the other hand the effluent discharged from these industries contaminates the water table and water sources. In this juncture, a novel technology should be developed to overcome these problems. Hence the present work focuses attention on the novel methods for treatment of tanner effluent and reuse for other purposes. For this purpose the experiments have been conducted by embedding UF and RO. Experiments have been performed for both UF and RO by varying the pressure and load to the membranes against the flux. Finally, based on the experimental results a suitable embedded system has been suggested for treating tannery effluent.

Keywords: Waste water, RO, UF, BOD, COD, Tannery Effluent

1. INTRODUCTION:

Leather is material that has a reasonable resistance, good chemical stability and acceptable thermal behavior. This material is obtained by means of specific reaction among carboxylic groups of the protein fiber network of animal skin (collagen) and tanning reagents. In today scenario industrial waste water reuse is becoming nearly a duty to contribute to water consumption reduction due to water scarcity in around Erode district of India. Besides; the legal standards are becoming increasingly stringent. Thus those industries with a great water and chemical consumption are required to exhaustive waste water treatment and water reuse. Tanning industries use large quantities of water approximately 15 to 20 m³ per tone of raw skin. During tanning process large amounts of waste water sludge and solid containing chromium, sodium chloride and sulfate are produced. The tannery effluents are characterized by high COD and BOD and conductivity values. The composition of the effluent varies according to the tanning process used and the type of leather to be obtained. The characteristics of the raw waste water from a tannery includes chrome tanning and finishing of cattle hides are shown in Table 1. Waste water is the effluent of the tannery that has a fast interaction with environment. The amount of waste water varies between 30 and 50 L per kilogram of the processed skin (Alexander K.T.W et al., (1992) from, the total amount of liquids, nearly 10 % corresponds to the tanning stage and the remainder to the other stages of processing (dehairing, pickling, neutralization, dyeing and washing). As it can be

observed that COD and SS values approximately five times higher than municipal water waters and high salt concentration similar to that of brackish water.

In order to minimize the pollution of these waters, some of the authors propose the adoption of integrated cleaner technologies (Rao J.R et al., 2003) and the treatment mainly by means of membrane technologies of the waste streams from particular process. It would drive to both water reuse and removal of pollutants that would not be included in the global waste water. Cassanoa and Molinari (1997,2001) studied experimentally the treatment of the unhairing waste stream., pickling solution by means of a RO system and chromium tanning effluent (to reuse water and chemicals by combining UF and RO) Galianna et al (2005) the use of nanofiltration for pickling and tanning effluents in order to minimize the sulphate ions concentration in the global waste water Galiana M.V et al (2005). However the high polluted partial waste streams make difficult the membrane operations Mantari *et al* (2005) In addition, recycling not sufficient for the water reuse after a conventional treatment of global waste water. Other authors suggest an integrated treatment of the global effluent for water reuse. The first step is a physical-chemical treatment of the waste water in order to reduce the suspended solids considerably. This entails COD and BOD5 reduction too. Only few process are able to separate salts from waste water. Reverse osmosis will be more feasible than evaporation, ion exchange or nano filtration because of the conductivity value and the high chloride ion concentration of the waste water. Suthanthararajan et al (2004) proposed an exhaustive tertiary treatment for the biological treated waste water from a tanning industry consisting of a sand filter, a photochemical oxidation step, a softener, chemical dosage cartridge filter NF and RO. This proposed treatment showed obviously excellent point of view these costs can be assumed by most of tanning industries.

On the other hand the operation of a biological reactor for tannery waste waters is sometimes difficult due to high conductivity and the presence of chromium and organic substances coming from finishing operations which can damage the reactor biomass.

The present work focus treatment method for tannery waste which consisting of physical-chemical process (carried in the factory), filtration, ultrafiltration and reverse osmosis is evaluated for water reuse.

1.1 Materials and Methods

The present work was divided into three stages: waste water characterization, UF and RO experiments.

1.2 Waste water characterization

Integrate waste water samples were taken from the tannery plant (**EKM Tannery, Erode**) after being treated with physical-chemical process. The samples were collected in the frequency of one hour at various location and mixed samples was analyzed for further study. The main analyze parameters were COD, turbidity, pH, conductivity, total solids (TS) suspended solids (SS), sulphate, chlorides, and colour.

1.3 UF experiments

Tannery effluent was treated physical-chemically in the industry and filtered at the laboratory with a 25 micron cartridge filter previously to UF experiments. The scheme of UF is shown in Figure 1, UF module was plane with an effective membrane area of 0.009 m². Four polyetersulphone (PES) membranes of different cut off (3,10,30,100 kDa) were tested at different transmembrane pressures (1,2 and 3 bar) For all test the cross-flow velocity was 1.3 m/s and the temperature was held at 25 C. The permeate and reject were recycled to the feeding tank. Periodically permeate flux (Jp), conductivity and pH were determined. In addition at end of each experiments COD, colour, suspended solids and turbidity were analyzed.

1.4 RO experiments

Ro experiments were performed in lab scale plant equipped with pressure vessel that contains one spiral wounded membranes element. The membrane tested was from Hydranautics with an effective area of 2.8 m². The operating conditions were three different transmembranes pressures (20,25 and 30 bar) a feed flow rate of 500 l/h and a temperature of 25 C. Permeate and reject streams were recycled to feed tank.

1.5 Results and Discussion

The characterization of the physical-chemically treated wastewater from tannery was shown in Table 2. It can be seen that the COD and alts concentrations are considerably higher than those measured for municipal waste water.

1.6 UF experiments

UF experiments were carried for both distilled water and tannery waste water. The results are shown in Figure 3. From this figure it can be seen that the measured fluxes at different transmembrane pressure. As expected the higher transmembrane pressure the higher permeate fluxes were achieved. However, from figure 3 it can be seen that the flux sharply increased from 10 to 30 kDa deviating from a lineal flux evaluation with the membrane cut off. In case of tannery waste water experiments the best result in terms of flux and rejection were obtained P= 2 bar and a cross flow

velocity 1.5 m/s. Table 3 shows the characteristic of feed and permeate streams at these operating conditions. For all membranes it can be observed an appreciable turbidity and colour drop after UF process. Nevertheless, COD values hardly decreased. This can be explained as since COD was mainly soluble consisting in hydrolyzed proteins of low molecular weights. The presence of inorganic reduction agents could contribute to the high COD values. The influence of the membranes cutoff on the COD separation was almost negligible. This fact determines the selection of low fouling membranes for the RO step. The variation of the fluxes with operating time is shown in Figure 4a. Fluxes were very low in comparison with those obtained with distilled water figure 4. While the permeate fluxes of the membranes and 10kDa were very low from the beginning of experiments.

The highest flux was achieved by the 30kDa membrane. This flux was even slightly higher than that obtained with the 100 kDa. This behavior can be explained by the effect of the solutes molecular size on the membrane fouling. Table 3 shows the characterization of the feed and permeates streams for the RO experiments. As expected salt and COD rejections were higher than 98%. Permeates can be reused in tannery seen in those process that require the lowest salt concentration like the dyeing one. The evolution of the permeates fluxes with the time at three different transmembranes pressure in the RO tests can be observed in Figure 5.

For these three transmembrane pressures, the steady state was reached after a brief period of time remaining the flux practical constant during the rest of experiments. the solutes concentration was too high enough to produce scaling and fouling problems in the experiments. At 30bar the permeate flux was nearly 40l at steady state.

CONCLUSION

- Reverse Osmosis is necessary for water reuse in a plant when o high chloride concentration
- The combination of a physical-chemically treatment with ultrafiltration was not efficient to remove soluble COD of the waste water.
- The selection of UF membrane was based on the permeate flux rate
- The quality of RO permeate was high enough even after for its reuse in tannery process.
- In spite of organic matter contents of the UF permeate no fouling problems were observed.

References

- APHA Standard methods for the examination of water and waste water, 20th edi 1998.
- Cassano E. Drioli and Molinari R., " Recovery and reuse of chemicals in unhairing,degreasing and chromium tanning process by membranes, Desalination, 113,1997,251-256.
- Cassano „A Molinnari R. Romano and Drioli. E" Treatment of aqueous effluents of the leather industry by membrane process", J.Memb.Science 181,2001 111-126.
- Rao., J.R., Chandrababu., C.Muraidharn,N.B Unni P.G. and Ramasami.T" Recouping the waste water: a way forward for cleaner leather processing , J.Cleaner production, 11(2003) 591-599.
- Sunthanthararajan R. Ravindranath E., Cits, Umamageshwari B. Ramesh T. and RajamaniS." Membrane application for recovery and reuse of water from treated tannery waste water" Desalination 164, 2004, 151-156.

Table 1. Characteristics of tannery effluent

Parameter	Tannery effluent
COD,mg/l	5000-5500
BOD, mg/l	3000-3500
Suspended solids (SS), mg/l	2500-3000
Cr+2, mg/l	80-100
SO4 2-	1800-2000
Cl-, mg/l	5000-6000
pH	8-9
Conductivity, ms/cm	10-12

Table 2. Characterization of the physical-chemically treated waste water from tannery

Parameter	Feed stream
pH	7-9
Conductivity, ms/cm	10-13
COD, mg/l	2700-3600
Sulphates, mg/l	1300-2400
Chlorides, mg/l	2500-3000
TS, mg/l	11000-25000
SS, mg/l	500-800
Colour	0.9-2
Turbidity, NTU	65-95

Table 3. Characterization of Feed and Permeate from RO

Sample	Conductivity, ms/cm	Colour	COD, mg/l	Turbidity, NTU
Feed	12	0.72	2531	53.2
Permeate 100kDa	11.92	0.1	2259	5.7
Permeate 30kDa	11.97	0.1	2133	6.82
Permeate 10kDa	12.03	0.18	2222	8.02
Permeate 3 kDa	11.8	0.12	2197	6.3

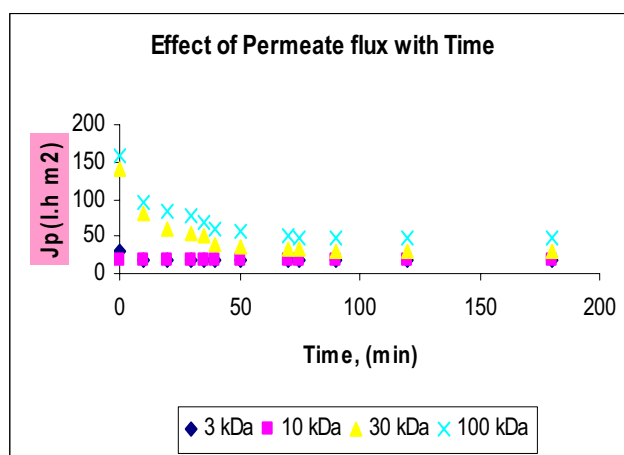


Figure 1.

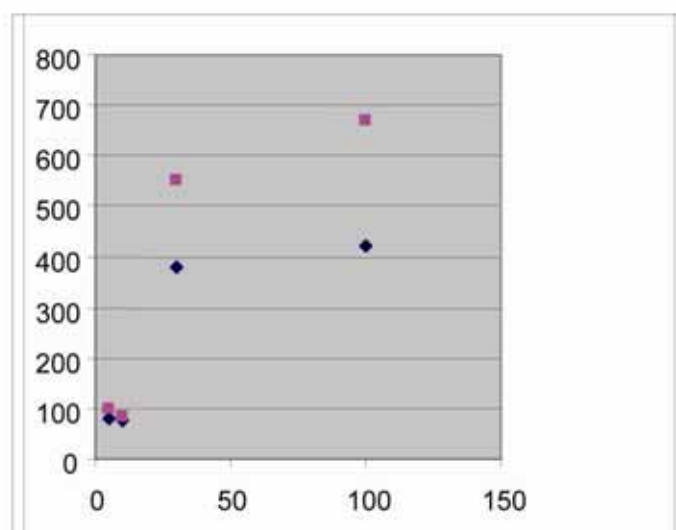


Figure 2.

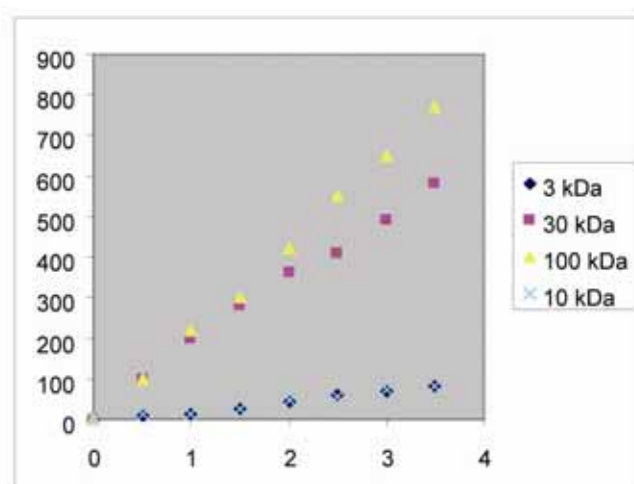


Figure 3.

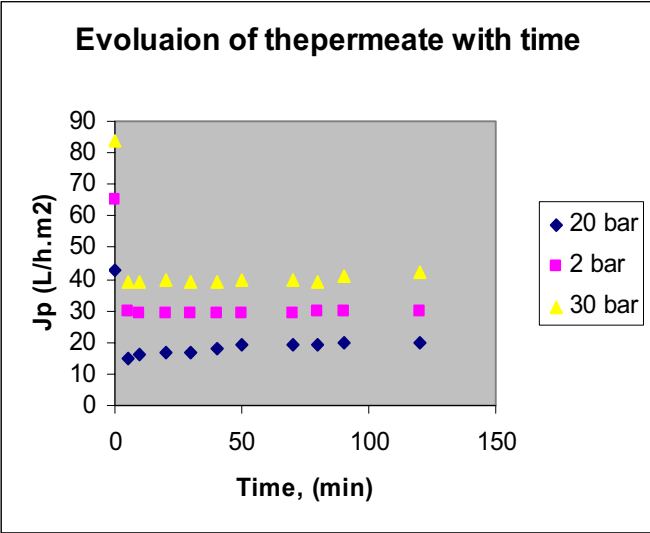


Figure 4.

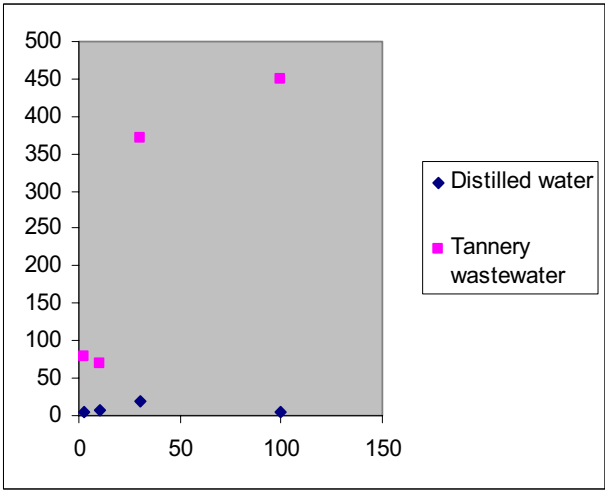


Figure 5.



Study on the Tensile Performance of PTT Fiber

Yuanyuan Zheng

Composites Institute

Tianjin Polytechnic University

Tianjin 300160, China

E-mail: yuanyuanzheng1983@163.com

Jialu Li

Composites Institute

Tianjin Polytechnic University

Tianjin 300160, China

Ruizhou Li

Textile and Apparel Institute

Hebei University of Technology

Shijiazhuang 050018, China

Abstract

To deeply study the mechanics performance of PTT fiber and develop the application domain of PTT fiber, in this article, we implement comparative research of tensile performance to PTT fiber and PET fiber respectively in wet condition and dry condition through experiments, and indicate the advantage of PTT fiber. And based on the experiment result, we study the tensile performance of PTT fiber after acid disposal and alkali disposal, which indicates the acid and alkali resistance of PTT fiber and establishes the base to better be applied in the actual production for PTT fiber.

Keywords: PTT, PET, Tensility, Acid resistance, Alkali resistance

1. Introduction

PTT fiber is a sort of new poalkalister material, and it is assembled by terephthalic acid (TPA) and 1,3-propandiol (PDO), and the homolog of poalkalithylene terephthalate (PET) and poly butylene terephthalate (PBT), and it has many advantages of PET fiber, PBT fiber and PA fiber, such as good elasticity, plasticity, chromaticity, and low pollution to the environment, and it is called as the large fiber in the 21st century (Chen, 2005, p.7-12).

With the extensive use of PTT fiber in the spinning industry, it is urgent to research its performances, especially the tensile performance of PTT fiber. Based on many experiments, in this article, we analyze and study the tensile performance of PTT fiber in four conditions including dry condition, wet condition, acid condition and alkali condition, which possesses certain directional meanings for the spinning technology.

2. Experiment

2.1 Sample

The sample is the PTT fiber with the length of 38mm and the fiber fineness of 1.67dtex.

2.2 Instrument

The instrument in the experiments is the XQ-1 fiber strength elongation instrument.

2.3 The tensile experiment of PTT fiber in dry condition and wet condition

The testing conditions conclude that the distance between gripper is 10mm, the pre-tensile force is 0.1cN, the tensile speed is 10mm/min, and sample amount is 50 pieces, and the experiment results are seen in Table 1.

2.4 Acid resistance performance experiment of PTT fiber

2.4.1 Experiment reagent and instrument

The Experiment reagent and instruments include oil of vitriol, beaker, measuring cylinder, thermometer, scale, constant temperature water bathing pan, glass stick and constant temperature oven.

2.4.2 Experiment scheme

Respectively put up 5%, 20%, 40% and 60% vitriol liquors, and do the experiment once when the temperature raises 30°C every time from 30°C to 90°C, and every temperature is kept in 30min, 60min and 90min, and in every group, record 20 data and compute the average. The bathing ratio is 1:20, and the experiment results are seen in Table 2, Table 3 and Table 4.

2.5 Alkali resistance performance experiment of PTT fiber

2.5.1 Experiment reagent and instrument

The Experiment reagent and instruments include solid sodium hydroxide, beaker, measuring cylinder, thermometer, scale, constant temperature water bathing pan, glass stick and constant temperature oven.

2.5.2 Experiment scheme

Respectively put up 5%, 15% and 25% sodium hydroxide liquors, and do the experiment once when the temperature raises 20°C every time from 30°C to 70°C, and every temperature is kept in 15min, 30min and 45min, and in every group, record 20 data and compute the average. The bathing ratio is 1:20, and the experiment results are seen in Table 5, Table 6 and Table 7.

3. Result analysis of experiment

(1) From Table 1, we can know that the tensile degree of PTT fiber is high in the dry condition, and its breaking mightiness can achieve 8.7cN maximally, and its breaking tensile ratio can maximally achieve 81.3%, but in the wet condition, both the fiber breaking mightiness and the breaking tensile ratio reduce, and whether in the dry condition and in the wet condition, the breaking mightiness of PTT fiber is lower than PET fiber, but its breaking tensile ratio is far higher than PET fiber.

The reason is that the PTT fiber possesses the zigzag molecule structure which is easier to produce distortion, so the ability to resist the tensile and destroying of outside force is high, but the big molecule chain in the PET fiber almost presents a structure with complete stretch, only little stretch can completely extend the molecule, so the initial modulus of PET is higher, and the tensile recover elasticity is bad, and because the curve rigidity and the pliability of fiber are influenced by the initial modulus, so PTT fiber possesses high elasticity and good elasticity recovery ratio, and the fabric made by PTT fiber has better pliability than PET fiber.

(2) From Table 2, Table 3 and Table 4, we can know that, when the temperature is in 30°C, the breaking mightiness and the breaking tensile ratio of PTT after acid disposal change little, and with the increase of vitriol concentration, the breaking tensile ratio goes to increase, and when the temperature is in 60°C, the breaking intension and the breaking tensile ratio of PTT obviously reduce with the increase of vitriol concentration, but the influence of time to the breaking mightiness is not obvious, and the breaking tensile ratio gradually reduces with the prolonging of water bathing time, and when the temperature is in 90°C, two factors influence the PTT fiber breaking mightiness and breaking tensile ratio very significantly, and the vitriol concentration is higher and the disposal time is longer, the breaking mightiness and the breaking tensile ratio reduce more obviously.

The breaking mightiness and the breaking tensile ratio of PTT fiber gradually reduce with the increase of temperature, the increase of vitriol concentration and the prolonging of disposal time, and its change ranges are 0~60%of breaking mightiness and 0~28% of breaking tensile ratio.

(3) From Table 5, Table 6 and Table 7, we can know that the breaking mightiness and the breaking tensile ratio of PTT fiber after alkali liquors in different temperatures and different time period change little, and its breaking tensile increases little on the contrary, and its change ranges 0~24%of breaking mightiness and 0~58% of breaking tensile ratio.

4. Conclusions

The mightiness of PTT fiber is in the cotton fiber and the terylene fiber, and it is higher than cotton fiber, so it is can enhance the breaking of mixed spanning when PTT fiber is mixed with cotton fiber. The breaking mightiness is lower 20%~30% than terylene fiber, but its breaking tensile ratio is far higher than terylene fiber, so the PTT fiber possesses excellent tensile recovery performance. PTT fiber can resist alkali but not acid, so we should pay attention to this point when selecting the fiber or in the use process of PTT pure spinning and mixed spinning fabrics.

References

- Chen, Kequan. (2005). Development of PTT Products and its Commercial Production in Shanghai Petrochemical Co., Ltd. *Synthetic Fiber in China*. No.2. p.7-12.
- Fang, Xuejuan. (2005). The Structure, Property and Application of PTT Fiber and Fabric. *Synthetic Fiber in China*. No.2. p.32-34.

Liu, Qiuying & Zhang, Youhe. (2005). Development of Novel Ring-spun Yarns, Lecture 5 Properties of the New Type Poalkalister Fiber-PTT and the Textile Production Technology. *Advanced Textile Technology*. No.5. p.54-56.

Qiu, Yufa. (2005). Product Development with PTT Fiber. *Advanced Textile Technology*. No.6. p.35-36.

S. Deiss & E. Seidel. (2005). Continuous PTT Process. *Synthetic Fiber in China*. No.2. p.41-44.

Wei, Gaofu, Gu, Lixia, Dai, Zhibin & Changhua. (2005). The Research Advance of Poly(trimethylene terephthalate). *Synthetic Fiber in China*. No.2. p.1-6.

Wei, Gaofu. (2005). Synthetic Research on PTT. *Synthetic Fiber in China*. No.2. p.20-22.

Table 1. The tensile experiment results of PTT fiber in the dry or wet condition

Item	Dry condition		Wet condition	
	BF (cN)	ET (%)	BF (cN)	ET (%)
PTT	5.50	50.40	5.16	46.00
PET	8.50	33.04	8.40	32.30

Table 2. The acid resistance of PTT fiber in the water bathing temperature of 30°C

Item	5%		20%		40%		60%	
	BF (cN)	ET (%)	BF (cN)	ET (%)	BF (cN)	ET (%)	BF (cN)	ET (%)
30min	5.0	85.3	5.0	87.7	5.2	89.5	5.0	70.6
60min	5.0	74.1	5.1	82.2	5.5	84.6	5.6	89.6
90min	5.2	84.3	5.1	82.2	5.0	84.0	5.1	86.5

Table 3. The acid resistance of PTT fiber in the water bathing temperature of 60°C

Item	5%		20%		40%		60%	
	BF (cN)	ET (%)	BF (cN)	ET (%)	BF (cN)	ET (%)	BF (cN)	ET (%)
30min	5.3	87.8	5.1	92.5	4.8	89.0	4.4	68.6
60min	5.4	78.7	5.5	78.4	5.5	79.1	4.6	65.6
90min	5.2	87.6	5.6	84.2	5.4	81.3	4.1	61.6

Table 4. The acid resistance of PTT fiber in the water bathing temperature of 90°C

Item	5%		20%		40%		60%	
	BF (cN)	ET (%)	BF (cN)	ET (%)	BF (cN)	ET (%)	BF (cN)	ET (%)
30min	5.2	89.4	5.4	88.3	4.9	74.2	3.0	43.9
60min	5.3	78.2	4.8	71.9	5.3	88.5	2.6	38.2
90min	5.1	94.1	4.7	80.8	4.6	69.6	2.2	36.3

Table 5. The alkali resistance of PTT fiber in the water bathing temperature of 30°C

Item	5%		15%		25%	
	BF (cN)	ET (%)	BF (cN)	ET (%)	BF (cN)	ET (%)
15min	4.5	71.5	4.2	69.7	4.3	70.3
30min	4.7	73.5	4.4	70.6	5.1	82.1
45min	4.6	79.4	4.7	68.2	4.3	75.6

Table 6. The alkali resistance of PTT fiber in the water bathing temperature of 50°C

Item	5%		15%		25%	
	BF (cN)	ET (%)	BF (cN)	ET (%)	BF (cN)	ET (%)
15min	4.7	73.8	4.5	67.5	4.7	76.7
30min	4.9	79.7	4.6	72.3	4.2	69.2
45min	4.9	75.3	4.4	69.8	4.3	70.3

Table 7. The alkali resistance of PTT fiber in the water bathing temperature of 70°C

Item	5%		15%		25%	
	BF (cN)	ET (%)	BF (cN)	ET (%)	BF (cN)	ET (%)
15min	4.7	78.5	4.0	59.4	4.7	75.1
30min	4.6	78.0	4.7	74.3	4.4	74.8
45min	4.2	66.0	4.4	68.8	4.2	64.1



Acid Resistance Behavior of Concrete Made Using Untreated and Treated Tannery Effluent

K Nirmalkumar

Department of Civil Engineering, Kongu Engineering College

Perundurai-638 052, Tamil Nadu, India

E-mail: nirmal2555080@yahoo.co.in

V Sivakumar

Department of Chemical Engineering, Kongu Engineering College

Perundurai-638 052, Tamil Nadu, India

Abstract

There was a severe water problem especially in the summer season in and around Erode (Erode district, Tamil Nadu, India) where there is more number of tannery units. Hence an attempt was made to use the waste water from tannery industry for construction purpose, so that the shortage in water can be greatly reduced and the waste water can be suitably disposed for safe guarding the environment. The basic properties of the treated and untreated water from the tannery industry were tested and the results were found to be satisfactory such that it can be used for construction purposes. The mechanical properties like compressive strength, tensile strength, flexural strength etc were studied by casting various concrete specimens in form of cube, cylinders and beams etc and were found to be satisfactory. Hence some special properties like freeze and thaw test, alkali aggregate reaction, chloride attack, sulphate attack, acid resistance etc were considered and comparatively studied with the nominal potable water. In this paper acid resistance property is discussed in detail.

Keywords: Acid resistance, Sulphuric acid, Concure, Calcium nitrate

1. Introduction

Acid attack generally occurs where the calcium hydroxide is attacked vigorously, although all the Portland cement compounds are susceptible to degradation. Acidic solutions both mineral (such as sulphuric, hydrochloric, nitric, and phosphoric acids) and organic (such as lactic, acetic, formic, tannic, and other acids produced in decomposing silage) are about the most aggressive agents to concrete. Depending on the type of acid, the attack can be mainly an acid attack, or a combination of acid followed by a salt attack. It cannot cause deterioration in the interior of the specimen without the cement paste on the outer portion being completely destroyed. The rate of penetration is thus inversely proportional to the quantity of acid neutralizing material, such as the calcium hydroxide, C-S-H gel, and limestone aggregates. In practice, the degree of attack increases as acidity increases; attack occurs at values of pH below about 6.5, a pH of less than 4.5 leading to severe attack. The rate of attack also depends on the ability of hydrogen ions to be diffused through the cement gel (C-S-H) after calcium hydroxide ($\text{Ca}(\text{OH})_2$) has been dissolved and leached out.

2. Experimental

The natural river sand was used, tested and conforming to the specifications IS 2386 (Part II)-1963, IS 2386 (Part III)-1963, IS 2386 (Part IV)-1963 and IS 2386 (Part VI)-1963. The fines modulus of sand used is 2.80 with a specific gravity of 2.54. A good quality crushed granite coarse aggregates was used and the coarse aggregate was tested as per the specifications IS 2386 (Part III)-1963, IS 2386 (Part IV)-1963, IS 2386 (Part V)-1963, IS 2386 (Part VII)-1963 and IS 2386 (Part VIII)-1963. The crushing value of coarse aggregate is tested as per IS 9376-1979, and its impact value is tested as per IS 9377-1979. The cement used was 53 grade ordinary Portland cement conforming to IS 12269-1987. In addition few other properties were tested as per the procedure given by M S Shetty (2001) and Rangwala (1997). Concrete mixes were designed for M_{20} , M_{25} and M_{30} to study the mechanical strength properties and durability properties as per IS 10262-1982. But here only for M_{20} grade of concrete is discussed. Standard cylindrical steel moulds measuring 150mm diameter and 300mm height were used for the preparation of test specimen as per IS 10086-1982 which is used to determine the loss of weight of the specimen and cube of 150mm size is used to determine the reduction in compressive strength. The admixture was selected and used based on the guidelines of the

specifications IS 9103-1978 and ACI 212. The admixtures concare (2.5%) and calcium nitrate (2.0%) are added with respect to the weight of the cement.

As per Wallah(2006), the cubes are cast and immersed in 2% solution (2 litre sulphuric acid for 10 litre water) of sulphuric acid (H_2SO_4) after 28 days, 6months, 1 year, 2 year and 2.5 year for a period of 7 days. The visual examination, loss in weight and compressive strength are tested. To check the continuous effect, the cubes were cast and immersed after 28 days in 2% sulphuric acid for a period of 180 days, one year, two year and 2.5 year and the results were observed. But here only the 7 days immersion effect is considered and discussed in detail.

3. Results and Discussions

For M_{20} grade of concrete, the weight of the specimen cast using potable water decreases by about 2.27% after 28 days test and 1.75% after 2.5 year test, similarly the decrease in weight for specimen cast using untreated tannery water is about 3.30% after 28 days test and 2.80% after 2.5 year test and the decrease in weight for specimen cast using treated tannery water is about 3.28% after 28 days test and 2.77% after 2.5 year test. The comparison is graphically shown in figure 1.

The compressive strength of concrete specimen cast using potable water is 17.21 N/mm^2 after 28 days and 20.10 N/mm^2 after 2.5 year, similarly the compressive strength of concrete specimen cast using untreated tannery water is 17.93 N/mm^2 after 28 days and 20.82 N/mm^2 after 2.5 year and the compressive strength of concrete specimen cast using treated tannery water is 17.59 N/mm^2 after 28 days and 20.48 N/mm^2 after 2.5 year. The comparison is graphically shown in figure 2.

When 2.5% concare is added, the weight of the specimen cast using potable water decreases by about 2.23% after 28 days test and 1.73% after 2.5 year test, similarly the decrease in weight for specimen cast using untreated tannery water is about 3.26% after 28 days test and 2.76% after 2.5 year test and the decrease in weight for specimen cast using treated tannery water is about 3.25% after 28 days test and 2.74% after 2.5 year test. The comparison is graphically shown in figure 3.

The compressive strength of concrete specimen cast using potable water is 17.74 N/mm^2 after 28 days and 20.63 N/mm^2 after 2.5 year, similarly the compressive strength of concrete specimen cast using untreated tannery water is 18.46 N/mm^2 after 28 days and 21.35 N/mm^2 after 2.5 year and the compressive strength of concrete specimen cast using treated tannery water is 18.12 N/mm^2 after 28 days and 21.01 N/mm^2 after 2.5 year. The comparison is graphically shown in figure 4.

When 2.0% calcium nitrate is added, the weight of the specimen cast using potable water decreases by about 1.24% after 28 days test and 1.75% after 2.5 year test, similarly the decrease in weight for specimen cast using untreated tannery water is about 3.27% after 28 days test and 2.77% after 2.5 year test and the decrease in weight for specimen cast using treated tannery water is about 3.26% after 28 days test and 2.75% after 2.5 year test. The comparison is graphically shown in figure 5.

The compressive strength of concrete specimen cast using potable water is 17.83 N/mm^2 after 28 days and 20.72 N/mm^2 after 2.5 year, similarly the compressive strength of concrete specimen cast using untreated tannery water is 18.55 N/mm^2 after 28 days and 21.44 N/mm^2 after 2.5 year and the compressive strength of concrete specimen cast using treated tannery water is 18.21 N/mm^2 after 28 days and 21.10 N/mm^2 after 2.5 year. The comparison is graphically shown in figure 6.

4. Conclusion

The decrease in weight decreases with passage of time i.e after 28 days test, the decrease in weight is 2.27% but after 2.5 year test it is only 1.75% for potable water and this condition is same for all the specimens' cast using different water. This may be due to the reduction in permeability factor. However to reduce the effect of acid attack, the admixture's like concare (2.5%) and calcium nitrate (2.0%) are added and the results are also studied and discussed. There is a slight reduction in decrease in weight of the specimen, but however it is very marginal.

As for as the acid resistance factor is considered, there is no effect on concrete using treated and untreated tannery water. Hence it can be recommended that the treated and untreated tannery water can be used for construction purpose considering the other factors and properties.

References

ACI Committee 212 (2002), Classification of Admixtures, ACI manual of concrete practice, American Concrete Institute, Farmington Hills, USA.

IS 10086-1982, Indian Standard specification for moulds for use in tests of cement and concrete-V Reprint December 1995, Bureau of Indian Standard, New Delhi-110 002.

IS 10262-1982, Indian Standard Recommended guide lines for concrete mix design V print march 1998, Bureau of Indian Standard, New Delhi-110 002.

IS 2386 (Part II)-1963, Indian Standard Methods of test for aggregates for concrete: deteriorious materials and organic impurities, VIII reprint April 1996, Bureau of Indian Standard, New Delhi-110 002.

IS 2386 (Part III)-1963, Indian Standard Methods of test for aggregates for concrete: Specific gravity, density, voids, absorption & bulking, VIII reprint March 1997, Bureau of Indian Standard, New Delhi-110 002.

IS 2386 (Part IV)-1963, Indian Standard Methods of test for aggregates for concrete: Mechanical properties, IX reprint June 1996, Bureau of Indian Standard, New Delhi-110 002.

IS 2386 (Part V)-1963, Indian Standard Methods of test for aggregates for concrete: Soundness, VIII reprint November 1996, Bureau of Indian Standard, New Delhi-110 002.

IS 2386 (Part VI)-1963, Indian Standard Methods of test for aggregates for concrete: Mortar making properties of fine aggregates, VIII reprint April 1997, Bureau of Indian Standard, New Delhi-110 002.

IS 2386 (Part VII)-1963, Indian Standard Methods of test for aggregates for concrete: alkali aggregate reactivity, IX reprint June 1996, Bureau of Indian Standard, New Delhi-110 002.

IS 2386 (Part VIII)-1963, Indian Standard Methods of test for aggregates for concrete: Petrographic examination, VII reprint August 1991, Bureau of Indian Standard, New Delhi-110 002.

IS 9103-1978, Indian Standard Specification for addition of admixtures, Indian Standards Institution, New Delhi-110 002.

IS 9376-1979, Indian Standard Specification for Apparatus for measuring aggregate crushing value and 10% fine value. I reprint May 1997. Bureau of Indian Standard, New Delhi-110 002.

IS 9377-1979, Indian Standard Specification for apparatus for aggregate impact value, I reprint July 1990. Bureau of Indian Standard, New Delhi-110 002.

Rangwala (1997), Engineering Materials, Charotar publishers., pp 150-158.

Shetty M S (2003), Concrete Technology Theory and Practice – S.Chand & Company Ltd, pp 399-400,429-438, 449-501.

Wallah S.E and Rangan B.V (2006), Low calcium fly ash based geopolymer concrete: long term properties, research report GC2, Faculty of Engineering, Curtin University of Technology, Perth, Australia, available at espace@curtin or www.geopolymer.org.

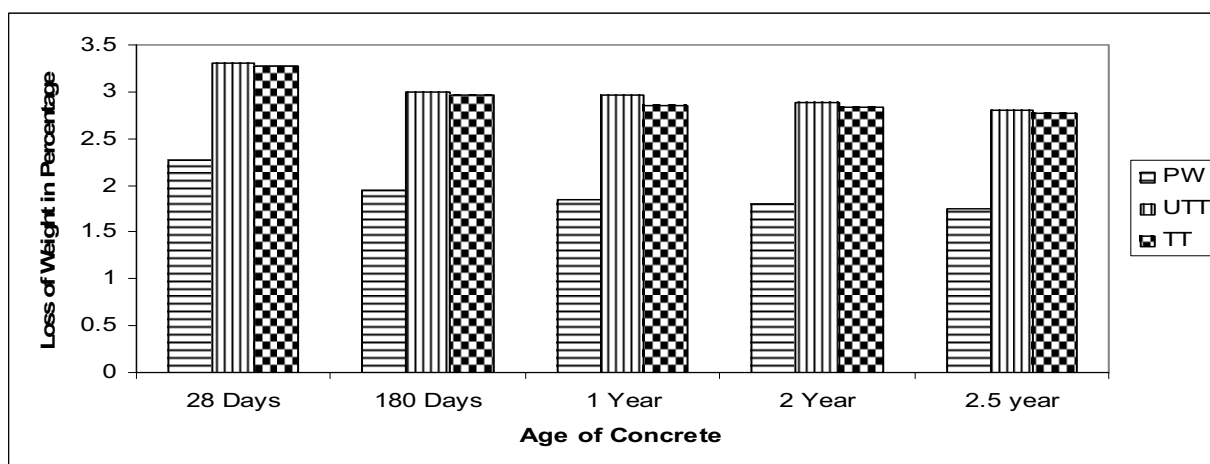


Figure 1. Comparison of decrease in weight due to acid attack for potable water, untreated tannery Water and treated tannery water for M₂₀ grade of concrete without adding admixture

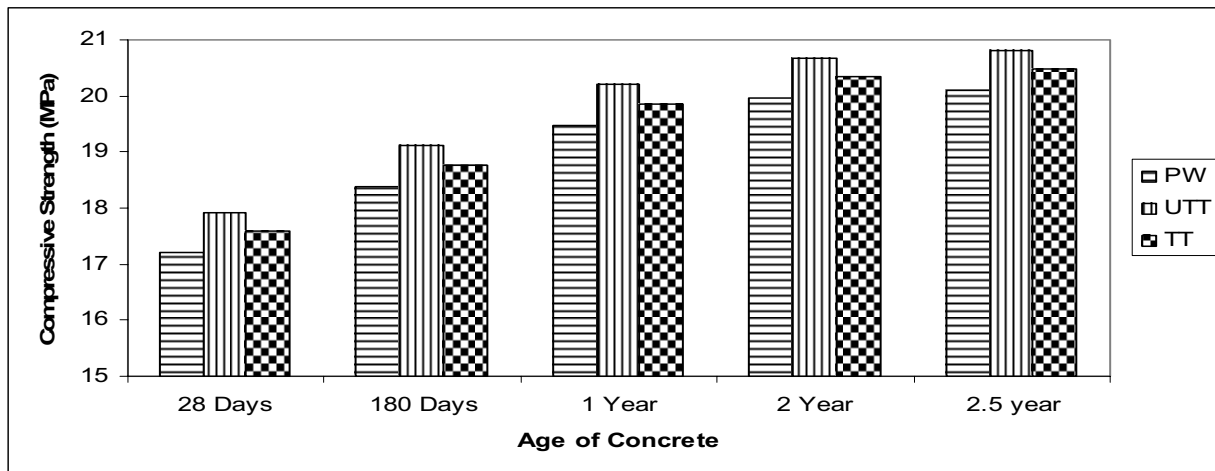


Figure 2. Comparison of compressive strength due to acid attack for potable water, untreated tannery Water and treated tannery water for M_{20} grade of concrete without adding admixture

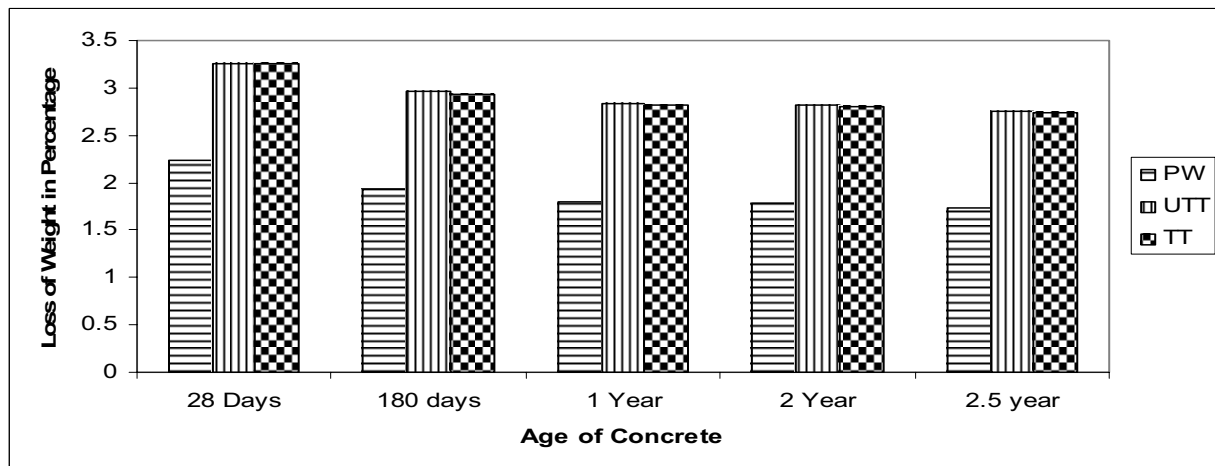


Figure 3. Comparison of decrease in weight due to acid attack for potable water, untreated tannery Water and treated tannery water for M_{20} grade of concrete adding 2.5% concare admixture

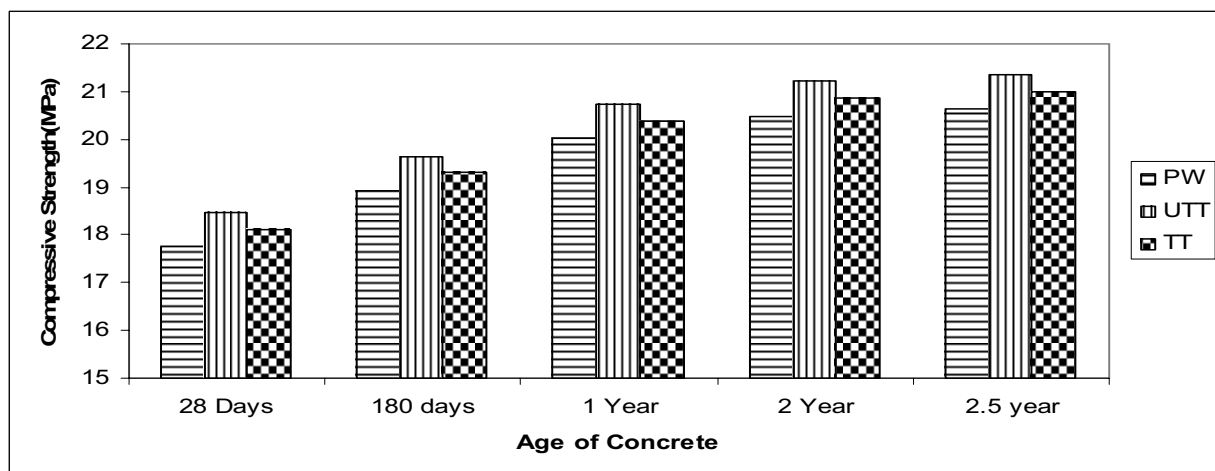


Figure 4. Comparison of compressive strength due to acid attack for potable water, untreated tannery Water and treated tannery water for M_{20} grade of concrete adding 2.5% concare admixture

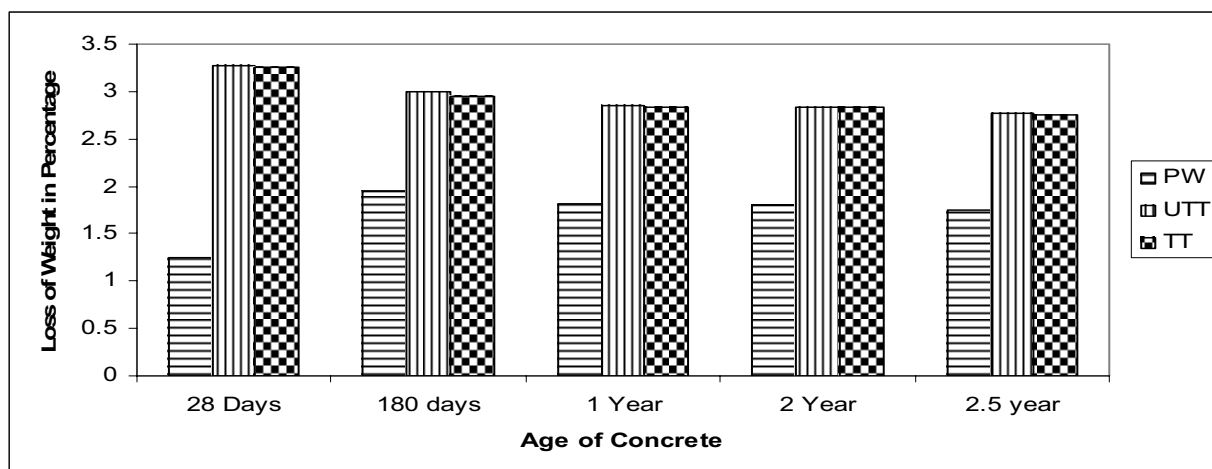


Figure 5. Comparison of decrease in weight due to acid attack for potable water, untreated tannery Water and treated tannery water for M₂₀ grade of concrete adding 2.0% calcium nitrate admixture

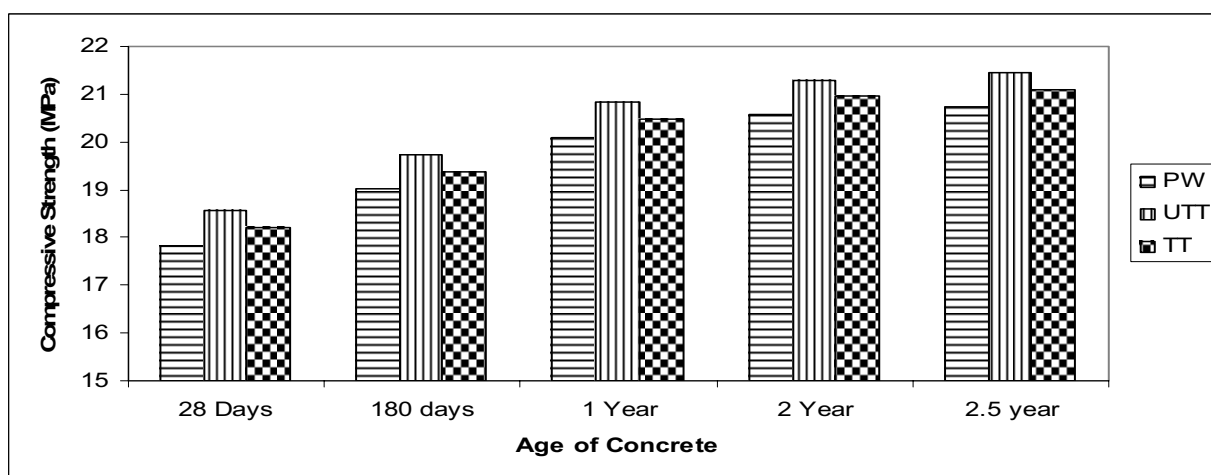


Figure 6. Comparison of compressive strength due to acid attack for potable water, untreated tannery Water and treated tannery water for M₂₀ grade of concrete adding 2.0% calcium nitrate admixture



Study of PVDF Tubular Ultrafiltration Membrane for Separating Oil/water Emulsion and Effect of Cleaning Method on Membrane

Huazhang Zhu (Corresponding author)

Key Lab of Hollow Fiber Membrane Materials & Membrane Process of Education Ministry

Tianjin Polytechnic University

TianJin 300160, China

Tel: 86-22-2452-8226 E-mail: zhuhuazhang1982@hotmail.com

Yujie Zhu

Institute of Material & Chemical Engineering

Tianjin Polytechnic University

Tianjin 300160, China

Tel: 86-22-2452-8226 E-mail: zyj_aj@hotmail.com

Abstract

Oil/water emulsion is treated with polyvinylidene fluoride (PVDF) tubular ultrafiltration membrane. The flux of PVDF tubular ultrafiltration membrane is tested by varying the operation pressure (from 0.06 Mpa to 0.25 Mpa), membrane surface velocity of flow (from 1.47 m/s to 3.69 m/s) and system running time (from 1 h to 20 h). The average membrane flux is up to 108.2 L/(m²·h) in proper experiment conditions. Then some cleaning methods are studied and the chemical cleaning has the best effect, the flux restoration rate is more than 92%. Oil concentration in permeate water was less than 10 mg/L. The rejection rate of oil was more than 90%. The cleaning periods were 24 h. Using PVDF tubular ultrafiltration membrane to treat oil/water emulsion is a feasible and economical method.

Keywords: PVDF, Tubular ultrafiltration membrane, Oil/water emulsion, Separating, Membrane cleaning

1. Introduction

Oil/water emulsion are common by-products of manufacturing operations, such as the machining and washing of metal parts. Usually, over 90% of these solutions is water. The oil is chemically emulsified into the water phase because of the presence of surfactants. The entire mixture, even though it contains less than 10% total oil, can not be discharged, because the COD is up to 11000 - 37000 mg/L (Gao, 1989, pp.32-45 and Jiang, 1986, pp.13-16). In addition, metals may be in it. So in most localities, these wastewater must be shipped off-site as hazardous waste which cost too much. Using traditional technology, such as chemical coagulation, to treat the oil/water emulsion is the common method. However, the amount of sludge production is huge, which is likely to cause the secondary pollution. What's more, the wastewater couldn't be reuse after the treatment, which may cause the great waste of water. On the other hand, since there are high dense oil and organic substances in oil/water emulsion, large quantities coagulant as well as the high operating costs are needed (Jiang, 1986, pp.13-16). Membrane filtration can be used to remove most of the water from the emulsion therefore reduce the volume of oil-containing solution.

Use ultrafiltration process to treat the oil/water emulsion not only can achieve the reuse of wastewater but also solve the secondary pollution problem (Lipp, 1988, pp.161-177 and Bilstad, 2001, pp.23-24). At present, there are many treatments with oil/water emulsion by using ultrafiltration or microfiltration membrane, such as flat membrane, hollow fiber membrane, ceramic tubular membrane. But the flux of flat membrane and hollow fiber membrane are too low and the ceramic tubular membrane is too expensive, which prevent from using of these membranes (Shao, 1992). Because its low costs and high separating efficiency, the PVDF tubular ultrafiltration membrane show a bright prospect in separating oil/water emulsion.

2. Experimental

2.1 Materials and equipment

The oil/water emulsion was prepared with emulsified oil (No.1 machine factory in TianJin) and tap water. The sodium hydroxide, sulfuric acid, sodium hypochlorite (FuChen Chemical Ltd. Tianjin). Spongy rubber ball membrane cleaning

system and evaluation system of membrane were equipped by lab. The oil concentration in the waste water is attainable by testing its absorbency with UV spectrophotometer (2450, SHIMADZU). PVDF tubular ultrafiltration membrane which rejection molecular weight were 100,000 (Tianjin Motian Membrane Eng&Tech Company).

2.2 Experimental methods

2.2.1 Membrane performance

This research used internal pressure PVDF tubular ultrafiltration membrane to treat oil/water emulsion. Under different running conditions, the flux and rejection rate to oil of membrane were investigated. The distilled water was used to determine the pure water flux of membrane. First, the membrane filtrated distilled water under certain operation pressure for about 2h to stabilize the flux of distilled water. Then oil/water emulsion were instead, then the membrane flux was recorded in certain running time.

2.2.2 Cleaning methods

Using different cleaning membrane methods to compare their effects of cleaning (flux restoration rate). The flux restoration rate was determined as follows: First, the membrane filtrated distilled water under certain operation pressure for about 2h to stabilize the flux1 of distilled water. Then oil/water emulsion were instead and the flux was test after certain running time. Third, one of the cleaning method was used to clean the membrane. Last, the membrane filtrated distilled water again and flux2 value was test. The ratio between flux2 and flux1 was the flux restoration rate. The higher it was, the better the clean effect was. Scanning electron microscopy (SEM) to observe the surface of fouling and cleaning membrane. All the experiments were carried out under room temperature(20°C).

The cleaning methods include: washed by water, washed by alkaline solution (1.5%) and washed by spongy rubber balls. The spongy rubber ball cleaning system was shown in Fig.1, the spongy rubber balls were added into the system from ball circulator and circulated together with water. Thus turbulence were formed by these balls, with the balls colliding the interface of tubular ultrafiltration membrane, cleaning was achieved (Hao,2005,pp.75-80).

3. Results and Discussions

3.1 Effect on operation pressure

Fig.2. shows the flux of different oil concentration in oil/water emulsion change with operation pressure. Regardless of different oil concentration, all the flux increase with operation pressure increasing, and reached to maximum at 0.20Mpa. This mainly because when the system runs, the membrane is compressed by the liquid, so the thickness of membrane decreased slightly which strengthen the liquid permeate resistance. When the operation pressure is beyond 0.20Mpa, the increase of flux caused by pressure increase is overcome by flux reduce caused by permeate resistance which increase with pressure increasing. So the flux decrease with pressure increasing when running pressure is beyond 0.20MPa.

3.2 Effect on membrane surface flow velocity

Fig.3 describes the membrane flux of different membrane surface flow velocity change with operation time. The flux increase significantly with the increase of membrane surface flow velocity, but the increase rate reduce. In addition, the flux decrease with the increase of running time under low flow velocity, while it is beyond 2.46 m/s, the flux almost unchange with the increase of running time. This is mainly because under high membrane surface flow velocity, the shear stress between flow and the membrane surface is large, which make it difficult for the oil drops in the water to adsorb membrane surface and reduce the fouling of membrane surface. When surface flow velocity is up to a certain level, this effect decreases, so the increase rate of flux decrease (Ma,2000,pp.191-200).

3.3 Effect on running time

Fig.4 shows the relationship between flux and system running time, the flux is gradually decrease with the increase of running time, after running 20h, the flux approximately reduce 30%. Obviously that is because of fouling of membrane. Therefore in the practical application, the membrane should be cleaned after the system running certain time in order to keep the steady flux.

3.4 The comparison of different membrane cleaning methods

In the treatment of oil/water emulsion using tubular ultrafiltration membrane, the flux was gradually decrease with the increase of running time, consequently different cleaning methods for the restoration of flux are studied. There were three cleaning methods in this research: chemistry cleaning, water cleaning and the spongy rubber ball cleaning, the effects of these methods had been compared in Fig.5.

It can be easily seen from Fig.5 that all of three methods can make the flux of membrane restore. But the effect of chemistry cleaning is better than the others. After the use of chemical cleaning, the flux almost fully restored to the initial value. The flux restoration rate is 95.7% while the values of water cleaning and spongy rubber ball cleaning are

40.2% and 75.6% respectively. From Fig.6 the flux was observed remained steadily in the following process. In the constantly running, membrane needs cleaning once a day.

Compared to the chemical cleaning and spongy rubber ball cleaning, water cleaning had the worst results, spongy rubber ball cleaning was slightly better than it, but still could not make the flux restore to the original value (Hao,2005,pp.75-80). The main reason is that the fouling (oil drops) attached on the membrane surface can be completely cleaned up by chemical cleaning, but not by the others. The water cleaning method could only partially remove the fouling on the membrane surface and spongy rubber balls which cycled in tubular ultrafiltration membrane system with cleaning fluid can most removed the fouling on the surface of membrane, so the flux can not fully restored.

In Fig.7 (a),the SEM micrograph shows that there are great mass of emulsified oil on membrane surface and well-distributed over the surface, thus the through resistance of water increased and the flux reduced. Fig.7 (b) shows the partial fouling still adhere to the membrane surface after the water cleaning. Fig.7 (c) and Fig.7 (d) show the membrane surface cleaned by spongy rubber ball and chemical solution, there are little emulsified oil on the membrane surface, so these two methods are feasible for the membrane cleaning.

3.5 The rejection rate to oil of tubular ultrafiltration membrane

In this experiment, the oil retention rate of PVDF tubular ultrafiltration membrane are shown in Table 1. The rejection rate constantly increased with the increase of oil concentration of raw water. The PVDF tubular ultrafiltration membrane have the great rejection to oil in emulsion, the filtrate can meet the need of treatment to oil/water emulsion.

4. Conclusions

In the process treatment oil/water emulsion with the PVDF tubular ultrafiltration membrane, the flux of PVDF tubular ultrafiltration membrane is greatly influenced by the running pressure, membrane surface velocity of flow and the running time. Flux reached max value when the operation pressure is 0.20Mpa. It increased with membrane surface flow velocity increase, but the increase rate gradually reduced. It also decreased lentamente with the increase of running time. The average flux is 108.2L/(m².h) when the running pressure is 0.20Mpa, membrane surface flow rate is 3.44m/s, the concentration of oil/water emulsion is 0.2g/L and the running time is 3 h.

The water cleaning method, the chemical cleansing and spongy rubber ball cleaning can make the flux restored after treatment of oil/water emulsion. The chemical cleaning methods was better and the flux can completely restore. The cleaning period is 24 h.

PVDF tubular ultrafiltration membranes have the great rejection rate to oil and the filtrate can meet the need of discharge or reuse. Using PVDF tubular ultrafiltration membrane to treat oil/water emulsion is a feasible approach.

References

- Gao,T. Y. (1989). Water Pollution Control Project, BeiJing :Higher Education Press. pp. 32-45.
- Jiang,C. X.M. (1986).Environment Pollution and Control, BeiJing :Higher Education Press. pp. 13-16.
- Lipp,P.,Lee,C.H.,Fare,A. G. & Fell,C. J. D.(1988). Fundamental study of the ultrafiltration of oil-water emulsions.*Journal of Membrane Science*,36, 161-177.
- Raymono,M.(1982).Ultrafiltration for oily waste water treatment. *Journal of Lubrication Engineers*, 38,16-18.
- Shao,G. (1992).Water treatments with membrane, BeiJing: Metallurgical industry press. (Chapter 2).
- Canziani,R., Emondi,V., Garavaglia,M.,Malpei,F.,Pasinetti,E.,& Buttiglieri,G.(2006).Effect of oxygen concentration on biological nitrification and microbial kinetics in a cross-flow membrane bioreactor (MBR) and moving-bed biofilm reactor (MBBR) treating old landfill leachate, *Journal of Membrane Science*, 286, 202–212.
- Hao,W. Ch., Liu,En. H., Sun,M., Shao,Q.,& Du,Q.Y.(2005).Study of washing system of a solid-liquid 2-phase tubular membrane.*Technology of Water Treatment*, 31, 77-80.
- Ma,H.,Bowman,C.N.&Davis,R.H.(2000).Membrane fouling reduction by backpulsing and surface modification. *Journal of Membrane Science*,173,191-200.

Table1.The Retention Rate to Oil of Membrane. Operation pressure was 0.20Mpa, running time was 6h, membrane surface flow rate was 3.44m/s

Concentration of raw water (g/L)	Concentration of filtrate (mg/L)	Retention rate (%)
0.2	6.5	96.8
0.6	9.6	98.4
1.0	9.5	99.0

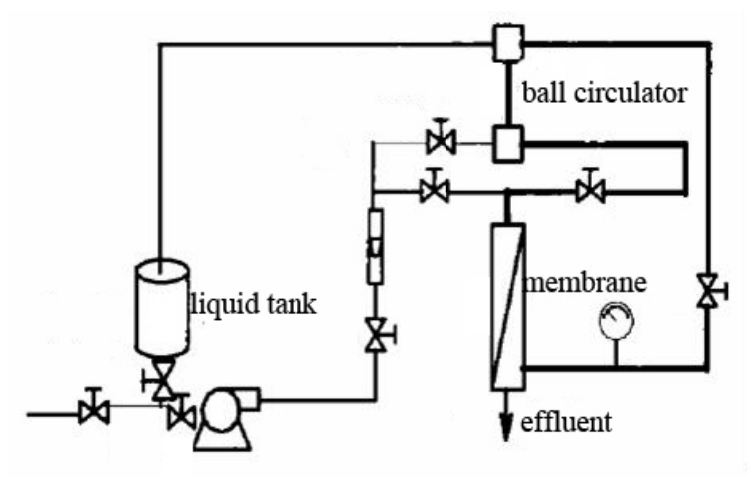


Figure 1. SchematicFlow-Sheet of Sponge Rubber Ball Cleaning System

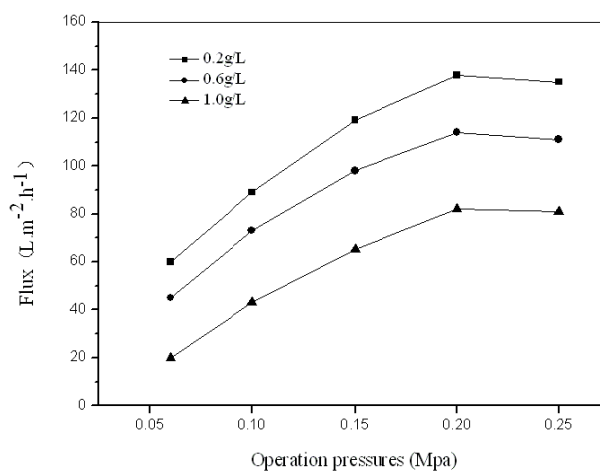


Figure 2. Flux Change with Operation Pressure. (Running time was 3h, membrane surface flow rate was 3.44m/s)

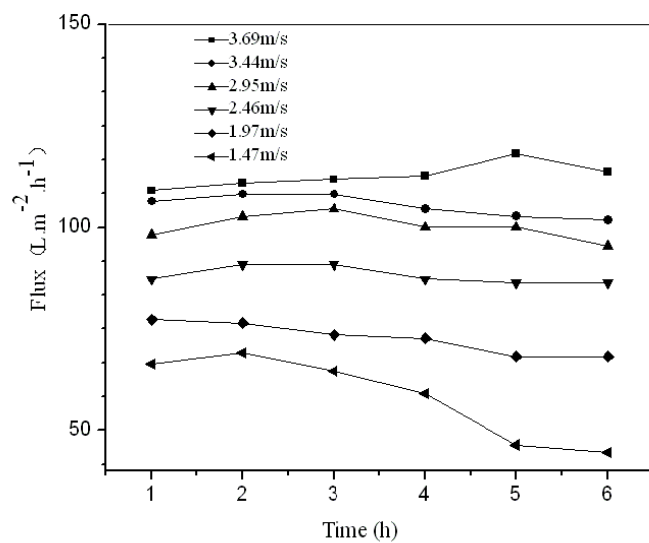


Figure 3. Flux Change with Membrane Surface Flow Velocity. (The concentration of oil/water emulsion was 0.2g/L, operation pressure was 0.20Mpa,)

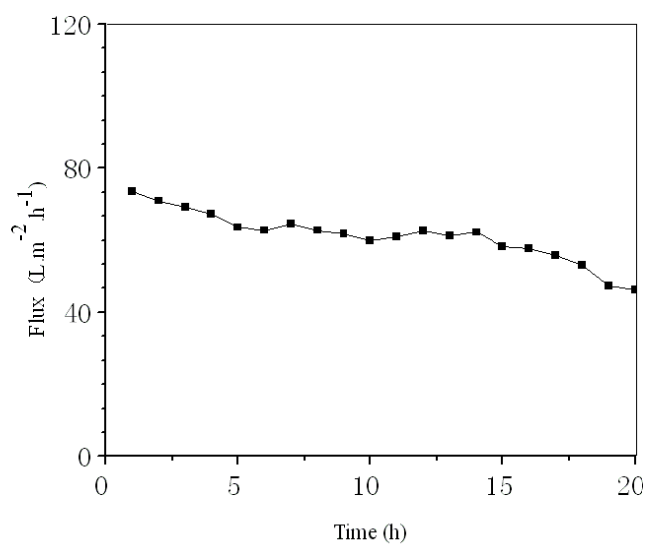


Figure 4. Flux Change with Running Time (The concentration of oil/water emulsion was 0.2g/L, operation pressure was 0.20Mpa, membrane surface flow rate was 3.44m/s)

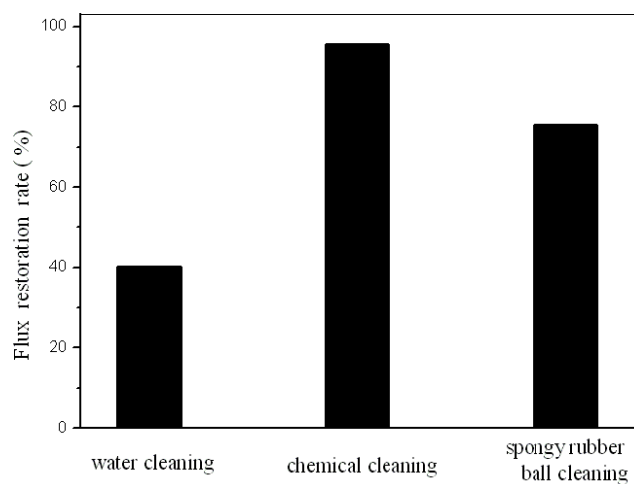


Figure 5. The Flux Restoration Rate of Three Cleaning Methods. (The concentration of oil/water emulsion was 1.0g/L, operation pressure was 0.20Mpa, operation, Running time was 20h, membrane surface flow rate was 3.44m/s)

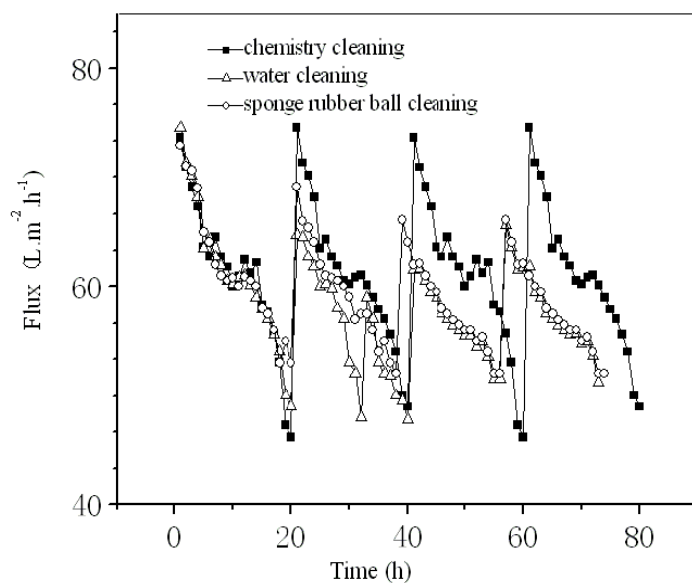


Figure 6. The Comparison of Different Membrane Cleaning Effects. (The concentration of oil/water emulsion was 1.0g/L, operation pressure was 0.20Mpa, membrane surface flow rate was 3.44m/s)

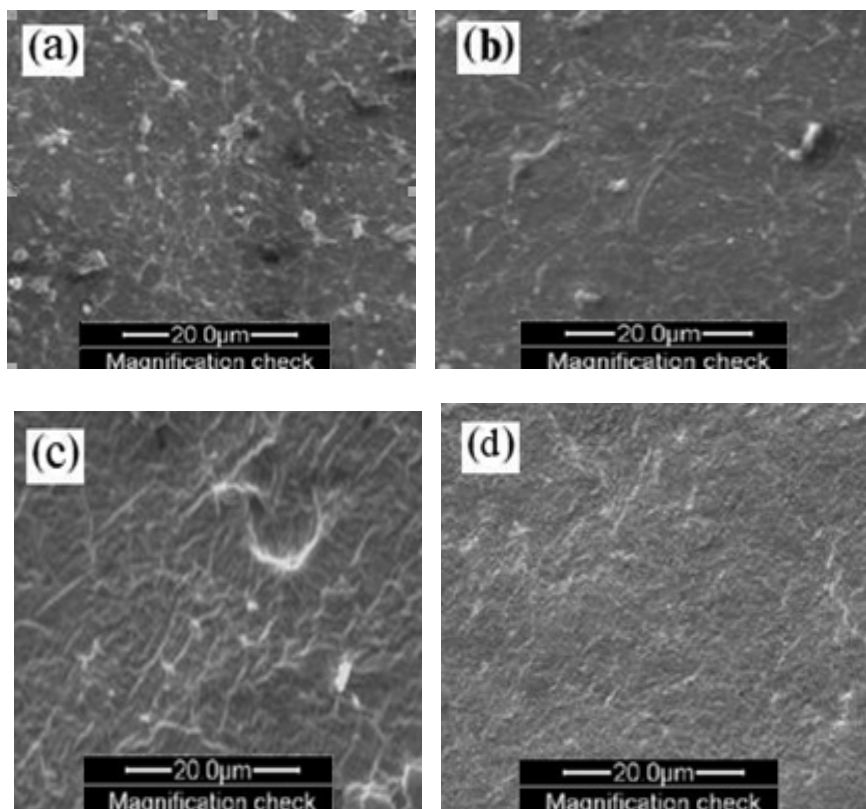


Figure 7. SEM Micrographs of PVDF Membrane Surface (a: fouled membrane; b: membrane after water cleaning; c: membrane after spongy rubber ball cleaning; d: membrane after chemical cleaning)



Strategies for Non-Parametric Smoothing of the Location Model in Mixed-Variable Discriminant Analysis

Nor Idayu Mahat (Corresponding author)

College of Arts and Sciences, Building of Faculty of Quantitative Sciences

Universiti Utara Malaysia

06010 Sintok, Kedah, Malaysia

Tel: 6-04-9284-098 E-mail: noridayu@uum.edu.my

W.J. Krzanowski

School of Engineering, Computer Science and Mathematics

University of Exeter

North Park Road, EX4 4QE Exeter, UK

Tel: 44-1392-725-279 E-mail: W.J.Krzanowski@ex.ac.uk

A. Hernandez

Escuela Universitaria de Estudios Empresariales, Universidad Complutense

Avda Filipinas 3, 28003 Madrid, Spain

Tel: 34-91-394-6746 E-mail: a.hernandez@emp.ucm.es

Abstract

The non-parametric smoothing of the location model proposed by Asparoukhov and Krzanowski (2000) for allocating objects with mixtures of variables into two groups is studied. The strategy for selecting the smoothing parameter through the maximisation of the pseudo-likelihood function is reviewed. Problems with previous methods are highlighted, and two alternative strategies are proposed. Some investigations into other possible smoothing procedures for estimating cell probabilities are discussed. A leave-one-out method is proposed for constructing the allocation rule and evaluating its performance by estimating the true error rate. Results of a numerical study on simulated data highlight the feasibility of the proposed allocation rule as well as its advantages over previous methods, and an example using real data is presented.

Keywords: Brier score, Error rate, Leave-one-out process, Location model, Pseudo-likelihood

1. Introduction

Various methods for constructing allocation rules in discriminant analysis with mixtures of variables have been proposed and discussed by researchers. Broadly speaking there are three possible strategies:

- (i) transform the variables so they are all of the same type, and then apply an allocation rule appropriate to this type;
- (ii) apply separate allocation rules to each type, and then combine the results for an overall classification;
- (iii) develop a model that pays regard to the separate types, and then derive an allocation rule from this model.

Strategy (i) entails possible loss of information (Krzanowski, 1993; Hand, 1997); strategy (ii) has had limited study (Wernecke, 1992; Xu et al., 1992), but strategy (iii) has received much more wide-spread attention. Some methods available so far are non-parametric kernel and nearest neighbour approaches (reviewed by Silverman and Jones (1989)), semi-parametric methods such as logistic discriminant analysis (Anderson, 1972) and fully parametric methods based on the location model (Chang and Afifi, 1974; Krzanowski, 1975).

The use of the location model in discriminant analysis has been discussed by many researchers (Chang and Afifi, 1974; Krzanowski, 1975, 1980; Daudin, 1986; Knoke, 1982; Vlachonikolis and Marriot, 1982; Titterton et al., 1981; Kiang, 2003). In a recent development, Asparoukhov and Krzanowski (2000) have shown how non-parametric smoothing can be used to estimate the classifier's parameters. This approach is particularly useful for situations with sparse data, where traditional maximum likelihood methods run into problems.

The aim of this paper is to carry out further investigation on non-parametric smoothing of the location model. Attention is focused on classifying objects with continuous and binary variables to one of two groups, but expanding the idea to more than two groups and more general categorical variables can be executed without difficulty. Existing methodology is summarized in the second section, problems with previous methods are highlighted and some new ideas are presented in the third section, a Monte Carlo study to investigate the methods is described in the fourth section and results are presented in the fifth section. We also compare the proposed methods with standard maximum likelihood ones in situations where the latter are possible. An example of real data is then presented, and brief conclusions are given in the final section.

2. Non-parametric smoothing of the location model

Suppose there are two groups, π_1 and π_2 , both of which consist of objects with binary and continuous variables. We denote the vector of binary variables as \mathbf{x} and the vector of continuous variables as \mathbf{y} , and let the former have q components, $\mathbf{x}^T = \{x_1, x_2, \dots, x_q\}$ while the latter has p components, $\mathbf{y}^T = \{y_1, y_2, \dots, y_p\}$. Hence, we may present the vector of variables observed on each object in both groups as $\mathbf{z}^T = (\mathbf{x}^T, \mathbf{y}^T)$.

Let each binary variable take a value of 0 or 1. Then we can express the q binary variables as a multinomial $\mathbf{s} = \{s_1, \dots, s_m\}$, where $m = 2^q$, and each distinct pattern of \mathbf{x} defines a multinomial cell uniquely, with \mathbf{x} falling in cell $s = 1 + \sum_{b=1}^q x_b 2^{b-1}$. We denote the probability of obtaining an object in cell s of π_i ($i = 1, 2$) by

p_{is} . Next, we assume the vector of continuous variables to have a multivariate normal distribution with mean $\boldsymbol{\mu}_{is}$ in cell s of π_i and a homogeneous dispersion matrix across cells and populations, $\boldsymbol{\Sigma}$, thus $\mathbf{Y}_{is} \sim \mathbf{N}(\boldsymbol{\mu}_{is}, \boldsymbol{\Sigma})$. The joint probability of observing an object in group π_i with associated \mathbf{x} and \mathbf{y} is

$$f(\mathbf{x}, \mathbf{y} | \pi_i) = \frac{p_{is}}{(2\pi)^{p/2} |\boldsymbol{\Sigma}|^{1/2}} \exp\left[-\frac{1}{2}(\mathbf{y} - \boldsymbol{\mu}_{is})^T \boldsymbol{\Sigma}^{-1}(\mathbf{y} - \boldsymbol{\mu}_{is})\right]. \quad (1)$$

The application of this joint probability to the problem of allocating a future object with mixed variables to one of two groups was first studied by Chang and Afifi (1974) and generalised by Krzanowski (1975). By assuming that the costs due to misallocating future objects in both groups are equal and that the covariance structures in both groups are homogeneous, we allocate a future object with the vector of observed variables $\mathbf{z}^T = (\mathbf{x}^T, \mathbf{y}^T)$ to π_1 if its \mathbf{x} falls in cell s of the multinomial variable and

$$(\boldsymbol{\mu}_{1s} - \boldsymbol{\mu}_{2s})^T \boldsymbol{\Sigma}^{-1} \left\{ \mathbf{y} - \frac{1}{2}(\boldsymbol{\mu}_{1s} + \boldsymbol{\mu}_{2s}) \right\} \geq \log\left(\frac{p_{2s}}{p_{1s}}\right), \quad (2)$$

otherwise to π_2 .

Usually, parameters $\boldsymbol{\mu}_{is}$, $\boldsymbol{\Sigma}$ and p_{is} are unknown and have to be estimated from initial samples, known as training sets. We focus here on estimating these parameters using non-parametric smoothing methods. The mean of the j th continuous variable y_j for cell s of group π_i is estimated through

$$\hat{\mu}_{isj} = \left\{ \sum_{k=1}^m n_{ik} w_{ij}(s, k) \right\}^{-1} \sum_{k=1}^m \left\{ w_{ij}(s, k) \sum_{r=1}^{n_{ik}} y_{rikj} \right\} \quad (3)$$

under conditions $0 \leq w_{ij}(s, k) \leq 1$ and $\sum_{k=1}^m n_{ik} w_{ij}(s, k) > 0$ where $s, k = 1, \dots, m$; $i = 1, 2$ and $j = 1, \dots, p$. In this form, n_{ik} is the number of objects of π_i that fall in cell k , y_{rikj} is the j th continuous variable value of the r th object falling in cell k of π_i and $w_{ij}(s, k)$ is the weight with respect to variable j and cell s of all objects of π_i that fall in cell k .

One may consider any suitable function for the weights, $w_{ij}(s, k)$, but we prefer the exponential function due to its simple form of

$$w_{ij}(s, k) = \lambda_{ij}^{d(s, k)}; \quad 0 \leq \lambda_{ij} \leq 1 \quad (4)$$

where $d(s, k) \in \{0, 1, \dots, q\}$. Here, $d(s, k)$ is the dissimilarity coefficient between the s th cell and the k th cell of binary vectors, measured using distance function $d(\mathbf{x}_s, \mathbf{x}_k) = (\mathbf{x}_s - \mathbf{x}_k)^T (\mathbf{x}_s - \mathbf{x}_k)$. All cells that have equal dissimilarity with respect to cell s will thus have equal weight in the estimation of cell means.

In any practical application, the degree of smoothing represented by λ_{ij} needs to be determined. One possible way of doing this is to select the set of smoothing parameters for continuous variables, Λ , as the values in the interval $[0, 1]$ that maximise the leave-one-out pseudo-likelihood function (Asparoukhov and Krzanowski, 2000)

$$\text{PL}_{loo}(\Lambda | D) = \prod_{r=1}^n p(\mathbf{y}_r | D - \mathbf{z}_r, \Lambda) \quad (5)$$

where $p(\mathbf{y}_r | D - \mathbf{z}_r, \Lambda)$ is the probability density of \mathbf{y}_r if object r falls in cell s of π_i and $D - \mathbf{z}_r$ is the training set of π_1 and π_2 objects with object r excluded.

Next, the smoothed cell means (3) are used in the estimation of the smoothed covariance matrix

$$\mathbf{V} = \frac{1}{n_1 + n_2 - g_1 - g_2} \sum_{i=1}^2 \sum_{s=1}^m \sum_{r=1}^{n_{is}} (\mathbf{y}_{ris} - \hat{\boldsymbol{\mu}}_{is})(\mathbf{y}_{ris} - \hat{\boldsymbol{\mu}}_{is})^T \quad (6)$$

where n_i is the number of objects of π_i and g_i is the number of non-empty cells in the training sets from π_i . Finally, Asparoukhov and Krzanowski (2000) employed the adaptive weighted near-neighbour estimators as originally proposed by Hall (1981), for estimating the cell probabilities. These estimators have the form

$$\hat{p}_{is} = n_i^{-1} \sum_{j=0}^L w_{ij} N_{ij}(s, k); \quad 0 \leq L \leq q-1 \quad (7)$$

where $s, k = 1, \dots, m; i = 1, 2$ and $N_{ij}(s, k)$ is the number of training objects from π_i that fall in cell k and are j binary variables distant from the cell s , $d(\mathbf{x}_s, \mathbf{x}_k) = j$. The weights, w_{ij} , are chosen to minimise mean squared error:

$$\Delta_i(w_{i0}, w_{i1}, \dots, w_{iL}) = \sum_{s=1}^m E(\hat{p}_{is} - p_{is})^2. \quad (8)$$

The proposed strategies for estimating the parameters are satisfactory, but some potential problems may arise in certain situations. The first problem concerns the choice of smoothing parameters by maximising the leave-one-out pseudo-likelihood function (5). This function may be satisfactory for data from normal populations, but less satisfactory if this assumption is not appropriate. Secondly, the estimation of cell probabilities using the adaptive weighted nearest neighbour method determines the amount of smoothing by computing the weights automatically. It is an easy technique, but Hall (1981) warned that sometimes these weights take negative or zero values. These phenomena usually happen when the probabilities are small and the sample is not sufficiently large. These problems are addressed in the rest of this paper, and some alternative methods are investigated.

3. Some modifications

3.1 Parameter estimations

The sample-based version of allocation rule (2) that assumes equal cost of misclassifying objects in both groups and homogeneous covariance matrix in the two groups, will allocate a future object, $\mathbf{z}^T = (\mathbf{x}^T, \mathbf{y}^T)$ to π_1 if it satisfies

$$(\hat{\boldsymbol{\mu}}_{1s} - \hat{\boldsymbol{\mu}}_{2s})^T \mathbf{V}^{-1} \left\{ \mathbf{y} - \frac{1}{2}(\hat{\boldsymbol{\mu}}_{1s} + \hat{\boldsymbol{\mu}}_{2s}) \right\} \geq \log \left(\frac{\hat{p}_{2s}}{\hat{p}_{1s}} \right) \quad (9)$$

and otherwise to π_2 , where $\hat{\boldsymbol{\mu}}_{1s}, \hat{\boldsymbol{\mu}}_{2s}, \mathbf{V}, \hat{p}_{1s}$ and \hat{p}_{2s} are the smoothed parameter estimates obtained from the training sets.

We keep both the smoothed estimators $\hat{\boldsymbol{\mu}}_{is}$ and \mathbf{V} as given in equations (3) and (6) respectively. However, we apply a restriction by having a single smoothing parameter, λ , across all continuous variables and groups. Therefore, a new

exponential function is

$$w(s, k) = \lambda^{d(s, k)}; \quad 0 < \lambda < 1 \quad (10)$$

and we use this quantity for estimating the cell means (3). The reason for imposing a single smoothing parameter is to have less complexity on the designed model and greater ease in handling the process for selecting the smoothing parameter.

We overcome the problem of obtaining negative or zero cell probabilities when using the adaptive weighted nearest neighbour (7) by imposing the following restrictions.

- (i) All weights, (w_{i0}, \dots, w_{iL}) should be between 0 and 1, so that any weight that is less than or equal to 0 is replaced by 0.00001 while any weight that is greater than or equal to 1 is replaced by 0.99999.
- (ii) If restriction (i) fails to avoid obtaining a zero probability, then any cell probability that has zero value is replaced by 0.00001.

In addition, we consider two alternative non-parametric smoothing methods for estimating p_{is} . These methods are;

3.1.1 The kernel method (Aitchison and Aitken, 1976) that estimates the probability of observing cell s of π_i as

$$\hat{p}_{is} = n_i^{-1} \lambda^q \sum_{j=0}^q N_{ij}(s, k) \left\{ \frac{1-\lambda}{\lambda} \right\}^j; \quad (1/2 \leq \lambda \leq 1) \quad (11)$$

where $N_{ij}(s, k)$ has the same interpretation as the adaptive weighted near-neighbour estimator which was discussed earlier and λ is a smoothing parameter.

3.1.2 The modified maximum likelihood estimator in the weighted form:

$$\hat{p}_{is} = \frac{\sum_{k=1}^m w(s, k) n_{is}}{n_i}. \quad (12)$$

In order to have the simplest allocation rule, we suggest that the weights $w(s, k)$ follow the exponential function (10), standardised to probabilities in each group by

$$\hat{p}_{is(std)} = \hat{p}_{is} / \sum_{s=1}^m \hat{p}_{is}. \quad (13)$$

We will term this the exponential method.

3.2 Selecting optimised smoothing parameters

Both the kernel and the exponential methods (11) and (13), as well as the estimation of cell means (3), need an identified value of the smoothing parameter, λ . Therefore, we investigate three different strategies for obtaining its value. The λ that satisfies a given criterion in each strategy is termed λ_{opt} .

The first strategy is to select λ_{opt} through the maximisation of the leave-one-out pseudo-likelihood function. This was successfully applied by Asparoukhov and Krzanowski (2000) and we are interested in studying its feasibility. The second and the third strategies choose λ_{opt} as the value that provides the best allocation performance as measured by the true error rate and the Brier score respectively. The choice of λ_{opt} based on the true error rate was used by Raudys and Jain (1991), who selected λ_{opt} for the Kernel window classifier as the value that provides the smallest classification errors. The error rate is computed by taking the proportion of the number of objects misclassified by the rule to the total number of objects in the sample.

The error rate takes a discrete value, so an alternative criterion that takes values from a continuum is considered. This criterion is known as the Brier score. Suppose $\delta(\pi_i | \mathbf{x}_r, \mathbf{y}_r)$ denotes the true group of object r in the training set, being equal to 1 if r is from π_i and 0 otherwise, and $f(\pi_i | \mathbf{x}_r, \mathbf{y}_r)$ is the probability that object r with measurements \mathbf{x}_r and \mathbf{y}_r belongs to π_i . Then for the two groups case, the Brier score is defined as (Hand, 1997)

$$\frac{1}{n} \sum_{r=1}^n \sum_{i=1}^2 \{ \delta(\pi_i | \mathbf{x}_r, \mathbf{y}_r) - f(\pi_i | \mathbf{x}_r, \mathbf{y}_r) \}^2. \quad (14)$$

To have a good estimate of the Brier score, an appropriate method that gives the best estimate of $f(\pi_i | \mathbf{x}_r, \mathbf{y}_r)$ has to be used. If the group densities $f(\mathbf{x}_r, \mathbf{y}_r | \pi_i)$ are known to follow the location model, we may obtain $f(\pi_i | \mathbf{x}_r, \mathbf{y}_r)$ easily through *Bayes theorem*:

$$f(\pi_i | \mathbf{x}_r, \mathbf{y}_r) = [p_i f(\mathbf{x}_r, \mathbf{y}_r | \pi_i)] \left\{ \sum_{i=1}^2 p_i f(\mathbf{x}_r, \mathbf{y}_r | \pi_i) \right\}^{-1} \quad (15)$$

where p_i is the prior probability of obtaining an object from π_i and

$$f(\mathbf{x}_r, \mathbf{y}_r | \pi_i) = \frac{p_{is}}{(2\pi)^{p/2} |\Sigma|^{1/2}} \exp \left[-\frac{1}{2} (\mathbf{y}_r - \boldsymbol{\mu}_{is})^T \Sigma^{-1} (\mathbf{y}_r - \boldsymbol{\mu}_{is}) \right]. \quad (16)$$

We estimate both (15) and (16) by replacing all the parameters ($\boldsymbol{\mu}_{is}$, Σ and p_{is}) with the values of the corresponding smoothed estimators ($\hat{\boldsymbol{\mu}}_{is}$, $\hat{\mathbf{V}}$ and \hat{p}_{is}) obtained from the training set, choosing prior probabilities appropriate to the substantive application. Like error rate, we choose the λ_{opt} that provides the smallest value of Brier score. The computation of both error rate and Brier score are performed through the leave-one-out process, so that biased estimation of these criteria is avoided and comparison among these three strategies for selecting λ_{opt} is done without bias.

3.3 Assessment of smoothed allocation rule

There are nine possible allocation rules altogether, obtained from the combination of the three different methods for smoothing cell probabilities and the three different strategies to choose λ_{opt} . In each of these rules the exponential smoothing method is used for estimating the cell means and the covariance matrix. We compare these rules by measuring their performance using misclassification of future objects as the criterion. For this purpose, the leave-one-out error rate is preferred because it removes the bias in the apparent error rate and easily represents a classifier's inaccuracy by giving the percentage of objects it misclassifies.

The methods for selecting λ_{opt} and evaluating rule performance both need the leave-one-out process. We conduct these leave-one-out processes in nested fashion; the *inner* leave-one-out is used to select the optimised smoothing parameter and the *outer* leave-one-out is used to measure rule performance. The details of the proposed design are outlined as follows:

1. Omit each object r in turn from the sample ($r = 1, \dots, n$).

1.1 Determine λ_{opt} from the sample without object r . Choose λ_{opt} that

1.1.1 maximises the leave-one-out log-likelihood function, or

1.1.2 minimises the leave-one-out error rate, or

1.1.3 minimises the leave-one-out Brier score.

of the $(n - 1)$ remaining object.

1.2 Compute $\hat{\boldsymbol{\mu}}_{is}$, $\hat{\mathbf{V}}$ and \hat{p}_{is} using the obtained value of λ_{opt} and the sample without object r .

1.3 Construct an allocation rule using the estimates obtained in (1.2).

1.4 Predict the group of object r . If correct, then $\text{error}_r = 0$, otherwise $\text{error}_r = 1$.

2. Compute the leave-one-out error rate, $\sum_{r=1}^n \text{error}_r / n$.

For option (1.1.2) in step 1.1, we evaluate the allocation rule performance over a set of values of λ in $(0, 1)$ and choose the value which provides the smallest leave-one-out error rate as λ_{opt} . However, we obtain λ_{opt} for both options (1.1.1) and (1.1.3) using built-in functions ('optimize' and 'nlminb') as provided in S-Plus. It is worth

emphasising that the optimised value obtained from any of these strategies is not necessarily the global optimum.

Since there are nine rules, we distinguish them by labelling each rule with the smoothing methods used to smooth the cell probabilities, thus we have (i) Nearest neighbour_{LL}, Nearest neighbour_{ER} and Nearest neighbour_{BS}, (ii) Kernel_{LL}, Kernel_{ER} and Kernel_{BS} and (iii) Exponential_{LL}, Exponential_{ER} and Exponential_{BS}. The subscripts refer to the strategies (log-likelihood, error rate and Brier score) for obtaining the optimised smoothing parameter, λ_{opt} .

4. Monte Carlo simulation

The rules discussed in the previous section were evaluated through simulations. We generated data having a mixture of continuous and binary variables by following Everitt and Merette (1990). Each object in group π_i is first assumed to have $p+q$ continuous random variables, $y_{i1}, \dots, y_{ip}, y_{i(p+1)}, \dots, y_{i(p+q)}$, taken from a multivariate normal distribution with mean μ_i and homogeneous dispersion matrix, Σ . The first p variables y_{i1}, \dots, y_{ip} are treated as observed variables, and the remaining $y_{i(p+1)}, \dots, y_{i(p+q)}$ as unobserved variables. The binary variables arise by discretising the latter continuous variables. This is done by converting $y_{i(p+1)}, \dots, y_{i(p+q)}$ to x_{i1}, \dots, x_{iq} using

$$x_{ij} = \begin{cases} 0 & \text{if } -\infty \leq y_{i(p+j)} < \delta_{ij} \\ 1 & \text{if } \delta_{ij} \leq y_{i(p+j)} < \infty \end{cases} \quad (17)$$

where δ_{ij} are thresholds, $i = 1, 2$ and $j = 1, \dots, q$. These thresholds are given by

$$\delta_{ij} = \Phi^{-1}(p_{ij}) \times \sigma_{y_{i(p+j)}} + \mu_{y_{i(p+j)}}$$

where p_{ij} is the target proportion of objects of π_i having $x_{ij} = 0$, $\mu_{y_{i(p+j)}}$ and $\sigma_{y_{i(p+j)}}$ are the mean and standard deviation of observed variable y_{p+j} in π_i respectively, and $\Phi^{-1}(\cdot)$ is the inverse cumulative standard normal integral. Assuming that the mean of \mathbf{y} is $\mathbf{0}$ and all variances are unity, then δ_{ij} is equal to the standard normal ordinate corresponding to the target proportion.

The dispersion matrix, Σ , unites the dispersion matrix of the continuous variables, Σ_p , the dispersion matrix of the binary variables, Σ_q , and the covariance between these two variables, Σ_{pq} , such that

$$\Sigma = \begin{pmatrix} \Sigma_p & \Sigma_{pq} \\ \Sigma_{pq}^T & \Sigma_q \end{pmatrix}$$

The set of parameters for generating artificial data sets is

n_i = sample size of π_i

p = number of continuous variables

q = number of binary variables

$\mu_i = (\mu_{i1}, \dots, \mu_{ip}, \mu_{i(p+1)}, \dots, \mu_{i(p+q)})$

the vector of means in π_i where $\mu_{i(p+1)} = \dots = \mu_{i(p+q)} = 0$

Σ = dispersion matrix

$i = 1, 2$

We set the following values

$n_i = 25, 50$ and 100 $p = 3$ $q = 2$

$\mu_1 = (1, 0, 0, 0, 0)$ $\mu_2 = (1.5, 1.5, 1.5, 0, 0)$

For the dispersion matrix, Σ , we defined two different matrices as follows:

$$\Sigma_1 = \begin{pmatrix} 1 & 0 & 0 & 0.2 & 0 \\ 0 & 1 & 0 & 0.5 & 0.5 \\ 0 & 0 & 1 & 0 & 0.4 \\ 0.2 & 0.5 & 0 & 1 & 0.5 \\ 0 & 0.5 & 0.4 & 0.5 & 1 \end{pmatrix}, \quad \Sigma_2 = \begin{pmatrix} 16 & 0 & 0 & 0.2 & 0 \\ 0 & 15 & 0 & 0.5 & 0.5 \\ 0 & 0 & 12 & 0 & 0.4 \\ 0.2 & 0.5 & 0 & 1 & 0.5 \\ 0 & 0.5 & 0.4 & 0.5 & 1 \end{pmatrix}$$

The differences between these two matrices is in their settings of Σ_p where the variances of the continuous variables are very small (unity) in the first matrix, whilst they are very dispersed in the second matrix. Finally, the largest proportions of the binary variable values are given in Table 1.

SET 1 in Table 1 gives large separation of cells, so we will have more objects in one category than in the other category for the same binary variable. Therefore, we expect to obtain many empty cells with this set especially when the size of sample is very small. SET 2 and SET 3 give moderate and small separation of cells respectively. In SET 3, full cells are expected. There are 18 combinations of (i) size of groups, $n_i = 25, 50$ or 100 , (ii) dispersion matrices, Σ_1 or Σ_2 and (iii) proportions in category of binary variables (see Table 1). Since the simulation process is extensive, we only had one artificial data set for each combination and we restricted our investigation to have equal sample size in both groups for these 18 data sets.

5. Results for simulated data

5.1 Selecting optimised smoothing parameters

Figure 1 shows the variability of λ_{opt} across one data set for the three allocation rules when they are chosen to minimise the leave-one-out Brier score. These examples are taken from data set 4, one of the 18 data sets generated in the previous section. The patterns of other data sets and the patterns that correspond to the other two optimisation criteria were similar.

Figure 1(a) illustrates the variability of λ_{opt} for smoothing cell means using the nearest neighbour rule while Figure 1(c) illustrates the variability of λ_{opt} for smoothing cell means and cell probabilities using the exponential rule. In both plots, the Y-axis represents the value of λ_{opt} and the X-axis represents the object r . Each point in these plots indicates the smoothing parameter value for the allocation rule constructed from the sample on omitting object r . The kernel rule applies two different smoothing parameters, one each for smoothing cell means and cell probabilities. So, we plot the corresponding λ_{opt} in the Y-axis and X-axis (Figure 1(b)). Each point in this plot represents the sample on omitting object r . All these plots show a clear scatter of points especially in Figure 1(c). They describe some differences in the amount of smoothing from one sample of size $(n - 1)$ to other samples of the same size. This variability occurs because different samples have slightly different distributions when a different object r is omitted.

We have labelled several points that are further from the majority by their omitted objects (Figure 1(a) and Figure 1(c)) and circled numbers (Figure 1(b)), to highlight the possibility of having potential outliers. This is quite interesting to highlight because we can see in each plot that different methods identify different potential outliers.

5.2 Performance of the smoothed allocation rules for normal populations

The performances of the smoothed allocation rules are depicted in Figure 2. Each plot displays the behaviour of the performance of each smoothed allocation rule, estimated through the leave-one-out error rate (Y-axis) and its relation to the distance between two groups measured through the Kullback-Leibler divergence (X-axis). The three lines in each plot represent the three different strategies for selecting λ_{opt} . As clearly seen, all plots show the same decreasing pattern when the distance between two groups increases. It is quite difficult to spot whether any single rule always gives the smallest estimated error rate when comparing all Figures 2(a), 2(b) and 2(c), so Table 2 shows the frequencies with which each allocation rule was best.

In this table, the best allocation rule refers to the one that gives the lowest error rate among the three for each of the 18 artificial data sets. The scoring system is as follows; we assign 1 point to a single best rule, 1/2 point to both rules if there are two winners, and 1/3 for all rules if all of them are the lowest. Among the smoothing methods, the nearest neighbour rule is clearly best when its λ_{opt} is chosen through the minimisation of the leave-one-out Brier score and the maximisation of the leave-one-out log-likelihood function, while the kernel rule is the winner when its λ_{opt} is chosen through the minimisation of the leave-one-out error rate. However, in terms of this criterion all three methods perform very similarly.

5.3 Investigation with non-normal populations

The rules where λ_{opt} is obtained through the maximisation of the normal log-likelihood function should show some deterioration when the data are in fact non-normal. In such a case, their performance should differ from those of the other rules because the other two criteria (i.e. optimising error rate and Brier score) do not rely on distributional assumptions.

To investigate the performance of the proposed rules under non-normal conditions, we chose randomly five out of the 18 generated data sets and transformed all continuous variables in these subsets using the inverse of Johnson's systems (Lachenbruch et al., 1973) so that they no longer had a multivariate normal distribution. The chosen transformations were: log-normal (data sets 1 and 8), logit (data sets 2 and 14) and hyperbolic sine normal function (data set 17). Details on these transformation can be found in Lachenbruch et al. (1973). To avoid complexity, the same transformation function was applied to the two groups. The same investigations as performed for normal populations were repeated, and results are shown in Table 3.

Our results do not show the expected effect, possibly because of the estimation of parameters, in which they have been smoothed for density estimation purposes. However, it is strongly advised that extra precautions need to be taken for dealing with this situation, and choosing smoothing parameter through inaccuracy measures is advised.

5.4 Comparison of maximum likelihood and smoothed classification rules

Smoothing is essential whenever some of the multinomial cells are either empty or have very few observations. In the former case it is impossible to construct the maximum likelihood classification rule in such cells, while in the latter case the rule will be very poorly estimated. However, it is also of interest to enquire how the smoothed rules will compare with maximum likelihood ones when all cells have sufficient numbers of objects in them. If the smoothed rules show good performance in this comparison, they can be applied very generally rather than only in cases where cell membership is sparse.

To investigate this question, we extracted from the foregoing data sets those that had observations in all the multinomial cells; there were 7 such sets among the normal ones and 3 among the non-normal ones. For each data set, the error rate and the Brier score were found for the maximum likelihood (ML) rule and for each of the three smoothed rules.

Results are shown in Table 4, where we give the number of sets in which the ML rule performed better than all the smoothed rule ("ML best"), the number in which all the smoothed rules performed better than ML ("ML worst"), and the number in which either one or two smoothed rules performed better than ML ("ML intermediate"). Noting that ML was beaten by at least one smoothed rule on both assessment criteria in nine of the ten data sets, these results therefore suggest that the smoothed rules constitute good classifiers whether the multinomial data are sparse or not.

6. Practical example

An example of using the proposed rules for a real problem is provided by data set 2 reported by Krzanowski (1975). These data concern patients suffering from jaundice. These patients comprise two groups: π_1 denotes patients who required medical treatment and π_2 denotes patients who required surgical treatment. There are 30 patients in π_1 and 63 patients in π_2 . Four continuous and three binary variables are available for distinguishing these two groups. Since the costs of misclassifying patients to wrong groups are unavailable, we assume equal costs and prior probabilities.

The performance of the proposed allocation rules is shown in Table 5. Since there are many cells without patients, no allocation rule can be derived through the maximum likelihood estimation. Among smoothed allocation rules, Nearest neighbour_{LL} is best. In fact, the numbers of misclassifications recorded by nearest neighbour rules are smaller than those for kernel and exponential rules. These findings are consistent with the ones in Table 2, where the nearest neighbour rules are best, followed by the kernel rules and finally the exponential rules.

7. Discussion

The results that we have obtained through simulation study and numerical example show that the choice of the optimised smoothing parameter depends on both the criterion used for the optimisation and the smoothing method. In respect of criterion, we recommend selecting λ_{opt} through minimisation of the leave-one-out Brier score due to its continuous nature and since it does not make any distributional assumptions. The continuous nature makes it more amenable to standard function optimisation routines, and avoids the problem of having many local optima with discrete error rate. Lack of distributional assumptions circumvents potential objections to the use of log-likelihood ratio.

As regards smoothing method, our findings show that the nearest neighbour rule is the best and is followed by the kernel rule. This situation may relate to the lower restriction of the smoothing applied by them. Despite always being the best, however, nearest neighbour needs to be handled carefully because it is sensitive to the occurrence of cells without objects. On the other hand, the kernel method is heavy in computational time relative to its competitors. Alternatively, one may choose the exponential method if using a single smoothing parameter is preferred. It is possible to use this method because its results are not much poorer than the others.

As a final comment, the use of smoothing methods in the location model should be based on the problem in hand, rather than being a mere tool of the estimation method.

References

- Aitchison, J. & Aitken, C. G. G. (1976). Multivariate binary discrimination by the kernel method. *Biometrika*, 63, 413-420.
- Anderson, J. A. (1972). Separate sample logistic discrimination. *Biometrika*, 59, 19-35.
- Asparoukhov, O. & Krzanowski, W. J. (2000). Non-parametric smoothing of the location model in mixed variable discrimination. *Statistics and Computing*, 10, 289-297.
- Chang, P. C. & Afifi, A. A. (1974). Classification based on dichotomous and continuous variables. *Journal of the American Statistical Association*, 69, 336-339.
- Daudin, J. J. (1986). Selection of variables in mixed-variable discriminant analysis. *Biometrics*, 42, 473-481.
- Everitt, B. S. & Merette, C. (1990). The clustering of mixed-mode data: A comparison of possible approaches. *Journal of Applied Statistics*, 17, 283-297.
- Hall, P. (1981). Optimal near neighbour estimator for use in discriminant analysis. *Biometrika*, 68, 572-575.
- Hand, D. J. (1997). Construction and assessment of classification rules. Chichester: John Wiley & Son.
- Kiang, M. Y. (2003). A comparative assessment of classification methods. *Decision Support Systems*, 35, 441-454.
- Knoke, J. D. (1982). Discriminant analysis with discrete and continuous variables. *Biometrics*, 38, 191-200.
- Krzanowski, W. J. (1975). Discrimination and classification using both binary and continuous variables. *Journal of the American Statistical Association*, 70, 782-790.
- Krzanowski, W. J. (1980). Mixtures of continuous and categorical variables in discriminant analysis. *Biometrics*, 36, 493-499.
- Krzanowski, W. J. (1993). The location model for mixtures of categorical and continuous variables. *Journal of Classification*, 10, 25-49.
- Lachenbruch, P. A., Sneeringer, C. & Revo, L. T. (1973). Robustness of the linear and quadratic discriminant function to certain types of non-normality. *Communications in Statistics*, 1, 39-56.
- Raudys, S. J. & A. K. Jain (1991). Small sample size effects in statistical pattern recognition: Recommendations for practitioners. *IEEE Transactions on Systems, Man and Cybernetics*, 13, 252-264.
- Silverman, B. W. & M. C. Jones (1989). E. Fix and J.L. Hodges (1951): An important contribution to nonparametric discriminant analysis and density estimation. *International Statistical Review*, 57, 233-247.
- Titterton, D. M., Murray, G. D., Murray, L. S., Spiegelhalter, D. J., Skene, A. M., Habbema, J. D. F. & Gelpke, G. J. (1981). Comparison of discrimination techniques applied to a complex data set of head injured patients. *Journal of the Royal Statistical Society*, 144, 145-175.
- Vlachonikolis, I. G. & Marriot, F. H. C. (1982). Discriminant analysis with mixed binary and continuous data. *Applied Statistics*, 31, 23-31.
- Wernecke, K. D. (1992). A coupling procedure for the discrimination of mixed data. *Biometrics*, 48, 497-506.
- Xu, L., Krzyzak, A., & Suen, C. Y. (1992). Methods of combining multiple classifiers and their applications to handwriting recognition. *IEEE Transactions on Systems, Man and Cybernetics*, 22, 418-435.

Table 1. Proportions in categories of binary variables.

Group		Proportions in category (binary variables, x_{ij})			
		$P(x_{i1} = 0)$	$P(x_{i1} = 1)$	$P(x_{i2} = 0)$	$P(x_{i2} = 1)$
SET 1	1	0.07	0.93	0.90	0.10
	2	0.85	0.15	0.05	0.95
SET 2	1	0.75	0.25	0.40	0.60
	2	0.30	0.70	0.15	0.85
SET 3	1	0.50	0.50	0.65	0.35
	2	0.40	0.60	0.55	0.45

Table 2. Frequency of being a winner among smoothing methods based on leave-one-out criteria.

Leave-one-out optimisation criteria	Smoothing method		
	Nearest neighbour	Kernel	Exponential
Error rate	6.00	7.00	5.00
Brier score	10.33	4.33	3.83
Log-likelihood	8.17	4.67	5.17

Table 3. Performance of the rules for non-normal populations.

Data set	Optimisation method for selecting λ_{opt}		
	Error rate	Brier score	Normal log-likelihood
Allocation rule: Nearest neighbour			
1	0.06	0.06	0.06
2	0.06	0.05	0.05
8	0.23	0.20	0.21
14	0.31	0.30	0.31
17	0.46	0.47	0.46
Allocation rule: Kernel			
1	0.04	0.06	0.06
2	0.04	0.05	0.05
8	0.21	0.19	0.21
14	0.29	0.30	0.30
17	0.47	0.47	0.47

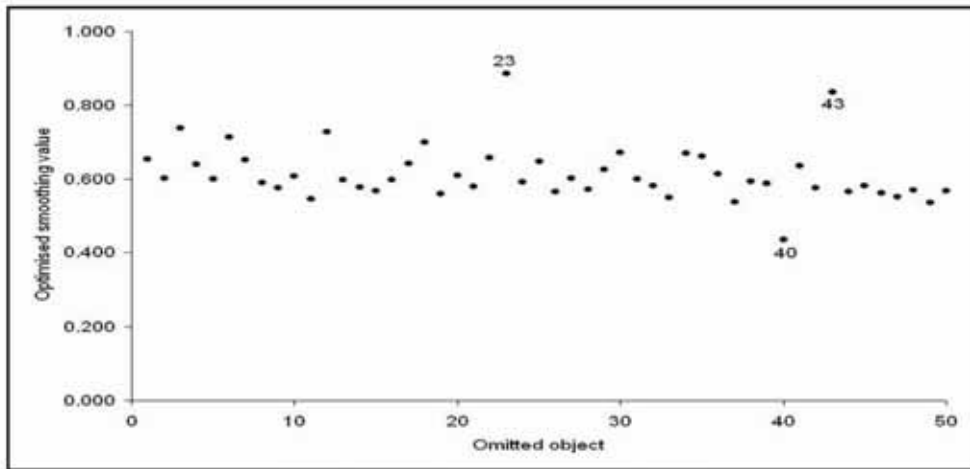
Allocation rule: Exponential			
1	0.06	0.06	0.06
2	0.04	0.05	0.05
8	0.22	0.20	0.22
14	0.32	0.31	0.33
17	0.49	0.48	0.45

Table 4. Comparison of the performance of the ML rule with those of the smoothed rules.

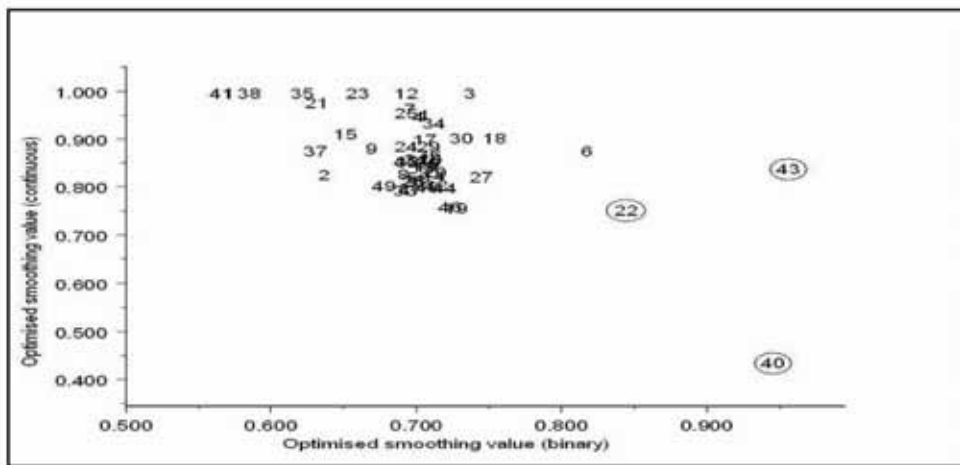
Criterion	Performance	Normal sets	Non-normal sets
Error rate	ML best	0	1
	ML intermediate	4	2
	ML worst	3	0
Brier score	ML best	0	0
	ML intermediate	2	1
	ML worst	5	2

Table 5. Location model assessment for jaundice patients.

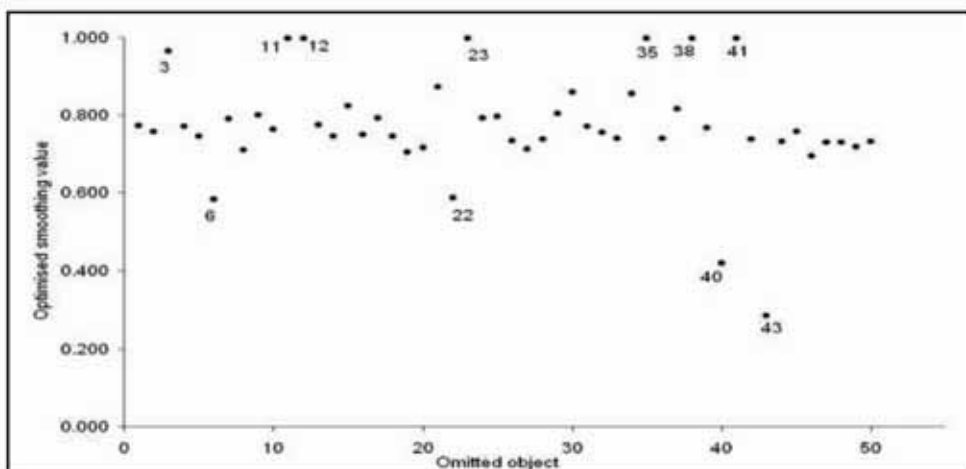
Procedure	Number of misclassifications
Maximum Likelihood Estimation	-
Nearest neighbour _{ER}	25
Nearest neighbour _{BS}	24
Nearest neighbour _{LL}	24
Kernel _{ER}	28
Kernel _{BS}	27
Kernel _{LL}	26
Exponential _{ER}	28
Exponential _{BS}	26
Exponential _{LL}	29



(a)

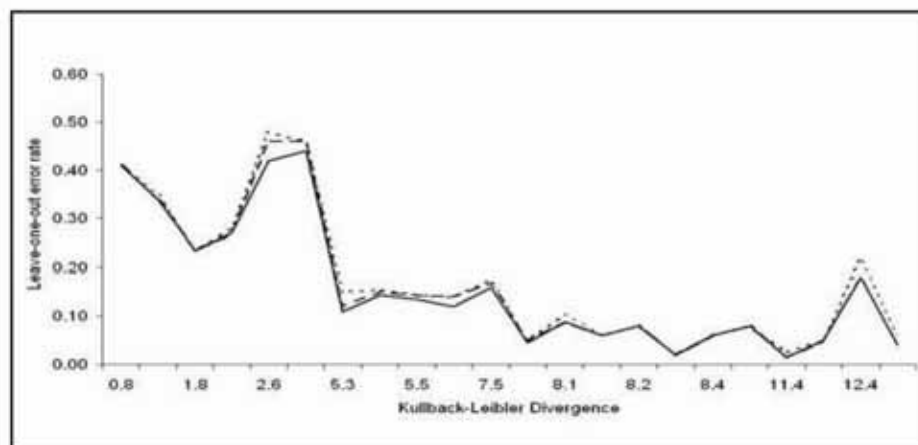


(b)

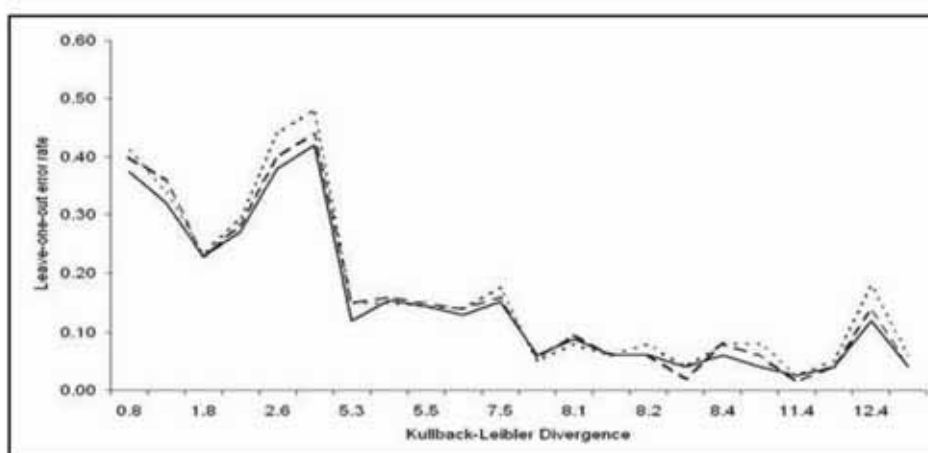


(c)

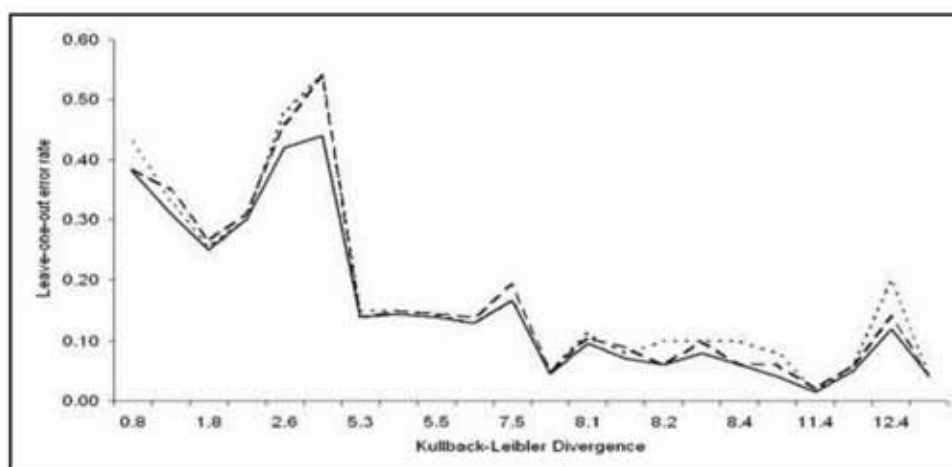
Figure 1. Example: λ_{opt} that minimises the leave-one-out Brier score
for (a) Nearest neighbour_{BS}, (b) Kernel_{BS} and (c) Exponential_{BS}.



(a) Nearest neighbour smoothing of the location model.



(b) Kernel smoothing of the location model.



(c) Exponential smoothing of the location model.

Figure 2. Performance of the smoothed allocation rules measured through leave-one-out error rate. λ_{opt} chosen through the optimisation of the leave-one-out log-likelihood function, ---- Brier score and ____ error rate.



Microstructure and Creep Behaviour of as-cast Ti-48Al-4Cr

Esah Hamzah (Corresponding author) & Maiiyeaalagan Kanniah

Department of Materials Engineering, Faculty of Mechanical Engineering

Universiti Teknologi Malaysia

81310 Skudai, Johor, Malaysia

Tel: 6-07-553-4563; fax: 6-07-556-6159 E-mail: esah@fkm.utm.my

Mohd Harun

Industrial Technology Division

Malaysian Institute for Nuclear Technology Research

Bangi, 43000 Kajang, Selangor, Malaysia

The research is financed by Malaysian Ministry of Science, Technology and Innovation (MOSTI) under the IRPA program (Project No. 09-02-06-0002 EA-002). (Sponsoring information)

Abstract

The microstructure and creep behaviour of as-cast beta phase contained gamma titanium aluminide with nominal composition of Ti-48Al-4Cr (at.%) was investigated. Constant load tensile creep test were performed at temperatures between 600-800°C and initial stresses from 150-180MPa. Data indicates that the alloy exhibit both steady state and minimum creep behaviour depending upon the temperature and stress. Microstructure before and after creep deformation were examined using scanning electron microscopy techniques. The possible reason for the transition from steady state to minimum creep behaviour was suggested.

Keywords: Microstructure, Creep, TiAl

1. Introduction

TiAl based alloys are considered as promising structural materials for high temperature aerospace and automotive applications. This is essentially due to some attractive properties such as low density ($\rho \sim 3.8 \text{ g/cm}^3$), high specific strength σ/ρ , high specific stiffness E/ρ , high temperature strength retention and resistance against 'titanium fire'. Single phase TiAl suffers from both poor room temperature ductility and fracture toughness. Therefore, no effort has been made to develop structural materials on the basis of single phase TiAl. In contrast, considerable improved ductility and toughness can be achieved in two phase alloys. Thus, during recent years extensive research has been carried out to develop two phase base alloys consisting of γ -TiAl and α_2 -Ti₃Al for structural applications. The most promising alloys are based on Ti-48at.% Al compositions with ternary or quaternary additions. The properties of these alloys are quite sensitive to microstructure; duplex structures show higher tensile ductility, for example up to 2.2% in binary Ti-48Al and up to 4% in ternary or quaternary alloys, whereas fully lamellae structures have poor ductility but higher creep resistance.

Although extensive research had been directed to improve the creep resistance (which is the primary importance for high temperature application) of two phase TiAl, however, still the design creep limit could not be meet. The presence of third phase, β , had been avoided from the beginning due to its brittleness at room temperature. Presence of β phase is thought to worsen the poor room temperature ductility. Therefore, β phase contained TiAl had never been studied extensively. Despite all the assumptions, β phase contained alloys had been reported to improve room temperature ductility and high temperature formability. The role of β phase at room and high temperature is still subject to controversy. Although, β phase had been avoided due to deterioration of room temperature ductility, however, currently it is subject of interest.

The aim of the present work is to study the microstructure and creep behaviour of β phase contained TiAl, namely Ti-48at.%Al-4at.%Cr.

2. Experimental procedures

The material investigated in this study have the nominal composition of Ti-48at.%Al-4at.%Cr. The alloys were produced by plasma melting casting in the form of 2kg buttons. The alloy will be referred in atomic percentage hereafter.

Samples before and after creep tests were examined using Phillips XL40 scanning electron microscope and Zeiss Supra 35VP field emission scanning electron microscope in back scattered electron (BSE) mode.

Flat samples with dimension, 3mm x 2mm with 15mm gauge length were prepared for the creep test. Prior to creep test, the test pieces were ground along the gauge length in the longitudinal direction to prevent premature crack initiation at surface defects during creep.

The constant load tensile creep test was conducted using Mayes TC 20 High Temperature Creep Testing Machine, consisting three zone temperature furnace and a loading lever arm ratio of 10:1 in air. The test temperatures were maintained constant with a precision of $\pm 1^{\circ}\text{C}$ and monitored for 2 hours before the test. The temperature was monitored during the creep test by using a thermocouple in contact with the gauge section of the sample. The sample was allowed to soak at test temperature for 1 hour before the load was applied. The strain was measured using a HTD type extensometer which is attached with two linear voltage displacement transducers (LVDT) with resolution of $\pm 1\mu\text{m}$ and a data logger. The strain was measured for every 1 second intervals at the start of the creep test, increasing to a maximum interval of 15 minutes. The test was interrupted after 20 hours and the samples were left to cool in air to room temperature.

3. Experimental Results

3.1 Microstructural Characterisation

The as-cast microstructure prior to creep testing was examined carefully and quantitatively in order objectively to distinguish later any creep induced microstructural changes. Figure 1(a) and (b) shows the optical and SEM-BSE micrograph of typical nearly lamellae microstructure in the gauge region of creep samples of as-cast Ti-48Al-4Cr. The microstructure of Ti-48Al-4Cr consists three phase which are the lamellae (300-600 μm), fine gamma (5-10%) and beta (2-5%) phase. The beta grains are observed to be irregular in shape together with fine γ grains along grain boundaries. Therefore, it is very hard to distinguish between γ and β grains of Ti-48Al-4Cr at low magnifications. Although indiscernible from optical micrograph, SEM image in figure 1(b) clearly reveals the presence of β phase (bright contrast) along lamellae grain boundaries. EDX analysis is conducted to further verify the fine γ and β phase. EDX analysis showed spot A have less chromium content whereas spot B are enriched with chromium. This result verifies that spot A is fine γ (dark contrast) whereas spot B (bright contrast) is beta phase. This verification is based on the fact that chromium is a strong β stabilizer. This type microstructure appears to be commonly observed in β containing TiAl alloy, e.g. Ti-46Al-(1.5-2)Cr-2Mo-0.25Si-0.3B, Ti-46.5Al-2Cr-2Nb-0.8Mo-0.2W-0.2Si and Ti-45-10Nb. The x-ray diffraction pattern is shown in figure 1(c). In the as-cast condition, peaks due to α_2 and γ are evident. Additionally, diffraction peaks due to b.c.c. structure were identified. The x-ray data indicate that the irregularly shaped particles enriched in Cr visible in figures 1(a) and 1(b) are the β phase.

3.2 Creep Behaviour

Figure 2(a) and (b) illustrates the creep strain (%) versus time (hrs) and strain rate (hr^{-1}) versus time (hours) for creep tests at temperatures ranging between 600-700 $^{\circ}\text{C}$ and identical initial stress of 180MPa respectively. Analysis on the creep curves of figure 2(a) shows Ti-48Al-4Cr exhibit no instantaneous creep strain at 600 and 700 $^{\circ}\text{C}$ with initial stress of 180MPa. Both these creep curves has almost identical shape. Figure 2(b) shows that Ti-48Al-4Cr exhibits steady state behaviour at these temperature-stress regimes. The creep strain increases rapidly in the primary creep regime until strain rate gradually falls to a steady-state value. No minimum creep behaviour is observed over these temperature-stress regimes. The steady state creep rate at 600 and 700 $^{\circ}\text{C}$ were 8.49×10^{-6} and $1.42 \times 10^{-5} \text{s}^{-1}$ respectively. Creep testing is also attempted at 800 $^{\circ}\text{C}$ with initial stress of 180MPa. However, the sample failed upon loading. It is quite interesting to note that Ti-48Al-4Cr which exhibit quite low creep strains and steady state creep rate at temperatures between 600-700 $^{\circ}\text{C}$ failed upon loading at 800 $^{\circ}\text{C}$ with the same initial stress of 180MPa. Therefore a creep test is attempted with initial stress of 150MPa to study the behaviour of Ti-48Al-4Cr at 800 $^{\circ}\text{C}$ and possible cause for the sudden failure with initial stress of 180MPa.

Figure 3(a) and (b) illustrates the creep strain (%) versus time (hrs) and strain rate (hr^{-1}) versus time (hours) for creep tests at 800 $^{\circ}\text{C}$ and initial stress of 150MPa respectively. Ti-48Al-4Cr exhibit 0.32% of instantaneous creep strain and immediately undergoes a short primary creep and reaches a minimum value before the onset of tertiary creep. Ti-48Al-4Cr exhibits minimum creep behaviour at this condition of temperature and stress as shown in figure 3(b). This type of creep behavior is also referred as 'inverse creep' where the creep curve can be divided into two regimes, before and after the minimum creep rate, instead of the common three. The minimum creep rate is $8.5 \times 10^{-5} \text{s}^{-1}$. The sample

failed after 16.5 hours. From this result, it is evident that the transition between steady state to minimum creep behaviour occurs at temperature between 700 to 800°C.

3.3 Creep Deformed Microstructure

SEM-BSE microstructures of crept samples are shown in figure 4(a)-(c). SEM examination indicates that the β phase at the grain boundaries decreased. On the other hand, extensive amount of β phase was observed at the α_2/γ lamellae interfaces. This was contrast to the initial as-cast microstructure. It is reported that β phase is softer than the other two phases (α_2 and γ) at elevated temperatures because of its more open bcc structure. That is, β phase can be deformed more easily than α_2 and γ phases. Therefore, upon deformation, the β phase is expected to act like a lubricant layer, and therefore, reduces the creep resistance of the alloy. Dynamic recrystallization which often been associated with high temperature deformation of TiAl is not significant in the case of β phase contained TiAl. β phase is found to play major role during creep deformation.

3.4 Creep Fracture

The fracture surface of Ti-48Al-4Cr sample creep deformed to fracture ($\epsilon = 7.98\%$) at 800°C with initial stress of 150MPa is shown in figure 5. A 'dimple like' appearance is observed. However, the intergranular brittle character of creep fracture is still evident. The 'dimples' are likely to be result of cavity nucleation whereas the intergranular brittle fracture had been suggested due to the β phase at grain boundary which is to be origin for crack nucleation. These cracks propagate rapidly during final stage of creep and thus lead to the observed failure along grain boundaries.

4. Discussion

Ti-48Al-4Cr exhibits nearly lamellae microstructure consisting lamellae, fine γ and β phase. Addition of Cr up to 4 at.%, introduces β phase (bcc structure). The lamellae structure consists of alternating laths of the γ -TiAl and α_2 -Ti₃Al phases. Such lamellae structure results from the solid state phase transformation of the primary disordered α dendrites. The single fine γ regions surrounding the lamellae grains result from the transformation of the aluminum rich interdendritic melt due to incompleteness of the peritectic reactions. The two peritectic reactions, $L + \beta \rightarrow \alpha$ and $L + \alpha \rightarrow \gamma$, is hardly to be completed due to limited diffusion caused by the formation of a solid envelope of the peritectic phase, avoiding the physical contact between the reactants. As far β phase is concerned, even though it is found to exist together with $\alpha(\alpha_2)$ and γ phases in β stabilizer added TiAl, attention has been paid mainly to the role of β phase in the mechanical properties but not to the formation mechanism of the microstructure as well as the phase equilibria among β , α and γ phases. Therefore, the microstructural formation in the alloys under development or study has in most case been interpreted based on the binary phase diagram, since the amount of the additive elements is not large. However, little attempt has been made to establish the phase relationship among the β , α and γ at elevated temperatures.

Although countless research had associate titanium aluminide with minimum creep behaviour, however long term creep test at low stresses had shown that titanium aluminide exhibits steady state creep behaviour. In this investigation, beta phase contained TiAl, as-cast Ti-48Al-4Cr exhibited steady state creep behaviour at temperatures from 600-700°C with initial stress of 180MPa, minimum creep behaviour at 800°C with initial stress of 150MPa and failed upon loading at 800°C with initial stress of 180MPa. From this result it is evident that the transition from steady state to minimum creep behaviour occurs between 700 to 800°C. This transition which causes limited secondary stage and quick onset of tertiary creep stage is due to the microstructural instabilities. Although the creep deformed SEM-BSE microstructures of as-cast Ti-48Al-4Cr is similar in all the three condition of temperature-stress investigated in this study where extensive amount of β phase was present on the α_2/γ lamellae interfaces in contrast with the initial microstructure, there is particular microstructural instability which responsible for the quick onset of tertiary stage at 800°C. The open bcc structure of β phase becomes more significant at temperatures between 700-800°C and responsible for the quick onset of tertiary creep regime. It is well established that β phase limits the ductility of TiAl at room temperature due to its brittleness. However, at high temperature its open bcc structure causes it to be very ductile. It is evident from the large creep strain (7.98%) exhibited before rupture (figure 3(a)) and dimple like fractured surface after creep-rupture test at 800°C as shown in figure 5. Therefore, β phase is detrimental at both room and high temperature due to its extreme effect on ductility. However, this study shows that β phase might be useful at intermediate temperatures. This is due to the excellent creep resistance of Ti-48Al-4Cr at temperatures from 600-700°C. The effect of β phase on ductility is believed to be moderate at the intermediate temperatures. The transition from steady state to minimum creep behaviour is most probably occurs when the open bcc of β phase is significant at temperature between 700-800°C.

The majority studies had addressed the creep behaviour of gamma TiAl based on the phenomenological description of pure metal creep. Despite the fact that creep curves of TiAl have a general shape that is similar to pure metals, the limited nature of secondary creep and increased importance of tertiary or 'inverse' creep suggest that the traditional method for describing pure metal creep is not valid for TiAl. In the absence of a pure metal description of power-law creep, an alternative method for modeling the creep behaviour of gamma TiAl is needed. Fitting the mechanical data to the existing creep mechanisms without detail understanding on the behaviour of the material as a function of

microstructural variation or creep regime would not be appropriate. A detailed TEM study is necessary for understanding the real creep mechanisms.

5. Conclusions

1. As-cast Ti-48Al-4Cr exhibits nearly lamellae microstructure with coarse lamellae grains (300-600 μ m) and fine γ and β grains at the lamellae grain boundaries. The β phase has body centered cubic crystal structure.
2. As-cast Ti-48Al-4Cr exhibit steady state creep behaviour at 600-700 $^{\circ}$ C with initial stress of 180MPa and minimum creep behaviour at 800 $^{\circ}$ C with initial stress of 150MPa. It failed upon loading at during creep test 800 $^{\circ}$ C and initial stress of 180MPa.
3. Extensive formation of β phase is observed at the α_2/γ lamellae interfaces whereas the initial β phase at grain boundaries decreased after creep deformation at all the temperature-stress conditions investigated.
4. A dimple like fracture surface is observed after creep rupture test at 800 $^{\circ}$ C and initial stress of 150MPa.
5. The transition from steady state to minimum creep behaviour occurs at temperature between 700-800 $^{\circ}$ C. The transition is suggested due to the significant open bcc structure of β phase at high temperature.
6. Although presence of β phase is found to be detrimental for high temperature creep resistance, it has significant good effect for the intermediate temperature creep resistance.

References

- Appel, F. & Wagner, R. (1998). Microstructure and Deformation of Two-Phase γ -Titanium Aluminides. *Materials Science and Engineering*, R22, 187-268.
- Chen, W.R., Triantafillou, J., Beddoes, J. & Zhao, L. (1999). Effect of Fully Lamellar Morphology on Creep of a Near γ -TiAl Intermetallics. *Intermetallics*, 7, 171-178.
- Clemens H & Kestler H. (2000). Processing and Applications of Intermetallic γ -TiAl-Based Alloys. *Advance Engineering Materials*, 2, 551-570.
- Dlouhy, A. & Kucharova, K. (2004). Creep and Microstructure of Near-Gama TiAl Alloys. *Intermetallics*, 12, 705-711.
- Duarte, A., Viana, F., Henrique, M. & Santos, C.M. (1999). As-Cast Titanium Aluminides Microstructure Modification. *Materials Research*, 2, 1-5.
- Jewett, T.J., Ahrens, B. & Dahms, M. (1997). Stability of TiAl in the Ti-Al-Cr System. *Materials Science and Engineering Part A*, A225, 29-37.
- Kawabata T, Fukai H & Izumi O. (1998). Effect of ternary additions on mechanical properties of TiAl. *Acta Materillia*, 46(6), 2185-2194.
- Kim, H.Y. & Hong, S.H. (2002). The Effect of Microstructures on Creep Behavior of Ti-48Al-2W Intermetallic Compounds. *Materials Science and Engineering Part A*, A329-331, 788-794.
- Kim, Y.W. & Dimiduk, D.M. (1991). Progress in Understanding of Gamma Titanium Aluminides. *Journal of the Minerals, Metal and Materials Society*, 43 (8), 40-47.
- Lipsitt, H.A., Blackburn, M.J., & Dimiduk, D.M (2002). High-Temperature Structural Applications. In Westbrook, J.H. & Fleischer, R.L. (Eds). *Intermetallic Compounds: Volume 3, Principles and Practice* (pp. 472-499). United Kingdom: John Wiley and Sons Ltd.
- Schillinger, W., Clemens, H., Dehm, G. & Bartels, A. (2002). Microstructural Stability and Creep Behavior of a Lamellar γ -TiAl Based Alloy with Extremely Fine Lamellae Spacing. *Intermetallics*, 10, 459-466.
- Shao, G. & Tsakiroopoulos, P. (1999). Solidification Structures of Ti-Al-Cr Alloys. *Intermetallics*, 7, 579-587.
- Shi JD, Pu ZJ, Zhong ZY & Zou DX. (1992). High Temperature Deformation Behaviour of Beta-Gamma TiAl Alloy. *Scripta Materillia*, 27, 1331-1336.
- Sun, F.S., Cao, C.X., Kim, S.E., Lee, Y.T. & Yan, M.G. (2001). Alloying Mechanism of Beta Stabilizers in a TiAl Alloy. *Metallurgical and Materials Transactions A*, 32A, 1573-1589.
- Takeyama, M., Ohmura, Y., Makoto Kikuchi & Matsuo, T. (1998). Phase Equilibria and Microstructural Control of Gamma TiAl Based Alloys. *Intermetallics*, 6, 643-646.
- Viswanathan, G.B., Kartikeyan, S., Mills, M.J. & Vasudevan, V.K. (2001). Creep Properties of a Fully Lamellar Ti-48Al-2Cr-2Nb Alloy. *Materials Science and Engineering Part A*, A319-321, 833-837.
- Wang, J.G. & Nieh, T.G. (2002). Creep of a Beta Phase-Containing TiAl Alloy. *Intermetallics*, 8, 737-748.

Zhang, D., Arzt, E. & Clemens, H. (1999). Characterization of Controlled Microstructures in a γ -TiAl (Cr, Mo, Si, B) Alloy. *Intermetallics*. 7, 1081-1087.

Zhang, W.J., Chen, G.L., Appel, F., Nieh, T.G & Deevi S.C. (2001). A Preliminary Study on the Creep Behavior of Ti-45Al-10Nb Alloy. *Materials Science and Engineering Part A*, A315, 250-253.

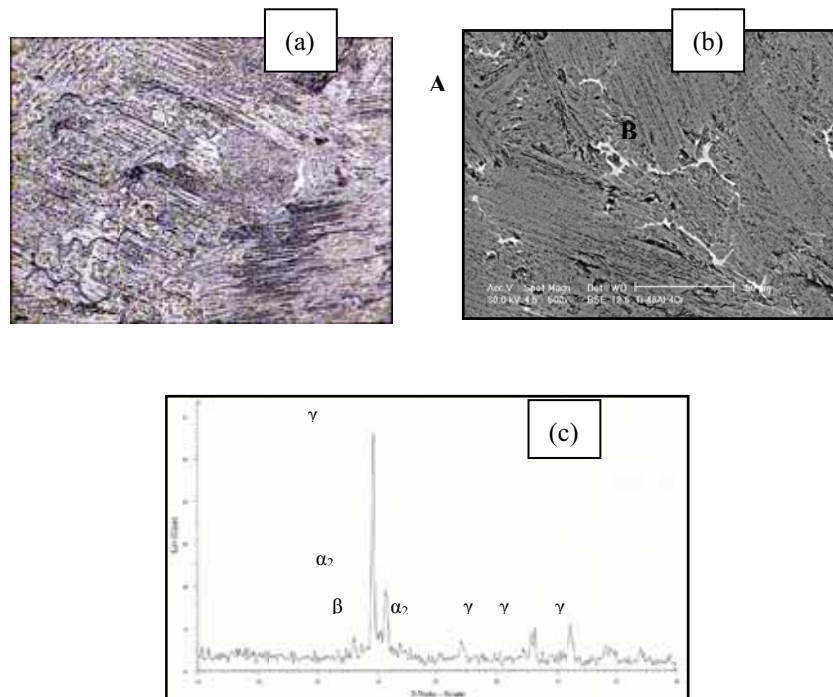


Figure 1. (a) Optical microstructure (200x), (b) SEM-BSE microstructure (500x) and (c) XRD result of as-cast Ti-48Al-4Cr.

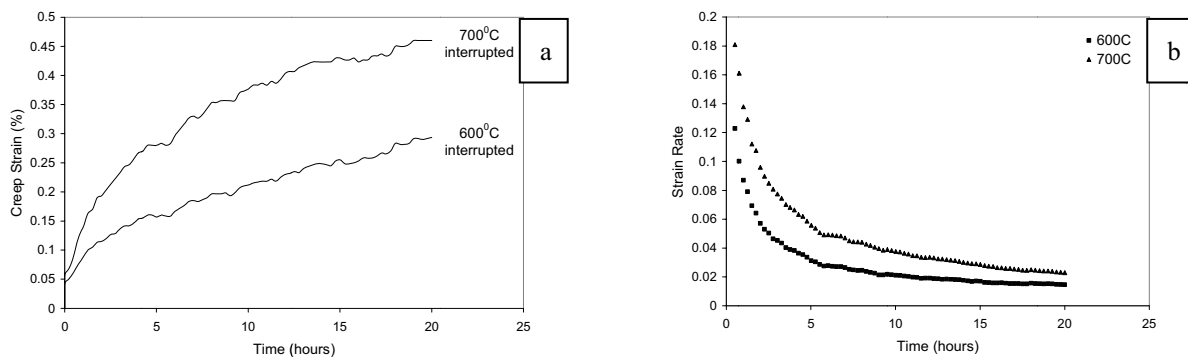


Figure 2. Creep curves of Ti-48Al-4Cr at temperatures ranging between 600-700°C and identical initial stress of 180MPa (a) creep strain (%) vs time (hours) and (b) strain rate (hr^{-1}) vs time (hours)

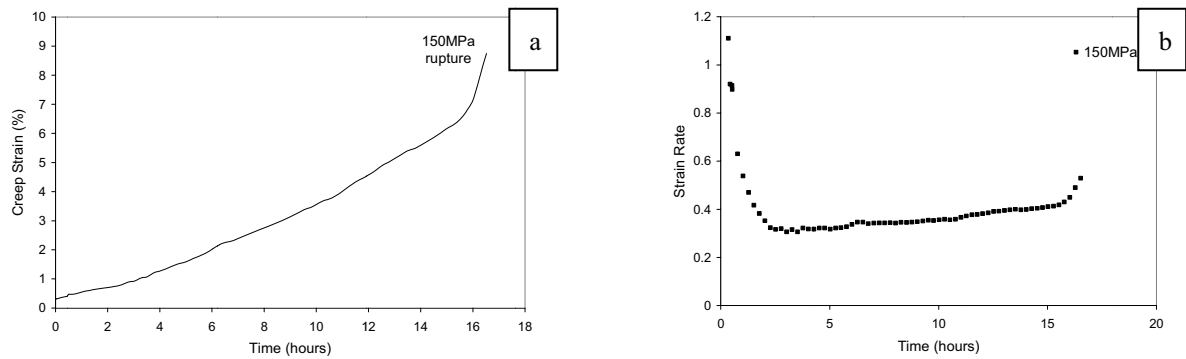


Figure 3. Creep curves of Ti-48Al-4Cr at 800°C and initial stress of 150MPa
(a) creep strain (%) vs time (hours) and (b) strain rate (hr⁻¹) vs time (hours)

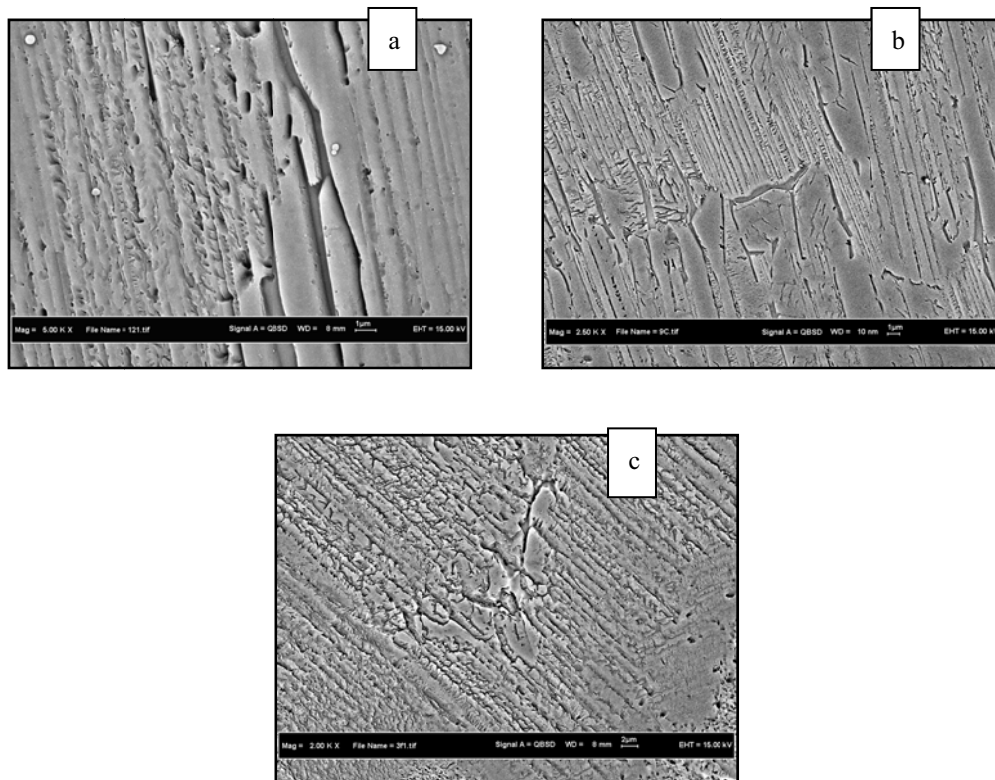


Figure 4. SEM-BSE micrograph showing microstructure of as-cast Ti-48Al-4Cr (a) after 20hours of creep deformation at 600°C and initial stress of 180MPa (5000x), (b) after 20hours of creep deformation at 700°C and initial stress of 180MPa (2500x) and (c) at near rupture surface after creep-rupture test at 800°C and initial stress of 150MPa (2000x).

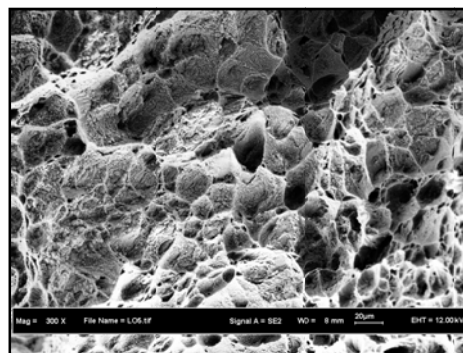


Figure 5. Fracture surface of as-cast Ti-48Al-4Cr after creep at 800°C and initial stress of 150MPa (300x)



A Study on the Effects of Higher Order Mode Wave on Mufflers Performance

Hongguang Liu, Senlin Lu & Falin Zeng

School of Automobile and Traffic Engineering

Jiangsu University

Zhenjiang, Jiangsu, China

Tel: 86-511-8878-0271 E-mail: lhg@ujs.edu.cn

Zhangping Lu

School of Mechanical Engineering;

Jiangsu University

Zhenjiang, Jiangsu, China

Jiangkun Zhou

School of Automobile and Traffic Engineering

Jiangsu University

Zhenjiang, Jiangsu, China

Abstract

Based on the existence of higher order mode waves (HOMW) in expansion mufflers is proved theoretically, a 3-D FEM is used to obtain the four-pole parameters of a muffler which are in turn used to calculate the transmission loss. With this method, the distribution of sound pressure in a muffler is calculated, the effects of HOMW on the muffler performance are investigated and a technique to improve the muffler performance is put forward. It is shown that, because of HOMW, the sound wave in expansion chamber is not in plane form; HOMW can descent capability of muffler, and the position of inlet and outlet is important to the performance of mufflers.

Keywords: Muffler, Higher order model wave, FEM

1. Introduction

Expansion mufflers have several advantages, such as back pressure is little and the noise elimination performance is steady, so they are used in lots of engines. At present, the formula using to analysis the expansion muffler performance was established by Davis in the early 1950's. This formula was built up on the basis of the plane wave model, assuming that the sound in the expansion chamber propagates in plane form in a stationary medium. Their analysis revealed that the transmission loss is related with the area expansion ratio m and the non-dimensional frequency parameter kl and is a periodic function. Namely

$$TL = 10 \log_{10} \left[1 + \frac{1}{4} \left(m - \frac{1}{m} \right)^2 \sin^2 kl \right] \quad (1)$$

Where k is the wave number and l is the length of the expansion chamber.

However, due to the existent of higher order model wave(HOMW), when the frequency increases in certain extent, the sound waves in the expansion chamber is not linear anymore, and the muffler performance do not accord with the Eq.(1). With the development of the computer, the non-linear problems of sound field in mufflers are paid to more and more attention, including the effects of HOMW on muffler performance or the 3-D effects of the muffler and the effects of airflow on muffler performance and so on, and numerical calculation method is one of the important research methods. Narayana predicts muffler performance and the effects of HOMW with numerical method; Sahasrabudhe investigates the effects of HOMW by means of 3-D FEM and the four-pole network. Lu Senlin et al uses the 3-D FEM of the ANSYS process combining with four-pole network to research HOMW, and it acquires favorable effect. The method will be used to discuss HOMW and its effects on muffler performance in this paper.

2. HOMW in a tube

Most expansion mufflers consist of various tubes, so the HOMW merely in a rotundity tube is discussed simply now. Assuming that there is a tube, its diameter is $2a$, r is the radius of polar coordinate, θ is angle of polar coordinate and the Z coordinate is along the tube length (see Fig 1), the sound wave equation in the tube can be obtained by:

$$\frac{1}{r} \frac{\partial}{\partial r} \left(r \frac{\partial p}{\partial r} \right) + \frac{1}{r^2} \frac{\partial^2 p}{\partial \theta^2} + \frac{\partial^2 p}{\partial z^2} = \frac{1}{c^2} \frac{\partial^2 p}{\partial t^2} \quad (2)$$

Let the general solution for this equation be

$$p = R(r)\Theta(\theta)Z(z)e^{j\omega t} \quad (3)$$

And Substituting Eq. (3) to Eq. (2), we obtain

$$\left. \begin{aligned} \frac{d^2 Z}{dz^2} + k_z^2 Z &= 0 \\ \frac{d^2 \Theta}{d\theta^2} + m^2 \Theta &= 0 \\ \frac{d^2 R}{dr^2} + \frac{1}{r} \frac{dR}{dr} + \left(k_r^2 - \frac{m^2}{r^2} \right) R &= 0 \end{aligned} \right\} \quad (4)$$

Where k_r and k_z are the wave number in the direction of r and z respectively. At the same time, both k_r and k_z satisfy the equation

$$k_r^2 + k_z^2 = k^2 = \frac{\omega^2}{c^2} \quad (5)$$

Where c is sound speed.

For the equation with variable z in formula (4), the solution can be given by

$$Z(z) = A_z e^{-jk_z z} \quad (6)$$

For the equation with variable θ , we can obtain the solution of

$$\Theta(\theta) = A_\theta \cos(m\theta + \varphi_m) \quad (7)$$

Because the relation of $\Theta(\theta) = \Theta(m\theta + 2\pi)$ should be satisfied, the m in Eq. (7) must be positive integer.

The third equation in the formula (4) is a standard Bessel equation, in which the variable is $(k_r r)$, and the general solution is given by:

$$R(k_r r) = A_r J_m(k_r r) + B_r N_m(k_r r) \quad (8)$$

Where $J_m(k_r r)$ and $N_m(k_r r)$ are Bessel function and Norman function respectively? According to Norman-function emanative at the zero point, $B=0$ should be admitted, then simplified the Formula (7) to

$$R(k_r r) = A_r J_m(k_r r) \quad (9)$$

So the sound pressure in the tube can be obtained by

$$p_m = A_m J_m(k_r r) \cos(m\theta - \varphi_m) e^{j(\omega t - k_z z)} \quad (10)$$

Then the corresponding radial velocity is

$$v_{rm} = A_m \frac{jk_r}{\rho_0 \omega} \left[\frac{dJ_m(k_r r)}{d(k_r r)} \right] \cos(m\theta - \varphi_m) e^{j(\omega t - k_z z)} \quad (11)$$

Assuming the muffler wall is rigid, that is when $r=a$, $v_r = 0$, thus gained

$$\left[\frac{dJ_m(k_r r)}{d(k_r r)} \right]_{(r=a)} = 0 \quad (12)$$

According to Bessel function is a recursive function, the following equations can be obtained:

$$J_{m-1}(k_r a) = J_{m+1}(k_r a) \quad (m > 0) \quad (13)$$

$$J_1(k_r a) = 0 \quad (m=0) \quad (14)$$

To solve above equations, a series roots can be obtained. Using two integer m and n to represent the serial numbers of these roots, and recording corresponding k_r as k_{mn} , then the part of roots of the equation can be obtained which are shown in Table 1.

Consequently, the sound pressure can be written in following form

$$p_{mn} = A_{mn} \cos(m\theta - \varphi_m) J_m(k_{mn} r) e^{j(\omega t - k_z z)} \quad (15)$$

Where $k_z = \sqrt{k^2 - k_{mn}^2}$

Eq.(15) express the (m, n)order simple waves may be generated in the tube. Among them the (0,0) order is the main wave, while the rest is the high order waves.

3. Numerical analysis of the muffler performance.

Because of HOMW in mufflers, the sound wave doesn't keep in plane wave, so the transmission loss doesn't accord with Eq.(1) anymore. In this paper, the transmission loss is calculated by means of 3-D FEM and four-pole network to investigate the effects of HOMW on muffler performance.

Transmission loss of a muffler can be denoted by four-pole parameters, namely

$$T = 20 \lg \left[\frac{1}{2} \left(A + D + \frac{\rho c}{S_0} C + \frac{S_0}{\rho c} B \right) \right] \quad (16)$$

Where A, B, C, D is four-pole parameters of the muffler; S_0 is cross-sectional area of the Inlet/outlet tubes of mufflers; ρ is air density.

When the sound wave in expansion chamber is plane wave, the four-pole parameters are showed as follow respectively:

$$A = \cos kl, \quad B = j \frac{\rho c}{S} \sin kl, \quad C = j \frac{S}{\rho c} \sin kl, \quad D = \cos kl$$

Where l is the length of the tubes; S is cross-sectional area of the tubes.

Because of HOMW, the sound wave in expansion chamber is not plane wave, so the formula to calculate four-pole parameters by using the theory of plane wave is not suitable. Then 3-D FEM is employed to obtain the four-pole parameters of the muffler which are in turn used to calculate the transmission loss with Formula(16).

By the definition of four-pole parameters, we know that:

$$\left\{ \begin{array}{l} A = \left. \frac{p_0}{p_r} \right|_{V_r = 0} \\ B = \left. \frac{p_0}{V_r} \right|_{p_r = 0} \\ C = \left. \frac{V_0}{p_r} \right|_{V_r = 0} \\ D = \left. \frac{V_0}{V_r} \right|_{p_r = 0} \end{array} \right. \quad (17)$$

Where p_0 and p_r are denoted the sound pressures at the inlet and outlet of the muffler respectively; V_0 and V_r are the volume speed of medium at the inlet and outlet of the muffler respectively.

Accordingly, FEM can be used to obtain the sound pressure and volume speed when the outlet sound pressure is zero (the short circuit state) and volume speed is zero (the open circuit state) respectively, and the Formula(17) can be employed to get the four-pole parameters.

The author used the ANSYS to obtain the parameters p_0, p_r, V_0 and V_r under this two states. In calculation process, the p_0 is given by the form of mechanical boundary condition of the inlet. In order to calculate simply, let $p_0 = 1$, and the p_r is obtained by using the FEM directly. For getting the V_0 and the V_r , we can calculate sound pressure at three equidistant point along the axis of Inlet/Outlet tube of the muffler, and then calculate the volume speeds, the V_0 and the

V_r of the muffler by Formula (18) and (19)

$$V = -j \frac{S_0}{\rho \omega} \frac{\partial p}{\partial n} \quad (18)$$

$$\frac{\partial p}{\partial n} \approx \frac{-p_3 + 4p_2 - 3p_1}{2h} \quad (19)$$

Where p_1 , p_2 and p_3 are the sound pressures at three equidistant points following the direction of the axes and near the end of inlet/outlet tubes, h is the distance between two points, V is volume speed at the end of inlet/outlet tubes.

Because the diameter of the inlet /outlet tubes of muffler is much small, and then the sound wave transmits in plane form in the tubes, the volume speed have enough precision which obtained by using the above formulas.

The calculation process of finite element consists of building model, generating mesh, applying load and boundary conditions and solutions. The work should be divided into two parts; First, to calculate the sound pressure of the muffler under the open circuit state ; Second, to obtain the sound pressure of the outlet tube of muffler under the short circuit state with the mechanical boundary condition $p_r = 0$; Lastly, we get the data by using the Matlab interface program and second post-processing procedures to calculate the four-pole parameters and the transmission loss according to the above Formulas.

4. The effects of HOMW on muffler performance

From the table 1, we know that the cut-off frequency of the minimum HOMW in circular tube corresponds to the non-dimensional parameter of $ka = k_{1,0} a = 1.84$. If the value is less than 1.84, the sound wave is in plane form, or else is not in plane form anymore.

Fig2.shows the acoustic pressure contours in a coaxial expansion muffler obtained by making use of the FEM while $ka=1.5$ and $ka=4$ respectively. Obviously, when ka equals 1.5, the sound wave is in plane form in the whole muffler except the outlet and inlet of the expansion chamber. However, when ka is equals to 4, due to the effect of HOMW, the sound wave in the expansion chamber is not in plane form anymore, so 1-D sound wave theory is not suitable, but the sound wave is also in plane form in the Inlet/Outlet tubes.

From formula (1), we know that transmission loss of the simple expansion muffler is periodic function of $kl = \pi$ which is shown by the broken lines in Fig3. The real lines in Fig(3) show the transmission loss by making use of FEM and four-pole parameters. From the Fig(3), we conclude that when the frequency of the sound is less then the cut-off frequency (corresponding the $ka=1.84$), the two lines are tallied. When ka is larger than 1.84, HOMW begins to come forth in muffler, but its effect is small at beginning, and the difference of the result from FEM and plane wave analysis is little. When the (2,0)mode existent, the value of academic is different from that of FEM, but they are not obvious. However, when ka is larger than the value corresponding the (0,1)mode the disparity of them is clear, so the muffler comes invalidated..

From the table(1), we conclude that the number of cut-off frequency ka of the (0,1) mode is 3.83. when $a=0.12\text{m}$ and $c=400\text{m/s}$, the cut-off frequency is about 2000Hz, and that is to say HOMW affects performance above the middle-high frequency about 2000Hz mainly. Although the basic frequency of the exhausting noise is in low-frequency, the airflow noise of muffler has more energy in the middle-high frequency. Moreover, considering the fact that the human ear is less sensitive to low frequency than middle-high frequency of the audible range , and A-weighting filter network provides less respond to low-frequency range, the noise of the middle-high frequency takes more advantages.

5. The improvement of the muffler performance.

Commonly, HOMW of the muffler is inevitable. However, the transmission of the sound wave in conduit depends not only on the geometrical dimension of the conduit, but also on the location of the source and the acoustic boundary conditions . The above-mentioned effect of HOMW on the muffler performance aims at the coaxial mufflers, namely the sound source is located on the center line of the chamber. If we change the location of sound source, the transmission of the sound wave in the expansion chamber is altered at the same time. In order to make the frequency of the excited HOMW is higher than certain frequency of the exhaust noise, we can change the configurations of mufflers to suppress the excitation of some HOMW. For example, when inlet and/or outlet tubes are coaxial with the expansion chamber, (1, 0) and (2, 0) modes are not excited effectively. However, when the Inlet tube offsets the axes of an expansion chamber by a distance of 0.63 times the radius, the (0,1)mode can be suppressed effectively. The above conclusion is also suitable for the outlet tube. Accordingly, if we put the one of outlet tube or inlet tube on the axes of the expansion chamber and another at the location offsetting the axes a distance of 0.63 times the radial of chamber, the disabled frequency of the muffler can be increased and the muffler performance is improved. The broken lines in Fig(4) show the transmission lose corresponding the outlet tube is coaxial with the expansion chamber, and the inlet tube

offsets a certain distance. From the Figure (4) we conclude that when the outlet tube is coaxial with expansion chamber and the inlet tube offsets a certain distance, the muffler performance is improved obviously, and its noise reduction capacity keeps large until ka equals to 6.5, above which the energy of the exhaust noise is very small.

6. Conclusion

From above analysis, we conclude that:

- (1) Due to the existence of HOMW, the sound wave in mufflers is not in plane form in the middle-high range of frequency, so the 1-D acoustics formula is not suitable anymore
- (2) HOMW does effects the noise reduction performance of expansion mufflers in the middle-high frequency range.
- (3) Choosing the appropriate configuration of muffler can decrease the effects of HOMW and improve the performance of mufflers.

References

- Du, Gonghan, Zhu Zemin & Gong, Xiufeng. *the Foundation of Acoustics*. Nanjing: the Publishing Company of Nanjing University.
- Lu, Senlin & Liu, Hongguang. Numerical analysis of engine muffler with 3-D FEM. [J]. *Transaction of CSICE*. 2003, 21(5): 346-351. (in Chinese).
- Narayana TSS, Munjala ML. prediction and measurement of the four-pole parameters of a muffler including higher order mode effects [J]. *Noise Control Engineering Journal*. 2005. 53(6): 240-246.
- Sahasrabudhe A D, Anantha Ramus, Munjal ML. Matrix condensation and transfer matrix techniques in 3-D analysis of expansion chamber muffler[J]. *Journal of Sound and Vibration*. 1991, 143(3): 371-394.
- Sahasrabudhe AD, Munjal ML & Anatha Ramu S. Design of expansion chamber mufflers incorporating 3-D effects. [J]. *Noise Control Engineering Journal*, 1992, 38(1): 27-38.

Table1. Values of $k_m a$

n	m		
	0	1	2
0	0	1.841	3.054
1	3.884	5.322	6.705
2	7.051	8.536	9.965

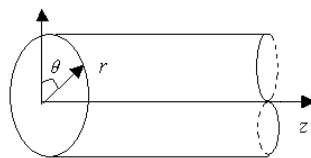


Figure 1. a sound pipe

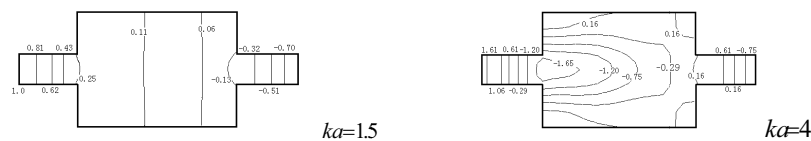


Figure 2. Acoustic pressure contours in a muffler

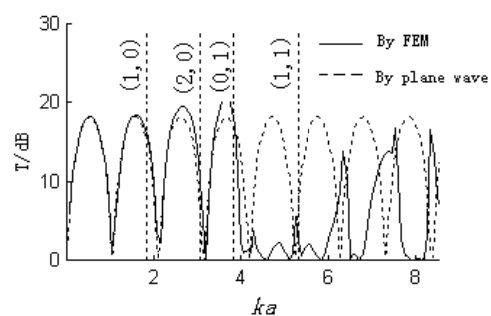


Figure 3. TL results expected from plane wave analysis and FEM

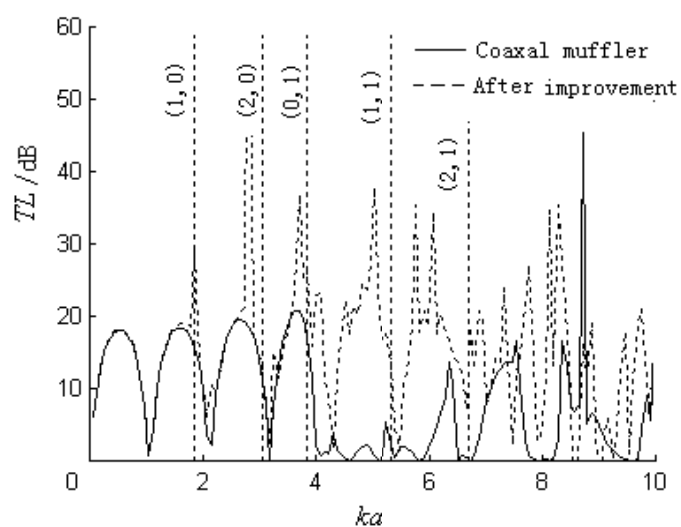


Figure 4. TL comparison of inlet-offset and coaxial expansion muffler



Development and Analysis of Taper Tool Path for Micro Turning Operation

Azuddin Mamat (Corresponding author)

Department of Engineering Design and Manufacture

Faculty of Engineering, University of Malaya

50603, Kuala Lumpur, Malaysia

Tel: 60-3-7967-5265 E-mail: azuddin@um.edu.my

Mohd Afif Mohd Rosli

Department of Engineering Design and Manufacture

Faculty of Engineering, University of Malaya

50603, Kuala Lumpur, Malaysia

Tel: 60-3-7967-5383 E-mail: ahmadafif@gmail.com

Abstract

This paper presents the taper tool path scheme for micro turning of brass. Based on tool path technique for straight cutting, tool paths for taper shape are produced. This study covers the effect of cutting parameters with the use of different tool path method. The result shows that reverse cut is considered to be the most accurate as it has the smallest figure of average difference in the intended dimension. This is followed by step cut, whole cut and disk-2 cut. It shows which tool path is the most suitable for high precision machining. Defects and accuracy of the desired dimension in several tool path methods are observed and discussed.

Keywords: Micro turning, Taper turning, Cutting defects

1. Introduction

Technology progress is inevitable. Through technology advancement, the demands of part products are also changing. With parts needed are getting smaller, new manufacturing technology are developed to compensate traditional methods which are unable to carry out the needs. One of the developments in manufacturing industry is toward miniaturization. Furthermore, with a highly competitive part production industry, many manufacturing companies in various countries are changing their production into high-quality parts. Precision and smoothness is greatly considered for this advance manufacturing part production.

In micro mechanical machining, there are several operation included in this category, such as micro milling, micro press and micro turning machine. All of these processes have the same operation as their conventional counterparts, but with scaled down workpiece and part produced. However, as the workpiece becomes smaller and the features are more detailed, manual machining using conventional method is almost impossible. Thus, the use of computer numerical control (CNC) machine is necessary.

Micro machining technology is still new in the industry and some parts are not thoroughly developed. Micro machining is considered to be an operation process at a dimension of 1 to 999 micrometer. However, a new limit is set; which are 1 to 500 micrometer for micromachining and 500 to 999 micrometer for macro machining according to McGeough J, (2002). In a micro-scale fabrication industry, precision and speed are needed during operation. However, not all machines are suitable for these requirements. Therefore, computer numerical control machines are used as it is the only equipment which can provide quick and accurate machining operations for workpieces that involve complex shapes according to Lin SCJ, (1994). Several factors are needed to be checked during the operation in developing micro scale products. Precise control of the machine and machining parameters, such as feed rate, depth of cut and rpm are important (M. Azizur Rahman, et. al, 2006)

Micro turning, a part of micro scale machining process using solid tool, its material removal process is almost similar to normal turning operation. Definite 3D shapes on micro scale can be produced using micro turning operation as it uses solid cutting tools. Numerical Control (NC) programming is applied in micro turning operation to accurately and precisely control the cutting tool motions during operation (M. Azizur Rahman et. al., 2005). Precision is very

essential when machining at micro scale as the tolerance becomes crucial parameter. If a tolerance of $+15\text{ }\mu\text{m}$ is needed for 10mm diameter, thus in a same ratio, $+15\text{nm}$ of tolerance is applied for $10\text{ }\mu\text{m}$ diameter. In order to work in micro scale, user control is vital according to Zinan Lu et. al.(1999). However, there are other issues having to be considered during micro turning operation.

One of the most important issues is the fact that the cutting force tends to bend the workpiece during operation. Therefore, it would affect machining accuracy and limit the machinable size (T. Masuzawa, 2000). During operation, the thrust force from the tool deflects the work piece. The workpiece would vibrate at tangential direction of the tool-workpiece contact region as the cutting tool block the vibration along the normal direction report by Lim HS et. al. (2002).

Thus, the control of reacting force during operation is important. The value of the cutting force must be lower than the value that causes plastic deformation of the workpiece to overcome workpiece deflection during operation according to Z. Lu and T. Yoneyama, (1999), and Lu. Z et. al (1999). Because, as the diameter of the workpiece is reduced, rigidity against the defection of the workpiece by the cutting force decreases. The relationship between the cutting force and the cutting speed can be seen. As the value of force is related to the cutting area, speed is increased to lower the cutting force produced. Therefore, higher speed is required in micro turning operation to get the optimum result (Zinan Lu et. al,1999).

Other than that, the depth of cut is also a very influential cutting parameter. When cutting with low depth of cut, thrust force is the dominating force. Meanwhile, if a very small depth of cut is used, plastic deformation (rubbing and burnishing) is dominant, which generate high thrust force. On the other hand, when turning at large depth of cut, tangential force is dominating over thrust force (M. Azizur Rahman et. al. (2005). Thus, the value of depth of cut must be determined beforehand with the above consideration.

In micro turning process, if the feed rate is increased, the contact area of tool and workpiece would also increases. This will raise the material removal rate, and the forces on the workpiece will be affected. As speed increases, material removal rate is decreased, which reduces the tool force due to shorter work-tool contact length (M. Azizur Rahman et. al. 2005) Cutting force decreases as the cutting speed increases. From the findings, specific cutting force increases as the cutting area is reduced and then decreases at certain limit (Zinan Lu et. al. 1999). This shows that increment of area of cut would increase cutting force. Thus, deflection and the cutting force could be controlled by adjusting the force and the present diameter of the workpiece. To minimize deflection of workpiece and preventing plastic deformation, step size can be applied. The step size can be determined using both equations above.

According to M. Azizur Rahman et.al (2006), there are 4 cutting scheme would be featured in the software that generates the NC codes. All of the cutting schemes have to be applicable for both straight and tapered features of the workpiece feature. There are namely whole cut, step cut, reversed cut and disk 2 cut. Whole or parallel cutting from a conventional turning operation, are not suggested to be applied in micro turning operation. From the findings by M. Azizur Rahman, et. al, (2006) the workpiece would tend to deflect. During the cutting operation the workpiece diameter would be reduced and the unsupported length will be increases. It is due to the low level of sustainability of the micro scale workpiece to the deflection and bending stress generated from the tool. For tapered features on part, taper turning operation has to be done. From M. Azizur Rahman, et. al, (2006), it introduce micro taper cutting by cutting parallel to the axis of the workpiece and machining parallel to the tapered surface. It concludes that turning parallel to the taper surface is relatively better in the manufacturing efficiency and time saving point of view. Tapering and chamfering design in workpiece would have high demand in near future. However, current information of tapering and chamfering cutting for micro turning operation is not in depth and comprehensive. Therefore, this study will investigate the effect of tool path for taper shape in micro turning.

2. Taper Tool Path in Micro turning

2.1 Whole Cut Taper Tool Path

Whole cutting is a simple cutting operation which applied the cutting technique of conventional turning. There are two types of tapered feature, outward and inward tapering of whole cut tool path as shown in figure 1. Outward taper is when the start diameter is smaller than the end diameter, while inward taper is vice versa. For outward tapered feature, straight rough cutting is done until the workpiece diameter is equal to diameter of the end point. The finishing cut is done with an angle of the tapered feature with finish depth of cut, as the end point of cutting tool moves. For inward tapering, straight rough cutting is done until it reaches the diameter of start point. Finish cutting is done starting from start point and ends with a finish depth of cut. This is repeated until the end diameter is equals to the end point diameter. The repeated cutting is done with the end point periodically lowered with a finish depth of cut.

2.2 Step Cut Tool Path

From figure 2, single pass of the tool path for step cut is shown for both outward and inward tapering. For outward tapering, in a single pass, straight rough cutting is done repeatedly with a rough depth of cut until it reaches the actual

dimension plus a clearance of finish depth of cut. Finish cutting starts with cutting by an angle of the tapered feature and repeated until the actual dimension of the feature. While for inward tapering, repeated straight rough cutting starts until it reaches the actual dimension, plus a clearance of finish depth of cut. Then, finish cut with an angle of feature by the actual dimension of the feature.

2.3 Reverse Cut Tool Path

Single pass of tool path for reverse cut is shown for both outward and inward tapering as shown in figure 3. For outward tapering, straight rough cutting is done without a depth of cut until it reaches the actual dimension of the feature. However, it is done from back to front. Then, finish cutting with an angle of the tapered feature through the actual dimension of the feature to the start point of the pass. The pass would be repeated to meet the required feature. While for inward tapering, straight rough cutting starts without depth of cut until it reaches the actual dimension. Then, finish cut with an angle of feature by the actual dimension of the feature. The pass would be repeated to form the required feature. Both of the cutting operation starts with a shift towards the end point by L back to the original position of the pass.

2.4 Disk-2 Cut Tool Path

From Figure 4, a single pass of the tool path for disk-2 cut at tapered feature is shown. For outward tapering, it starts off with a shift by L toward the end point and then rough cut straight until reaches the diameter of the feature plus finishes depth of cut. The tool would cut toward the start point of the pass horizontal value with tapered angle of the feature. Then, the tool cuts inward toward the feature. Finally tool moves toward diameter of the end of cut with an angle of the feature. While for inward tapering, the tool path is a mirror image to the tool path of the outward tapering, which can be seen on the right part of the figure.

2.5 Points Definition

For all taper cutting operations, tool paths are defined by point to point definition for the moves. These points are provided by the input from part dimension. However, there are some points position that are not provided by the part dimension for certain tool path scheme which the software have to generate. Tool path scheme which uses a cutting thickness during cutting operation would have the numerical calculation program to generate some points. The points needed are the one in horizontal plane between the start point and the end point. In the input, the user would define the start point and the end point. The feature wanted must be straight from one to another. However, the tool paths generated have to be repeated with a value of thickness parameter. Thus, there would be an end point for every pass of the operation toward the feature end point. Here, the end point has to be generated as shown in figure 5. In this study, triangle theorem is used to solve the problem. If the feature of two 90 degrees triangles is the same but only scaled down, the dimension could be attained if we know the dimension one of the triangles. This can be further explained using Figure 6.

The needed point can be obtained using the following equation:

$$\frac{L}{H} = \frac{l}{h}$$

where

- L = length between start and end point
- H = height between start and end point
- l = length between start and the point needed
- h = height between start and the point needed

The value of start and end point can be attained from the input file and the value of L and H can be calculated. While, the value of l is actually cutting thickness used. Therefore, the value of h can be obtained using the above equation.

3. Equipment, Cutting Parameters and Part Dimension

The experiment was conducted using multipurpose miniature Mikrottools DT110 machine. It has the capability to machine a workpiece in 3 axes direction with accuracy to 0.0001 mm. The motion controller of this machine can execute NC codes. The machine was selected for its high accuracy machining facility. The machined part was measured using a NIKON VM-250 Computer Measuring Microscope (CMM) machine. Since the effect of material is not studied, only brass rods with 7.0 mm diameter were used. The cutting tool material used in this study is tungsten carbide. The cutting parameters such as spindle speed, depth of cut, feed rate and cutting thickness were used for the experiment. Part shape and size are kept constant for every machining operation. Figure 7 shows dimensions of the machined part. Table 1 shows cutting parameters used to run the experiment.

The measurements are done toward the accuracy of the features such as horizontal length (A), tapered length (B), tapered angle (C) and vertical length (D). After each workpieces have been machined with a certain cutting path scheme, measurements are taken and the accuracy percentages are calculated. Figure 8 shows a sample of machined brass rod using tapered tool path.

4. Result and Discussion

The machined part is observed and measured to check its accuracy and finishing using a CMM machine.

4.1 Whole Cut Taper Tool Path

The features from whole cutting method are considered in low condition if compared with other cutting method. Figure 9 shows an output of taper cutting using whole cut tool path. The surface finish is not fine enough for micromachining operation and the tapered feature part is not completely cut away. Other than that, during operation, the front part of workpiece is being chipped off due to long cutting size relative to its small diameter as shown in figure 10. It is because of the small workpiece being affected by deflection and bending stress.

4.2 Step Cut Taper Tool Path

By observation, the finish of step cutting method is excellent. The edges of the features are clearly visible and machined properly. Figure 11 shows a part produce using step cut tool path for taper cutting. However, defects of the part are the burrs at the end of the part as shown in figure 12. There are also undercuts from the wide angle face of the tool. Other than that, the face of the part is not fine for micromachining operation.

4.3 Reverse Cut Taper Tool Path

Features from the reverse cutting method are the best in this study. The edges are accurate and the finishing is smooth. Figure 13 shows a part produce using reversed cut tool path for taper cutting. There are no defects, except for some burrs, undercuts and unmachined part. The burrs are located at the sharp taper and the outer diameter of the part. Other than that, it is perfect.

4.4 Disk-2 Cut Taper Tool Path

The end of the part is not being cut completely in this operation using disk-2 cutting method. Some of the chips are not being cut off and still at the part as shown in figure 14. The edges between the tapered features are not fine and as sharp as reverse cutting. Moreover, there are some bumps and hills on the surface and the taper, i.e. not that smooth. Figure 15 shows a part produce using Disk-2 cut tool path for taper cutting. There are also an undercuts at the part due to the angle face of the tool. Additionally, there are some burrs at the reverse taper of the part.

4.5 Measurement

The measurements of each cutting path scheme are summarized in a graph form as shown in figure 16. It is noticed that the maximum percentage difference is at feature B (tapered length) for the entire tool path scheme and followed by feature A (horizontal length), D (vertical length) and C (tapered angle). This is due to errors occurring during reading the dimension of the workpieces because there are many burrs and uneven surface on the tapered part. Therefore, the tapered feature is hard to measure using CMM machine as it uses optical dimension/positioning.

While if compared between the tool path schemes, reverse cut is considered to be the most accurate as it has the smallest figure of average difference from the intended dimension. This is followed by step cut, whole cut and disk-2 cut. Thus, this shows which tool path is the most suitable for high precision machining. The results above are generated by using the same cutting parameters for the entire tool path scheme. However, it is impossible to require cutting parameters which are suitable for the entire cutting path. Therefore, the result would be varied from the optimal result of the tool path scheme selected.

5. Conclusions

The main purpose of this work is to explore the behavior of different cutting tool path for taper turning. The conclusions of this study are:

- 1) All tool path schemes are suitable for micro turning operation as the error range of the machined part is relatively low.
- 2) The four types of cutting path scheme are suitable for different situation in operation. The descriptions of application of cutting path scheme are stated below:
 - a) Whole cut - It is suitable for small metal removal and/or when short generation time is needed.
 - b) Step cut - The most suitable cutting path scheme in micro turning operation because the deflection and bending stress produced on the workpiece can be kept to minimum using its cutting step size
 - c) Reverse cut - This type of cutting path is suitable when using reverse faced tool (face of tool is heading in opposite direction)
 - d) Disk-2 cut - It is suitable when using a tool with dual cutting face as this cutting path will utilize both of them.

- 3) Tool with small rake angle is required during micro turning operation in order to be kept to minimum level of the undercut produced on the feature of the workpiece.
- 4) Many defects may occur during operation such as undercut, burr and chipped off surface.

References

- McGeough J, (2002), Micromachining of engineering materials, Dekker, New York.
- Lin SCJ, (1994), Computer numerical control, Essentials in programming and networking. Delmar, New York.
- M. Azizur Rahman, M. Rahman, A. Senthil Kumar, H.S. Lim and A.B.M.A. Asad, (2006), Development of micropin fabrication process using tool based micromachining, DOI 10.1007/s00170-004-2270-9, International Journal of Advanced Manufacturing Technology, 27: 939–944.
- H.S. Lim, A. Senthil Kumar and M. Rahman, (2002), Improvement of form accuracy in hybrid machining of microstructures, Journal of Electronic Materials, 31 (10) 1032–1038.
- K. Egashira and K. Mizutani, (2002), Micro-drilling of monocrystalline silicon using a cutting tool, Precision Engineering 26 263–268.
- M. Azizur Rahman, M. Rahman, A. Senthil Kumar and H.S. Lim, (2005), CNC microturning: an application to miniaturization, International Journal of Machine Tools & Manufacture, 45 631–639.
- Zinan Lu and Takeshi Yoneyama, (1999), Micro cutting in the micro lathe turning system, International Journal of Machine Tools & Manufacture, 39 1171–1183.
- T. Masuzawa, (2000), State of the art of micromachining, Annals of the CIRP, 49 (2) 473–488.
- Lim HS, Kumar AS and Rahman M, (2002), Improvement of form accuracy in hybrid machining of microstructures, Journal of Electron Material, 31(10):1032–1038.
- Z. Lu and T. Yoneyama, (1999), Micro cutting in the micro lathe turning system, International Journal of Machine Tools and Manufacture, 39 1171–1183.
- Lu Z and Yoneyama T. (1999), Micro cutting in the micro lathe turning system, International Journal of Machine Tools manufacturing 39:1171–1183.

Table 1. Cutting parameter for cutting a taper on brass rod

Cutting Parameter			Unit
Spindle Speed	Roughing	1200	rpm
	Finishing	1500	rpm
Depth of Cut	Roughing	0.5	mm
	Finishing	0.2	mm
Feed Rate	Roughing	40	mm/min
	Finishing	10	mm/min
Cutting Thickness	Constant	0.5	mm

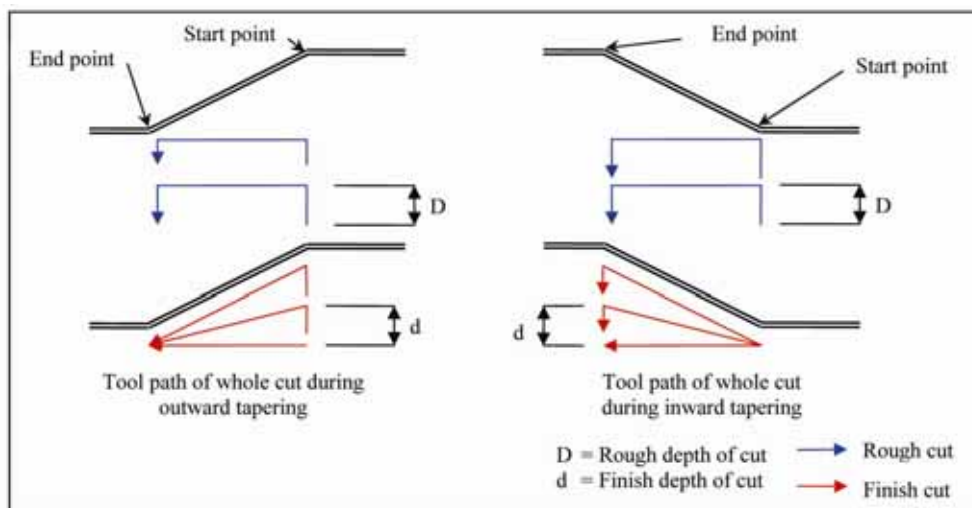


Figure 1. Whole cut tool path of tapered cutting

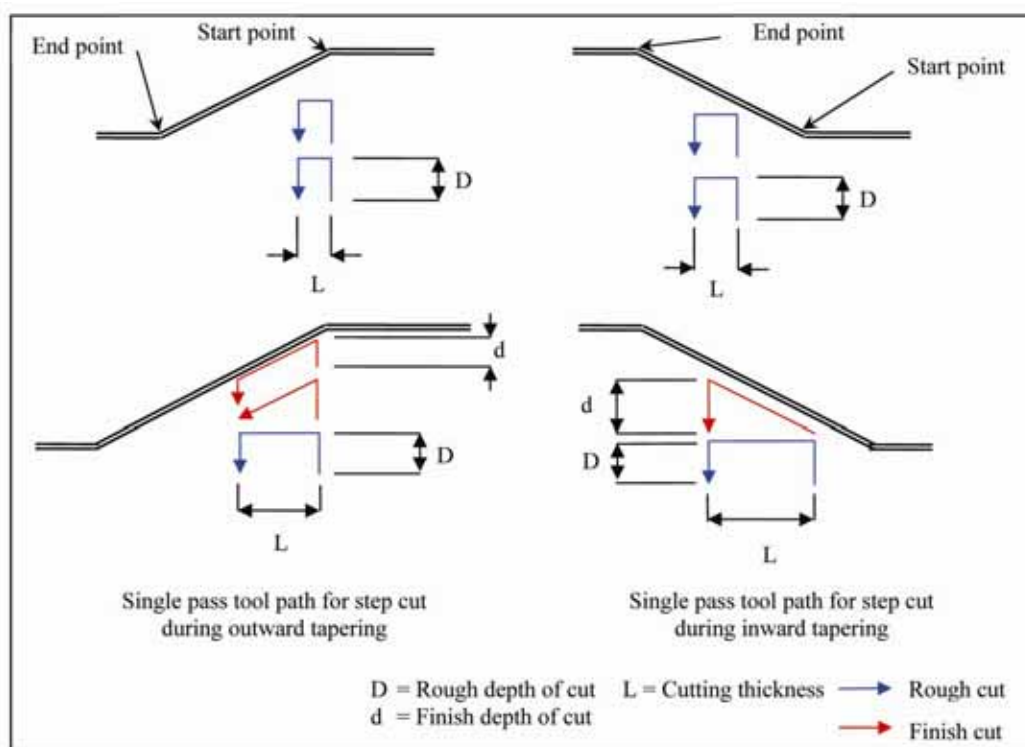


Figure 2. Step cut tool path of tapered cutting

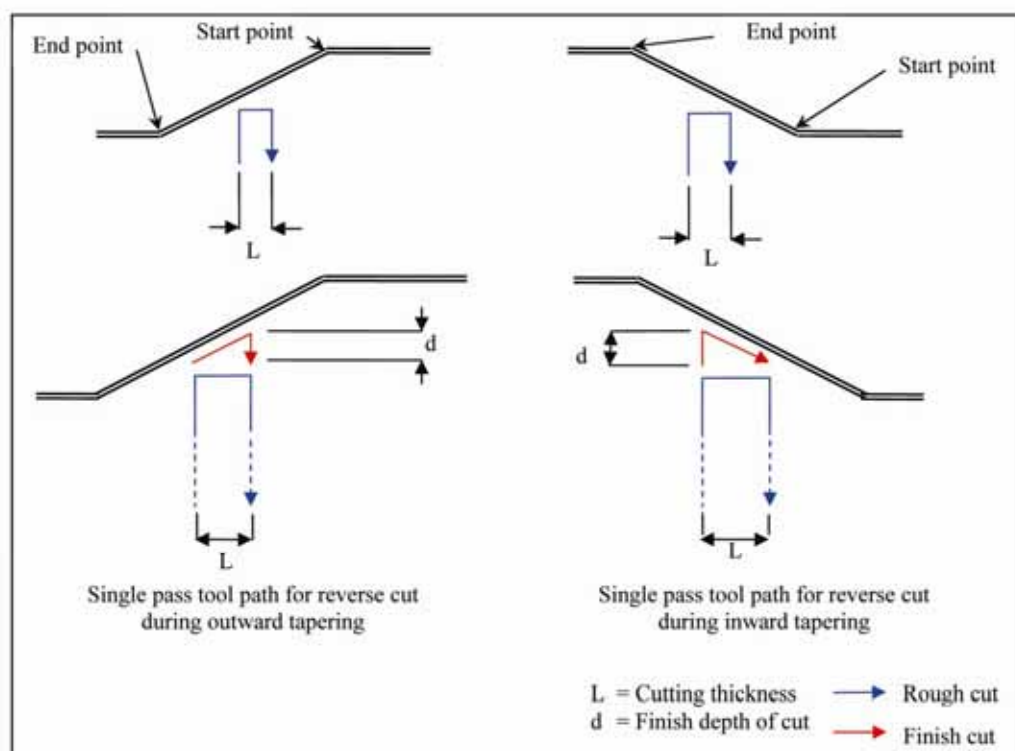


Figure 3. Reverse cut tool path of tapered cutting

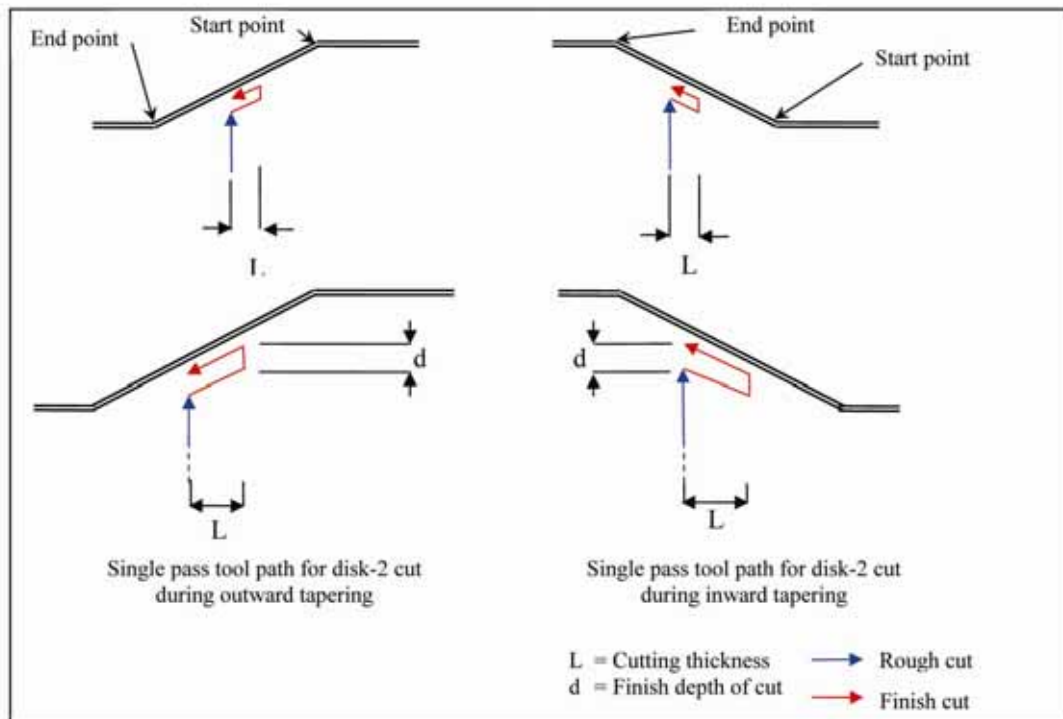


Figure 4. Disk-2 cut tool path of tapered cutting

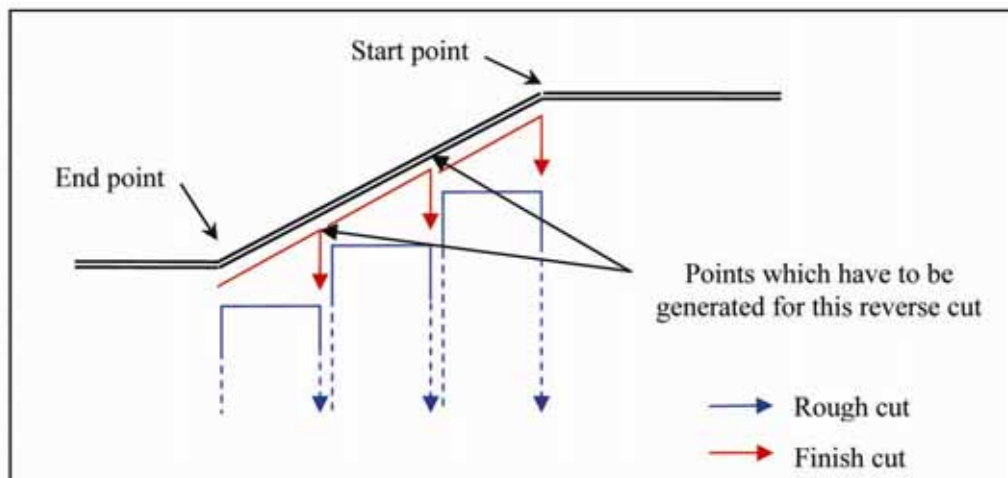


Figure 5. Points that need to be defined between start point and end point by software in reverse cut scheme

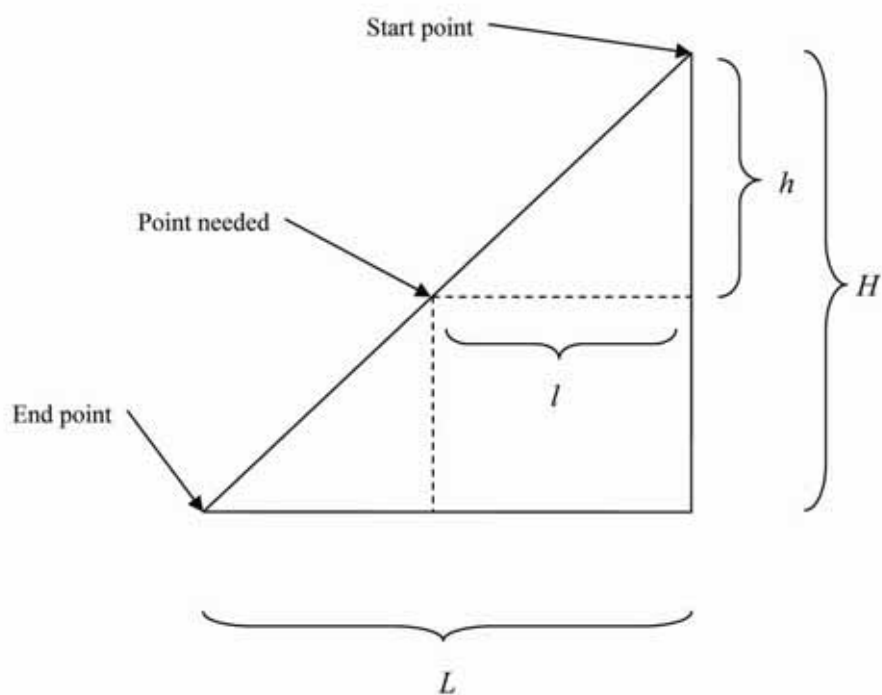


Figure 6. Picture to aid the definition of point between start point and end point

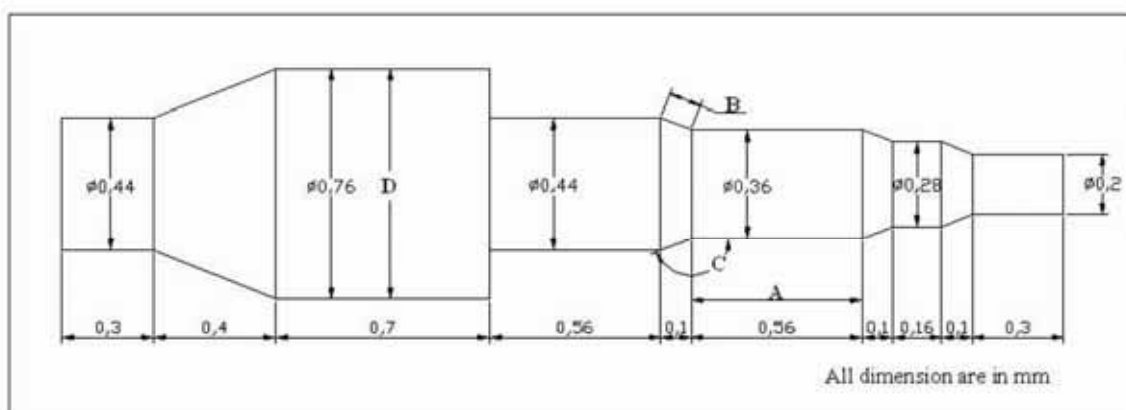


Figure 7. Dimensions of the workpiece feature for case study

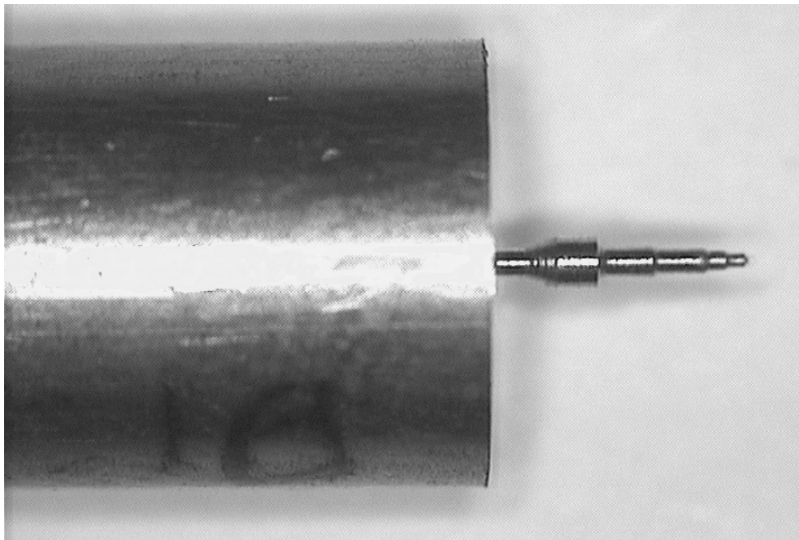


Figure 8. Sample of taper tool cutting of brass

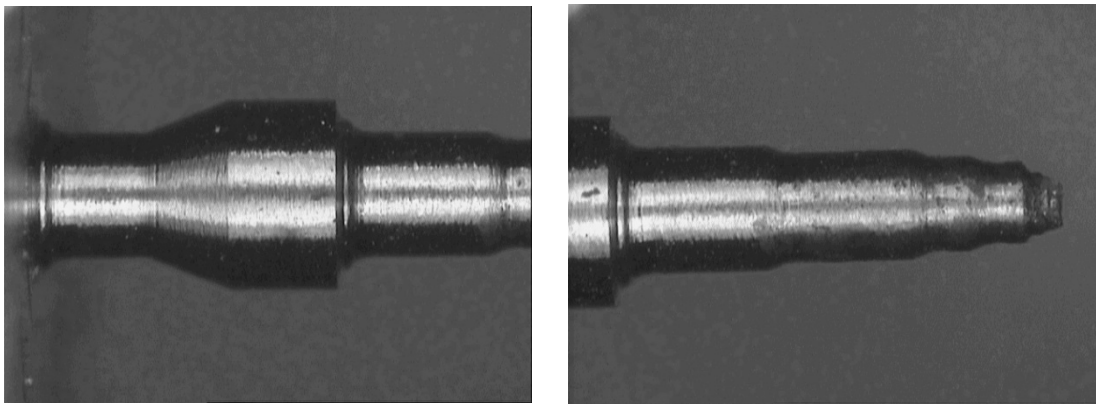


Figure 9. Taper cutting of brass rod using whole cut tool path.

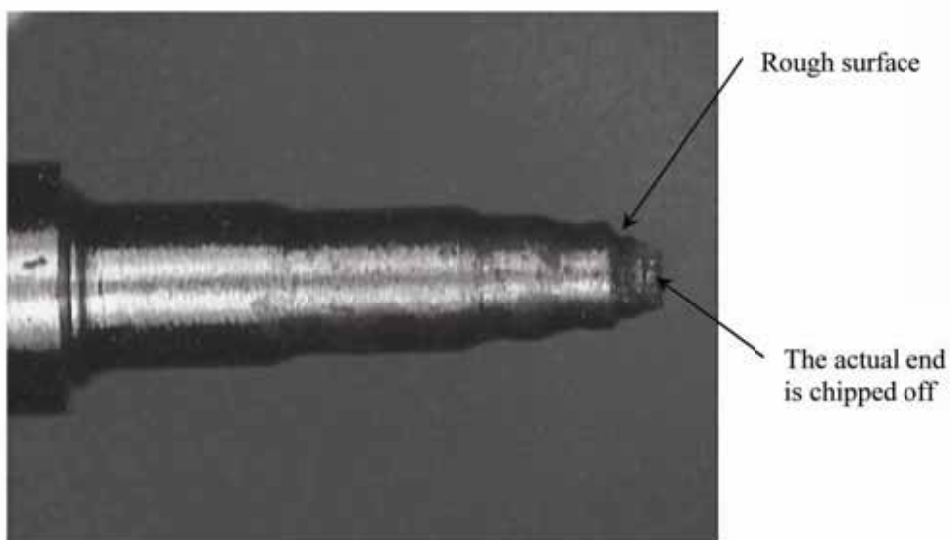


Figure 10. Defects in whole cutting operation

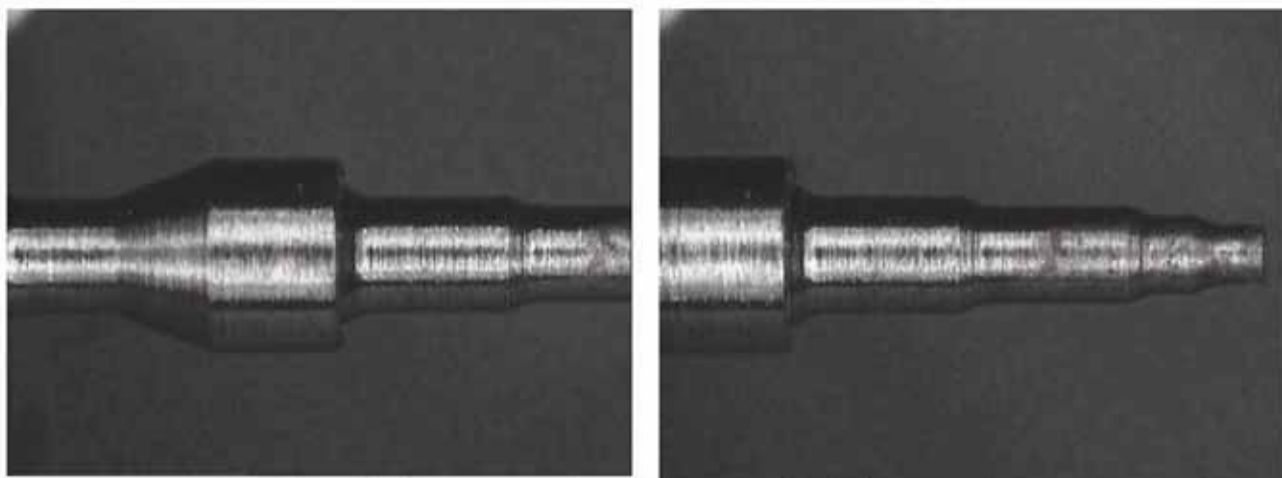


Figure 11. shows a part produce using step cut tool path for taper cutting.

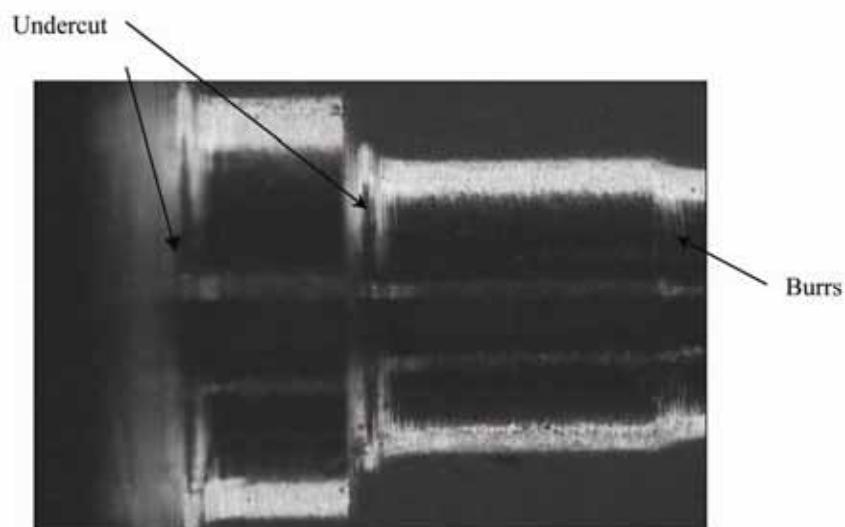


Figure 12. Defects in step cutting operation (scale of 1:0.0026)

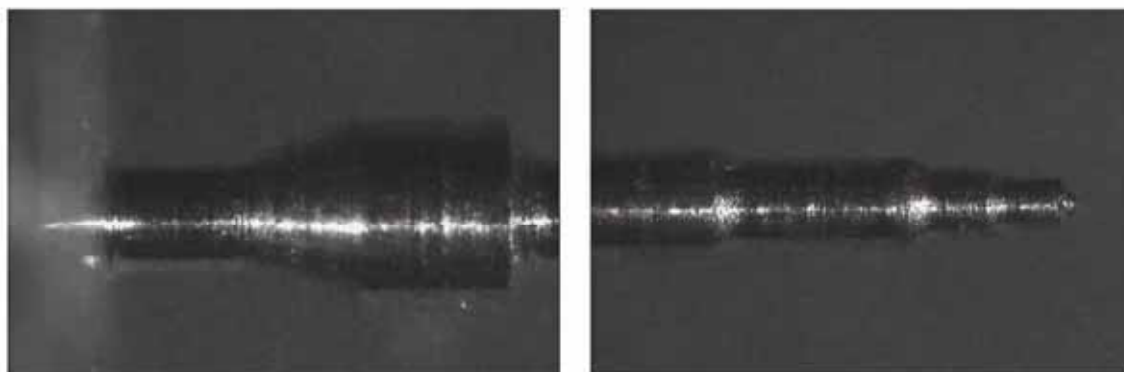


Figure 13. A part machined using reversed cut tool path for taper cutting.

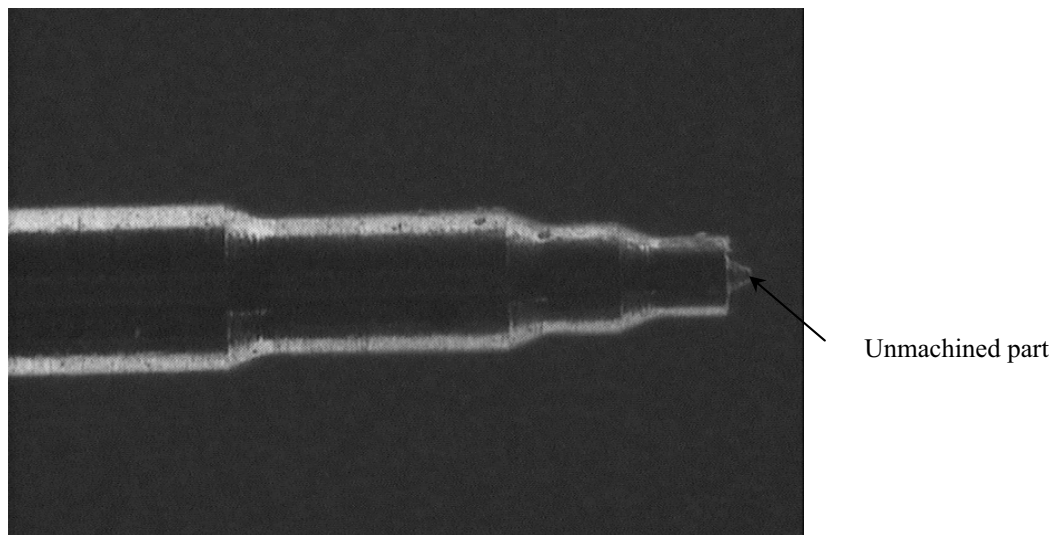


Figure 14. Defects in disk-2 cutting operation (scale of 1:0.000392)

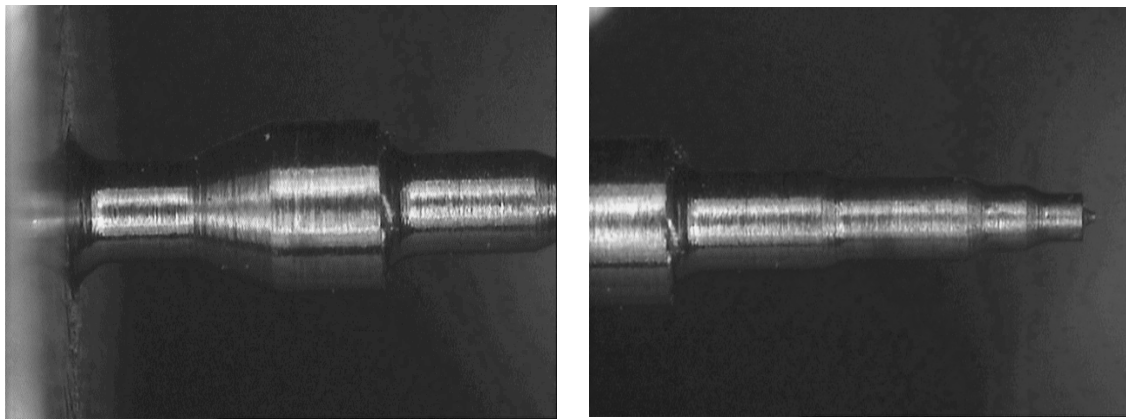


Figure 15. A part produce using Disk-2 cut tool path for taper cutting.

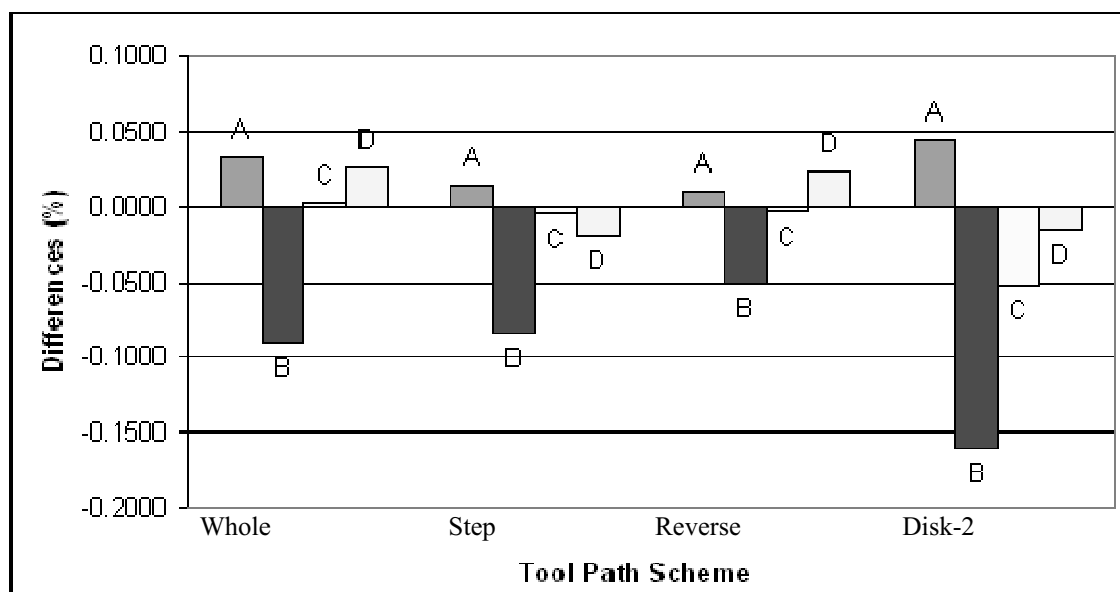


Figure 16. Graph of average percentage difference of the intended dimension from the machined part



The Dynamic Properties of a Perturbation System

Lizhen Zhang

Department of Mathematics
Tianjin Polytechnic University
Tianjin 300160, China
E-mail: lzhzhang@hotmail.com

Li Jia

Department of Mathematics
Tianjin Polytechnic University
Tianjin 300160, China
E-mail: jiali0@yahoo.cn

Abstract

In this paper, we study the dynamics of a perturbation system. Firstly, we consider the unperturbation system and give the types of the fixed points of the system by nullcline. Then we analysis the Dynamic behavior of the orbits around the fixed points. Further we study the dynamics of the perturbation system using the Melnikov methods, which possess some universality.

Keywords: Nullcline, Phase portrait, Melnikov Function, Manifold

1. Introduction

In recent years, Dynamical systems have had applications in science and engineering, more and more people recognize the nonlinearity, complexity and systematicness of the world. From the motion of the heavenly body to the movement of the microscopic particle all show the nonlinearity, complexity and systematicness (Huang, 2000). So the study for the action of the nonlinear systems is very important. In this paper, we study a nonlinear perturbation system (Liu, 1994; S, 1990). The system is

$$\begin{cases} \dot{x} = y \\ \dot{y} = x - x^3 - \varepsilon(y + f(x)) \end{cases} \quad (1)$$

where $(x, y) \in R^2$, $f(x)$ is a continuous function, $0 < \varepsilon \ll 1$.

When $\varepsilon = 0$, the unperturbation system of (1) is

$$\begin{cases} \dot{x} = y \\ \dot{y} = x - x^3 \end{cases} \quad (2)$$

First we consider the unperturbation system and give the types of the fixed points of the system by nullcline of the orbits of the system (2) and analyze the Dynamic behavior of the orbits around the fixed points, that is phase portrait. Further we study the dynamics of the perturbation system using the Melnikov methods, this methods possess some universality.

2. The phase portrait of the unperturbation system

In this paper, we will regard the ordinary differential equation possessing perturbation (1). Firstly, we think the unperturbation system of the system (1), that is (2).

From

$$\begin{cases} \dot{x} = 0 \\ \dot{y} = 0 \end{cases} \quad (3)$$

We have

$$\begin{cases} y = 0 \\ x - x^3 = 0 \end{cases}$$

Thus we know the system (2) has three fixed point(J,1999): $O(0,0)$, $A(-1,0)$, $B(1,0)$. We will study the vector field of the three fixed points by the nullcline of the orbits of the system (2). From this we can judge the types of these fixed points.

From (3), $y = 0, x = 0, x = \pm 1$ are four nullclines of the system (2). The four nullclines are divided into ten partitions each other. The ten partitions are:

- $(L_1) : x = 1, y > 0$
- $(L_2) : x = 1, y < 0$
- $(L_3) : 0 < x < 1, y = 0$
- $(L_4) : x > 1, y = 0$
- $(L_5) : -1 < x < 0, y = 0$
- $(L_6) : x = 0, y > 0$
- $(L_7) : x = 0, y < 0$
- $(L_8) : x = -1, y > 0$
- $(L_9) : x = -1, y < 0$
- $(L_{10}) : x < -1, y = 0$

And the four nullclines divide the plane xOy (R^2) into eight districts (the ten partitions are not included), that is

- $(A_1) : x > 1 \text{ and } y > 0$
- $(A_2) : x > 1 \text{ and } y < 0$
- $(A_3) : 0 < x < 1 \text{ and } y > 0$
- $(A_4) : 0 < x < 1 \text{ and } y < 0$
- $(A_5) : -1 < x < 0 \text{ and } y > 0$
- $(A_6) : -1 < x < 0 \text{ and } y < 0$
- $(A_7) : x < -1 \text{ and } y > 0$
- $(A_8) : x < -1 \text{ and } y < 0$

In order to confirm the direction of the orbits, we consider the nullclines of the ten partitions and the 8 districts. On the $\dot{x} = 0$, the nullcline is vertical. And on the $\dot{y} = 0$, the nullcline is horizontal (see figure 1). Because the situations is similarity, we only consider direction of the orbits through the half-line $L_1 : x = 1, y > 0$. In this situation, $x = 1, y > 0$, we have $\dot{x} > 0, \dot{y} = x - x^3 = 0$, so we can judge the direction of the orbits is horizontal to the right (see figure 1). On the left of the half-line $L_1 : x = 1, y > 0$, we have $0 < x < 1$, then $\dot{y} < 0, \dot{x} > 0, \frac{\dot{y}}{\dot{x}} > 0$. This is the direction of the orbits in district A_3 (see figure 1). The discussions of the districts $A_1, A_2, A_4 - A_8$ are similar to the district A_3 . So we have the following figure 1.

The ten partitions of divided by the four nullclines and the vector fields on the nullclines are:

- $(L_1) : x = 1, y > 0, \text{horizontal}, \dot{x} > 0, \text{to the right}$
- $(L_2) : x = 1, y < 0, \text{horizontal}, \dot{x} > 0, \text{to the left}$
- $(L_3) : 0 < x < 1, y = 0, \text{vertical}, \dot{y} > 0, \text{up}$
- $(L_4) : x > 1, y = 0, \text{vertical}, \dot{y} < 0, \text{down}$
- $(L_5) : -1 < x < 0, y = 0, \text{vertical}, \dot{y} < 0, \text{down}$
- $(L_6) : x = 0, y > 0, \text{horizontal}, \dot{x} > 0, \text{to the right}$
- $(L_7) : x = 0, y < 0, \text{horizontal}, \dot{x} < 0, \text{to the left}$
- $(L_8) : x = -1, y > 0, \text{horizontal}, \dot{x} > 0, \text{to the right}$
- $(L_9) : x = -1, y < 0, \text{horizontal}, \dot{x} < 0, \text{to the right}$
- $(L_{10}) : x < -1, y = 0, \text{vertical}, \dot{y} > 0, \text{up}$

The eight areas of divided by the four nullclines and the vector fields in these areas are:

- $(A_1) : x > 1 \text{ and } y > 0, \dot{y} < 0 \text{ and } \dot{x} > 0$
- $(A_2) : x > 1 \text{ and } y < 0, \dot{y} < 0 \text{ and } \dot{x} < 0$
- $(A_3) : 0 < x < 1 \text{ and } y > 0, \dot{y} > 0 \text{ and } \dot{x} > 0$
- $(A_4) : 0 < x < 1 \text{ and } y < 0, \dot{y} > 0 \text{ and } \dot{x} < 0$
- $(A_5) : -1 < x < 0 \text{ and } y > 0, \dot{y} < 0 \text{ and } \dot{x} > 0$
- $(A_6) : -1 < x < 0 \text{ and } y < 0, \dot{y} < 0 \text{ and } \dot{x} < 0$
- $(A_7) : x < -1 \text{ and } y > 0, \dot{y} > 0 \text{ and } \dot{x} > 0$
- $(A_8) : x < -1 \text{ and } y < 0, \dot{y} > 0 \text{ and } \dot{x} < 0$

From these, we can judge the fixed point $O(0,0)$ is a saddle point, $A(1,0), B(-1,0)$ are center point or focus. Of course we judge $A(1,0), B(-1,0)$ are center points of the system (2). So we can describe the phase portrait of the system (2) (see figure 2):

3. The Dynamics of the perturbation system

When $0 < \varepsilon \ll 1$, the dynamics of the system (1) is complexity, the period orbits and the rotation period orbits around the saddle point O and center points A, B of the system (2) are possibly rupture, forming stable and unstable manifolds. Following we judge the dynamics of the orbits by Malenkov methods [2].

Suppose

$$\begin{cases} P = y \\ Q = x - x^3 - \varepsilon(y + f(x)) \end{cases} \quad (4)$$

We have

$$\frac{\partial P}{\partial x} + \frac{\partial Q}{\partial y} = -\varepsilon < 0$$

By Benison criterion [3], we conclude that there doesn't exist closed orbits. So from there exist the small perturbation $-\varepsilon(y + f(x))$, the period orbits, homoclinic orbits and the rotation period orbits of (2) are all rupture. We must judge the change of the stable and unstable manifolds by Melnikov methods. Because the perturbation $(0, -(y + f(x)))$ is autonomous, the Melnikov function of the orbits $q_0(t)$ of (1) is

$$\begin{aligned} M(t_0) &= \int_{-\infty}^{+\infty} q_0(t) \wedge g(q_0(t)) dt \\ &= \int_D \left(\frac{\partial g_1}{\partial x} + \frac{\partial g_2}{\partial y} \right) dx dy \\ &= - \int_D \int dx dy \\ &= -S_D < 0 \end{aligned}$$

where $g = (g_1, g_2)$, $g_1 = 0$, $g_2 = -(y + f(x))$, D is the Area from one side $x > 0$ of the orbits of (1). From $M(t_0) < 0$, we can conclude the unstable manifolds which are included the stable manifolds. The orbits is showed in figure 3:

4. Conclusion

Judging the direction of the orbits by the nullcline is a good method, which is simple and clear. The Melnikov methods of orbits is maneuverability. This is rigorously analysis methods and this method is used others fields.

References

- Huang Runsheng, *Chaos and Application*, Wuhan University Press, Wuhan, (2000).
 J.Guckenheimer and P.holmes, *Nonlinear Oscillators, Dynamical Systems, and Bifurcations of Vector Fields*. Springer, (1999).
 Liu Zengrong, *Perturbation Criteria For Chaos*, Shanghai Scientific and Technological Education Publishing House, Shanghai, (1994).
 S.Wiggins, *Introduction to applied nonlinear Dynamical Systems and Chaos*, Spring-Verlag, (1990).

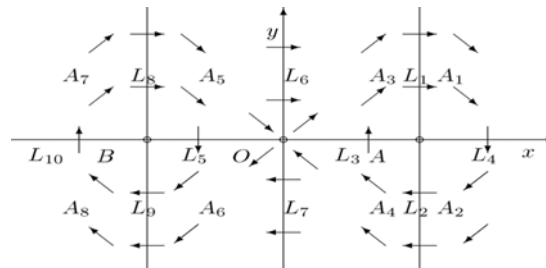


Figure 1. The nullclines of the system (2)

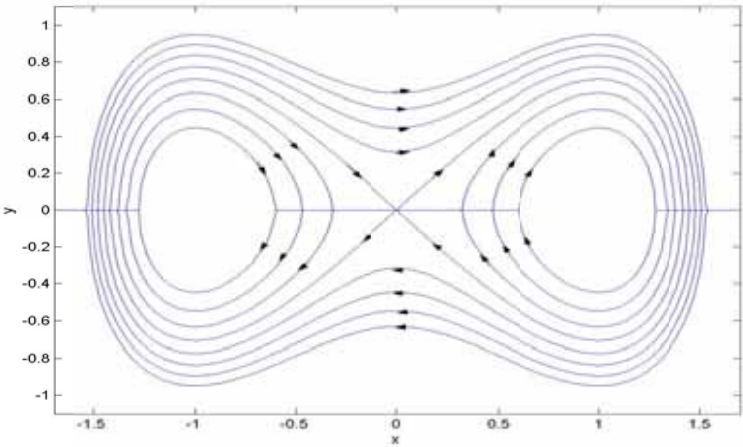


Figure 2. the phase portrait of the system (2)

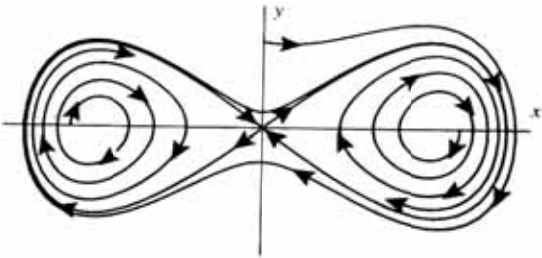


Figure 3. The orbits portrait of the perturbation system (1)

Editorial Board

Ahmad Mujahid Ahmad Zaidi Universiti Tun Hussein Onn Malaysia, Malaysia

Hamimah Adnan Universiti Teknologi MARA, Malaysia

J S Prakash Sri Bhagawan Mahaveer Jain College of Engineering, India

Musa Mailah Universiti Teknologi Malaysia, Malaysia

Sujatha. C.H Cochin University of Science and Technology, India

Sundus H Ahmed Ministry of Science and Technology, Iraq

Susan Sun Canadian Center of Science and Education, Canada

Sutopo Hadi University of Lampung, Indonesia

Wenwu Zhao Macrothink Institute, USA

A journal archived in Library and Archives Canada
A journal indexed in CANADIANA (The National Bibliography)
A journal indexed in AMICUS
A journal indexed in Zentralblatt MATH
A peer-reviewed journal in applied science research

Modern Applied Science

Monthly

Publisher Canadian Center of Science and Education

Address 4915 Bathurst St. Unit # 209-309, Toronto, ON. M2R 1X9

Telephone 1-416-208-4027

Fax 1-416-208-4028

E-mail mas@ccsenet.org

Website www.ccsenet.org

Printer William Printing Inc.

Price CAD.\$ 20.00

